



MONASH University

**Thermohaline Mixing in Low-Mass
Red Giant Stars**

Kate HENKEL

Supervisors:

Associate Professor Amanda I. KARAKAS

Professor John C. LATTANZIO

*A thesis submitted for the degree of Doctor of Philosophy at Monash
University in 2019*

Declaration of Authorship

I hereby declare that this thesis contains no material which has been accepted for the award of any other degree or diploma at any university or equivalent institution and that, to the best of my knowledge and belief, this thesis contains no material previously published or written by another person, except where due reference is made in the text of the thesis.

This thesis includes 2 original papers published in peer reviewed journals. The core theme of the thesis is stellar evolution of red giants. The ideas, development and writing up of all the papers in the thesis were the principal responsibility of myself, the student, working within the School of Physics & Astronomy under the supervision of Associate Professor Amanda Karakas and Professor John Lattanzio.

In the case of Chapters 1, 2, 3, 4, 5, and 6, my contribution to the work involved the following:

Thesis Chapter	Publication Title	Status	Nature and % of student contribution	Co-author name(s) Nature and % of Co-author's contribution	Co-author(s), Monash student
1, 2, 3, 4, 5	A phenomenological modification of thermohaline mixing in globular cluster red giants	Published	70%. Data analysis, writing of manuscript	1. Amanda Karakas, input into manuscript 15% 2. John Lattanzio, input into manuscript 15%	No No
6	Thermohaline mixing in extremely metal-poor stars	Published	70%. Data analysis, writing of manuscript	1. Amanda Karakas, input into manuscript 15% 2. Andrew Casey, input into manuscript 5% 3. Ross Church, input into manuscript 5% 4. John Lattanzio, input into manuscript 5%	No No No No

I have renumbered sections of submitted or published papers in order to generate a consistent presentation within the thesis.

Student signature: _____

Date: _____

The undersigned hereby certify that the above declaration correctly reflects the nature and extent of the student's and co-authors' contributions to this work. In instances where I am not the responsible author I have consulted

with the responsible author to agree on the respective contributions of the authors.

Main Supervisor signature:

Date:

Contents

Declaration of Authorship	iii
Abstract	ix
Acknowledgements	xi
1 Introduction	1
1.1 Low-mass stellar evolution	1
1.1.1 Introduction to stellar evolution	1
1.1.2 The importance of studying stellar chemical abundances	2
1.1.3 From the pre-main sequence to the Red Giant Branch	4
1.1.4 Hydrogen burning processes	5
1.1.5 After the main sequence	10
1.1.6 The Red Giant Branch	12
1.1.7 Extra mixing and the importance of carbon and lithium	16
1.1.8 Meridional circulation	20
1.1.9 Rotation	25
1.1.10 Thermohaline mixing	27
Problems with thermohaline mixing	28
1.1.11 Evolution to the Red Giant Branch tip and beyond	29
1.2 Observations of low-mass stars	31
1.2.1 Globular and open clusters in the Milky Way	31
1.2.2 Observations used in this thesis	32
Clusters: NGC6397	32
Other observations: SAGA database, Gaia-ESO, APOGEE	32
2 The Evolution code MONSTAR	37
2.1 Introduction	37
2.2 Equations of stellar structure	38
2.2.1 Constitutive equations	39
Pressure	39
Opacity	40
Energy	44
2.2.2 Boundary conditions	45
2.2.3 Solving the equations of stellar structure	45
Henyey method	46
2.2.4 Meshing routine	49
2.2.5 Timestepping	50
2.3 Reaction rates	50
2.4 Mass loss	50
2.5 Convection	51

Formal convective border	53
2.5.1 Convective overshoot	53
2.6 Thermohaline mixing	54
2.6.1 Mixing timescales	54
2.6.2 Nuclear burning timescales	55
3 Modifications to the Evolution code	59
3.1 Adding an additional temperature dependence	59
3.1.1 Choosing T_{crit}	60
3.1.2 Diffusion coefficients	66
4 The Nucleosynthesis code MONSOON	71
4.1 Introduction	71
4.2 Reaction rates	72
4.3 Solution method	72
4.3.1 Meshing routine	72
Mixing and mesh moving	73
Calculating compositions	73
4.3.2 Thermohaline mixing and convection: Two stream advective mixing	74
4.3.3 Diffusive mixing	76
5 Thermohaline mixing in globular cluster red giants	79
5.1 Introduction	79
5.2 Stellar models	80
5.2.1 Fitting stellar parameters	80
FDU and RGB bump magnitudes	81
Hertzsprung-Russell diagram	81
5.2.2 Nuclear burning timescales in our standard model	85
Lithium and carbon burning timescales in the ther- mohaline region	85
5.2.3 Motivation for studies and observational limitations	90
5.3 Test Cases and Results	94
5.3.1 Case 1: Independently changing v and l in the two stream advective mixing scheme	94
Single parameter results	94
5.3.2 Case 2: Changing v and l to maintain constant D in the two stream advective mixing scheme	95
Results	95
5.3.3 Case 3: Changing f_u and f_d in the two stream advective mixing scheme	95
Results	99
5.3.4 Case 4: Changing the thermohaline coefficient in the diffusive mixing scheme	99
Results	99
Evolution code vs nucleosynthesis code	101
5.4 Discussion and Conclusions	101
6 Thermohaline mixing in extremely metal-poor stars	107
6.1 Introduction	108
6.2 Theoretical models	110

6.3	Results	111
6.4	Discussion	111
6.4.1	Carbon-poor/lithium rich giants	116
6.4.2	Theoretical carbon offsets	117
6.4.3	CEMP star frequency	118
6.5	Conclusions	118
7	Thermohaline mixing in the Galactic disc	119
7.1	Introduction	119
7.1.1	Extra mixing	119
7.1.2	APOGEE	120
7.1.3	Gaia-ESO	123
7.2	Observations	125
7.2.1	Clusters	128
	NGC6752	129
	NGC2808	130
	NGC1851	130
	47 Tucanae (NGC104)	130
	NGC5927	130
	NGC2516	130
	NGC2243	131
	NGC4815	131
	NGC2547	131
	NGC6005	132
	M67 (NGC2682)	132
	NGC2264	132
	NGC6633	132
	NGC2451	133
	NGC6705	133
7.3	Models	133
7.4	Results	134
7.4.1	Solar and super-solar metallicities ($[\text{Fe}/\text{H}] = 0.0, +0.3$)	134
	Lithium	134
	Carbon	142
7.4.2	Sub-solar metallicities ($[\text{Fe}/\text{H}] = -0.5, -1.0, -1.5$)	142
7.5	Discussion	144
7.5.1	Solar and super-solar metallicities ($[\text{Fe}/\text{H}] = 0.0, +0.3$)	144
7.5.2	Sub-solar metallicities ($[\text{Fe}/\text{H}] = -0.5, -1.0, -1.5$)	145
7.5.3	Conclusions	146
7.6	Acknowledgements	147
7.7	Appendix	148
8	Conclusions and Future work	165
8.1	Concluding remarks	165
8.2	Future work	170
	Bibliography	173

“The obstacle in the path becomes the path. Never forget, within every obstacle is an opportunity to improve our condition.”

Ryan Holiday

The Obstacle Is the Way: The Timeless Art of Turning Adversity to Advantage

MONASH UNIVERSITY

Abstract

Faculty of Science

School of Physics and Astronomy

Doctor of Philosophy

Thermohaline Mixing in Low-Mass Red Giant Stars

by Kate HENKEL

Thermohaline mixing is a favoured mechanism for the so-called “extra mixing” on the red giant branch of low mass stars. It is triggered by the molecular weight inversion created above the hydrogen shell during first dredge-up when helium-3 burns via ${}^3\text{He}({}^3\text{He}, 2p){}^4\text{He}$. Modelling thermohaline mixing is a challenge. Traditionally, it is modelled as a diffusive process, though it is almost certainly advective. Additionally, using the standard linear 1D diffusive mixing scheme, we cannot simultaneously match carbon and lithium abundances with observations without using diffusion coefficients that are different by a factor of around 10. We investigate an advective mixing approach, as well as modifications to the standard 1D linear thermohaline mixing formalism. We develop a modified diffusive scheme with an explicit temperature dependence that can simultaneously fit carbon and lithium abundances to NGC6397 stars. We then discuss our application of this modified regime to extremely metal-poor (EMP) stars and to stars in higher metallicity regimes, namely $-1.5 < [\text{Fe}/\text{H}] < +0.3$. The main conclusion our results infer is that the extra mixing mechanism needs further investigation and more observations are required, particularly for stars in different clusters spanning a range in metallicity.

Acknowledgements

At the conclusion of this journey that has been my candidature, I want to broadly acknowledge the support and contribution of everyone I have known and interacted with. Your influence on my life has shaped me into who I am today.

Firstly, I want to thank the people who have shared offices with me. Anyone who has been at Monash for at least a couple of years knows that changing offices was a frequent requirement, and while I have shared offices with many students, it is the office that I finished my thesis in and its occupants that I want to give the most thanks to. It might be strange thanking office mates, but this group were great and made coming into the office fun. They were constantly welcoming, supportive, and interested in the daily chores and struggles of not only me but everyone. So, to Dave, Zac, Chloe, Conrad, Hayley, Mel, James, Daniel, Lucy, and Adelle, I wish you good luck and know you will all finish your theses in style. The friends I have made during my Ph.D. have kept me in the real world by providing fun times away from the thesis, and include Bec, Vaishali, and Gen. They have played a vital part in maintaining and improving my wellbeing.

There were many staff members in the School that I can thank for their general warm countenance and words of wisdom and support, though a few special members stick out amongst the rest. Firstly, Jean and Karen, who are wonderful human beings that were both so supportive, genuine, and caring. I also want to thank Alexis and Kris, both postgraduate coordinators during my time, who have been wonderfully helpful and supportive.

I need to make a special mention to a staff member who has shown me what passionate educators can do, and has given me so many opportunities that I can barely begin to thank them enough. Dr Jasmina Lazendic-Galloway, the staff member in the School with the longest surname, but also a never-ending supply of warm energy and enthusiasm for all she has a passion for. She opened me up to a world of teaching and education research that I never even realised was there, and has given me the opportunity to pursue my love of teaching and education further. Her generous and ceaseless support of me has been so valuable, and she may never know how much she has done for me, or what she has given me.

Along the same lines, I also want to thank the teaching associates I have worked with and the staff in the Physics and Astronomy Collaborative Environment (PACE) office. Lisa, Jenny, and Matthew were wonderful to work with, and I hope I get to work with them again in the future.

A lot has happened since I pursued my goal of becoming a Doctor of Philosophy. As I sit and write these acknowledgements, I realise that I have been editing this document for a long time, I am not the same person as I was when I first began, nor am I the same person as I was yesterday. I have learned much during my postgraduate studies, not just about astronomy, but about the world in which I live, myself, my relationships, and other people. The hardships encountered during my time studying forced me to pursue hobbies, and these hobbies gave me the opportunity to meet wonderful people, many of whom I can thank for keeping me sane. Once this

chapter of my life is over, I want to follow some new dreams that I have. I discovered my love of yoga and want to attain my yoga teacher training certification. I also discovered obstacle course racing and want to dedicate more time to training for races. These two aspects of my life allowed me to meet many people who have shaped where I have gone in life, and to those people I give them thanks. These people include Janie (my wonderful mentor), Adam, and Shane.

My family living back in Queensland need to be mentioned. Words of support and encouragement cannot go unappreciated. Especially my beautiful twin sister Emily. We have been going through our theses together (albeit many kilometres apart) but I thought about her every day. Her yearly visits to Melbourne did so much for my happiness and mean so much to me, so thank you from the bottom of my heart. A twin is hardly a relationship that can easily be described, and we share a bond like no other, and this has kept my emotions high.

Second last, I wish to thank my supervisors. Firstly, Professor John Lattanzio was instrumental in me starting a Ph.D. at Monash. Indeed, he "hired" me (long story) when I was an Honours student and took a big chance in doing so. I cannot express my gratitude that he took that chance on me and gave me the opportunity of a lifetime to follow my dreams of studying astrophysics. Secondly, Associate Professor Amanda Karakas has been incredible. She is unbelievably kind, genuine, caring, patient, knowledgeable, and I aspire to be like her. Her assistance and supervision has been invaluable.

And lastly, I want to thank the person with whom I get to discover all things in life with; my husband, Douglas. He has known me since I began my undergraduate back in 2009 and has been with me the entire journey. Learning how to manage me and my emotions has not been easy, but it has been a task that he has devoted unconditional time, energy, and love towards since before even taking any vows. I couldn't imagine my life without him - he keeps me strong, holds me up, and gives me life and love.

Chapter 1

Introduction

The content in the following sections was published in Henkel, K., Karakas, A.I., and Lattanzio, J.C. (2017), “A phenomenological modification of thermohaline mixing in globular cluster red giants”, *The Monthly Notices of the Royal Astronomical Society*, 469, 4, 4600-4612.

- §1.1.6 (except the first sentence and the last two sentences of paragraph 1),
- §1.1.7 (except the last sentence of paragraph 1, rewording of paragraph 2 to include a short discussion of the C/N ratio, the last paragraph)
- §1.1.10 (except the second sentence of paragraph 3 (which was altered from the published version), the last 2 sentences of paragraph 3, the second and third sentences of paragraph 2 in the **Rotation and other mixing mechanisms** section, and references to Figs. 1.14 and 1.15),
- Paragraph 2 in §1.2.1,
- §1.2.2, and
- Fig. 1.7.

Paragraph 2 in §1.2.2 was published in Henkel, K., Karakas, A.I., Casey, A.R., Church, R.P., and Lattanzio, J.C. (2018), “Thermohaline mixing in extremely metal-poor stars”, *Astrophysical Journal Letters*, 863, 1.

No other figures in this chapter have been published by the author and are referenced accordingly.

1.1 Low-mass stellar evolution

1.1.1 Introduction to stellar evolution

Low-mass stars are categorised as stars with masses $\lesssim 2.5 M_{\odot}$ ¹, where M_{\odot} is the mass of our Sun. Aside from the fact that our Sun is low-mass and its fate is of general interest to life on Earth, low-mass stellar evolution is

¹This mass distinction is based primarily on: 1) burning pathways of hydrogen on the main sequence, 2) the structure of the core after the main sequence (hydrogen burning), and 3) the ignition mechanism of helium at the end of the first giant branch. These events are detailed in this thesis chapter.

an important area of astronomical research. This is because low-mass stars are incredibly long-lived, unlike higher-mass stars that have very brief lifetimes. The lifetimes of low-mass stars are several billions of years long, e.g., our Sun will live for approximately 10 Gyr, making low-mass stars a “window” to the past because they retain the chemical signatures (in terms of location and time) of the protostellar gas from which they were born.

We can estimate the lifetime of a star if we know its mass (how much fuel it has) and luminosity (how quickly it is burning its fuel). Stars are predominantly comprised of hydrogen² and will consequently spend the majority of their lives burning hydrogen as their main fuel source (around 80% of their total lifetime, Schaller et al., 1992). Stellar mass plays the dominant role in determining the lifetime of a star. Stars with lower masses do not need to generate as much nuclear energy to counteract the opposing gravitational force compared to their higher-mass counterparts. Low-mass stars therefore live longer than high-mass stars because they use up their hydrogen fuel source much more slowly, e.g. a $0.8 M_{\odot}$ star will live ~ 1.7 times longer on the main sequence than the Sun, or around 17 Gyr, which is longer than the age of the Universe. The long lifetimes of low-mass stars mean that they have not lived long enough to evolve off the main sequence and have retained the majority of their primordial stellar material for significant portions of the lifetimes of the Universe and the Milky Way Galaxy.

1.1.2 The importance of studying stellar chemical abundances

To better understand stellar evolution, we observe the surface composition of stars. By observing many stars in different evolutionary phases, we can infer how the surface chemical abundances change over time. Astrophysicists can make predictions about how abundances will change over time by creating stellar models, which are then compared to observations of stellar populations, e.g. old low-mass stellar populations similar to those used in this thesis.

When a star dies, the interstellar medium is enriched with the material ejected by the star and the next generation of stars is born from this enriched gas. The chemical trends we observe reflect the nucleosynthesis that occurred in a previous stellar generation (or generations), and old stars therefore show very little enrichment. These stars have a small amount of elements other than hydrogen and helium, namely “metals”, and are considered “metal-poor” or have a low “metallicity” (e.g. our Sun has a metal content of around 1.4% by mass). These old, low-metallicity stars were presumably formed when the Milky Way was young and therefore trace star formation and stellar evolution in a low-metallicity environment. These stars retain the chemical signature and reflect the nucleosynthesis of some of the first stars in the Universe and Galaxy. By studying low-mass stellar evolution and this star formation-death cycle, we gain an understanding of the formation and chemical evolution of galaxies such as our own Milky Way.

²As a useful reference, the Sun is approximately 73.8% hydrogen by mass (Asplund et al., 2009).

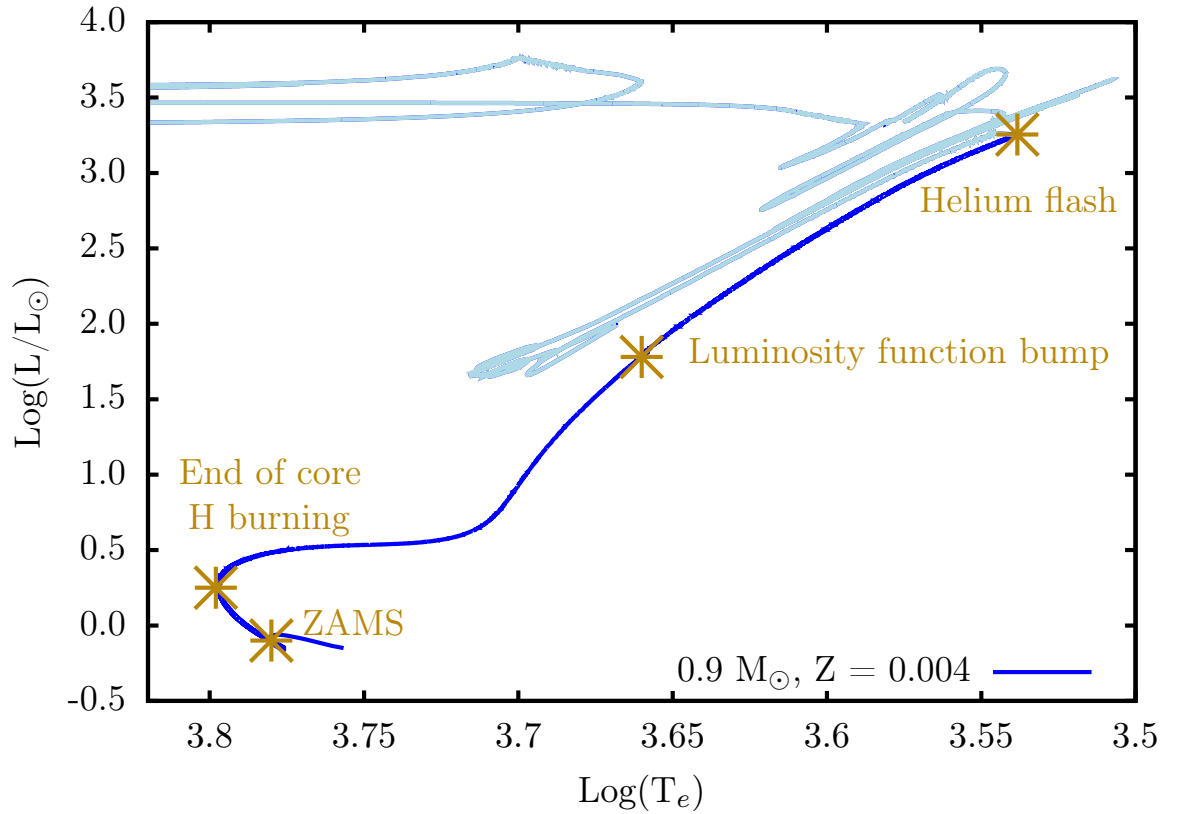


FIGURE 1.1: The evolutionary path of a $0.9M_{\odot}$, metallicity $Z = 0.004$ stellar model in the Hertzsprung-Russell diagram. Labelled on the curve are evolutionary stages, being the zero-age main sequence (“ZAMS”), end of core hydrogen burning (“End of core H burning”), the bump in the luminosity function (“Luminosity function bump”), and the helium flash (“Helium flash”). Details of these events are given in text. The dark blue curve represents evolution to the tip of the Red Giant Branch and the light blue curve shows further evolutionary stages including core helium burning and the Asymptotic Giant Branch. Stellar model provided by A. Karakas.

Where do these metals come from? The lightest elements in the Universe (i.e. hydrogen, helium, and trace amounts of lithium) were created in the Big Bang, and all other elements are created in stellar interiors³. Therefore, stellar mass also plays a vital role in the distribution of elemental abundances observed on Earth.

Stars with initial mass $\gtrsim 0.06M_{\odot}$ have cores hot enough to fuse hydrogen into helium, and stars with mass $\gtrsim 0.5M_{\odot}$ are able to undergo helium burning to produce carbon and oxygen (these processes are more detailed than stated here and are discussed further in §1.1.3). Although not the main focus of this thesis, stars with mass $\gtrsim 8M_{\odot}$ can ignite carbon, while stars with mass $\gtrsim 11M_{\odot}$ can ignite silicon to produce iron (and elements near iron on the periodic table, Phillips, 1999).

Some of the metals produced during a star’s life following the nucleosynthetic processes stated above are then expelled into the interstellar medium via processes such as supernova explosions or stellar winds (depending upon the initial mass of the star). The main factor determining the metallicity of a star is the composition of the proto-stellar gas from which it was born, which is polluted by gas released by previous stellar generations. Other factors include late stellar burning stages and significant mass loss.

This thesis focuses on the evolution of low-mass stars after core hydrogen burning when they have become red giants. In §1.1.3 I briefly describe the evolution of a low-mass star from the pre-main sequence to the first ascent red giant branch (RGB). In §1.1.6 I discuss the RGB in more detail, and in §1.1.11 I briefly discuss evolution beyond the RGB. Finally in §1.2 I discuss observations of low-mass stars and the observations used in this thesis.

1.1.3 From the pre-main sequence to the Red Giant Branch

Before focusing on the stellar lifecycle, it is pertinent to describe the way astronomers represent the evolution of a star. This is done via a Hertzsprung-Russell (HR) diagram, which plots stellar luminosity as a function of surface temperature. Fig 1.1 is an example of a HR diagram for a low-mass star of $0.9 M_{\odot}$ with metallicity $Z = 0.004$, where the value of Z satisfies $1 = X + Y + Z$, and X is the mass fraction of hydrogen, Y is the mass fraction of helium, and Z is the mass fraction of all other elements combined. For reference, the Sun has $Z = 0.014$.

Before reaching the main sequence (described above and marked as “ZAMS”, or zero-age main sequence, in Fig. 1.1, which denotes the location on a HR diagram of central hydrogen ignition), a star will follow a mass-dependent pre-main sequence track that maps its evolution from formation to stable main sequence hydrogen burning. For reasons stated above, we only focus our discussion on stars with masses $< 2.5 M_{\odot}$ and summarise a low-mass star’s descent to the main sequence:

³The exceptions to this are boron and beryllium, which are created from cosmic ray annihilation (Iliadis, 2007).

Stars with mass $M < 0.06M_{\odot}$: Core temperatures are not high enough to ignite hydrogen and these very low-mass stars eventually fade as brown dwarfs (Iben, 1965).

Stars with mass $0.06 < M < 0.35M_{\odot}$: As a star contracts towards the main sequence, energy production is generated through gravitational collapse, therefore the temperature is higher in the centre and the stellar surface becomes very cool. This produces a temperature gradient, and at these cool temperatures molecules absorb much of the released energy. This, combined with the temperature gradient, causes the star to be fully convective (Iben, 1965).

Stars with mass $M > 0.35M_{\odot}$: Here we focus on pre-main sequence tracks in the HR diagram. These stars begin their pre-main sequence lives with low surface temperatures, interiors dominated by convection, and are observed at the right-most part of the HR diagram. A star will contract and move towards the main sequence on the HR diagram⁴. During contraction, core temperatures rise and the interior becomes less opaque to radiation. Under these conditions, the most efficient form of energy transport in the interior at this time is radiation. Consequently, the core becomes radiative and grows with time (Iben, 1965).

During this phase of core growth prior to any nuclear burning, the star changes energy transport mechanisms from fully convective to almost fully radiative (a small convective outer layer still exists). Convection there cannot mix and redistribute a significant amount of stellar material and matter will preferentially “fall” towards the radiative centre (Iben, 1965). At temperatures of around 10^6 K, deuterium will burn according to ${}^2\text{D}(p,\gamma){}^3\text{He}$. Lithium, beryllium, and boron are also easily destroyed via proton captures to produce ${}^4\text{He}$ at these temperatures. Although deuterium, lithium, beryllium, and boron are almost completely converted into helium, their initial abundances are so low that this stage of nucleosynthesis changes the abundance of helium very little (Salaris and Cassisi, 2006).

The star moves to the left in the HR diagram, and this shift is more significant with increasing stellar mass.

1.1.4 Hydrogen burning processes

After pre-main sequence contraction onto the main sequence, stars less massive than $1.2 M_{\odot}$ will establish stable hydrogen burning in the core dominated by the proton-proton burning chains (or pp chains). The details of the pp chains are discussed in more detail in Chapter 2, however a summary of the three pp chains is below and illustrated in Fig. 1.2.

⁴During this contraction, there can also be a phase of accretion. This is a mechanism for forming T Tauri stars, an observed class of contracting pre-main sequence stars (Stahler, Shu, and Taam, 1980).

ppI:



ppII:



ppIII:



Of particular relevance to this thesis is the production and destruction of lithium. Equation 1.1b shows that lithium is created by electron capture onto beryllium and destroyed by proton capture to produce ${}^4\text{He}$. This electron capture occurs at a rate that is very weakly dependent upon temperature (Iliadis, 2007). Lithium destruction by proton capture however occurs rapidly at temperatures higher than ~ 2 MK. Therefore, lithium is easily destroyed in stellar interiors.

Cameron and Fowler (1971) postulated a scenario, known as the Cameron-Fowler Beryllium Transport mechanism, where lithium could be created in stars if ${}^7\text{Be}$ were transported to a cool region of the star before capturing an electron to produce ${}^7\text{Li}$ (i.e. the ppII chain). The crucial points in this scenario are that the transport of beryllium prior to electron capture must be rapid, and the beryllium must be transported to a region where temperatures are too low for lithium burning. In low-mass red giant stars, the outer envelope usually matches this temperature criterion. Therefore, a mixing mechanism must be present that brings beryllium from the burning region towards the surface. This mixing mechanism is discussed further in §1.1.7.

Hydrogen is also destroyed via the carbon-nitrogen-oxygen, or CNO, cycles when temperatures are $\gtrsim 5 \times 10^6$ K (Arnett, 1996) and is the dominant energy production source in stars more massive than $1.2 M_{\odot}$. The CNO cycles are shown in Fig. 1.3. Specifically, there are four sub-cycles in the CNO cycle, with the third and fourth sub-cycles occurring at temperatures of several 10^7 K. The CNO sub-cycles are detailed below (Arnett, 1996; Pagel, 1997). There are further higher order hydrogen burning chains that also occur at temperatures of several 10^7 K, e.g. the neon-sodium and magnesium-aluminium chains (not shown).

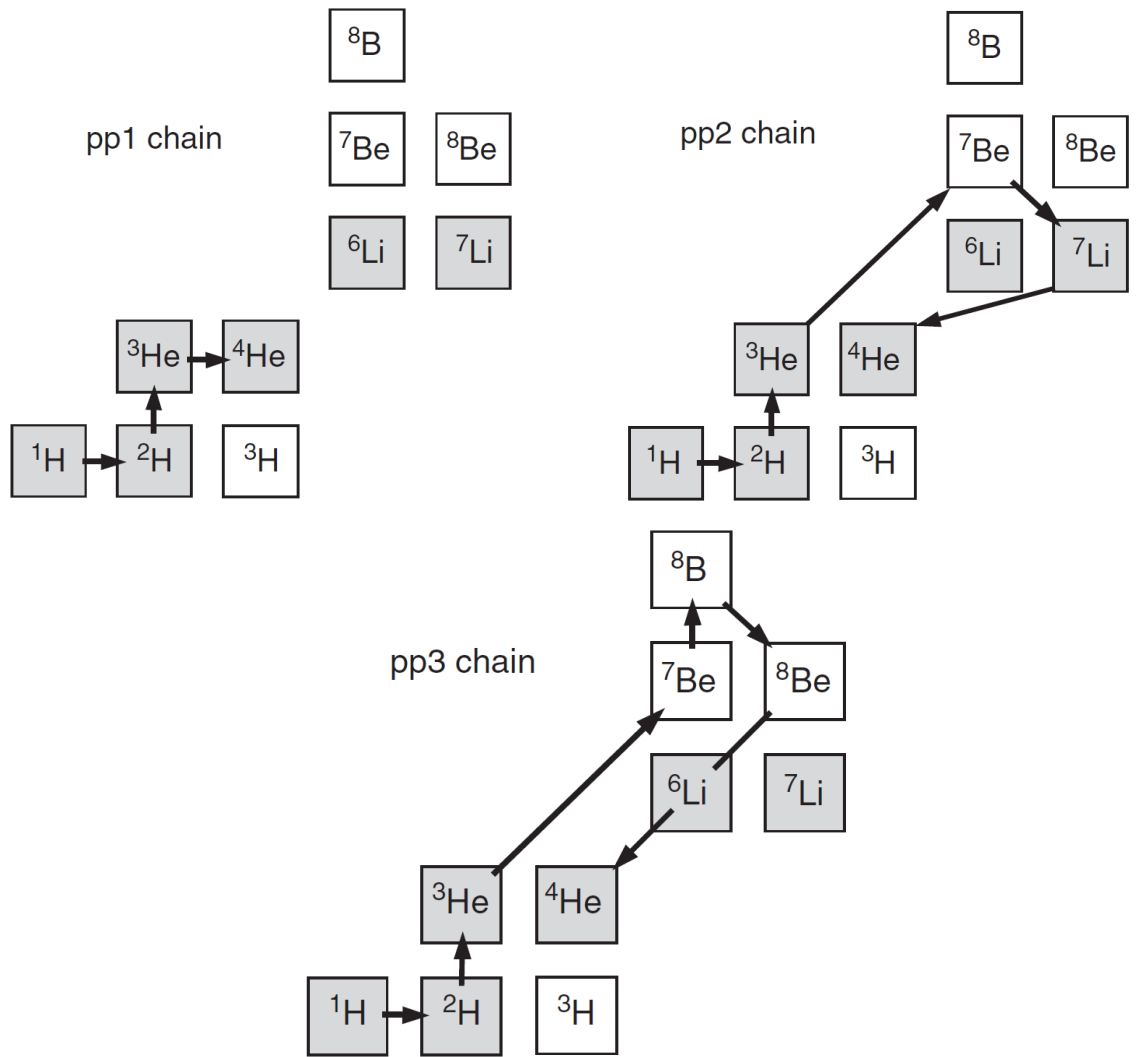


FIGURE 1.2: The pp chains represented in the chart of the nuclides. Arrows are specific nuclear reactions, stable nuclei are shaded squares. Figure is Fig. 5.2 from Iliadis (2007).

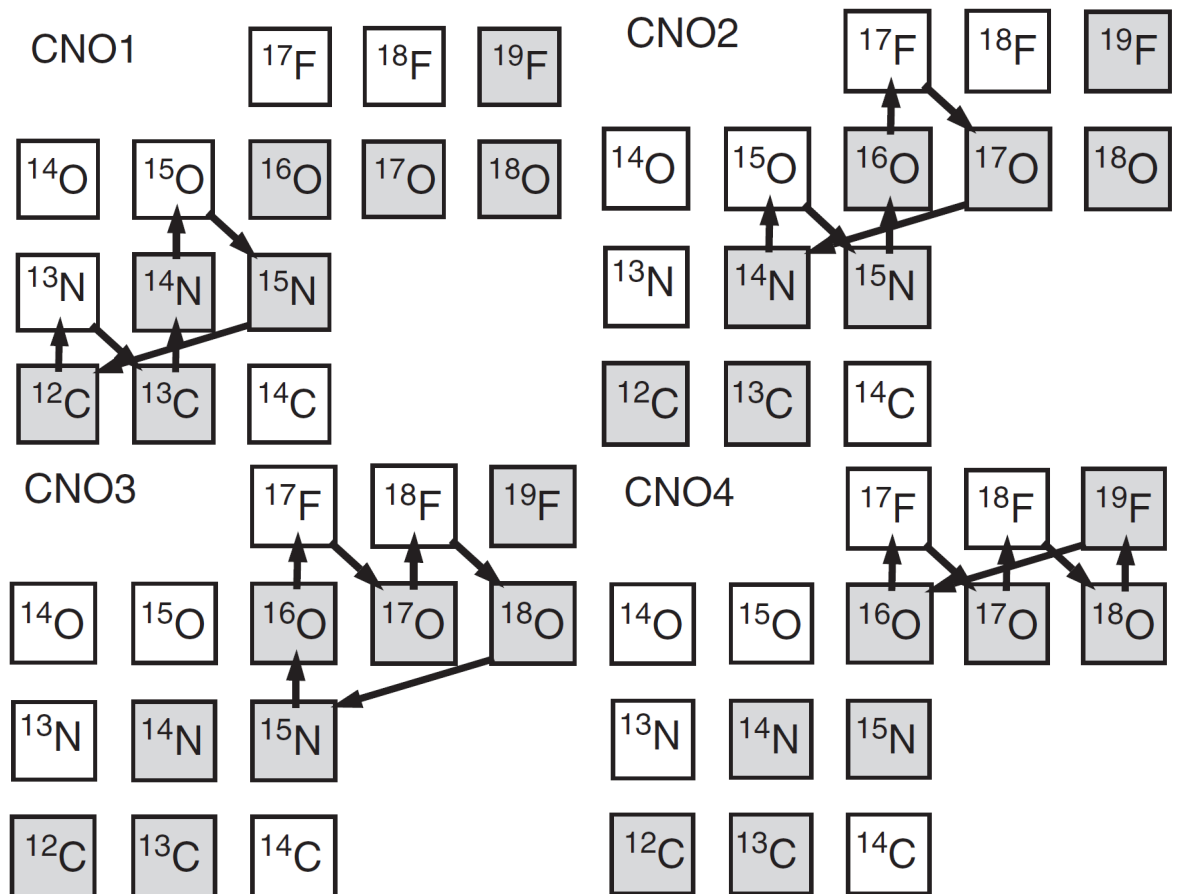


FIGURE 1.3: The CNO cycles represented in the chart of the nuclides. Arrows are specific nuclear reactions, stable nuclei are shaded squares. CNO1 is the the CN cycle in the text (Equation 1.2a), CNO2 is the ON cycle in the text (Equation 1.2b), CNO3 and CNO4 are the OF cycle branches in the text (Equations 1.2c and 1.2d).

Figure is Fig. 5.8 from Iliadis (2007).

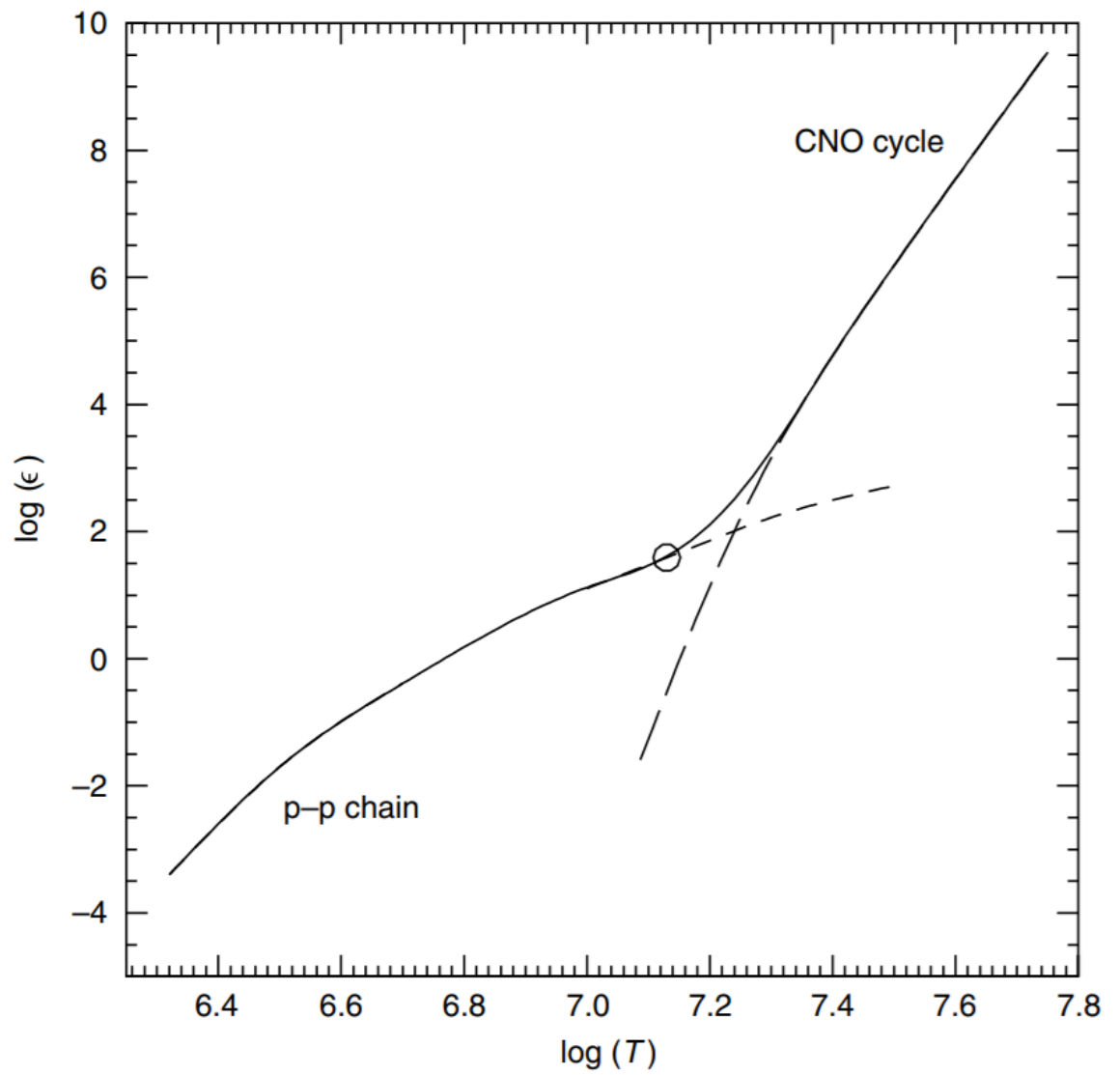


FIGURE 1.4: Rate of energy generation ϵ ($\text{erg g}^{-1} \text{s}^{-1}$) as a function of the temperature for the pp chain and the CNO cycle. The open circle marks the conditions in the centre of the Sun. Figure is Fig. 5.1 from Salaris and Cassisi (2006).

CN cycle⁵:



ON cycle:



OF cycle (third CNO cycle branch):



OF cycle (fourth CNO cycle branch):



A low-mass star will spend the vast majority of its life on the main sequence burning hydrogen via the pp chains and the CNO cycle in its radiative core. Intermediate- and high-mass stars burn hydrogen predominantly via the CNO cycles and have convective cores due to the higher temperature dependence of the CNO cycles compared to the pp chains, illustrated in Fig. 1.5. The rate of energy generation ϵ for a given reaction is dependent upon temperature according to $\epsilon \propto (T/T_0)^\nu$, where the value of ν for the ppI and CNO cycles are ~ 4 and 20 respectively (Iliadis, 2007; Ryan and Norton, 2010).

1.1.5 After the main sequence

Once the star runs out of hydrogen in the core, shown in Fig. 1.5, core hydrogen burning can no longer support the star. The inner layers of the star contract and eventually temperatures sufficient for hydrogen to burn in a

⁵The reactions listed are the first in the carbon-nitrogen (CN) cycle, shown in Equation 1.2a. The CN cycle is said to “bottleneck” or “stall” after these first three reactions due to ^{14}N proton capture being the slowest reaction in the cycle (Iliadis, 2007).

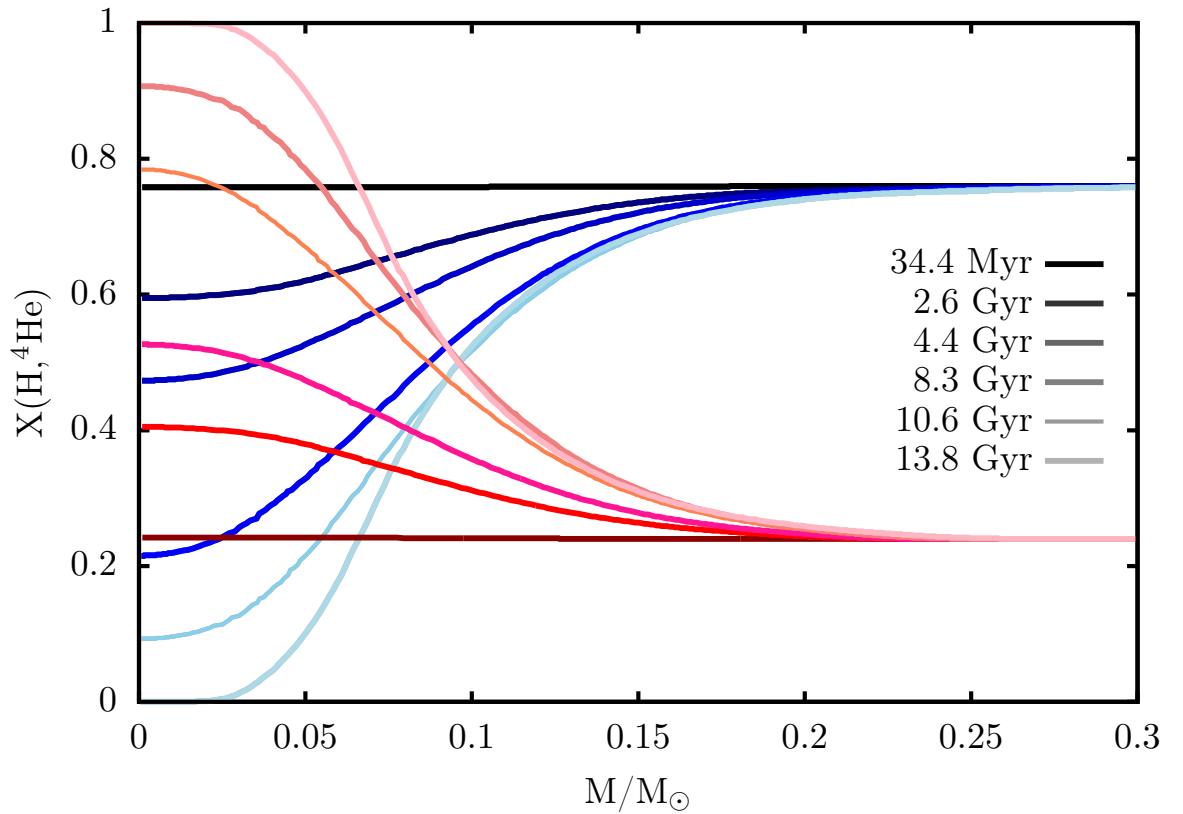


FIGURE 1.5: Mass fractions as a function of interior stellar mass of a $0.79M_{\odot}$, $Z = 0.000246$ stellar model. Hydrogen (blue curves) and helium-4 (red curves) are shown during main sequence evolution (time progressing from dark to light curves, shown in the legend). At this point in its evolution, the star has a radiative core and a convective envelope, which is evident from the shape of the abundance curves (homogeneous profiles indicate that the dominant mixing process is convection, whereas curved profiles are representative of nuclear burning).

shell are reached (hydrogen shell burning, or H shell) but not enough for core helium ignition, and the core is consequently inert and grows in mass as the hydrogen shell burns hydrogen into helium on top of it. The outer envelope expands once shell hydrogen ignition has occurred.

The star leaves the main sequence and crosses a region in the HR diagram known as the Hertzsprung Gap (between “End of core H burning” and the base of the giant branch in Fig. 1.1). Few stars are observed in this region because progression across the gap is very quick compared to the rest of the star’s lifetime and is on the order of the core thermal timescale⁶ (Pagel, 1997). The outer layer expansion causes a rapid drop in surface temperature while maintaining approximately the same luminosity, and appear red. The star has then moved to the base of the Red Giant Branch (RGB).

The inert helium core becomes very dense during core contraction, and contraction slows as electron degeneracy sets in. The core then becomes isothermal because there is no energy generation in the core, therefore, in accordance with radiative equilibrium, the temperature gradient is removed. In contrast, the core densities of higher-mass stars rise but do not reach the values required for electron degeneracy (Demarque and Mengel, 1971; Despain, 1981; Deupree, 1984; Kippenhahn and Weigert, 1990; Pagel, 1997; Dearborn, Lattanzio, and Eggleton, 2006; Salaris and Cassisi, 2006; Mocák et al., 2009; Iben, 2013; Karakas and Lattanzio, 2014).

1.1.6 The Red Giant Branch

Below we provide a brief description of a low-mass star’s life as a red giant.

As a low-mass star ascends the RGB, the energy generated by the H shell is transported to the surface easily via the convective envelope. This energy drives further expansion and cooling of the envelope, which leads to an increase in opacity and drives convection in the envelope (Karakas and Lattanzio, 2014). The mass location of the base of the convective envelope deepens, and eventually makes contact with the ashes of main sequence hydrogen burning and mixes these ashes to the surface. This process is called first dredge-up (FDU) and is the first major mixing event in a star’s life (Iben, 1964). The surface abundance changes expected due to FDU are increases in the abundances of ^3He , ^4He , ^{13}C , ^{14}N , and ^{17}O , and decreases (due to dilution) in the abundances of ^1H , ^2D , ^{12}C , ^7Li , ^7Be , ^8B , ^{16}O , and ^{18}O . The magnitude of these changes is dependent upon stellar mass and metallicity (Pagel, 1997; Karakas and Lattanzio, 2014).

First dredge-up leaves behind an abundance discontinuity, shown in Fig. 1.6, that becomes very important for subsequent evolution (Iben, 1964). This discontinuity is believed to inhibit any extra mixing between the H shell and envelope (Mestel, 1953; Kippenhahn and Weigert, 1990; Chanamé, Pinsonneault, and Terndrup, 2005). As the H shell converts hydrogen into

⁶Also known as the Kelvin-Helmholtz timescale, the thermal timescale is the time it takes for the core (in this instance) to radiate its thermal energy via contraction in the absence of nuclear burning. Thermal timescales are given by the equation $\tau_{\text{th}} \simeq (GM^2)/(RL)$, where G is the gravitational constant, M is the mass, R is the radius, and L is the luminosity (Pagel, 1997).

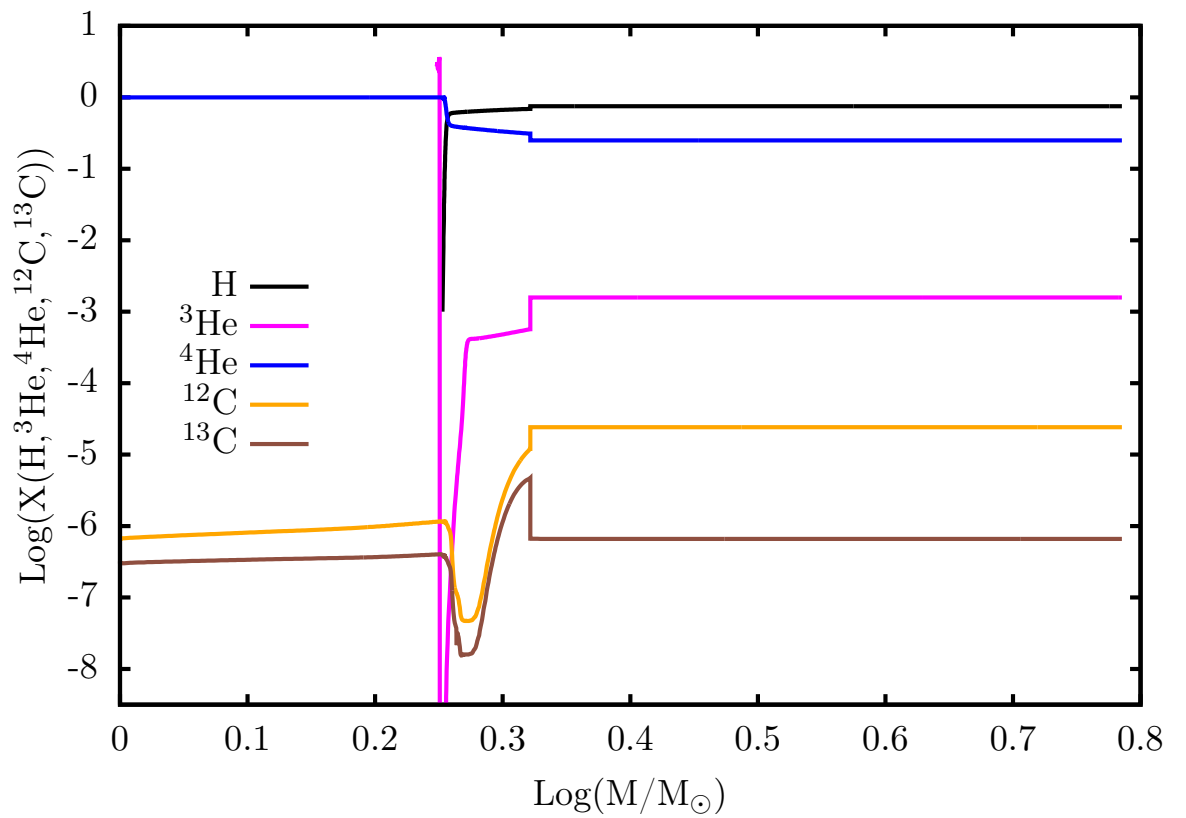


FIGURE 1.6: Mass fraction of hydrogen (black curve), helium-3 (magenta curve), helium-4 (blue curve), carbon-12 (orange curve), and carbon-13 (brown curve) as a function of interior stellar mass after first dredge-up of a $0.79M_{\odot}$, $Z = 0.000246$ stellar model. The abundance discontinuity is evident at $\simeq 0.32 M_{\odot}$.

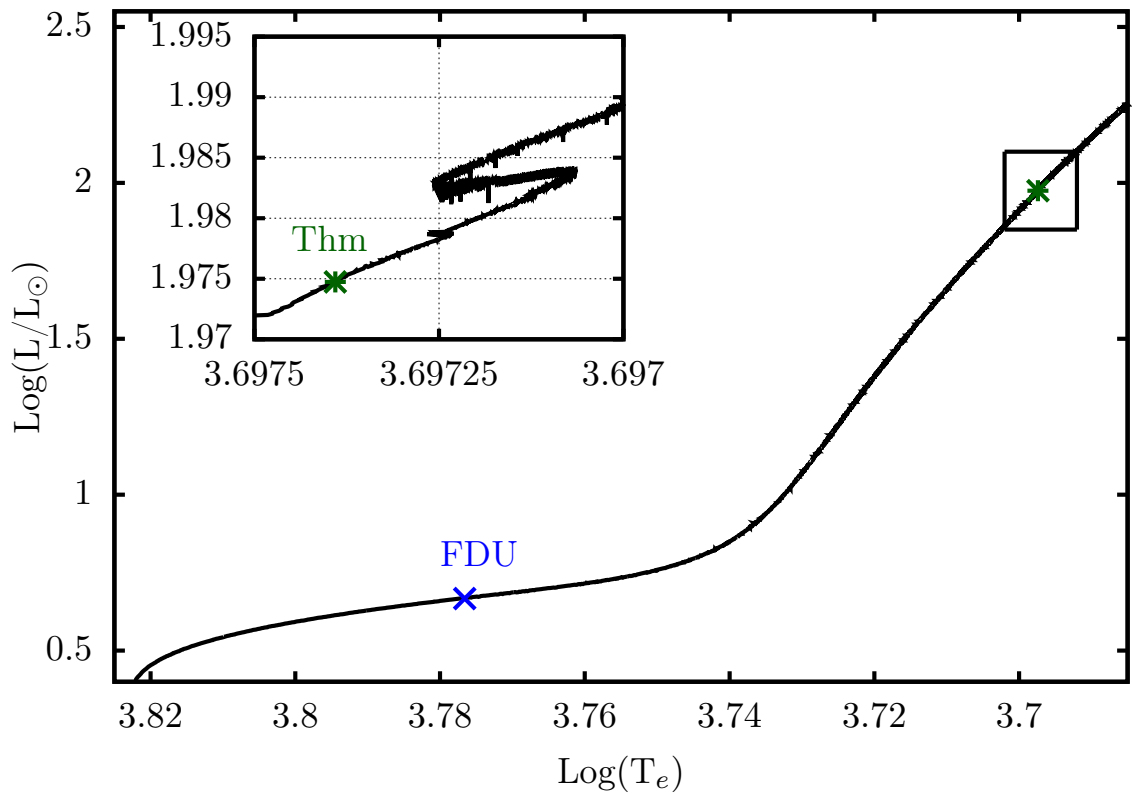


FIGURE 1.7: Evolutionary path of a $0.79 M_{\odot}$, $Z = 0.000246$ stellar model in the Hertzsprung-Russell (HR) diagram. The thermohaline mixing (“Thm”, green asterisk) point on the plot denote the location on the HR diagram where surface abundance changes occur in our model due to these events. The region of the luminosity function bump is shown in the inset. All labelled events are discussed further in text.

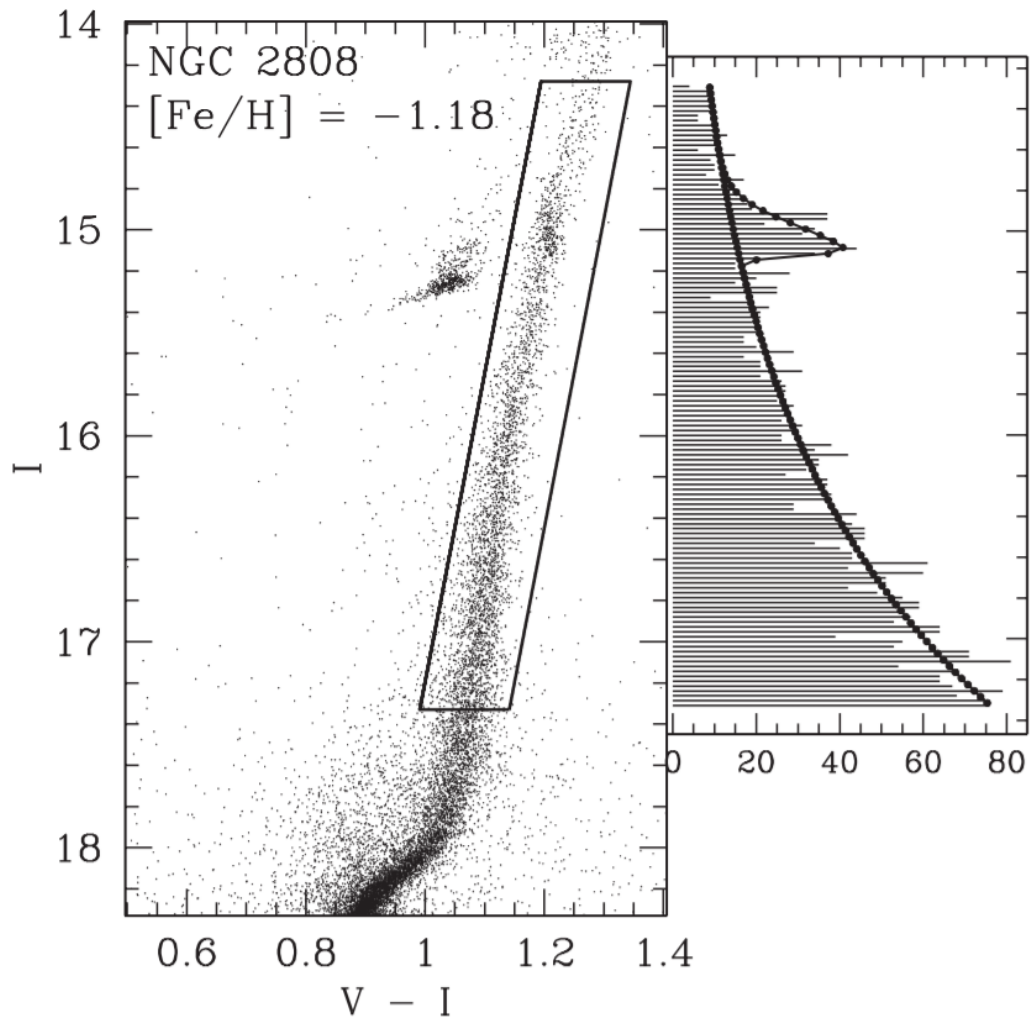


FIGURE 1.8: Left: Colour-magnitude diagram (equivalent to a Hertzsprung-Russell diagram) of the globular cluster NGC2808. The colour-magnitude selection contours are shown for the 3308 RGB and RGB bump stars. Right: Magnitude histogram of the 3308 RGB and RGB bump giants. The luminosity function bump can be clearly identified towards the top of the histogram. Image is Fig. 13 from Nataf et al. (2013).

helium, the inert helium core grows in mass. During core growth the H shell will move out (in mass) until it eventually reaches the hydrogen discontinuity left behind by FDU. The amount of available fuel and the opacity of the H shell increases and the rate of hydrogen burning drops, which causes a drop in luminosity but a rise in effective temperature. The star appears to retrace its path in the HR diagram during this structural change, shown in Fig. 1.7.

After the H shell passes through the hydrogen discontinuity, the luminosity will grow with core mass and the star will move up the RGB again almost along its original path, shown in Fig. 1.7. More stars are observed in this region of the HR diagram, producing a bump in the luminosity function (luminosity function bump, “LFB”, also known as the “RGB bump” or simply “bump”), which is a well-observed property of globular clusters⁷ and shown in Fig. 1.8 (Kippenhahn and Weigert, 1990; Riello et al., 2003; Nataf et al., 2013).

1.1.7 Extra mixing and the importance of carbon and lithium

Standard stellar evolution theory does not predict any further surface abundance changes beyond FDU during RGB evolution. It has been shown (for example, see Lambert and Ries, 1977; Gilroy and Brown, 1991; Charbonnel, Brown, and Wallerstein, 1998; Gratton et al., 2000; Smith and Martell, 2003; Shetrone, 2003; Weiss et al., 2004; Martell, Smith, and Briley, 2008; Smiljanic et al., 2009; Lind et al., 2009, to name a few) that standard models could not match observations and additional mixing mechanisms were required in the theory. This is particularly pertinent when explaining observations of low-mass stars, where the extra mixing mechanism appears to operate more effectively than in stars of higher-mass (this could also be somewhat dependent upon the long RGB lifetimes of low-mass stars Gratton et al., 2000; Spite et al., 2006; Aoki et al., 2007).

One of the key observations that provides evidence for the existence of extra mixing includes the sudden drop in surface ${}^7\text{Li}$ after FDU as shown in Fig. 1.9, which is taken from Lind et al. (2009) (this is also shown by others, including Charbonnel, Brown, and Wallerstein, 1998; Smiljanic et al., 2009). Other key pieces of evidence for extra mixing are observations of $[\text{C}/\text{Fe}]$ ⁸ (Suntzeff, 1981; Suntzeff, 1989; Carbon et al., 1982; Trefzger et al., 1983; Langer et al., 1986; Briley et al., 1990; Gratton et al., 2000; Bellman et al., 2001; Shetrone, 2003; Martell, Smith, and Briley, 2008; Shetrone et al., 2010), shown in Fig. 1.10, and C/N, shown in Fig. 1.11 (Charbonnel, 1994; Charbonnel, Brown, and Wallerstein, 1998). Both ratios, like lithium, show a sharp decline after FDU, confirming that there is a non-canonical mixing event occurring in the stellar interior after the completion of FDU. In particular, these observations are the signature of CN cycling (decrease in ${}^{12}\text{C}$ and increase in ${}^{14}\text{N}$, discussed in §1.1.3), indicating that the extra mixing mechanism connects the envelope to regions in the star where CN cycling is occurring. It is imperative to have observations of both carbon

⁷Globular clusters are discussed further in §1.2.1.

⁸Using standard nomenclature, $[A/X] = \log(A/X)_{\text{star}} - \log(A/X)_{\odot}$.

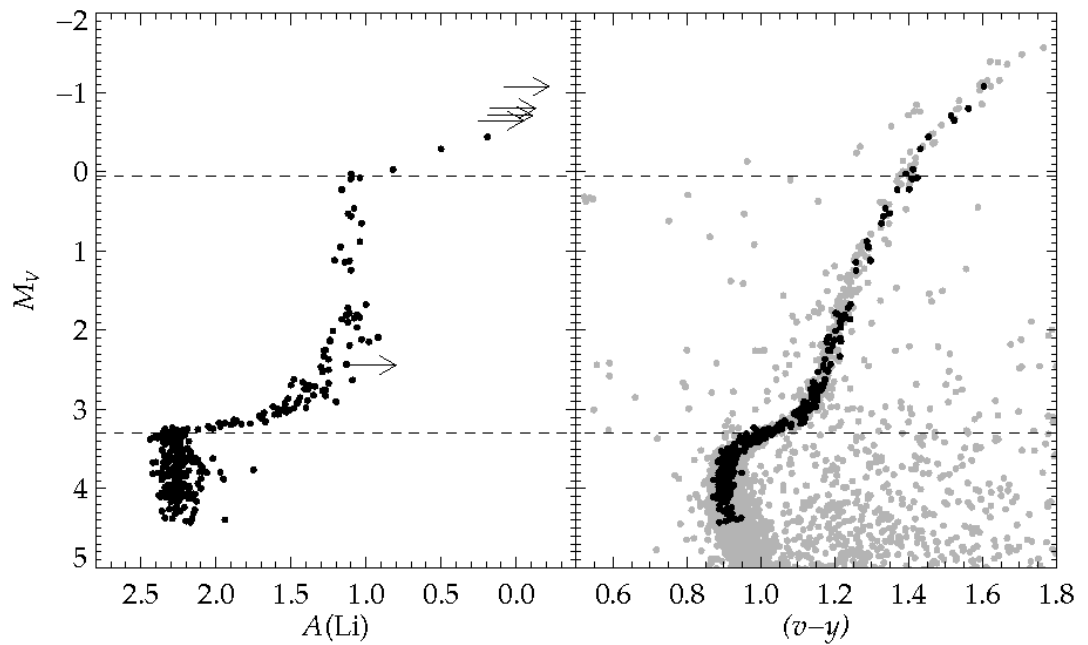


FIGURE 1.9: Left panel: Absolute visual magnitude as a function of surface lithium for NGC6397 stars. Horizontal arrows indicate upper limits. Right panel: Observational targets on the colour-magnitude diagram of NGC6397. In both panels, the horizontal dashed lines indicate the magnitudes of first dredge-up and the luminosity function bump. Figure is Fig. 5 from Lind et al. (2009).

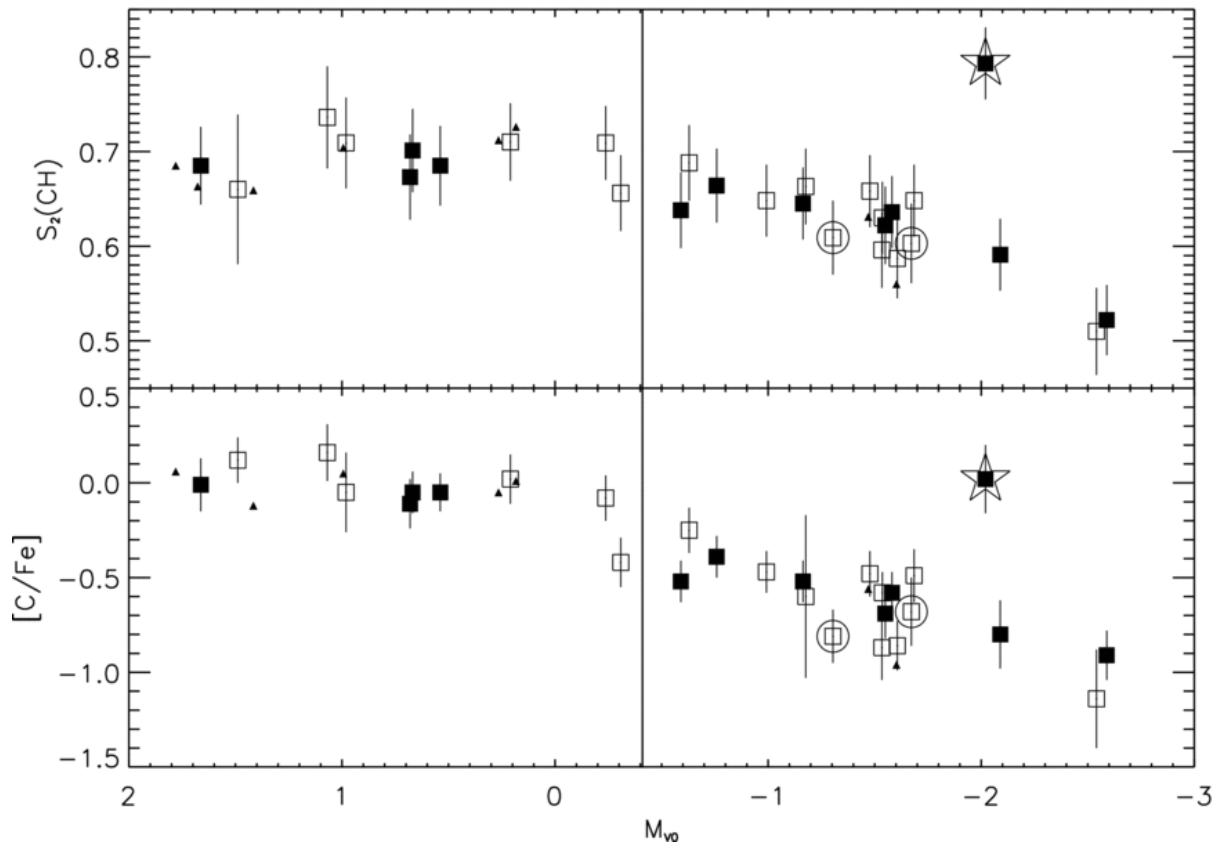


FIGURE 1.10: Top panel: CN-band strength as a function of absolute visual magnitude (M_{V0}) for NGC5466 stars. Bottom panel: $[\text{C}/\text{Fe}]$ as a function of absolute visual magnitude for NGC5466 stars. In both panels, the vertical line indicates the position of the luminosity function bump. CN-strong stars are filled squares, CN-weak stars are open squares, stars with a sufficient signal-to-noise (S/N) ratio for analysis but with suspected spectroscopic blending are small triangles, the outlier (possible CH star) is the open star, and possible AGB stars are open circles. Figure is Fig. 9 from Shetrone et al. (2010).

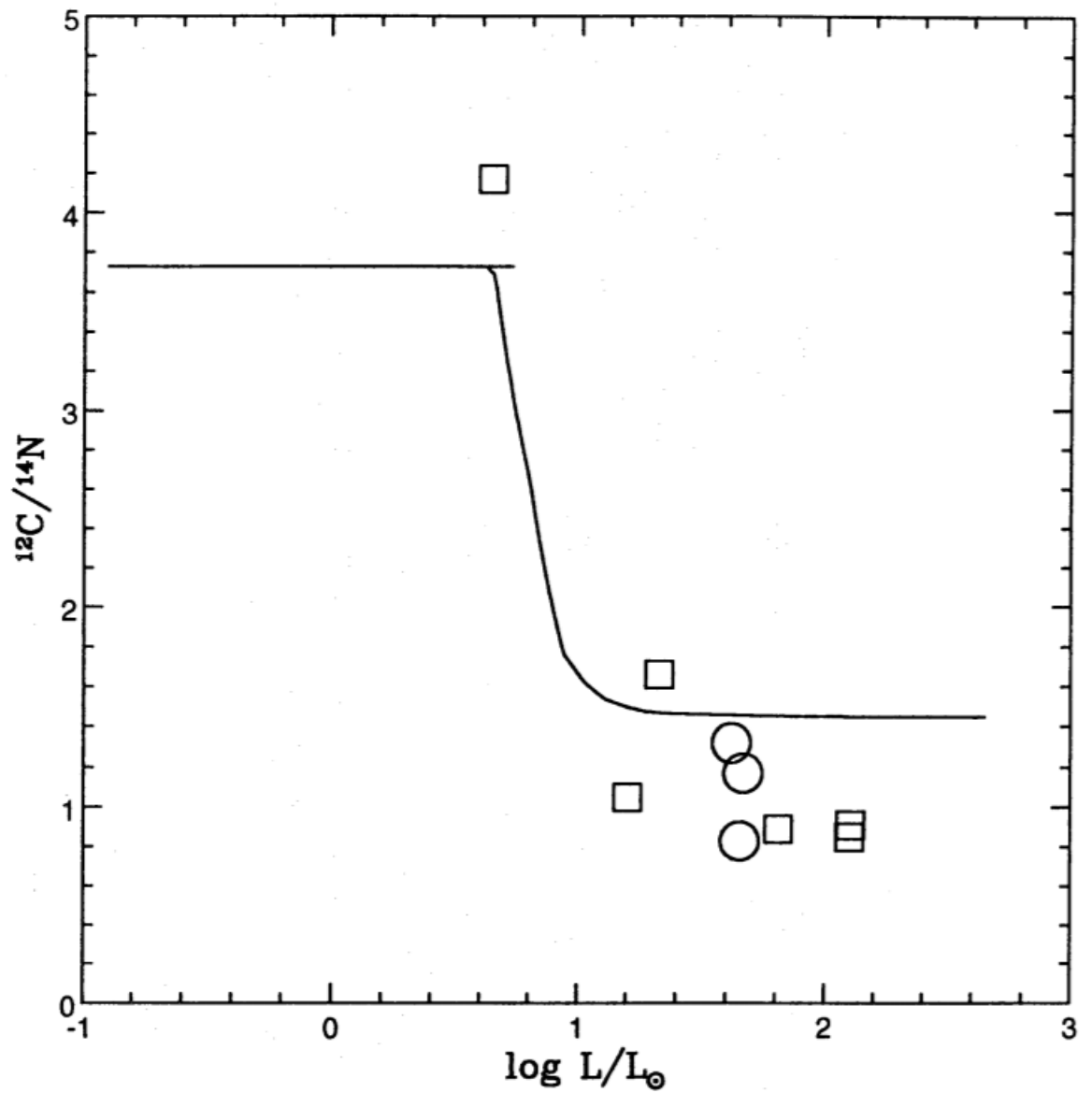


FIGURE 1.11: C/N as a function of luminosity (logarithm). The curve represents the theoretical evolution of the C/N ratio along the isochrone of M67 (with a main sequence turn-off mass of approximately $1.25 M_{\odot}$), and observations are M67 giants pre-helium flash (squares) and post-helium flash (circles). Observations are from Brown (1987). Figure is Fig. 8 from Charbonnel (1994).

and lithium in particular, because they undergo proton capture at different temperatures and are therefore independent indicators of extra mixing.

Additionally, the sudden decline appears to coincide with the LFB⁹. After the LFB, the hydrogen discontinuity is erased by the H shell and it is thought that extra mixing can then occur (Lattanzio and Wood, 2003; Charbonnel and Zahn, 2007; Karakas and Lattanzio, 2014). This connection of the H shell to the envelope allows abundance changes occurring below the convection zone to be observed on the surface. A schematic of extra mixing in a star is shown in Fig. 1.12.

Although observations of low-mass stars revealed the need for mixing beyond standard evolution theory, and the above description explains why extra mixing appears to coincide with the LFB, the physical mechanism of extra mixing had not been identified.

1.1.8 Meridional circulation

As stated above, the chemical signature of extra mixing clearly indicates the region where extra mixing is occurring, and while the region where extra mixing is occurring in stars is known, the mechanism still remains elusive.

One proposed explanation for extra mixing was meridional circulation. Meridional circulation is a mixing that occurs in radiative regions as a consequence of internal rotation (rotation is discussed below in §1.1.9) and is the main driver for internal transport of angular momentum but is considered to not contribute to chemical mixing in a significant way (von Zeipel, 1924a; von Zeipel, 1924b; Eddington, 1925; Vogt, 1925; Charbonneau and Michaud, 1991; Maeder and Zahn, 1998; Meynet and Maeder, 2002; Mathis et al., 2013; Rieutord and Beth, 2014; Kitchatinov, 2016; Mathis et al., 2018). It operates on the principle that rotation causes a star to become non-symmetrical, therefore the star cannot satisfy the conditions of hydrostatic and thermal equilibrium on spherical surfaces (von Zeipel, 1924a; von Zeipel, 1924b; Sweigart and Mengel, 1979). There is a pressure gradient between the equator and poles, and radiation flux variations initiate circulation currents along this pressure gradient (Eddington, 1925; Sweigart and Mengel, 1979). This is illustrated in Fig. 1.13.

Meridional circulation was first considered in main sequence stars to account for abundance anomalies in early type and Population I stars, however Sweigart and Mengel (1979) investigated this type of mixing as an explanation for the abundance changes of carbon of RGB stars (Paczynski, 1973). They concluded that meridional circulation can explain abundance changes of carbon on the RGB for stars in M92, however their results are dependent on the initial main sequence angular velocity. Additionally, Sweigart and Mengel (1979) do not consider observations of lithium and elemental carbon abundances, which also show signatures of extra mixing. Therefore, due to the limitations of meridional circulation, it is not a favoured explanation for extra mixing in RGB stars.

⁹This is discussed further in Chapter 5.

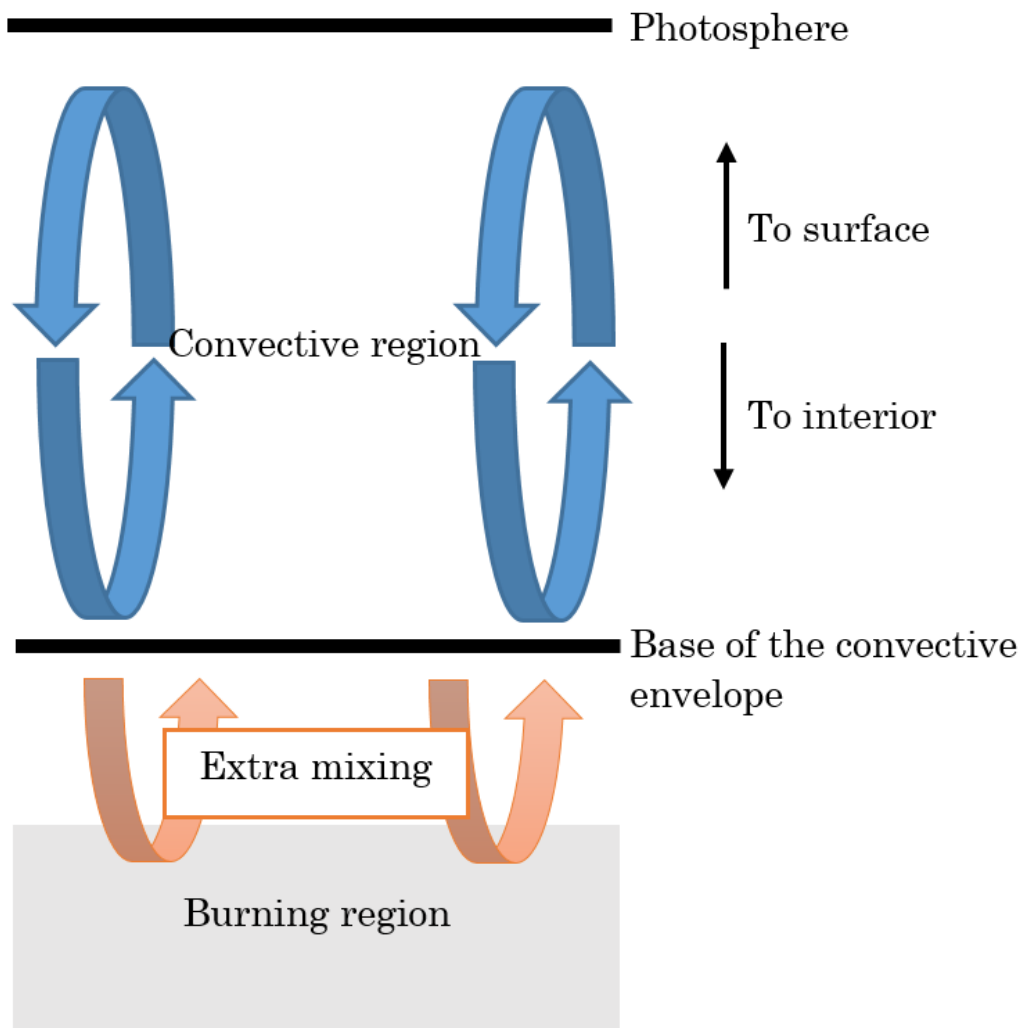


FIGURE 1.12: A schematic of extra mixing in a star. Image adapted from Lugaro et al. (2017).

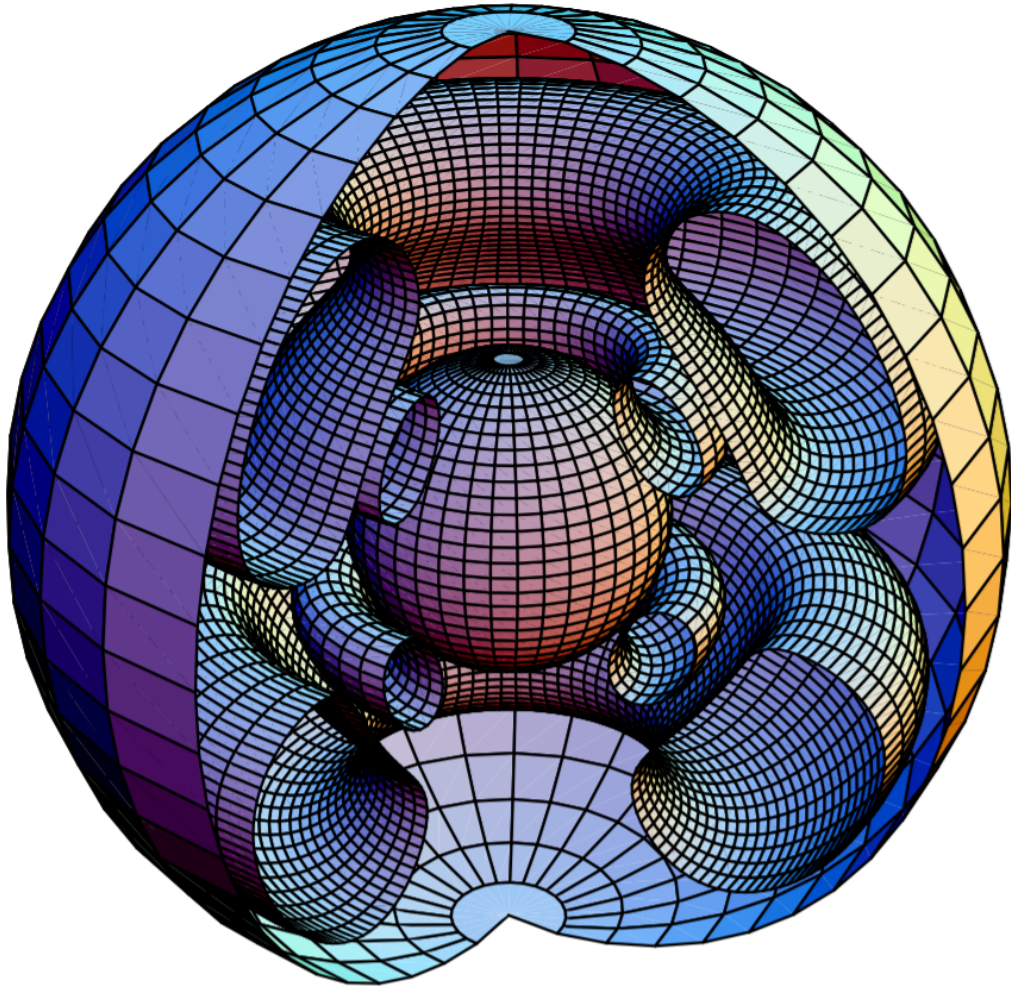


FIGURE 1.13: Meridional circulation lines in solar metallicity, $20 M_{\odot}$ star with initial stellar rotation velocity $v_{\text{ini}} = 300 \text{ km s}^{-1}$ at the beginning of hydrogen burning. The different “tubes” represent different meridional circulation velocities. Figure is Fig. 1 from Meynet and Maeder (2002).

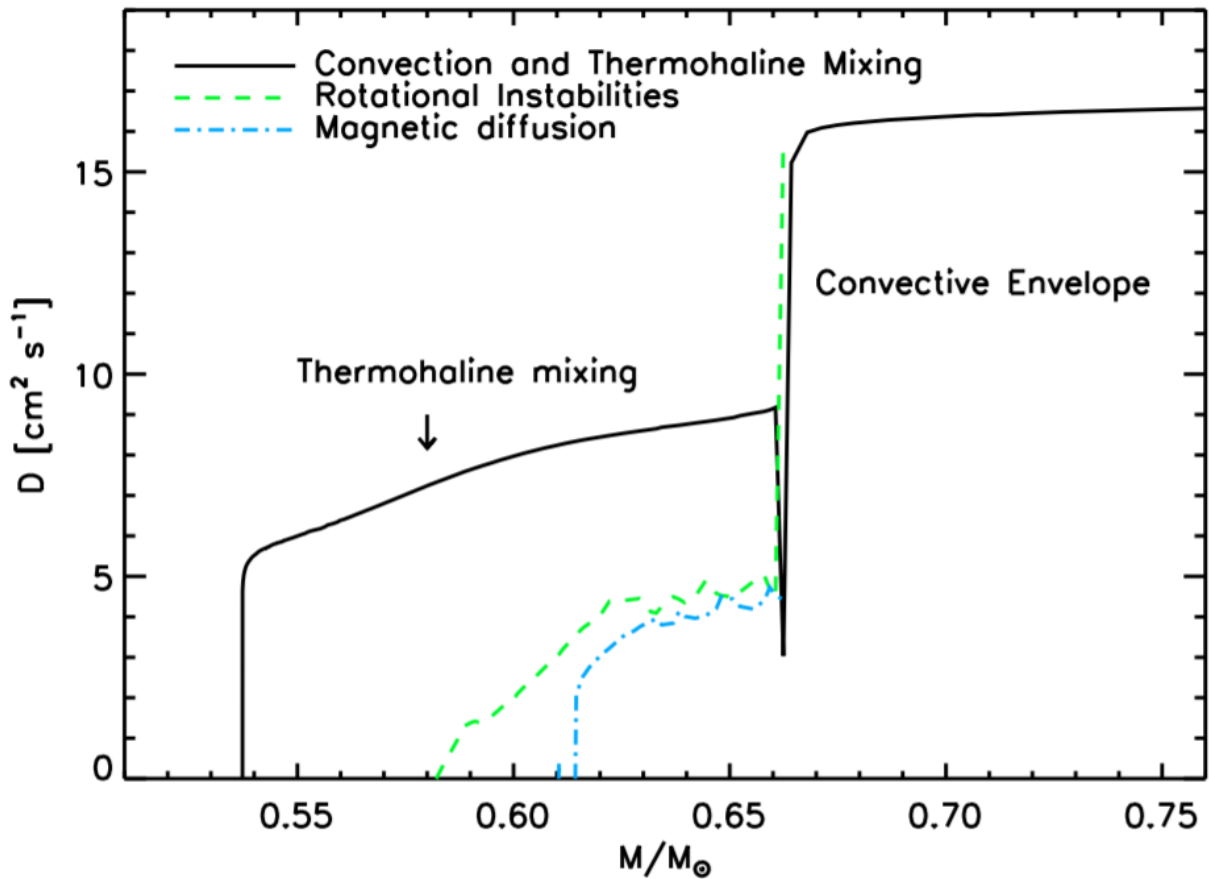


FIGURE 1.14: The diffusion coefficients of thermohaline mixing and convection (black solid curve), rotation (green dashed curve), and magnetic diffusion (blue dashed dotted curve) in the region between the H shell and the convective envelope for a $1 M_{\odot}$ model during core helium burning (horizontal branch and Asymptotic Giant Branch evolution). The thermohaline prescription is the same as for the RGB. Extra mixing may theoretically occur in core helium burning stars that experience minimal (or no) extra mixing on the RGB and therefore have a sufficient amount of ${}^3\text{He}$ to create a molecular weight inversion (Cantiello and Langer, 2010). Figure is Fig. 9 from Cantiello and Langer (2010).

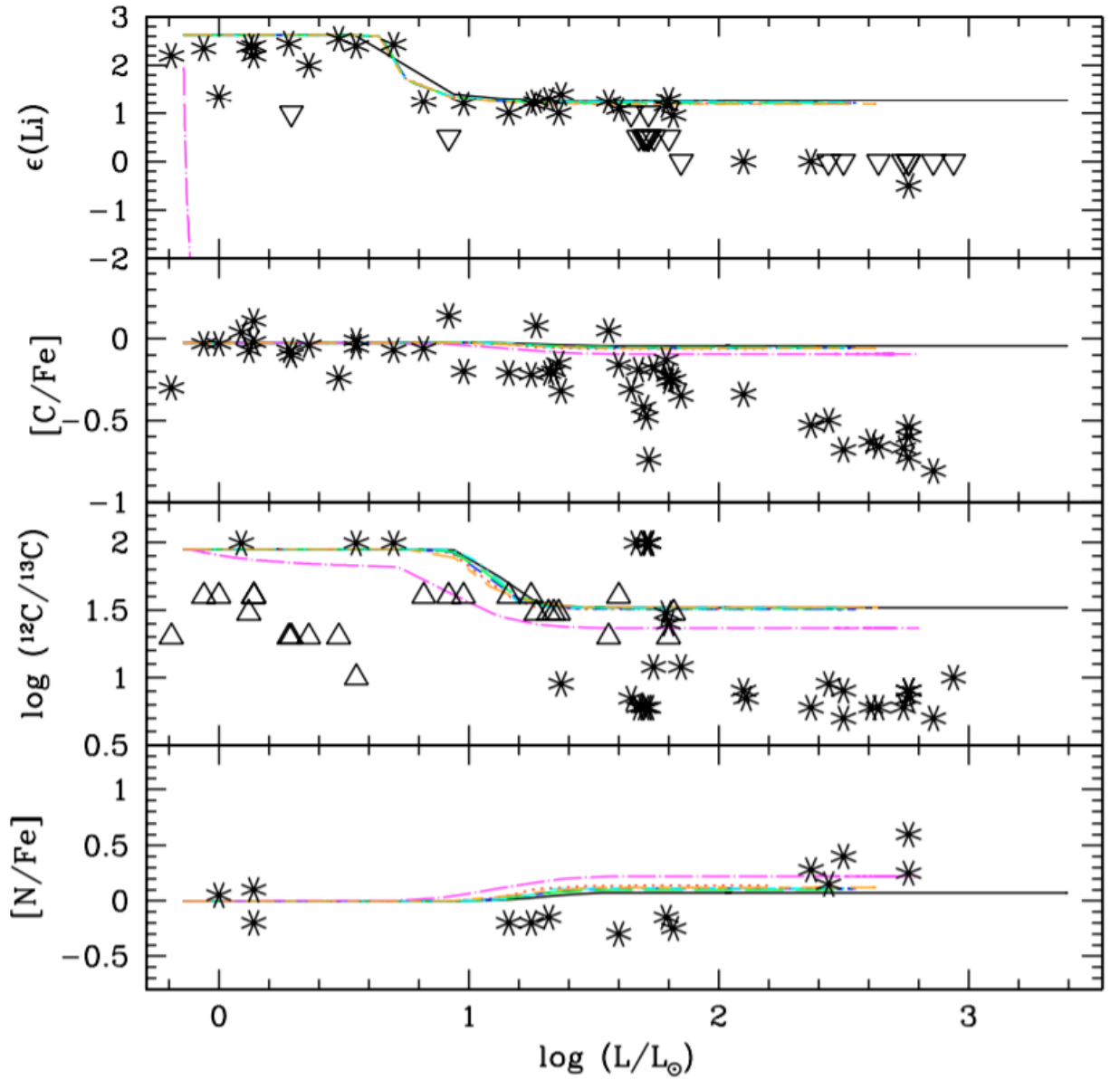


FIGURE 1.15: The evolution of the abundances of $\epsilon(\text{Li})$, $[\text{C}/\text{Fe}]$, $^{12}\text{C}/^{13}\text{C}$, and $[\text{N}/\text{Fe}]$ as a function of luminosity. The coloured lines represent different models that vary in rotation input physics (for details see Palacios et al., 2006). Data are from Gratton et al. (2000), where black asterisks are actual measurements, open triangles are lower limits, and open downward triangles are upper limits. Figure is Fig. 15 from Palacios et al. (2006).

1.1.9 Rotation

Most 1D stellar models do not include rotation, though it is known that stars rotate and this fact has been a source of discussion surrounding the (currently) unexplained mixing seen above the LFB. In three papers, Charbonnel and Lagarde (2010), Lagarde et al. (2011), and Lagarde et al. (2012b) constructed a grid of models that included both rotation and thermohaline mixing (discussed below), and combined these effects by adding the diffusion coefficients of each. This method does not account for any possible interaction between the two instabilities. This issue is discussed by Cantiello and Langer (2010) who state that the diffusion coefficient for rotationally-induced instabilities is much lower than the value for thermohaline mixing by several orders of magnitude. This is illustrated in Fig. 1.14. Canuto (1999) show that horizontal forces caused by rotation decrease the ability of thermohaline mixing, though Medrano, Garaud, and Stellmach (2014) found the opposite: the horizontal instabilities created by rotation increase the efficiency of thermohaline mixing in their 3D simulations.

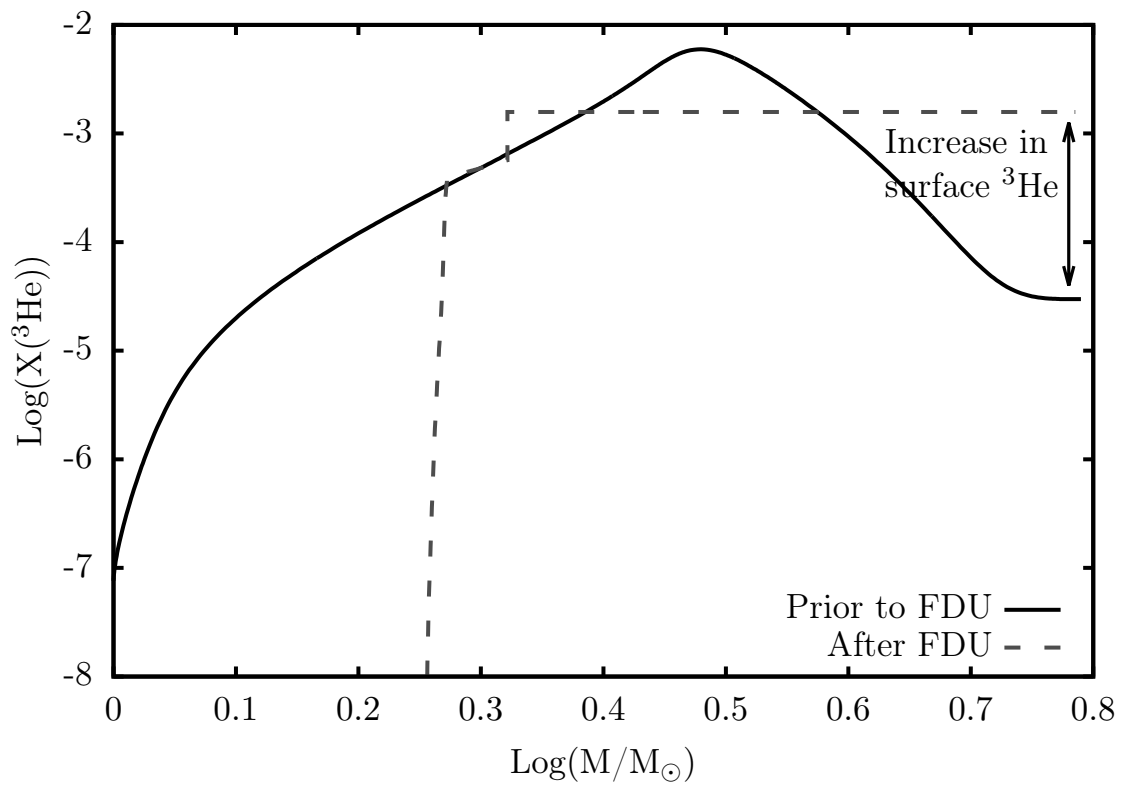


FIGURE 1.16: ^3He abundance profile as a function of interior stellar mass prior to FDU (black curve) and after FDU (dashed grey curve) of a $0.79M_\odot$, $Z = 0.000246$ stellar model. The increase in the surface ^3He abundance is marked in the figure.

It is clear that there is much that is not understood in this area. Stellar models with rotation alone cannot reproduce the observations, which show that the effects of other extra mixing mechanisms are more significant in the low-mass stars we are discussing (Palacios et al., 2006). Rotation also fails to provide a solution to the ${}^3\text{He}$ problem because the rotation transport coefficient is far too low to alter surface abundances (unlike thermohaline mixing, Palacios et al., 2006; Charbonnel and Zahn, 2007). This is shown in Fig. 1.15. Although rotation alone cannot account for the extra mixing seen on the RGB (Chanamé, Pinsonneault, and Terndrup, 2005; Palacios et al., 2006), a combination of instabilities (such as rotation, internal gravity waves, and thermohaline mixing) could prove to be a candidate (Denissenkov, Pinsonneault, and MacGregor, 2009; Denissenkov, 2012). Maeder et al. (2013) theoretically examine the interactions of instabilities (including thermohaline mixing) in rotating stars, an analysis that had been missing from the literature. The theoretical analysis of Maeder et al. (2013) has not been implemented in any studies to date. Edelman et al. (2017) show that a diffusion approximation for rotation in their one-dimensional simulation cannot adequately reproduce the horizontal diffusion profile in their 2D hydrodynamic simulation, and detailed studies are required to improve the approximations made in 1D codes.

1.1.10 Thermohaline mixing

A popular theory that offers a solution to extra mixing is thermohaline mixing. First introduced by Ulrich (1972) and then advanced further by Kippenhahn, Ruschenplatt, and Thomas (1980) in a general stellar context, an environment suitable for thermohaline mixing occurs naturally in low-to intermediate-mass stars after FDU (Eggleton, Dearborn, and Lattanzio, 2008). During core hydrogen burning, ${}^3\text{He}$ is efficiently destroyed in the core but is produced outside the core. The ${}^3\text{He}$ abundance peaks in the star at a mass coordinate of around $0.5 M_{\odot}$ in our example, shown in Fig. 1.16, due to the second reaction in Equation 1.1a. The surface convective layer is too thin in mass to redistribute ${}^3\text{He}$ from deeper in the star and too cool for effective pp chain reactions.

After FDU, ${}^3\text{He}$ is homogenised in the outer layers and it is in this way that the surface value of ${}^3\text{He}$ in low-mass stars increases (Fig. 1.16). Once the outer layers are lost to the interstellar medium during later stages of evolution, the amount of ${}^3\text{He}$ released is significant. This gives rise to the ${}^3\text{He}$ abundance problem discussed by many authors since the mid 1990's (e.g., Hata et al., 1995; Olive et al., 1995; Eggleton, Dearborn, and Lattanzio, 2006), where the amount of ${}^3\text{He}$ observed in the interstellar medium matches what is predicted from Big Bang nucleosynthesis but is much lower than the enrichment predicted from low-mass stellar models. This is discussed in more detail by Eggleton, Dearborn, and Lattanzio (2006) and Lagarde et al. (2012a) and references therein.

Therefore if observations of the interstellar medium (see Gloeckler and Geiss, 1996; Geiss and Gloeckler, 1998, for observations of the local interstellar medium and the proto-solar cloud respectively) are correct, then the theory of low-mass stellar evolution must be incomplete and some process

(or processes) must destroy ${}^3\text{He}$ in low-mass stars. Helium-3 can undergo fusion via ${}^3\text{He}({}^3\text{He}, 2\text{p}){}^4\text{He}$ once the H shell has advanced to regions where temperatures are sufficient for ${}^3\text{He}$ fusion (e.g., Denissenkov and Herwig, 2004). This fusion process creates more particles than it consumes and produces a mean molecular weight (μ) inversion (Eggleton, Dearborn, and Lattanzio, 2006). Eggleton, Dearborn, and Lattanzio (2006) proposed mixing would occur via the Rayleigh-Taylor instability, however Charbonnel and Zahn (2007) linked this phenomenon to thermohaline mixing. A cooler layer of higher μ material sits atop a hotter, lower μ layer undergoing ${}^3\text{He}$ fusion. “Fingers” of material from the hotter ${}^3\text{He}$ fusion layer penetrate into the layer above, mixing material towards the surface. The effect is shown in Fig. 1.17 with warm salty water and cool fresh water, where thermohaline mixing in this example is a competition of heat and salinity diffusion. Destruction of ${}^3\text{He}$ in this way can “solve” the ${}^3\text{He}$ problem described above (Lagarde et al., 2012a).

Problems with thermohaline mixing

Thermohaline mixing was originally discovered in an oceanographic context that is incomparable (beyond a general sense) to stellar conditions. Cantiello and Langer (2010) show that the dimensionless Prandtl number, σ , the ratio of the kinematic viscosity to the thermal diffusivity, is very small in stars at 10^{-6} . However, the Prandtl number in water (where thermohaline mixing was first discovered) is around 7 (Cantiello and Langer, 2010). Low Prandtl numbers (i.e. when $\sigma \rightarrow 0$) result in the (stellar) environment becoming unstable to turbulence. This is shown in the simulations performed by Bascoul (2007) where fluid environments with low Prandtl numbers are dynamically unstable and turbulent. Whether thermohaline mixing can operate in such turbulent conditions is still under debate (Busse, 1978; Merryfield, 1995; Bascoul, 2007; Cantiello and Langer, 2010; Traxler, Garaud, and Stellmach, 2011a; Traxler, Garaud, and Stellmach, 2011b; Vauclair and Théado, 2012; Medrano, Garaud, and Stellmach, 2014).

Angelou et al. (2015) attempted to match their stellar models to observations of lithium and carbon in globular cluster RGB stars. They could not find a simultaneous match, which led them to the conclusion that the diffusive mixing scheme adopted for thermohaline mixing may not be complete or the most appropriate.

However, important benefits of the thermohaline mechanism as a possible solution to extra mixing are that it naturally begins at the LFB and the thermohaline environment naturally occurs during normal RGB evolution. Indeed, it is also possible that the thermohaline instability triggers other instabilities that may then dominate or contribute to mixing.

1.1.11 Evolution to the Red Giant Branch tip and beyond

Here we briefly describe the evolution of a low-mass star beyond the RGB. We do so briefly for completeness although these evolutionary phases are not the main focus of this thesis.

As a star evolves up the RGB, the inert helium core mass (and consequently core temperature) increases. Eventually, core temperatures will be high enough for helium burning at around 10^8 K, recalling that the core is electron degenerate in these low-mass stars (Pagel, 1997; Phillips, 1999). Higher-mass stars however have only mildly degenerate cores once helium burning temperatures are reached and consequently ignite helium non-degenerately (Kippenhahn and Weigert, 1990; Pagel, 1997; Iben, 2013).

In low-mass stars, helium ignites off-centre due to neutrino losses, which causes the centre of the inert He core to be cooler than surrounding regions¹⁰. The excess energy released would *usually* be counteracted by core expansion, however the pressure of the degenerate matter is largely insensitive to changes in temperature. The rate of fusion then becomes uncontrolled and a thermal runaway occurs in an event called the core helium flash, where the luminosity of the stellar core increases by many orders of magnitude. This occurs at the tip of the RGB and terminates RGB evolution as shown in Fig. 1.1 (Mestel, 1952; Pagel, 1997).

The energy generated during the helium flash is sufficient to break degeneracy, however almost none of the energy is transported to the surface due to absorption by the core and the layers above the core. Once degeneracy is lifted and helium burning has commenced, the core expands while the outer layers contract (Kippenhahn, Weigert, and Weiss, 2012). The star proceeds to the Horizontal Branch during this structural readjustment, shown in the top panel of Fig. 1.18. While on the Horizontal Branch, carbon and oxygen abundances increase in the core as helium burns via the triple alpha and carbon alpha reactions (${}^4\text{He}(2\alpha,\gamma){}^{12}\text{C}$ and ${}^{12}\text{C}(\alpha,\gamma){}^{16}\text{O}$ respectively). As was the case when the star left the main sequence, once core helium burning can no longer support the star, the resulting carbon-oxygen (CO) inert core does not have a sufficient temperature to ignite another fuel source (e.g. carbon, Doherty et al., 2017). The core becomes degenerate and helium burns in a shell surrounding the core called the helium burning shell, or He shell. The He shell is located deeper in the star than the H shell and is separated from the H shell by an intershell region, as shown in Fig. 1.19. As before, core contraction and envelope expansion occur during this process, causing the temperature of the H shell to drop. Hydrogen burning “switches off” as the star starts ascending the early Asymptotic Giant Branch (AGB, as shown in the top panel of Fig. 1.18). As the name suggests, a star on the AGB ascends asymptotically to the RGB on a HR diagram (Pagel, 1997; Phillips, 1999).

¹⁰The full explanation of the process is quite detailed (for an excellent description of the process, see Iben, 2013). Briefly, neutrino-antineutrino pairs produced in the core are responsible for energy losses (and decreasing temperatures) in the central region of the core. This is the dominant neutrino energy-loss mechanism in RGB stars at the RGB tip (Iben, 2013).

During the ascent of the AGB, the outer convective envelope deepens and eventually penetrates the ashes of main sequence (partial) hydrogen burning, as was the case with FDU on the RGB. The effects of this event, called second dredge-up (SDU), are only observable on the surface of intermediate-mass stars with masses $> 4 M_{\odot}$ (the exact value is dependent upon metallicity, as shown in Fig. 7 of Karakas and Lattanzio, 2014). In the low-mass stars we consider in this thesis, SDU is not deep enough for observable surface abundance changes to occur. The two shells (the “switched off” H shell and the burning He shell) come closer together in mass as the He shell becomes thinner. After SDU, the star re-contracts and temperatures eventually rise high enough to reignite the H shell. This marks the beginning of the first instability of the thermally pulsing AGB (TP-AGB) phase, shown in Fig. 1.18.

Thermal pulses are a result of an increase in the luminosity of the thermally-unstable thin He shell, a phenomena called the Thin Shell Instability (Pagel, 1997). When the H shell reignites, due to their proximity, the temperature of the He shell increases. The temperature sensitivity of helium burning¹¹ is such that the luminosity of the shell increases dramatically, and for the next $\sim 10^5$ years, the intershell region between the two shells expands and become convective. The H shell cools and switches off during the power-down phase (Karakas and Lattanzio, 2014), which lasts for several hundreds of years. The outer convective envelope may then penetrate the former intershell region in an event called the third dredge-up (TDU, Pagel, 1997). The mass and metallicity dependence of TDU occurrence in stars is one of the major puzzles in current astrophysical research (Kippenhahn, Weigert, and Weiss, 2012). Eventually, the star contracts, reigniting the H shell, which will burn for another $\sim 10^5$ years, and the next thermal pulse can begin (Forestini and Charbonnel, 1997; Karakas and Lattanzio, 2014).

Mass loss on the AGB occurs through strong stellar winds and can be vigorous at up to a few $\sim 10^{-4} M_{\odot}/\text{year}$ or higher (Vassiliadis and Wood, 1993), which is several orders of magnitude higher than the mass-loss rate typically observed for RGB stars (Cassisi and Salaris, 2013). The tenuously-held outer envelope is eventually expelled (the mechanism is still unknown), producing a beautiful planetary nebula. The remaining CO core eventually cools and the star dies as a CO white dwarf, shown in the bottom panel of Fig. 1.18.

There are other known types of white dwarfs, the common ones being helium and oxygen-neon white dwarfs. Helium white dwarfs are the remnants of low-mass metal-poor RGB stars that have lost most of their envelope on the RGB due to interactions with a companion. They consist of a helium core with a thin envelope on the Horizontal Branch, however their mass is too low to ignite helium and they eventually fade as a helium-rich white dwarf (Kippenhahn and Weigert, 1967; Driebe et al., 1998). Oxygen-neon white dwarfs are the remnants of intermediate-mass stars of $6 - 8 M_{\odot}$ that have experienced core carbon burning and formed an oxygen-neon

¹¹Recalling that the energy generation rate is dependent upon temperature according to $\epsilon \propto (T/T_0)^{\nu}$, for helium burning, the value of ν is ~ 41 (Iliadis, 2007; Ryan and Norton, 2010).

degenerate core (Pagel, 1997; Dufour et al., 2007). Details on late stellar evolutionary phases are provided in Doherty et al. (2017).

1.2 Observations of low-mass stars

To learn more about low-mass stars, we observe their surface chemical abundances and make inferences about their evolutionary stage, interior mixing, age, and primordial chemical signature. To gain an understanding about the birth and evolution (chemically and dynamically) of galaxies, we need to observe many stars (e.g. star clusters or a large number of stars not necessarily in a cluster). By doing this, we can tag chemically-similar stars, with the ultimate goal being to reconstruct the history of the Milky Way Galaxy (Freeman and Bland-Hawthorn, 2002).

If we make the assumption that all stars in clusters were born in homogeneous gas clouds, we can also assume that a small fraction of stars still remain bound in star clusters (open and globular clusters), and that the majority have since dispersed and been distributed throughout the Galaxy (Bland-Hawthorn, Krumholz, and Freeman, 2010). Therefore, it should theoretically be possible to identify stellar siblings based upon a unique chemical signature, provided that the chemical space is large enough. If this can be achieved, the location and time of stellar births can be traced back through the history of the Milky Way (Bland-Hawthorn, Sharma, and Freeman, 2014). Vital components of the success of chemical tagging are the precision of the observations and selection of tagging candidates, and this is where low-mass, low-metallicity stars become incredibly important. By remaining (relatively) “pristine” from birth, these types of stars are an ideal option for chemical tagging candidates (Freeman and Bland-Hawthorn, 2002).

In this thesis we use observations of surface compositions of low-mass RGB stars to infer details of the mixing occurring in the interior. The mixing referred to specifically is the extra mixing mechanism occurring on the RGB of low-mass stars. We focus on observations that provide insights into the operation of the extra mixing mechanism (i.e. surface lithium and carbon abundances). We use observations of stars in different populations, including metal-poor ($-2 < [\text{Fe}/\text{H}] < -0.7$) globular clusters, the extremely metal-poor population ($[\text{Fe}/\text{H}] \sim -3$) in the halo, and open clusters ($-0.6 < [\text{Fe}/\text{H}] < +0.6$), to explore extra mixing over a wide range of metallicities.

1.2.1 Globular and open clusters in the Milky Way

In our Galaxy, stars reside in either globular clusters, open clusters, or the field. Globular clusters contain very old (around 12 Gyr old), low-mass stars, whereas open clusters contain comparatively younger (younger than around 4 Gyr), higher-mass stars. Field stars are not currently associated with a cluster (though they may have originated in clusters).

Globular clusters are an ideal laboratory for studies of extra mixing in stars. This is because globular clusters contain hundreds of thousands of low-mass stars, and the globular cluster population covers a large range in metallicity. By observing and obtaining chemical abundances of globular cluster stars, we can trace a relatively co-eval¹², large population over many all stellar evolutionary stages of the HR diagram, from the main sequence to beyond the giant branches (RGB and AGB). This is imperative to our understanding of how abundances in similarly-aged stars progress over time (Briley et al., 1990; Gilroy and Brown, 1991; Gratton et al., 2000; Shetrone, 2003; Smith and Martell, 2003; Weiss et al., 2004; Martell, Smith, and Briley, 2008; Lind et al., 2009).

Open clusters generally contain younger, higher-metallicity stars than globular clusters, and therefore provide an opportunity for analysis on a population of stars that complements our investigation into the globular cluster NGC6397 (more on this below in §1.2.2) because it allows us to study extra mixing over a large metallicity range. The open cluster and field stars in this thesis are in mass and metallicity ranges where the effects of extra mixing are predicted to be observable, therefore in Chapter 7 we investigate mixing in high-metallicity stellar populations more thoroughly.

1.2.2 Observations used in this thesis

Clusters: NGC6397

The change due to thermohaline mixing in surface lithium and carbon abundances is particularly evident for the old metal-poor globular cluster NGC6397, where the lithium abundance has been shown to vary with luminosity, and a noticeable drop in the abundance is evident after FDU (e.g., Fig. 1.9, which is Fig. 5 from Lind et al., 2009). Furthermore, there are carbon abundances for NGC6397 (Briley et al., 1990), and it is the only globular cluster to date that has observations for both carbon (Briley et al., 1990) and lithium (Lind et al., 2009) along the RGB. Therefore this cluster is the ideal place for us to start our investigation, hence we fit our stellar models to the globular cluster NGC6397.

Other observations: SAGA database, Gaia-ESO, APOGEE

SAGA database

The Stellar Abundances for Galactic Archeology (SAGA) database (Suda et al., 2008) is a compilation of galactic and stellar surveys that include thousands of extremely metal-poor stars, many of which have carbon, nitrogen, and lithium abundances. Access to extensive data is imperative to our investigations of the thermohaline mixing mechanism in metallicity regimes other than the metal-poor (i.e., $[\text{Fe}/\text{H}] = -2$ as in NGC6397), and the SAGA

¹²However, although not directly related to our problem, globular clusters are known to harbour multiple populations (Gratton, Sneden, and Carretta, 2004; Gratton, Carretta, and Bragaglia, 2012), where these populations are correlated with spreads in the abundances of light elements (e.g., C, N, O, Na, Cottrell and Da Costa, 1981; Bastian and Lardo, 2018).

database allows us to analyse stars with $[\text{Fe}/\text{H}] \sim -3$ (discussed in more detail in Chapter 6).

However, we acknowledge the inevitable presence of observational biases in our SAGA sample, which is statistically incomplete and biased towards bright giants and stars with high carbon abundances (Pols et al., 2009). In our sample of stars with observed carbon isotopic ratios, we do not find any indicators of strong trends/biases, notably of metallicity with surface gravity (i.e. a Malmquist bias, Malmquist, 1922) or towards stars with high carbon abundances (refer to Chapter 6 for the full discussion).

Gaia-ESO

GES uses the Fibre Large Array Multi-Element Spectrograph (FLAMES) multi-fiber facility on the Very Large Telescope (VLT, Pasquini et al., 2002) to target more than 10^5 stars in the Milky Way (Gilmore et al., 2012). GES aims to measure abundances for at least 12 elements (including Na, Mg, Si, Ca, Ti, V, Cr, Mn, Fe, Co, Sr, Zr, Ba) for field stars, and additional elements (e.g., Li) for metal-rich clusters (Gilmore et al., 2012).

Homogeneous GES data, specifically abundances of carbon and lithium, for Galactic field and cluster stars will provide insights into many aspects of stellar evolution. This is particularly the case for thermohaline mixing in the higher metallicity regime ($[\text{Fe}/\text{H}] > -1.5$). This is discussed in detail in Chapter 7 (also see Lagarde et al., 2018).

APOGEE

The Apache Point Observatory Galactic Evolution Experiment (APOGEE) is using high-resolution, high signal-to-noise infrared (H-band) spectroscopy to survey over 100,000 red giants across the full range of the Galactic bulge, bar, disc, and halo (Allende Prieto et al., 2008).

The majority of work done with APOGEE data to date has been on galaxy evolution (refer to Anders et al., 2017; Fernández-Alvar et al., 2017; Schiavon et al., 2017; Tang et al., 2017, and references therein). Lithium is not included as part of the chemical elements observed in the APOGEE survey, however ^{12}C and ^{14}N are observed and both of these elements show a signature of extra mixing on the RGB after FDU (^{12}C decreases and ^{14}N increases). It can be reasoned, therefore, that carbon and nitrogen abundances can be used as a tracer of mass (and stellar age). APOGEE is discussed in detail in §7.1.2.

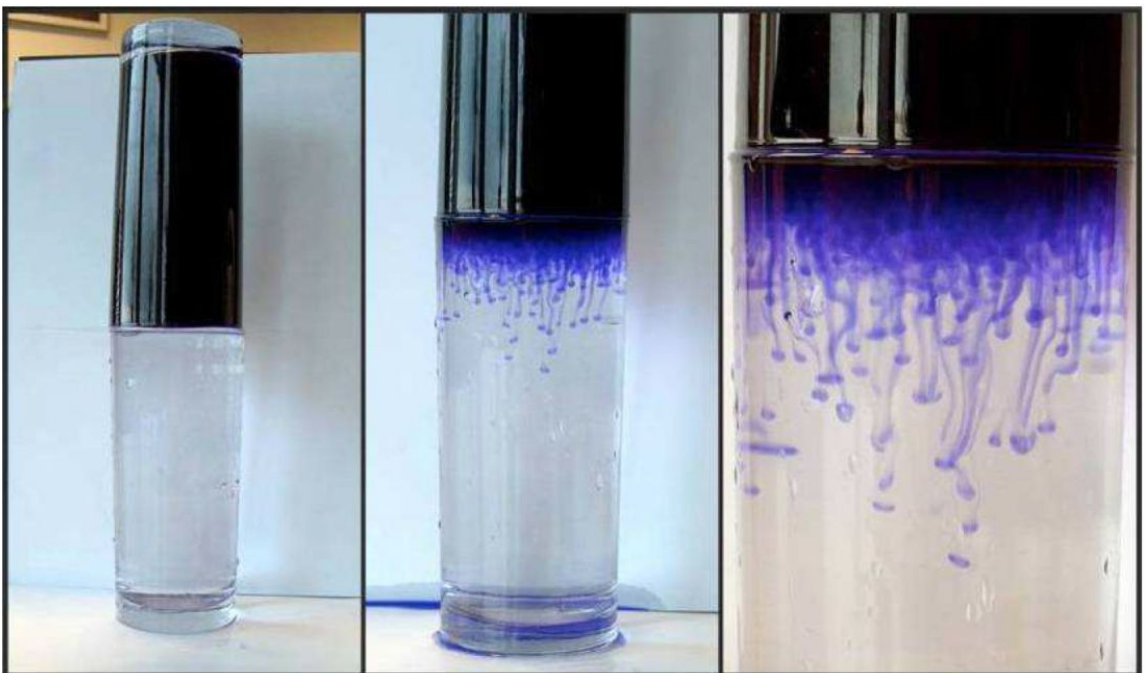


FIGURE 1.17: Thermohaline fingers. Warm salty water is coloured blue and sits atop cool fresh water. Image from Karakas and Lattanzio (2014). Photo taken and experiment performed by E. Glebbeek and R. Izzard.

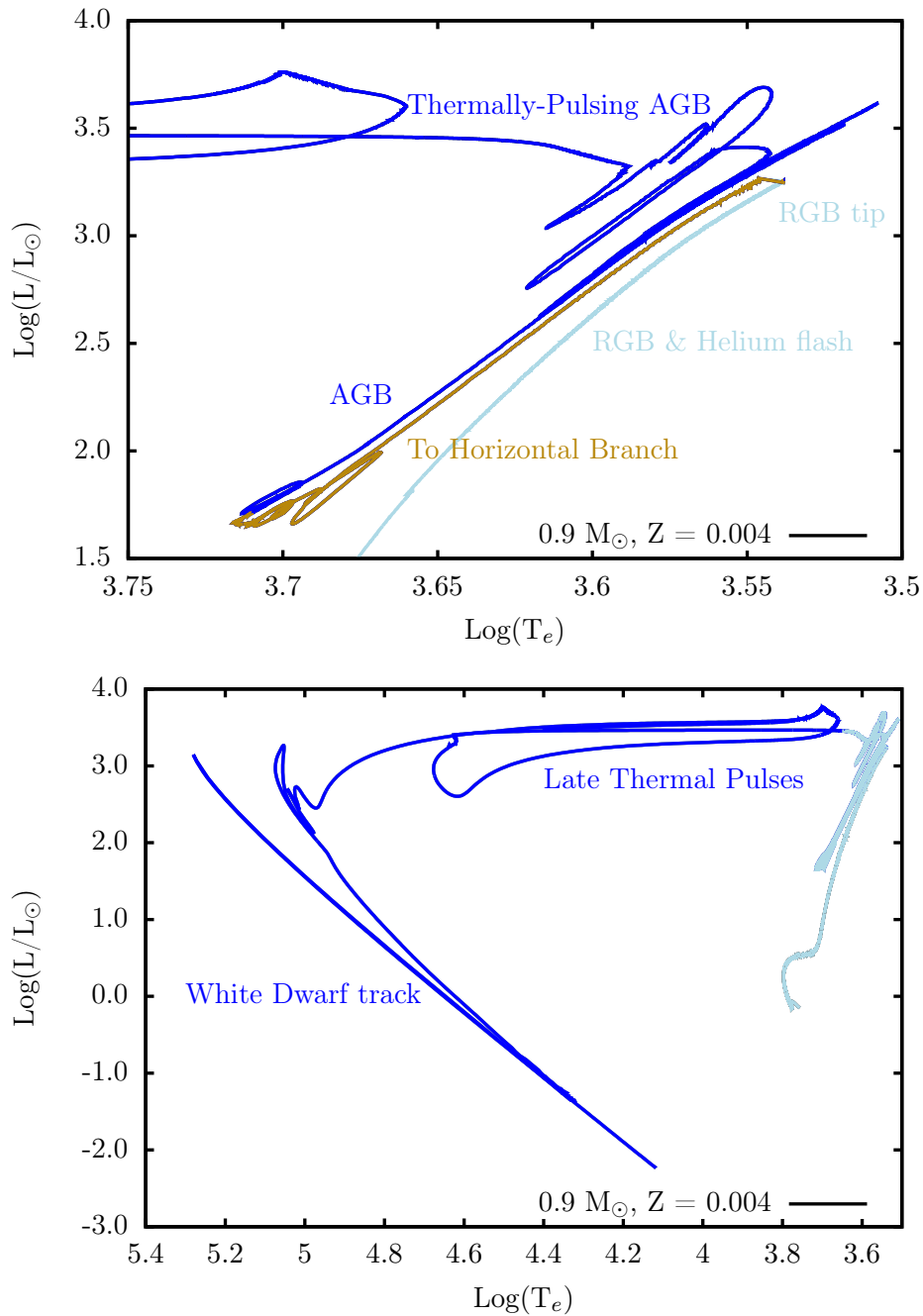


FIGURE 1.18: Hertzsprung-Russell (HR) diagram for a $0.9 M_{\odot}$, $Z = 0.004$ star. Top panel: The region of the RGB, AGB, and thermally-pulsing AGB phase (labelled, colours correspond to HR diagram curve). The details of each phase are in text. Bottom panel: The full HR diagram including the white dwarf track and late thermal pulses. The dark blue curve is the part of the HR diagram corresponding to the late thermal pulses and white dwarf track evolutionary phases, and the light blue curve is evolution prior to these phases. Stellar model provided by A. Karakas.

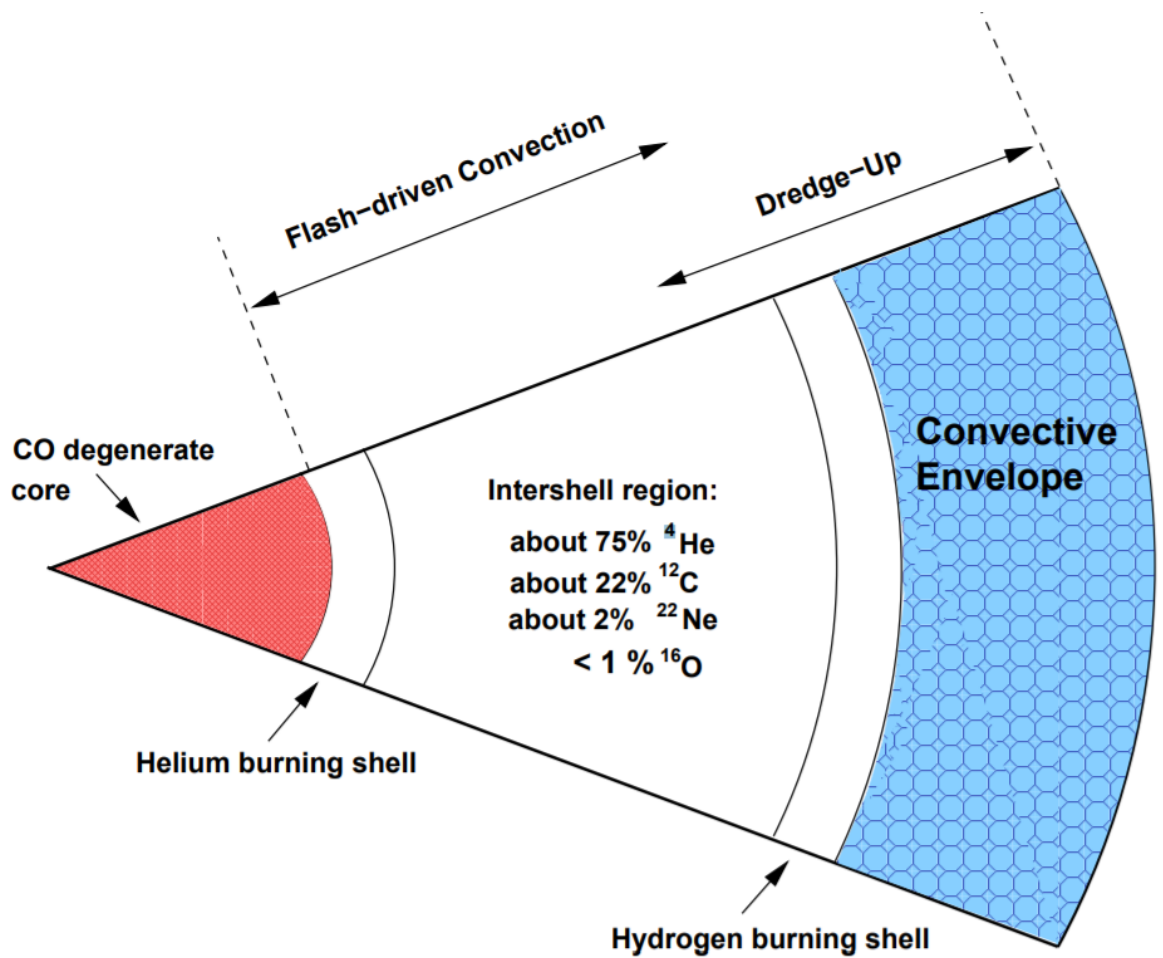


FIGURE 1.19: A schematic of the structure of an AGB star (not to scale). Figure is Fig. 14 from Karakas and Lattanzio (2014), original figure from Karakas, Lattanzio, and Pols (2002).

Chapter 2

The Evolution code MONSTAR

The following content was published in Henkel, K., Karakas, A.I., and Lattanzio, J.C. (2017), “A phenomenological modification of thermohaline mixing in globular cluster red giants”, *The Monthly Notices of the Royal Astronomical Society*, 469, 4, 4600-4612:

- Paragraph 1 in §2.1,
- Paragraph 5 in **Opacity** (§2.2.1),
- §2.3,
- Paragraph 1 in §2.5,
- §2.5.1,
- §2.6,
- §2.6.1, and

No figures or tables in this chapter have been published by the authors. All figures are referenced appropriately.

2.1 Introduction

All stellar models have been run using MONSTAR, the Monash version of the Mt. Stromlo stellar evolution code (Campbell, 2007; Campbell and Lattanzio, 2008; Angelou, 2014; Angelou et al., 2015; Henkel, Karakas, and Lattanzio, 2017). MONSTAR calculates the stellar structure of a single star in one dimension, assuming spherical symmetry. Rotation and magnetic fields are currently not included in MONSTAR.

At a given point in time in the evolution of a star (timestep), MONSTAR determines a mathematical model for the structure of the star by solving the equations of stellar structure outlined in §2.2. To solve the main equations of stellar structure, constitutive equations that define pressure, opacity, and energy in terms of density, temperature, and composition are required. These equations are detailed in §2.2.1.

2.2 Equations of stellar structure

Below are the equations of stellar structure that the evolution code solves at every timestep.

1. Radius equation

$$\frac{\partial r}{\partial m} = \frac{1}{4\pi r^2 \rho}, \quad (2.1)$$

2. Pressure equation

$$\frac{\partial P}{\partial m} = \frac{-Gm}{4\pi r^4}, \quad (2.2)$$

where m is the mass at radius r .

3. Temperature gradient equation

$$\frac{\partial T}{\partial m} = \frac{-3 \kappa L_r}{4ac T^3 16\pi^2 r^4}, \quad (2.3)$$

where L_r is the luminosity at radius r .

4. Luminosity equation

$$\frac{\partial L}{\partial m} = \epsilon + \epsilon_{\text{grav}} - \epsilon_{\nu}, \quad (2.4)$$

where ϵ is the energy generated from nuclear reactions, ϵ_{grav} (commonly called the gravitational energy term) is the energy generated by stellar material through thermodynamic processes, ϵ_{ν} is the energy lost due to neutrino processes (energy is lost because neutrinos do not interact with stellar material in a significant way).

5. Composition equations

- Changes due to nuclear reactions

$$\frac{\partial X_i}{\partial t} = \frac{m_i}{\rho} \left(\sum_j r_{ji} - \sum_k r_{ik} \right), \quad i = 1, \dots, k, \quad (2.5)$$

where X_i is the unit mass fraction consisting of nuclei i , m_i is the mass of nuclei i , r_{ji} is the reaction rate transforming nuclei j into nuclei i , r_{ik} is the reaction rate transforming nuclei i into nuclei k , $(\partial X_i / \partial t)_{\text{nuc}}$ is the change in abundances of nuclei i from nuclear reactions.

- Abundance changes in convective regions

Developed by Campbell (2007), in MONSTAR we model the change in abundances according to

$$\frac{dX_i}{dt} = \frac{\partial X_i}{\partial t} + \frac{\partial}{\partial m} \left((4\pi r^2 \rho)^2 D \frac{\partial X_i}{\partial m} \right), \quad (2.6)$$

where D is the diffusion coefficient of the mixing process in the region.

All other variables have their usual meanings and all variables are in cgs units. Note that in convective regions, the temperature gradient is calculated from the mixing length theory (this is discussed in more detail in §2.5; Böhm-Vitense, 1958) and is close to the adiabatic temperature gradient (Salaris and Cassisi, 2006; Campbell, 2007; Angelou, 2014).

2.2.1 Constitutive equations

Accompanying the above equations of stellar structure (Equations 2.1-2.6) are constitutive equations listed below.

1. Pressure

$$P = P(\rho, T, \text{composition}), \quad (2.7)$$

2. Opacity

$$\kappa = \kappa(\rho, T, \text{composition}), \quad (2.8)$$

3. Energy

$$\epsilon = \epsilon(\rho, T, \text{composition}), \quad (2.9)$$

- Energy generation from nuclear reactions

$$\epsilon_n = \epsilon_n(\rho, T, \text{composition}), \quad (2.10)$$

- Energy loss from neutrinos

$$\epsilon_\nu = \epsilon_\nu(\rho, T, \text{composition}), \quad (2.11)$$

where “composition” is the chemical composition of elements in terms of relative abundance and distribution throughout the star. Pressure, opacity, and energy are discussed further below.

Pressure

Pressure is also affected by the levels of ionisation and degeneracy, which are also dependent upon temperature and density. The ionisation states of hydrogen and helium are treated with the Saha equation. This degeneracy level is assessed using a degeneracy parameter

$$\Theta = \frac{k_B T}{E_F}, \quad (2.12)$$

where Θ is the degeneracy parameter, k_B is the Boltzmann constant, T is the temperature, and E_F is the Fermi energy (maximum energy of an electron at 0K).

If degeneracy $\simeq 0$, we consider the contributions to the total pressure to be from the perfect electron gas and radiation (total ionisation) according to the equation

$$P = P_g + P_r = \frac{N_0 k}{\mu} \rho T + \frac{1}{3} a T^4 = \frac{R}{\mu} \rho T + \frac{1}{3} a T^4, \quad (2.13)$$

where the variables take their usual meaning, P_g is the gas pressure, and P_r is the radiation pressure (Clayton, 1983).

Partial degeneracy is solved in MONSTAR using fitting formulae by Beudet and Tassoul (1971).

Opacity

There are 4 types of processes leading to radiative opacity

1. Bound-bound absorptions are the absorption of a photon by an atom. A bound electron will make a transition to a higher energy state (without being ionised). The reversal is a photon being re-emitted and the electron returning to a lower energy state.
2. Bound-free absorption is the absorption of a photon by an atom. A bound electron will gain enough energy from the photon to be ionised. The reversal of this process is called radiative recombination.
3. Free-free absorption is the absorption of a photon by a “free” or “continuum” electron as the electron passes an ion. The electron will transition to a higher energy state. The reversal of this process is called bremsstrahlung.
4. Free electron scattering. This process goes by other names, including Compton scattering, or in nonrelativistic situations, Thomson scattering.

The type of opacity dominant within a stellar region changes with temperature. Bound-bound and bound-free absorptions dominate at low temperatures, i.e. the atmospheres of the giants considered in this thesis (Iben, 2013). Additionally, at low temperatures (i.e. in the outer layers), molecules contribute significantly to the opacity through electron transitions and transitions between rotational and vibrational molecular states (Salaris and Cassisi, 2006). Therefore, we also include tables that vary in particular abundances (detailed in Table 2.1). As ionisation becomes more “complete” at higher temperatures, free-free absorptions dominate. At even higher temperatures, the process of free electron scattering dominates (Clayton, 1983). Dust also contributes to stellar opacity.

Opacity cannot be calculated using a single formula and must be in tabular form, and due to the dependence of opacity upon temperature and density as stated above, opacity tables are split into 3 categories:

1. Low temperature,
2. High temperature, and

3. Conductive opacities (included in the high temperature opacity tables).

On a density-temperature plane as shown in Fig. 2.1, the divide between the main sources of opacity is apparent. We emphasise that the figure shows the *general region* on a density-temperature plane where main sources of opacity dominate, and the “true” representation on such a figure is much more complicated. Table 2.1 is a summary of the tables included in MONSTAR. In the final column of Table 2.1, we list the literature references for the opacities and also the references for the included tables where molecular opacities are taken into consideration.

High-temperature opacities are provided by the OPAL opacity tables (Iglesias and Rogers, 1996). Also included are fixed-metal distribution (OPAL type-1) tables that have the solar mixture composition of Grevesse and Noels (1993) and α -element enhancement¹ of Achim Weiss (Iglesias and Rogers, 1996). Tables variable in C and O content (OPAL type-2) are based upon abundances of Grevesse and Noels (1993). MONSTAR uses low-temperature (below 10^4 K) tables with variable C and N content from Lederer & Aringer (2009, Karakas, Campbell, and Stancliffe, 2010; Angelou et al., 2015).

Conductive opacities are included in the high temperature opacity table and are more complex (Hubbard and Lampe, 1969; Raikh and Iakovlev, 1982; Itoh et al., 1983; Mitake, Ichimaru, and Itoh, 1984, for more details see Table 2.1). Radiation and convection dominate energy transport for most of the evolution, and conduction only becomes significant when densities are high enough for the electron gas to be degenerate, such as in the cores of RGB and AGB stars. Electron-electron scattering is ignored in this case since the cross-sections are small compared to electron-ion scattering. Additionally, under degenerate conditions, a gas is essentially a sea of negative charge of uniform density, therefore electrons do not scatter due to electron-electron interactions.

Opacity tables need to be interpolated to obtain the correct values for the conditions in a star at a given location. In MONSTAR, this interpolation is linear. At a given (interpolated) metallicity, opacity tables are interpolated for varying H, C, and N mass fractions at all mass coordinate points (mesh points, described further in §2.2.4). Interpolation of H, C, N, radius, and temperature are performed on a mesh point-by-mesh point basis in relevant regions of the star.

¹Alpha-element (O, Ne, Mg, Si, Ca, Ti) abundances are an indicator of the contribution of supernovae (SNe) to the primordial gas in a stellar population. Type Ia SNe are thermonuclear explosions once thought to be caused by mass accretion onto a white dwarf, however this is in debate (e.g. see Salaris and Cassisi, 2006, and references therein). This type of SNe also produce mainly iron-peak elements. Type II (core collapse) SNe are the final stage of high-mass stars’ lives and produce mainly α -elements. Therefore, a relatively old, metal-poor stellar population will be enhanced in α -elements due to contributions by Type II SNe but not Type Ia (Salaris and Cassisi, 2006).

Opacity type	$\log(T)$ range	$\log(\rho/T^3)$ range	References
Low temperature	2.70 – 4.50 3.20 – 4.050	–8.0 – 1.0 –7.0 – 1.0	Opacities: Alexander (1975) and Alexander, Rypma, and Johnson (1983) Abundances: Grevesse and Noels (1993, variable C, O), Lederer and Aringer (2009, variable C, N)
Intermediate temperature	3.75 – 8.70	–8.00 – 1.00	Opacities: Iglesias and Rogers (1996) Abundances: Grevesse and Noels (1993, for CNO-Ne, CO-N, C-N), Grevesse and Sauval (1998, for CNO-Ne, CO-N, C-N)
Conductive opacities	3.70 – 8.70	–5.75 – 5.00	Non-relativistic electron conductivity: Iben (1975) analytic fit to Hubbard and Lampe (1969) and Itoh et al. (1983) Relativistic electron conductivity: Fitting formulae of Itoh et al. (1983) and Mitake, Ichimaru, and Itoh (1984) Solid material: Raikh and Iakovlev (1982)
High temperature	8.60 – 10.10	–5.50 – 0.95	Opacities: Iglesias and Rogers (1996) Abundances: Lederer and Aringer (2009, for C, O, Ne)

TABLE 2.1: Opacity tables in MONSTAR. Abundance references are for the included tables that vary in the abundance of the elements listed.

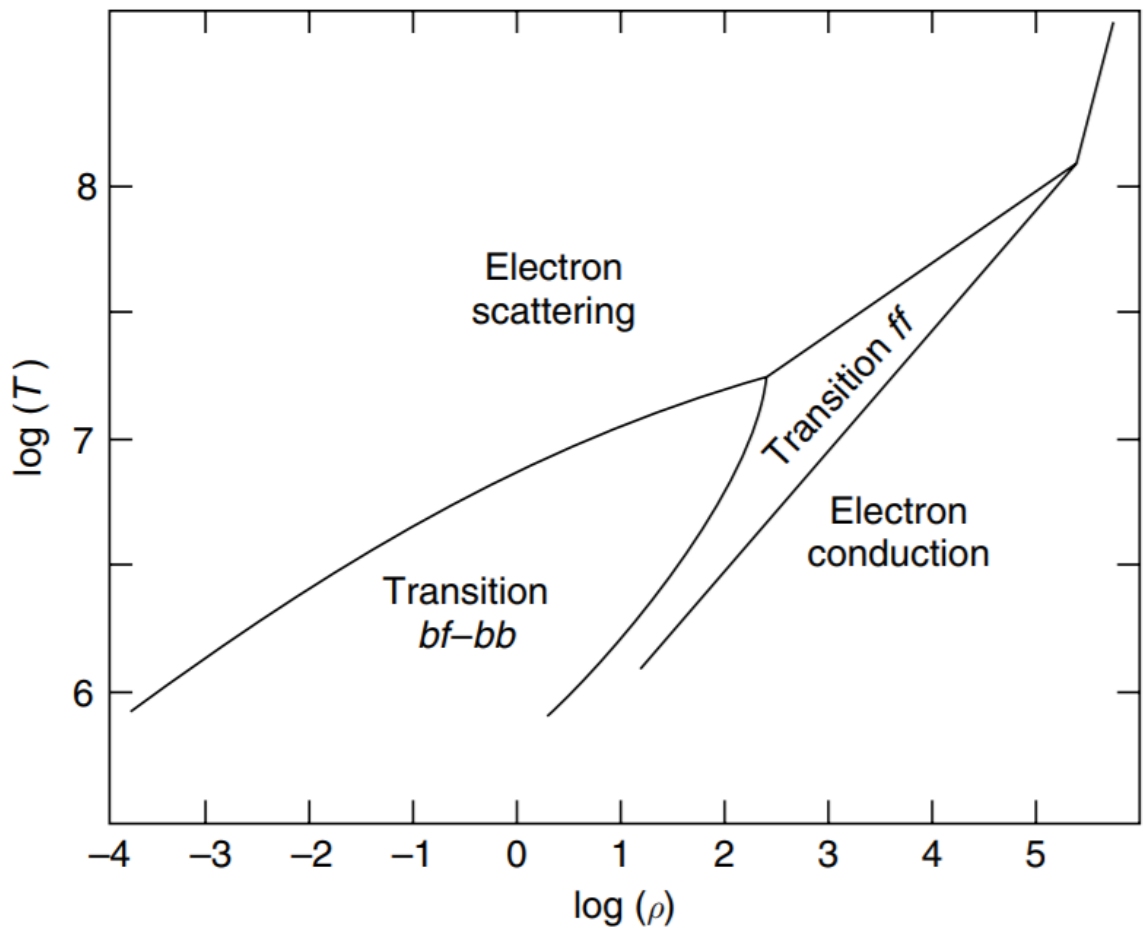


FIGURE 2.1: Opacity processes as shown in the temperature-density plane. Figure is Fig. 3.2 from Salaris and Cassisi (2006).

Energy

The third constitutive relation, nuclear energy, requires a formula for every reaction rate related to nuclear energy production in the star, particularly the main nuclear energy producers during stellar evolution, which are the pp chains (Equation 1.1), the CNO cycles (Equation 1.2), the triple alpha reaction ($3^4\text{He} \rightarrow ^{12}\text{C}$), and the carbon alpha reaction ($^{12}\text{C}(^4\text{He},\gamma)^{16}\text{O}$).

Stellar codes include and calculate as many reactions as is necessary to obtain sufficient accuracy in terms of energy generation and abundances. In MONSTAR, the reaction rates and energy generation reactions considered are below. Not mentioned are the triple alpha and carbon alpha reactions, which are stated above and included in MONSTAR but do not require further explanation.

Each of the mentioned reactions proceed at a different rate, therefore the slowest rate for each chain/cycle determines how quickly the process occurs. Similarly, some rates occur so rapidly relative to other reaction rates in the chain/cycle that they can be approximated as “instantaneous” and ignored. This is detailed below. *We emphasise that in terms of energy generation, all reactions are included in MONSTAR, whereas for determining the rate at which a chain/cycle proceeds, only the slowest reactions need to be considered for reasons stated above.*

pp chains: For the ppI chain, the lifetime of deuterium against a proton is, by far, the shortest of all the lifetimes in the pp chains. By the time deuterium has reach its equilibrium value, it is acceptable to assume that the abundance of H has not changed. Therefore we can assume D is in equilibrium at all times and can simplify by saying $\text{H}(2\text{p},\nu)^3\text{He}$. The lifetime of ^3He against itself is dependent upon temperature and the abundance of ^3He . In terms of energy generation and rates, one must consider both the $\text{H}(\text{H},e^+)\text{D}$ reaction and the $^3\text{He}(^3\text{He},2\text{p})^4\text{He}$ reaction (Pagel, 1997; Iliadis, 2007).

Of the ppIII chain reactions, the rate of only the $^7\text{Be}(\text{p},\gamma)^8\text{B}$ reaction is included in MONSTAR. The simplified pp chains are below.

- ppI chain: $\text{H}(\text{H},e^+)\text{D}$, $^3\text{He}(^3\text{He},2\text{p})^4\text{He}$
- ppII chain: $^3\text{He}(^4\text{He},\gamma)^7\text{Be}$, $^7\text{Be}(e^-, \nu)^7\text{Li}$, $^7\text{Li}(\text{p}, ^3\text{He})^4\text{He}$
- ppIII chain: $^7\text{Be}(\text{p},\gamma)^8\text{B}$

CNO cycle: For the CNO cycle operating at around 25 MK, the fastest burning (proton capture) species is ^{15}N followed by ^{13}C , ^{12}C , ^{17}O , ^{14}N , and lastly ^{16}O . Therefore the rate that the CNO cycle proceeds is governed by the rate that ^{16}O burning occurs. It should be noted that although most CNO proton-capturing reactions are considered, $^{15}\text{N}(\text{H},\gamma)^{16}\text{O}$ occurs only around 4 times per 10,000 reactions (Pagel, 1997).

At temperatures below around 100 MK, which is the case for low-mass stars, the lifetimes of ^{13}N , ^{15}O , and ^{17}F against proton capture are much longer than their lifetimes against beta-decay, and it is therefore reasonable to assume that these decays are instantaneous and need not be considered. Therefore we can state: $^{12}\text{C}(\text{p},\gamma e^+ \nu)^{13}\text{C}$, $^{13}\text{C}(\text{p},\gamma)^{14}\text{N}$, $^{14}\text{N}(\text{p},\gamma e^+ \nu)^{15}\text{N}$,

$^{16}\text{O}(p,\gamma e^+ \nu)^{17}\text{O}$. In summary, the simplified CNO cycles are below (Pagel, 1997; Iliadis, 2007).

- CN cycle: $^{12}\text{C}(p,\gamma)^{13}\text{N}$, $^{13}\text{C}(p,\gamma)^{14}\text{N}$, $^{14}\text{N}(p,\gamma)^{15}\text{O}$
- ON cycle: $^{16}\text{O}(p,\gamma)^{17}\text{F}$

2.2.2 Boundary conditions

We define boundary conditions such that in the core we have

$$m = 0, \quad r = 0, \quad L = 0, \quad (2.14)$$

and at the surface

$$m = M, \quad T = 0, \quad P = 0, \quad (2.15)$$

where M is the total stellar mass. The surface boundary conditions are physically unreasonable. They are at what is called “radiative zero”, but are unphysical because the temperature and pressure will never be zero. We define the surface of the star using optical depth, which is the number of mean free paths of radiation travelling outwards from the stellar interior before escaping. The equation for optical depth $\tau_\lambda(z)$ is

$$\tau_\lambda(z) = \int_z^\infty \kappa_\lambda(z') \rho(z') dz', \quad (2.16)$$

where z' is height above the specified layer z , and all other variables have their usual meanings (Pagel, 1997). The surface temperature of a star, which we consider to be a blackbody, occurs at optical depth $\tau = 2/3$ and most of the radiation generated in the star escapes at this location (Iben, 2013). Therefore we define the surface of the star to be at $\tau = 2/3$.

2.2.3 Solving the equations of stellar structure

In the evolution code, we use a Lagrangian mesh for several reasons. Mass is the preferred coordinate because it is intuitively and intricately linked with the gaseous material inside the star, unlike radius, which is an Eulerian coordinate. The form of the mass variable in MONSTAR is

$$x = \left(\frac{m}{M} \right)^{1/3} \quad (2.17)$$

where x is the independent variable. We define mass in this way because it allows the derivatives of variables that include mass to be finite at the centre (Campbell, 2007; Angelou, 2014). Mass (or rather x in MONSTAR) is the independent variable in the stellar structure equations (Equations 2.1-2.4) because it does not change significantly during stellar evolution until the

AGB where the star experiences severe mass loss (although a small amount of mass is also lost on the RGB). This is unlike radius, which changes significantly as the star ages, e.g. as the star leaves the main sequence and expands to become a red giant.

During events such as expansion where the Eulerian coordinate radius will change significantly, parameters such as the composition would need to be recalculated at every mesh point, compounding errors and computational time. To reiterate, during expansion and contraction, radius will change significantly whereas mass will not (the mass coordinate moves with the gas).

We have 4 first-order differential equations to solve, as well as 2 surface and 2 core boundary conditions. The method used to solve these equations in MONSTAR is the Henyey method (Henyey, Forbes, and Gould, 1964), which is a relaxed generalised Newton-Raphson.

Henyey method

To solve a stellar model using the Henyey method, we first construct a star that contains spherically symmetrical mass shells (since x is our independent variable). If N is the number of shell boundaries in our star, we therefore have $N - 1$ mass shells (not necessarily equal mass spacing), where the shell boundaries (mesh points) are at $i = 1, \dots, N$. Fig. 2.2 is a schematic of mass shells in the Henyey method.

We have the 4 differential equations of stellar structure

$$\frac{dy^j}{dM} = f^j(y^1, y^2, y^3, y^4) \quad j = 1, 2, 3, 4 \quad (2.18)$$

where

- $j = 1$ is the equation for radius,
- $j = 2$ is the equation for pressure,
- $j = 3$ is the equation for luminosity, and
- $j = 4$ is the equation for temperature.

Therefore, all variables are defined at all shell boundaries

$$y_i^j \text{ for } j = 1, 2, 3, 4 \text{ for } i = 1, \dots, N. \quad (2.19)$$

Additionally, there are the boundary conditions

Core	Surface
$r_1 = y_1^1 = 0$	$P_N = y_N^2 = 0$
$L_1 = y_1^3 = 0$	$T_N = y_N^4 = 0.$

Due to the presence of these boundary conditions, we must determine the difference approximations, which allow the differential equations to be approximated according to

$$A_i^j = \frac{y_i^j - y_{i+1}^j}{M_i - M_{i+1}} - f^j(y_{i+1/2}^1, y_{i+1/2}^2, y_{i+1/2}^3, y_{i+1/2}^4), \quad (2.20)$$

where the first term of the right-hand side of Equation 2.20 is the difference approximation to our differential equations at a mesh point i , and the second term is the approximation to f^j across the shell (i to $i + 1$) where we take the approximation to be in the centre of the shell ($i + 1/2$). We have two options when approximating stellar structure values within a mass shell ($y_{i+1/2}$), being the

1. Arithmetic mean: $y_{i+1/2}^j = \frac{(y_i^j + y_{i+1}^j)}{2}$, or
2. Geometric mean: $y_{i+1/2}^j = \sqrt{y_i^j y_{i+1}^j}$.

The arithmetic mean is, however, not the most appropriate way to determine the mean of a set of values because it is weighted towards the largest value, which becomes particularly problematic when the values of y_i^j and y_{i+1}^j are several orders of magnitude apart (though this could be alleviated with smaller mesh spacings). To obtain a (more) appropriate representation of the mean, in MONSTAR we take the geometric mean. It can be noted that we cannot *strictly* enforce the boundary conditions if we take the geometric mean of our shells.

For all i and j , we want $A_i^j = 0$. If we approximate y_i^j from a previous/starting model, then A_i^j will not equal zero. The first-order expansion of the Taylor series for A_i^j gives

$$\delta A_i^j = \sum_{k=1}^4 \frac{\partial A_i^j}{\partial y_i^k} \delta y_i^k + \sum_{k=1}^4 \frac{\partial A_{i+1}^j}{\partial y_{i+1}^k} \delta y_{i+1}^k, \quad (2.21)$$

Henyeys relaxation method depends on approximations and is therefore sensitive to errors. There are two main sources of error: (1) rounding error, and (2) truncation error. *Rounding errors* are due to the fact that we can only compute to a finite number of decimal places. *Truncation errors* occur when we truncate the above Taylor series expansion.

We also want $A_i^j + \delta A_i^j = 0$. To solve for δA_i^j , we write in matrix form $\mathbf{H}\delta = -\mathbf{A}$, where \mathbf{H} is the Henyey matrix. Therefore we define δ and \mathbf{A} as column vectors each with $4(N - 1)$ elements

$$\delta = (\delta y_1^2 \quad \delta y_1^4 \quad \delta y_2^1 \quad \delta y_2^2 \quad \dots \quad \delta y_{N-1}^4 \quad \delta y_N^1 \quad \delta y_N^3)^T, \quad (2.22)$$

$$\mathbf{A} = (A_1^1 \quad A_1^2 \quad A_1^3 \quad A_1^4 \quad \dots \quad A_{N-1}^1 \quad A_{N-1}^2 \quad A_{N-1}^3 \quad A_{N-1}^4)^T. \quad (2.23)$$

The Henyey matrix \mathbf{H} will therefore be

$$\mathbf{H} = \begin{array}{cccccccc}
\frac{\partial A_1^1}{\partial y_1^2} & \frac{\partial A_1^1}{\partial y_1^4} & \frac{\partial A_1^1}{\partial y_2^1} & \frac{\partial A_1^1}{\partial y_2^2} & \dots & 0 & 0 & 0 & 0 \\
\frac{\partial A_1^2}{\partial y_1^2} & \frac{\partial A_1^2}{\partial y_1^4} & \frac{\partial A_1^2}{\partial y_2^1} & \frac{\partial A_1^2}{\partial y_2^2} & \dots & 0 & 0 & 0 & 0 \\
\vdots & \vdots & \vdots & \vdots & \ddots & \vdots & \vdots & \vdots & \vdots \\
0 & 0 & 0 & 0 & \dots & \frac{\partial A_{N-1}^3}{\partial y_{N-1}^3} & \frac{\partial A_{N-1}^3}{\partial y_{N-1}^4} & \frac{\partial A_{N-1}^3}{\partial y_N^1} & \frac{\partial A_{N-1}^3}{\partial y_N^3} \\
0 & 0 & 0 & 0 & \dots & \frac{\partial A_{N-1}^4}{\partial y_{N-1}^3} & \frac{\partial A_{N-1}^4}{\partial y_{N-1}^4} & \frac{\partial A_{N-1}^4}{\partial y_N^1} & \frac{\partial A_{N-1}^4}{\partial y_N^3}.
\end{array} \quad (2.24)$$

We need to solve \mathbf{H} for δ , which is relatively simple due to the number of zeroes. Therefore, many simple matrix-solving techniques are satisfactory.

We then check to see if $A_i^j + \delta A_i^j = 0$ is satisfied satisfactorily. If not, the model is considered to have not converged and a new Henyey matrix is constructed based upon the new value for $y_i^j + \delta y_i^j = y_i^j$. The process repeats until convergence is achieved.

There are many conditions for convergence. Below are two that we use in MONSTAR.

1. Sufficiently small corrections:

$$\frac{\delta y_i^j}{y_i^j} < \text{some specified value for all } i, j = 0.001 \text{ in MONSTAR, and}$$

2. Current values must satisfy the equations of stellar structure:

$$\Delta_i^j = \frac{A_i^j}{\left(y_i^j - y_{i+1}^j\right) (M_i - M_{i+1})} < \text{some specified value for all } i, j = 0.001 \text{ in MONSTAR.}$$

We note that multiple conditions for convergence are employed according to the behaviour of the stellar structure equations and the complexities of convergence during different phases of evolution.

In summary, the general steps of Henyey method are:

1. Assume structure of star.
2. Approximate the differential equations of stellar structure based on assumption in (1) or on corrections after the first iteration.
3. Differential equations of stellar structure not satisfied.
4. Corrections applied to differential equations.
5. Differential equations are more nearly satisfied.
6. Repeat (2) - (5) until corrections are below a specified value.
7. If successive (in time) models are being produced, take a small timestep Δt .

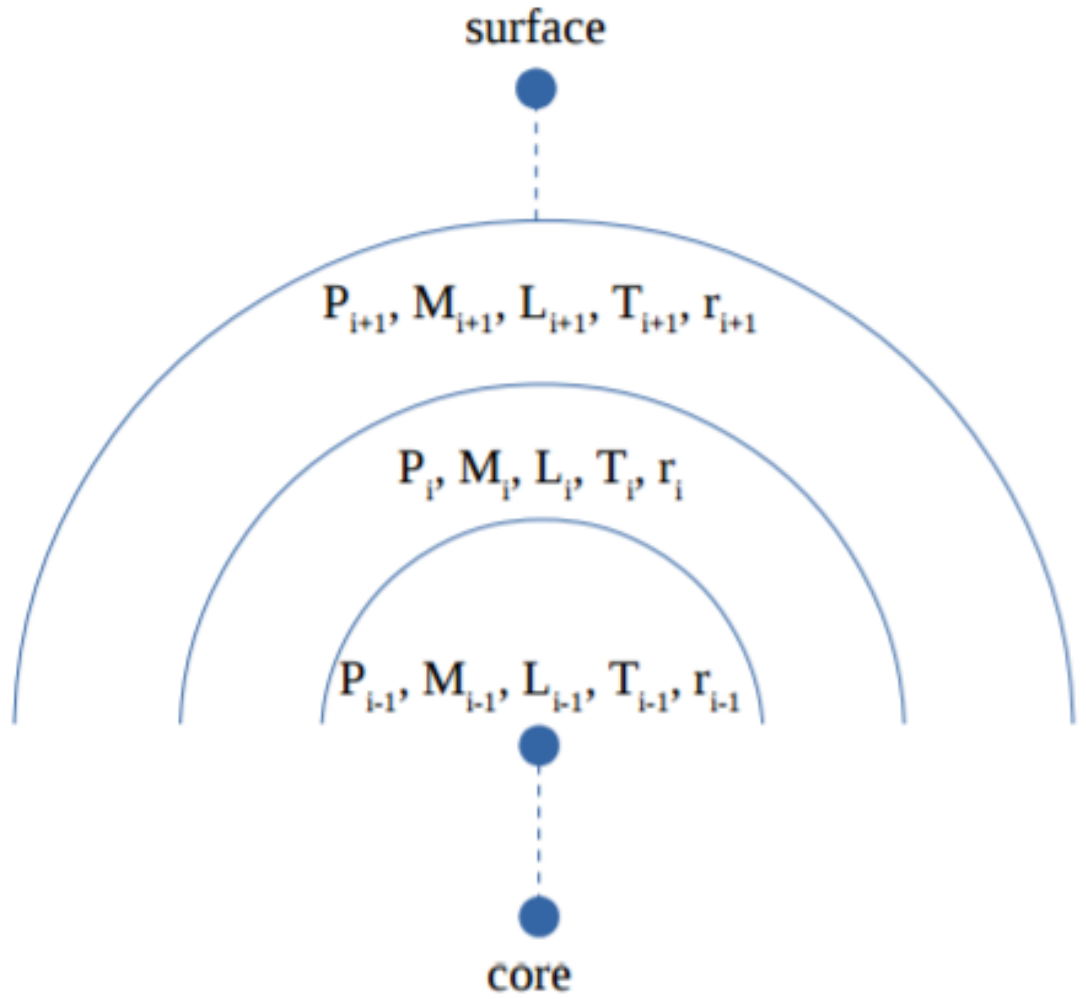


FIGURE 2.2: Schematic of mass shells used in the Henyey method.

8. Re-evaluate the change in composition $\{X_Z\}$ of star due to burning/mixing.

The steps above are then repeated for a new model at $t + \Delta t$.

2.2.4 Meshing routine

To adequately resolve the variables required for solving the stellar evolution equations, we require a one-dimensional mesh of points distributed throughout the star that are defined by their mass coordinate. At each mesh point boundary, we determine temperature (T), pressure (P), radius (r), elemental abundances ($X(\text{abund})$), internal energy (U), opacity (κ), and density (ρ), whereas luminosity (L), convective velocity (v), and the diffusion coefficient (D) are solved at a point between mesh points, shown in Fig. 2.3. There are limitations on changes in the values of L, T, P, r , and $X(\text{abund})$ between adjacent mesh points and consecutive models to ensure sufficient resolution, which are set in the parameter file (Angelou, 2014).

MONSTAR employs a combination of geometric and arithmetic criteria, where a geometric criterion limits the maximum value of the ratio between two adjacent abundance values and an arithmetic criterion limits the maximum change in any element. This combination of criteria results in a mesh grid that is non-uniformly distributed. MONSTAR's adaptive mesh also allows the addition and removal of mesh points as required in particular regions of the star during specific evolutionary stages, e.g. during thermohaline mixing where higher resolution is required (Angelou, 2014).

2.2.5 Timestepping

Once we have converged on solutions for the equations of stellar structure (Equations 2.1- 2.6) for the star at this point in time, nuclear burning demands that a timestep be taken to determine the updated composition and therefore evolution of said star. It can be seen that the only equation of stellar structure (including the constitutive relations) that depends on time is the composition, therefore we use the change in composition over time to inform the stellar properties of the next timestep.

The change in composition at the current and previous timesteps are calculated for the initial model (the previous and current timesteps are both read from starting model file). Usually, these newly calculated values are used as initial guesses for the next stellar model, however, the compositions at each point in the star could then be linearly extrapolated. MONSTAR could also linearly extrapolate the central temperature and pressure values to be used to re-solve the equations of stellar structure.

MONSTAR will select the smallest timestep that will satisfy seven abundance change criteria, including changes at a given mesh point between consecutive models in the values of temperature, pressure, abundances, and abundance ratios, and changes in the total luminosities of hydrogen burning, and radiated luminosity (for more details, see Angelou, 2014). For reference, during FDU the timestep is typically between 2 and 10 million years, however when structural and/or abundance changes are occurring during hydrogen shell burning, the timestep can be as short as a few hundred thousand years.

2.3 Reaction rates

MONSTAR has a network of nine species (^1H , ^3He , ^4He , ^7Be , ^7Li , ^{12}C , ^{13}C , ^{14}N , ^{16}O , and a tenth particle ensuring baryonic conservation). The reaction rates used in MONSTAR are detailed below in Table 2.2 (Angelou et al., 2015).

2.4 Mass loss

Mass loss in RGB stars is a source of uncertainty in theoretical models. We include mass loss in MONSTAR by utilising empirical mass loss formulae.

Reaction rate	Source
${}^1\text{H}(p, e^+ \nu_e) {}^2\text{H}$	Harris et al. (1983)
${}^3\text{He}({}^3\text{He}, 2p) {}^4\text{He}$	Caughlan and Fowler (1988)
${}^3\text{He}({}^4\text{He}, \gamma) {}^7\text{Be}$	Caughlan and Fowler (1988)
${}^{12}\text{C}(p, \gamma) {}^{13}\text{N}$	Caughlan and Fowler (1988)
${}^{14}\text{N}(p, \gamma) {}^{15}\text{O}$	Champagne (private communication)
${}^7\text{Be}(e^-, \nu_e) {}^7\text{Li}$	JINA REACLIB Cyburt et al. (2010)
${}^7\text{Be}(p, \gamma) {}^8\text{B}$	Angulo et al. (1999)
${}^7\text{Li}(p, {}^4\text{He}) {}^4\text{He}$	Descouvemont et al. (2004)
${}^{13}\text{C}(p, \gamma) {}^{14}\text{N}$	Angulo et al. (1999)

TABLE 2.2: Key reaction rates in MONSTAR.

The mass loss prescription on the RGB is from Reimers (1975) with $\eta_R = 0.4$ (Constantino et al., 2016) and given by

$$\dot{M} (M_\odot \text{ yr}^{-1}) = 4 \times 10^{-13} \eta_R \frac{RL}{M}, \quad (2.25)$$

where all variables have their usual meanings and are in solar units.

2.5 Convection

Convection is modelled according to the mixing length theory (MLT; Böhm-Vitense, 1958) where a blob of material with velocity v travels a distance l before losing its identity to its surroundings. The simplest form of the diffusion coefficient D_{conv} for this scenario is

$$D_{\text{conv}} = (1/3)vl. \quad (2.26)$$

We calculate the mixing length l by assuming that it is some factor α_{MLT} of the pressure scale height H_P

$$l = \alpha_{\text{MLT}} H_P. \quad (2.27)$$

The pressure scale height is defined as

$$H_P = \frac{dr}{d \ln P} = \frac{PR^2}{\rho GM} = \frac{P}{\rho g}. \quad (2.28)$$

We do not know the value of α_{MLT} a priori therefore it is treated as a free parameter that is usually calibrated to the Sun. In MONSTAR we generally adopt $\alpha_{\text{MLT}} = 1.75$. Early versions of MONSTAR employed instantaneous mixing to the convective region when the blob of material loses its identity, i.e. the convective turnover timescale is much shorter than the thermal (Kelvin-Helmholtz) and nuclear burning timescales, therefore the convective region can always be considered homogeneous.

As outlined in Campbell (2007) and Campbell and Lattanzio (2008), time-dependent diffusive mixing has been implemented in later versions of

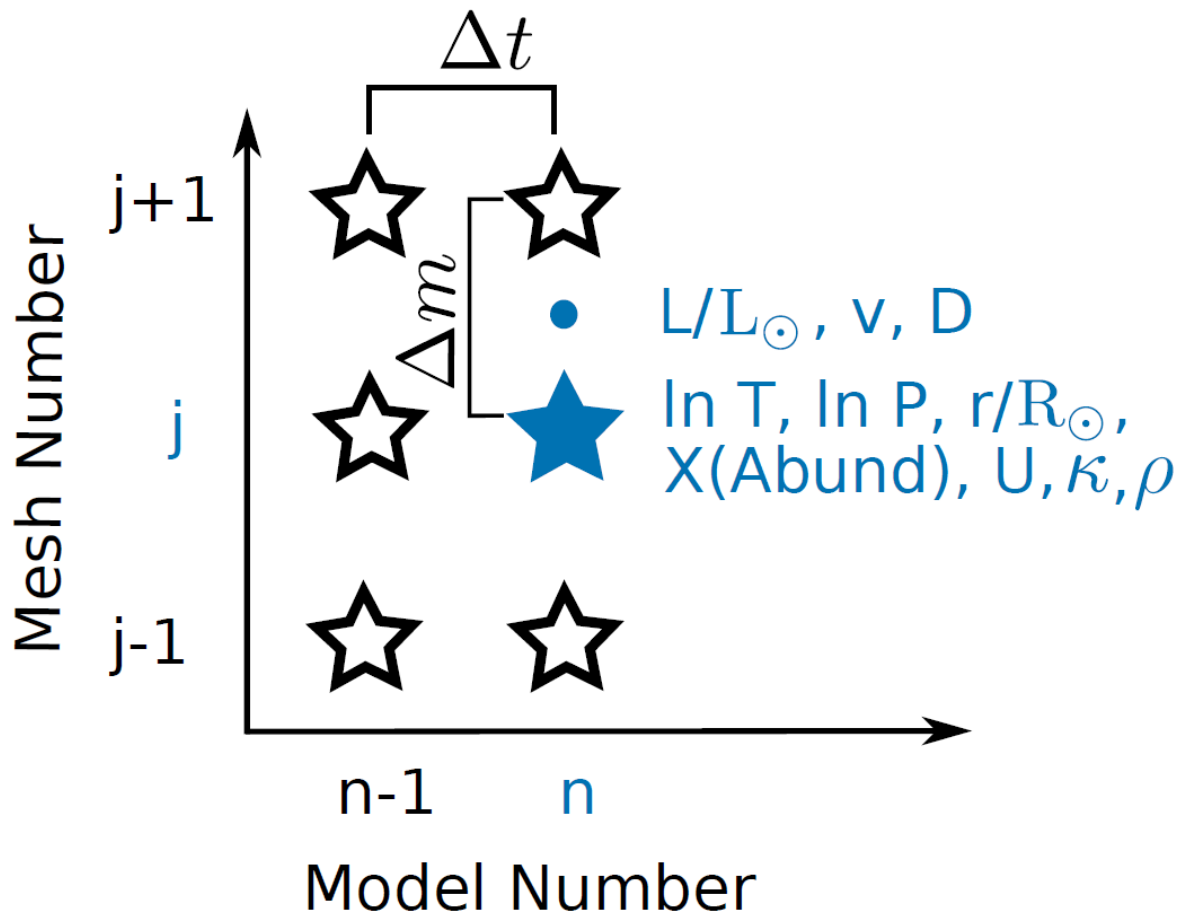


FIGURE 2.3: A schematic of MONSTAR's mesh as a function of time (model number). Temperature ($\ln T$), pressure ($\ln P$), radius (r/R_{\odot}), mass fraction (X) of the species in MONSTAR, internal energy (U), opacity (κ) and density (ρ) are calculated at mesh point boundaries (stars). Luminosity (L/L_{\odot}), convective velocity (v) and the diffusion coefficient (D) are calculated at the midpoint of the cell (filled blue circle). Figure is Fig. 3.1 from Angelou (2014).

MONSTAR. To elaborate, instead of the chemical composition becoming instantaneously homogeneous, the blob of material diffuses into its surroundings. In MONSTAR, it does this via non-steady state diffusion according to Fick's second law

$$\frac{dX_i}{dt} = \frac{\partial}{\partial m_r} \left(\sigma D \frac{\partial X_i}{\partial m_r} \right), \quad (2.29)$$

where $\sigma = (4\pi r^2 \rho)^2$ and D is given in Equation 2.26 (Campbell, 2007).

Diffusion is implemented in a semi-coupled manner, i.e. for each iteration, instantaneous mixing is replaced with Equation 2.29. To solve Equation 2.29, the implicit method described by Meynet, Maeder, and Mowlavi (2004) is used

$$\frac{X_j^{t+1} - X_j^t}{\Delta t} = \frac{\sigma_{j-1/2}}{\Delta m} D_{j-1/2} \left(\frac{X_j^{t+1} - X_{j-1}^{t+1}}{r_j - r_{j-1}} \right) + \frac{\sigma_{j+1/2}}{\Delta m} D_{j+1/2} \left(\frac{X_{j+1}^{t+1} - X_j^{t+1}}{r_{j+1} - r_j} \right). \quad (2.30)$$

We evaluate the value of $D_{j+1/2}$ (equivalent to D_{conv} in Equation 2.26) using

$$D_{j+1/2} = \frac{D_{j+1} D_j}{f D_{j+1} + (1-f) D_j}, \quad (2.31)$$

where $f = 0.50$ in MONSTAR. To solve for D we use Equation 2.26, which requires knowing the values of l and v . As stated above, we calculate l using Equations 2.27 and 2.28. To evaluate v , we use

$$v = \frac{l}{\tau_{\text{conv}}}, \quad (2.32)$$

where $\tau_{\text{conv}} = l^2 / D_{\text{conv}}$ is the convective turnover timescale.

Formal convective border

The Schwarzschild criterion is adopted to find convective boundaries, which states that convection occurs if the temperature gradient is larger than the adiabatic gradient (Pagel, 1997)

$$\nabla \equiv \frac{d \log T}{d \log P}. \quad (2.33)$$

2.5.1 Convective overshoot

Convective overshoot is included following the procedure of Herwig et al. (1997), which inserts an exponential decay in the velocity of overshooting material. Let H_P be the pressure scale height, f_{OS} a scaling factor, and the velocity scale-height H_v be

$$H_v = f_{OS} H_P. \quad (2.34)$$

We set $f_{OS} = 0.14$ for material overshooting the convective boundary to match the observed location of FDU and the RGB bump for NGC6397 RGB

stars (discussed in more detail below). The diffusion coefficient for overshooting material, D_{OS} , at a distance z from the convective boundary is

$$D_{OS} = D_0 e^{-2z/H_v}, \quad (2.35)$$

where D_0 is the diffusion coefficient at the convective boundary. Note that the only convective boundary in our models is at the base of the convective envelope for our models of NGC6397 red giants (where models are only run to the tip of the RGB).

The value of f_{OS} in Equation 2.34 affects the depth of FDU and consequently the luminosity of the RGB bump. A high overshoot factor means that more material overshoots the convective envelope border and FDU is deeper. As the H shell advances in mass during normal RGB evolution, it will encounter the discontinuity caused by FDU sooner, resulting in a lower bump luminosity.

2.6 Thermohaline mixing

As outlined in Angelou (2014), thermohaline mixing is implemented in MONSTAR following the prescription for the diffusion coefficient for thermohaline mixing as given by Ulrich (1972), Kippenhahn, Ruschenplatt, and Thomas (1980), and Charbonnel and Zahn (2007):

$$D_t = C_t K(\phi/\delta) \frac{-\nabla \mu}{(\nabla_{\text{ad}} - \nabla)}. \quad (2.36)$$

The dimensionless parameter C_t is formally given by

$$C_t = (8/3)\pi^2\alpha^2, \quad (2.37)$$

where α is the aspect ratio of thermohaline ‘‘fingers’’, $\phi = (\partial \ln \rho / \partial \ln \mu)_{P,T}$, $\delta = (\partial \ln \rho / \partial \ln T)_{P,\rho}$ ($\phi = \delta = 1$ for an ideal gas), and all other symbols have their usual meanings. The value of α is not known a priori, hence we treat C_t as a free parameter.

2.6.1 Mixing timescales

In regions where mixing is modelled by a diffusion equation, a particle will travel with velocity v (cm s⁻¹) over a mixing length l (cm). The diffusion coefficient is related to v and l by

$$D \equiv \frac{1}{3}vl, \quad (2.38)$$

where D is in cm² s⁻¹.

We calculate the timescale τ_{thm} of mixing in this region by using the relation

$$\tau_{\text{thm}} = \frac{l}{v}, \quad (2.39)$$

or

$$\tau_{\text{thm}} \equiv \frac{l^2}{D_{\text{thm}}}. \quad (2.40)$$

2.6.2 Nuclear burning timescales

We calculate the nuclear burning timescales for the elements of interest as outlined below. Nuclear burning timescales, which are (often) strongly dependent upon temperature, dictate whether there is net production or destruction of an element in particular regions of a star. Analysing these timescales provides insight into how the abundance of an element changes within the star and over time. This is a useful analysis tool employed in our study in Chapter 5 to understand the thermohaline mechanism, and specifically how particular elemental abundances of interest (e.g., lithium and carbon) change over time and during RGB evolution.

We have the general equation for the timescale of X against reactions with element a

$$\tau_a(X) = \frac{1}{n_a \langle \sigma v \rangle},$$

where $\tau_a(X)$ is the timescale of element X against reactions with a in s, n_a is the number density of element a in cm^{-3} , and $\langle \sigma v \rangle$ is related to the reaction rate coefficient and units depend upon the reaction. We let $\lambda = N_A \langle \sigma v \rangle$ be the reduced reaction rate. This is the value usually reported as the 'reaction rate' in reaction rate databases. For binary rates (i.e. $A + B \rightarrow C + D$), the units of λ is $\text{cm}^3 \text{s}^{-1} \text{mol}^{-1}$.

Also, we know that

$$n_a = \frac{X_a \rho}{m_a},$$

where X_a is the mass fraction of element a , ρ is the density in g cm^{-3} , and m_a is the mass of species a in g.

We can estimate the mass of species a using the mass in amu of element a (A_a) and the mass of 1 amu m_u

$$m_a \approx A_a m_u.$$

Additionally, $m_u = 1/N_A$, where N_A is Avogadro's number, in mol^{-1}

$$m_a = \frac{A_a}{N_A}.$$

Therefore

$$n_a = \frac{X_a \rho N_A}{A_a}.$$

We then have

$$\begin{aligned} \tau_a(X) &= \frac{A_a}{X_a \rho N_A \langle \sigma v \rangle}, \\ &= \frac{A_a}{X_a \rho \lambda}. \end{aligned}$$

The reaction rate, r , is determined to be

$$r = N_a N_X \langle \sigma v \rangle (1 + \delta_{aX})^{-1},$$

where δ_{aX} is the Kronecker delta for reactions between a and X .

In MONSTAR, the reaction rate, r_{code} , is

$$\begin{aligned} r_{code} &= \frac{X_a \rho N_A}{A_a} \frac{X_X \rho N_A}{A_X} \langle \sigma v \rangle (1 + \delta_{aX})^{-1} && \text{cm}^{-3} \text{s}^{-1}, \\ &= \frac{X_a X_X}{A_a A_X} \rho N_A \rho N_A \langle \sigma v \rangle (1 + \delta_{aX})^{-1} && \text{cm}^{-3} \text{s}^{-1}, \end{aligned}$$

where A_a is the mass of species a in amu and A_X is the mass of species X in amu.

$$\begin{aligned} r_{code} &= \frac{X_a X_X}{A_a A_X} \rho N_A \rho \lambda (1 + \delta_{aX})^{-1} && \text{cm}^{-3} \text{s}^{-1}, \\ &= \frac{X_a X_X}{A_a A_X} \rho N_A \lambda (1 + \delta_{aX})^{-1} && \text{g}^{-1} \text{s}^{-1}, \\ &= \frac{X_a X_X}{A_a A_X} \rho N_A \lambda (1 + \delta_{aX})^{-1} && \text{g}^{-1} \text{s}^{-1}. \end{aligned}$$

Therefore, we obtain for λ

$$\lambda = \frac{r_{code} A_a A_X (1 + \delta_{aX})}{X_a X_X \rho N_A}. \quad (2.41)$$

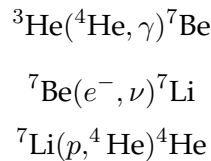
The reaction rate in the stellar evolution code, which we defined to be r_{code} , will therefore be

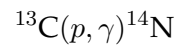
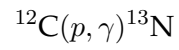
$$r_{aX} = \frac{X_a X_X}{A_a A_X} \rho N_A \lambda (1 + \delta_{aX})^{-1} \quad \text{g}^{-1} \text{s}^{-1}.$$

For our nuclear burning timescales, we obtain

$$\tau_a(X) = \frac{X_X N_A}{r_{code} A_X (1 + \delta_{aX})}. \quad (2.42)$$

In this thesis, pertinent to our investigations is the evolution of the abundances of ${}^7\text{Li}$, ${}^{12}\text{C}$, and ${}^{13}\text{C}$. To understand the abundance changes we see at the surface, in Chapter 5 we analyse the timescales of ${}^7\text{Li}$, ${}^{12}\text{C}$, and ${}^{13}\text{C}$ against proton capture, and Be against electron capture, according to the burning/destruction equations below.





In the thermohaline region, the burning timescales of ^3He , ^{12}C , and ^{13}C are typically much longer than the timestep defined in §2.2.5 during RGB evolution. However, the burning timescale of ^7Li can be of the same order of magnitude as the timestep (though the burning timescale is highly dependent upon temperature), and the timescale of ^7Be against electron capture is generally much shorter than the timestep. This is discussed further in §3.1.1.

Chapter 3

Modifications to the Evolution code

The content in §3.1 (except where referencing figures and the section **The effect of modifying i and o**) was published in Henkel, K., Karakas, A.I., and Lattanzio, J.C. (2017), “A phenomenological modification of thermohaline mixing in globular cluster red giants”, *The Monthly Notices of the Royal Astronomical Society*, 469, 4, 4600-4612.

The unpublished content is included in §3.1.1 and §3.1.2 (including associated figures), which was completed in response to the reviewer’s comments but deemed unnecessary for the final manuscript.

No figures or tables in this chapter have been published by the authors, however Fig. 3.4 is similar to the published figure Fig. 5.6 (Henkel, Karakas, and Lattanzio, 2017). All figures are referenced appropriately.

3.1 Adding an additional temperature dependence

Recalling that D_t is related to v and l according to Equation 2.38, when we modify D_t we effectively modify the mixing velocity and/or mixing length. Through the dimensionless value of C_t we can produce different values of D_t to match the observations, which could reveal characteristics of the extra mixing mechanism at the base of the convective envelope during RGB evolution. Manipulating D_t expands the parameter space and increases the likelihood of being able to simultaneously match surface carbon and lithium abundances to observations. This may provide us with information on what is missing in the standard implementation. We perform these tests using MONSTAR with mixing modelled by a diffusion equation, as usual.

We can manipulate D_t to modify abundances of ${}^7\text{Be}$, ${}^7\text{Li}$, ${}^{12}\text{C}$, and ${}^{13}\text{C}$ in the thermohaline region by adding a new temperature dependence on D_t . We do this by setting a “critical temperature” T_{crit} with “inner” i and “outer” o factors such that

$$D_{\text{new}} = \begin{cases} i \times D_t & \text{if } T > T_{\text{crit}}, \\ o \times D_t & \text{if } T < T_{\text{crit}}. \end{cases} \quad (3.1)$$

To elaborate, from the base of the thermohaline region to the radial location of T_{crit} we multiply the diffusion coefficient D_t as given in Equation 2.36 by

a factor i . Similarly, from the location of T_{crit} to the envelope we multiply D_t by a factor o .

3.1.1 Choosing T_{crit}

The analysis in this chapter is done at the epoch “This study” for a $0.79 M_{\odot}$, $Z = 0.000246$, $[\text{Fe}/\text{H}] = -2.0$ model with the standard thermohaline mixing formalism, and the same model with our modified thermohaline mixing formalism described above (in §3.1) and shown in Fig. 3.1. We select this epoch because it is at the beginning of the luminosity function bump. This is a significant evolutionary point in terms of extra mixing because it is where the hydrogen burning shell connects to the hydrogen abundance discontinuity and the effects of extra mixing are observable on the stellar surface (detailed in §1.1.7).

In Figs. 3.2 and 3.3 we show the effect of changing the value of T_{crit} when $i > o$ and $o > i$ respectively on surface abundances. The distinction between $i > o$ and $o > i$ when varying T_{crit} becomes clear by analysing the figures. To explain the effects, in Fig. 3.4 we show the mixing, production (of ${}^7\text{Li}$ and ${}^7\text{Be}$) and destruction (of ${}^7\text{Li}$, ${}^7\text{Be}$, ${}^{12}\text{C}$, ${}^{13}\text{C}$, and ${}^3\text{He}$) timescales in the thermohaline region, and in Fig. 3.5 we show the abundances of lithium (top panel) and carbon (bottom panel).

When $i > o$ as in Fig. 3.2, the carbon destruction timescale is much slower than the mixing timescale over the thermohaline region except near the base of the region where the timescales for ${}^{12}\text{C}(p,\gamma){}^{13}\text{C}$ and diffusive mixing are approximately equal (see Fig. 3.4). When T_{crit} is low (close to the base of the envelope), fast mixing with a higher diffusion coefficient (high i) dominates the thermohaline region in terms of radius. This leads to flatter abundance profiles, as shown in Fig. 3.5, as well as a reduction in the decline of surface $[\text{C}/\text{Fe}]$ and $A(\text{Li})$. The effect is reversed when T_{crit} is increased and slow mixing dominates the region. When this occurs, abundance profiles are more representative of burning (increasing depletion with depth/temperature) and the decline of surface abundances increases.

The surface lithium profile in the top panel of Fig. 3.2 shows that the decline of lithium is similar when $T_{\text{crit}} = 8$ MK and 10 MK but is faster when $T_{\text{crit}} = 4$ MK. From the base of the thermohaline region to $\log(R/R_{\odot}) \sim -0.8$, lithium destruction is the shortest timescale and this remains true at the radial locations of 8 and 10 MK. For these high T_{crit} values the majority of the thermohaline region is mixing slowly since $i > o$, however when $T_{\text{crit}} = 4$ MK the majority of the region is mixing more quickly (see the top panel of Fig. 3.5). Additionally, at the location of 4 MK, lithium production is faster than lithium destruction. Lithium is produced just below the convective envelope but is brought down quickly to hotter temperatures where it is burnt. This is why the lithium profile shows increased depletion when $T_{\text{crit}} = 4$ MK compared to 8 and 10 MK.

When $i < o$ and T_{crit} is modified, the situation appears more complicated, as shown in Fig. 3.3. Comparing the three blue curves for the T_{crit} values, the least depletion of both surface carbon and lithium occurs when $T_{\text{crit}} = 10$ MK. This is intuitive because, as was discussed earlier, since $o > i$

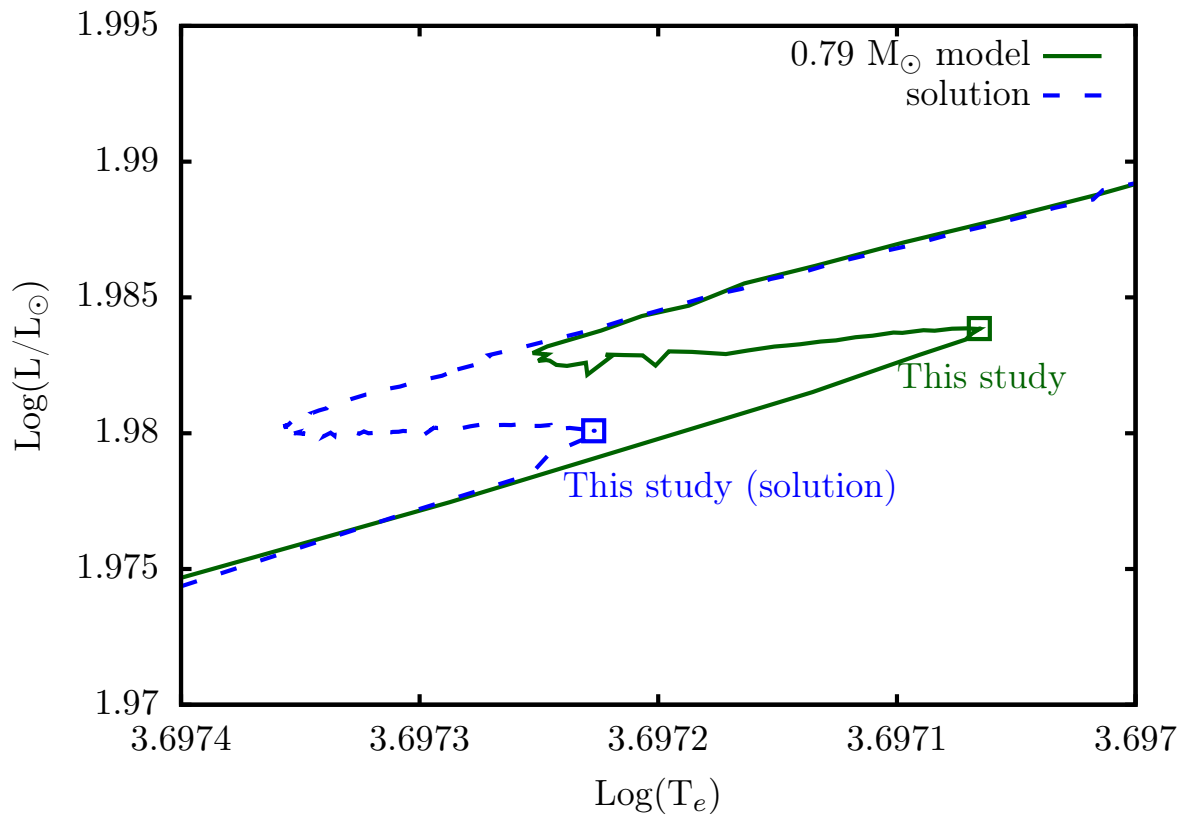


FIGURE 3.1: The evolutionary path of a $0.79 M_{\odot}$, $Z = 0.000246$, $[\text{Fe}/\text{H}] = -2.0$ model with the standard thermohaline mixing formalism (dark green curve) compared to a model with all of the same parameters except with our thermohaline mixing temperature dependence modification ($i = 3.0$ and $o = 0.1$ “solution” model, blue dashed curve) in the Hertzsprung-Russell diagram.

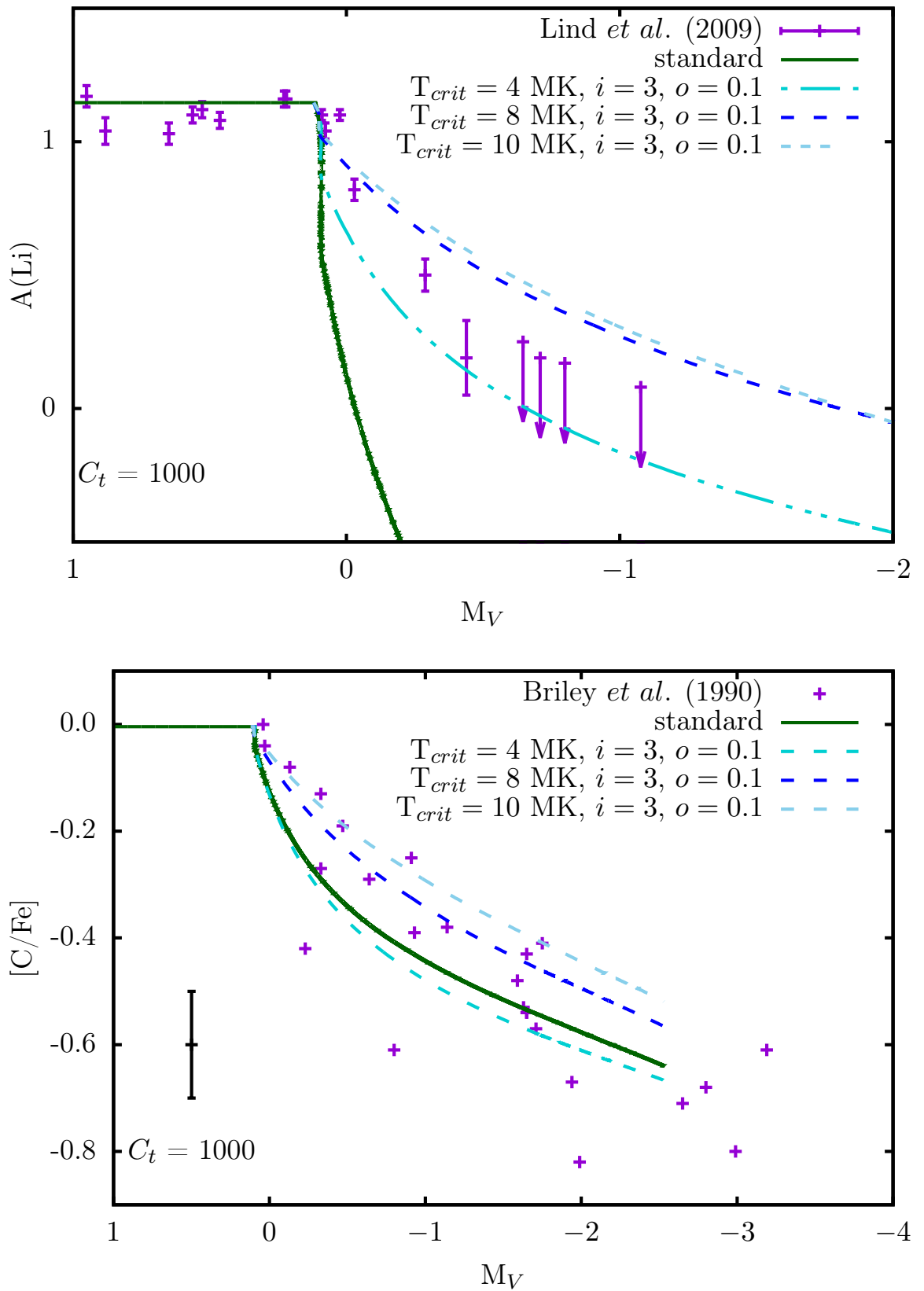


FIGURE 3.2: Top panel: Theoretical surface lithium abundances (curves) compared to observations with errors (purple points, Lind *et al.*, 2009). Bottom panel: Theoretical carbon abundances (curves) compared to observations with a 0.1 dex error bar (purple points, Briley *et al.*, 1990). In each panel the dark green curve is when the thermohaline mixing free parameter C_t is 1000. The dashed curves are models with $i = 3.0$, $o = 0.1$ and varying values of T_{crit} (detailed in the legend).

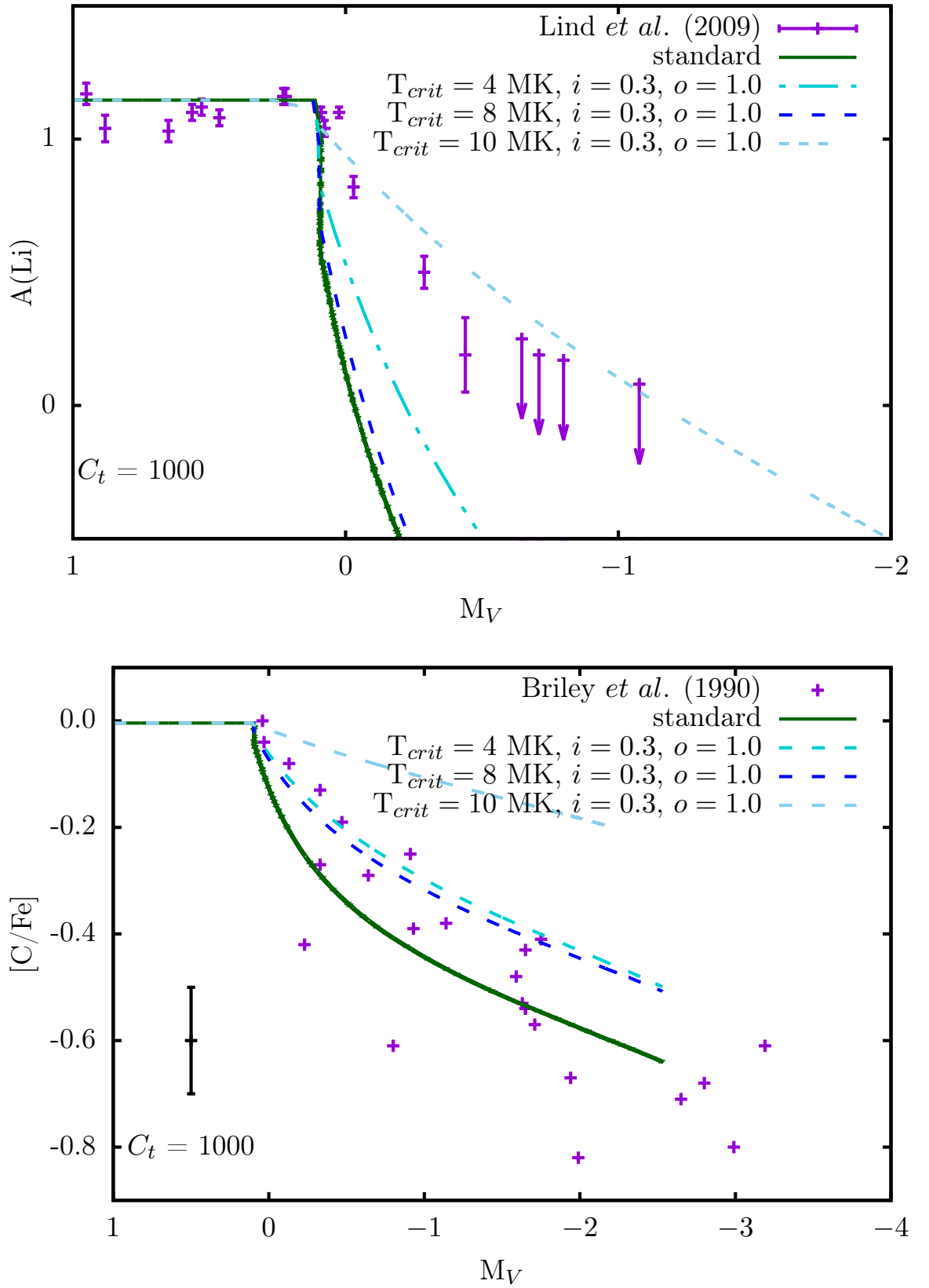


FIGURE 3.3: Top panel: Theoretical surface lithium abundances (curves) compared to observations with errors (purple points, Lind et al., 2009). Bottom panel: Theoretical carbon abundances (curves) compared to observations with a 0.1 dex error bar (purple points, Briley et al., 1990). In each panel the dark green curve is when the thermohaline mixing free parameter C_t is 1000. The dashed curves are models with $i = 0.3$, $o = 1.0$ and varying values of T_{crit} (detailed in the legend).

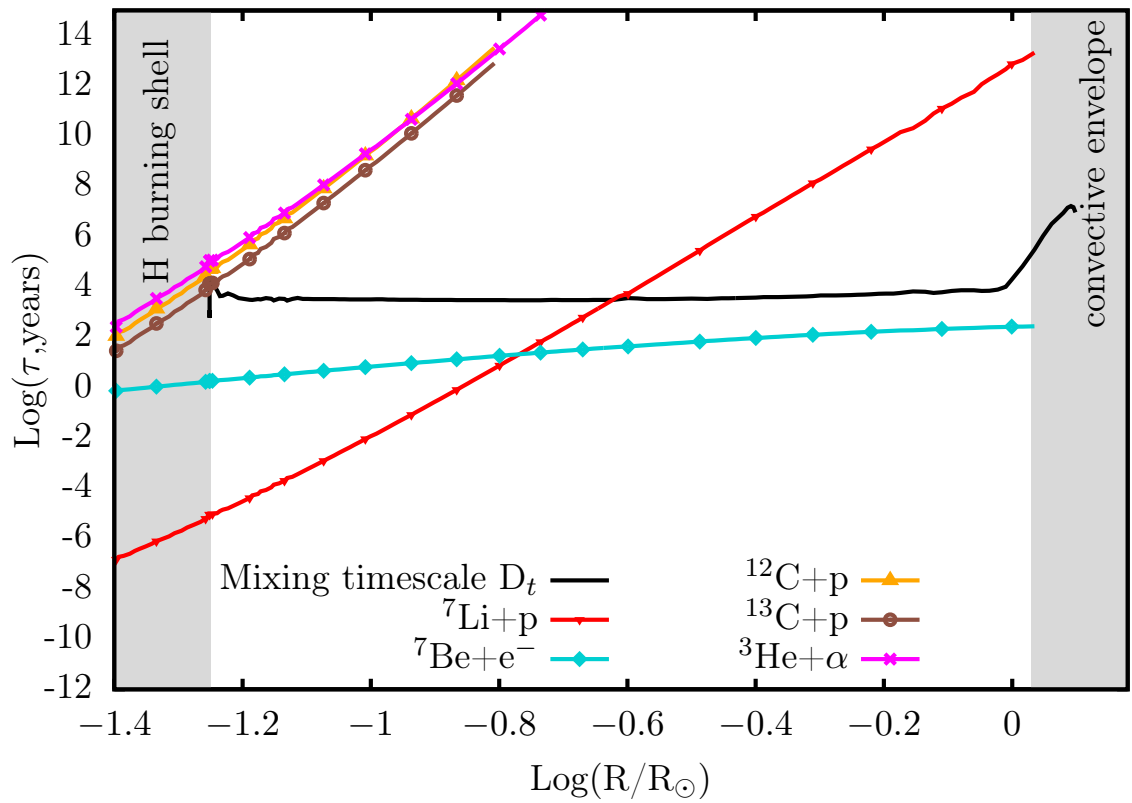


FIGURE 3.4: The log of mixing timescales (years; black curve) and nuclear burning timescales of ${}^7\text{Li}+\text{p}$ (red), ${}^7\text{Be}+\text{e}^-$ (turquoise), ${}^{12}\text{C}+\text{p}$ (orange), ${}^{13}\text{C}+\text{p}$ (burgundy), and ${}^3\text{He}+\alpha$ (magenta) in our $0.79M_{\odot}$ model at the point labelled “This study” in Fig. 3.1

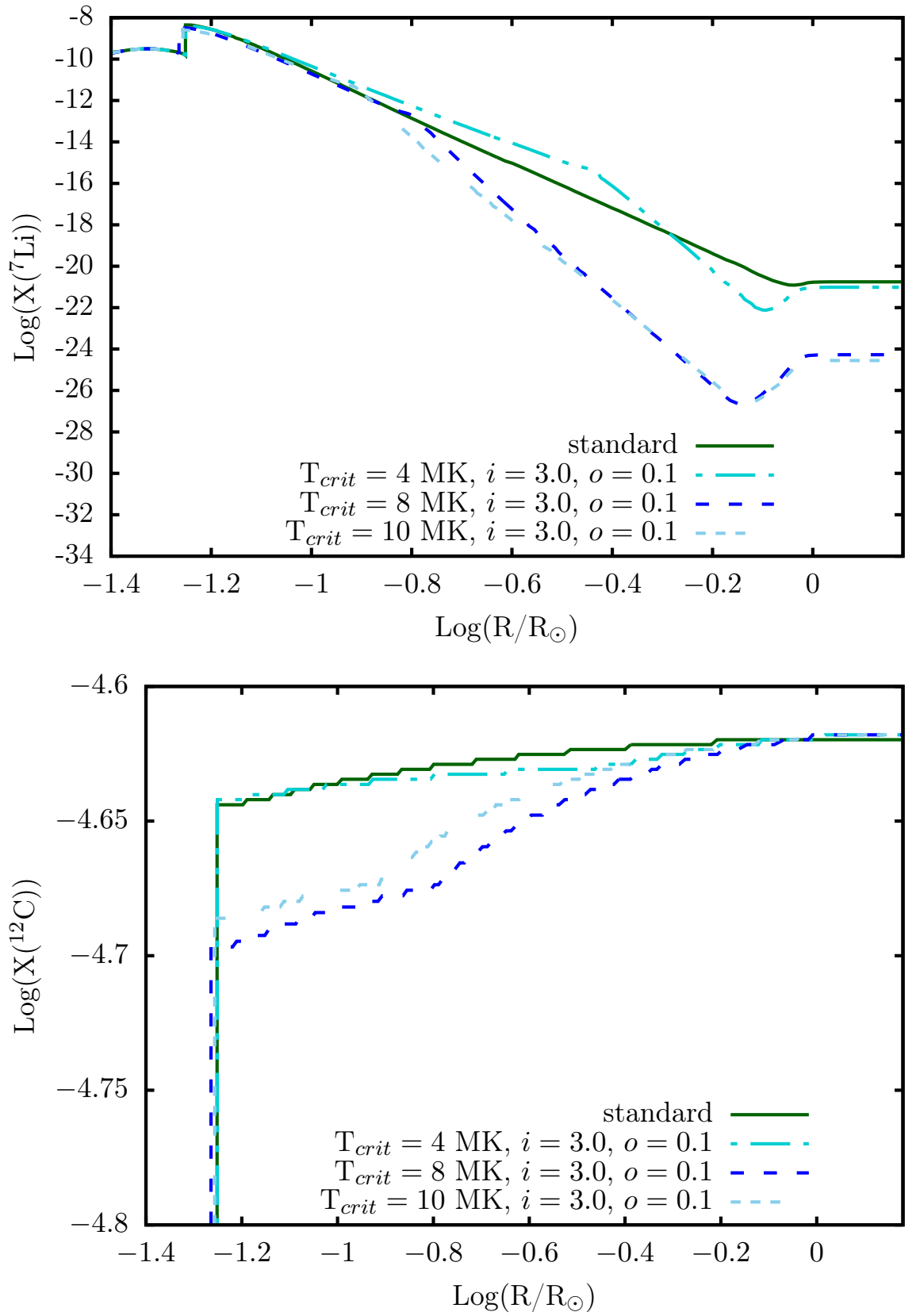


FIGURE 3.5: The effect of varying T_{crit} on the interior ^7Li (top panel) and ^{12}C (bottom panel) abundances as a function of radius. The values of i and o are given in the legend.

faster mixing dominates the thermohaline region and produces flatter profiles and less depletion. However, what is not intuitive is the fact that more depletion occurs when $T_{\text{crit}} = 8$ MK compared to 4 MK for both carbon and lithium. When T_{crit} is sufficiently close to the base of the envelope, i.e. when $T_{\text{crit}} = 4$ MK, there is increased surface depletion of carbon and lithium as expected because i is low and composition profiles are more representative of burning. When $T_{\text{crit}} = 8$ MK, mixing is slower in the hotter part of the region where elements efficiently burn and faster in the cooler part, therefore freshly-produced material is quickly brought down into the hot region where it is burned due to slow mixing. The same effect is not seen when $T_{\text{crit}} = 10$ MK because the radial width of the hot region where mixing is slower is too small, whereas 8 MK is located approximately in the middle of the thermohaline region.

3.1.2 Diffusion coefficients

The HR diagram tracks in Fig. 3.1 of the modified and standard models show that the H shell in the solution model encounters the discontinuity before the standard model does. The mass coordinate at the top of the H shell during the LFB is shown in Fig. 3.6.

Indeed, Fig. 3.6 shows that the H shell in the modified model has advanced further at a given luminosity (in interior stellar mass) than the standard model, which is why the LFB for the modified model is at a slightly lower luminosity (~ 0.004 in the log) than the standard model. This is a result of the modifications made to the thermohaline diffusion coefficient of our modified model. Fresh material is mixed faster towards the inner regions and as mass is moved inwards, the H shell advances further. This also produces a flatter abundance profile of elements.

The thermohaline diffusion coefficient of the modified model compared to the standard model is shown in Fig. 3.7. Interestingly, the result is not intuitive. One might intuitively expect that the diffusion coefficient of the solution should be a factor i different in the region where $T > T_{\text{crit}}$ and similarly for o where $T < T_{\text{crit}}$ however this is not the case. Despite the two stellar models being at the same corresponding evolutionary epoch, their structures differ due to the modifications in structure that were caused by evolution with a different thermohaline diffusion coefficient. This becomes evident when we evaluate the terms of the diffusion coefficient equation (Equation 2.36). In Fig. 3.8 we show that the temperature, density, and thermal diffusivity at corresponding epochs for our modified and standard models are in agreement. However there is a difference between the modified and standard models' mean molecular weight gradient, shown in Fig. 3.9. Thermohaline mixing is inherently driven by a molecular weight gradient therefore mixing via thermohaline mechanisms acts to reduce the molecular weight gradient until it no longer exists. It is worth noting that the molecular weight gradient is quite "jagged" in the regions where there is a sudden change in the gradient, i.e. at the base of the thermohaline zone and the radial location of T_{crit} where the diffusion coefficient changes from $D_t \times i$ to $D_t \times o$, and is due to the star adjusting to the changes.

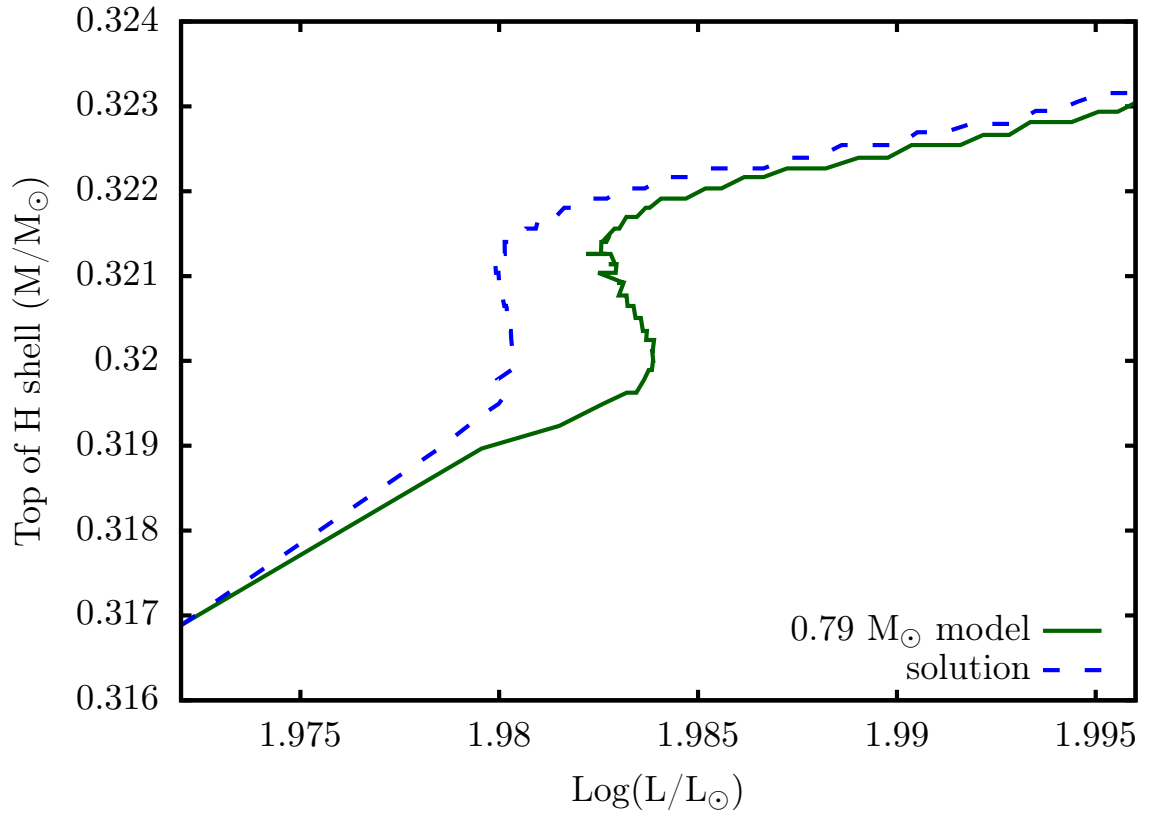


FIGURE 3.6: Mass at the top of the H shell ($X(\text{H}) = 0.66$) versus radius for our $0.79 M_{\odot}$ model (dark green solid curve) compared to our solution (blue dashed curve).

There is a clear resemblance between Figs. 3.7 and 3.9. In the inner region below $\log(R/R_{\odot}) \sim -0.8$ the modification to the diffusion coefficient has increased the speed (and length) over which material is mixed. Material is mixed in this region faster than in the standard model, which causes the molecular weight gradient to be lower than the standard case. For the outer region beyond $\log(R/R_{\odot}) \sim -0.8$ where material is mixing much slower, the molecular weight gradient is higher. Therefore when i is increased and o is lowered, the molecular weight gradient reacts in a way that acts opposed to the effect of implementing i and o .

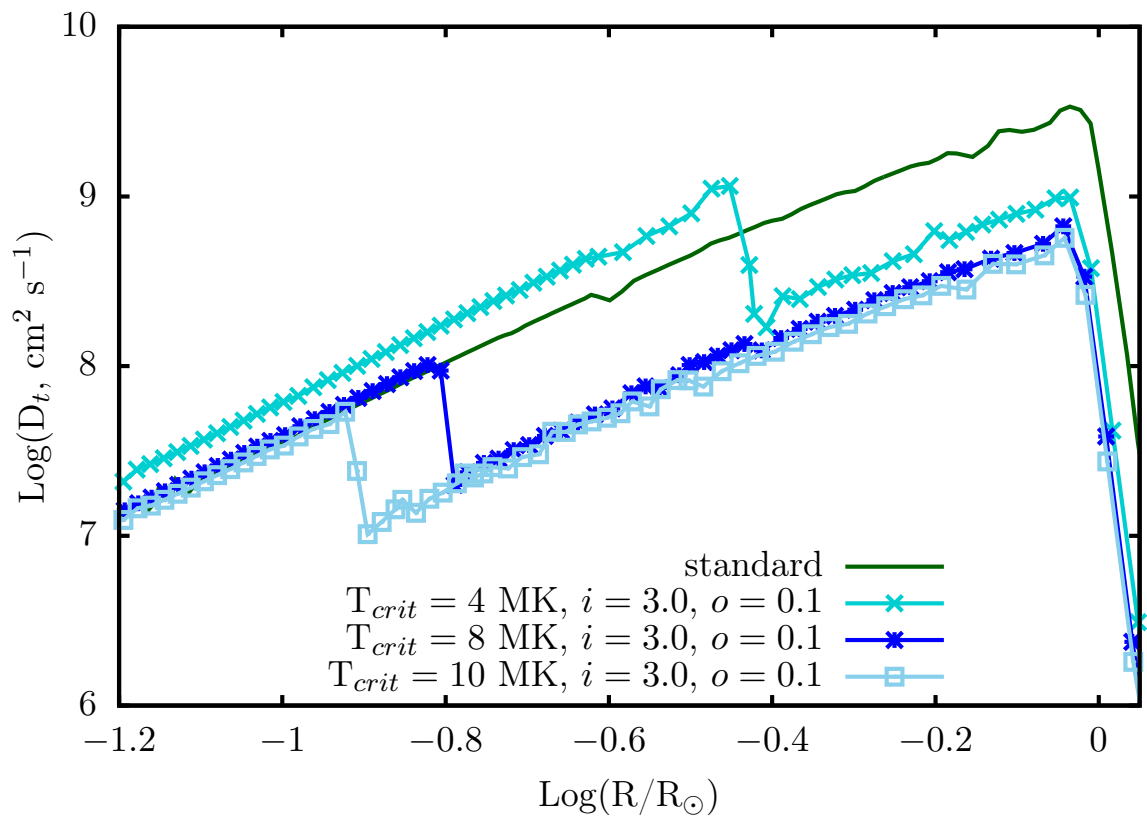


FIGURE 3.7: The effect of varying T_{crit} on the diffusion coefficient D_t as a function of radius. The values of i and o are given in the legend.

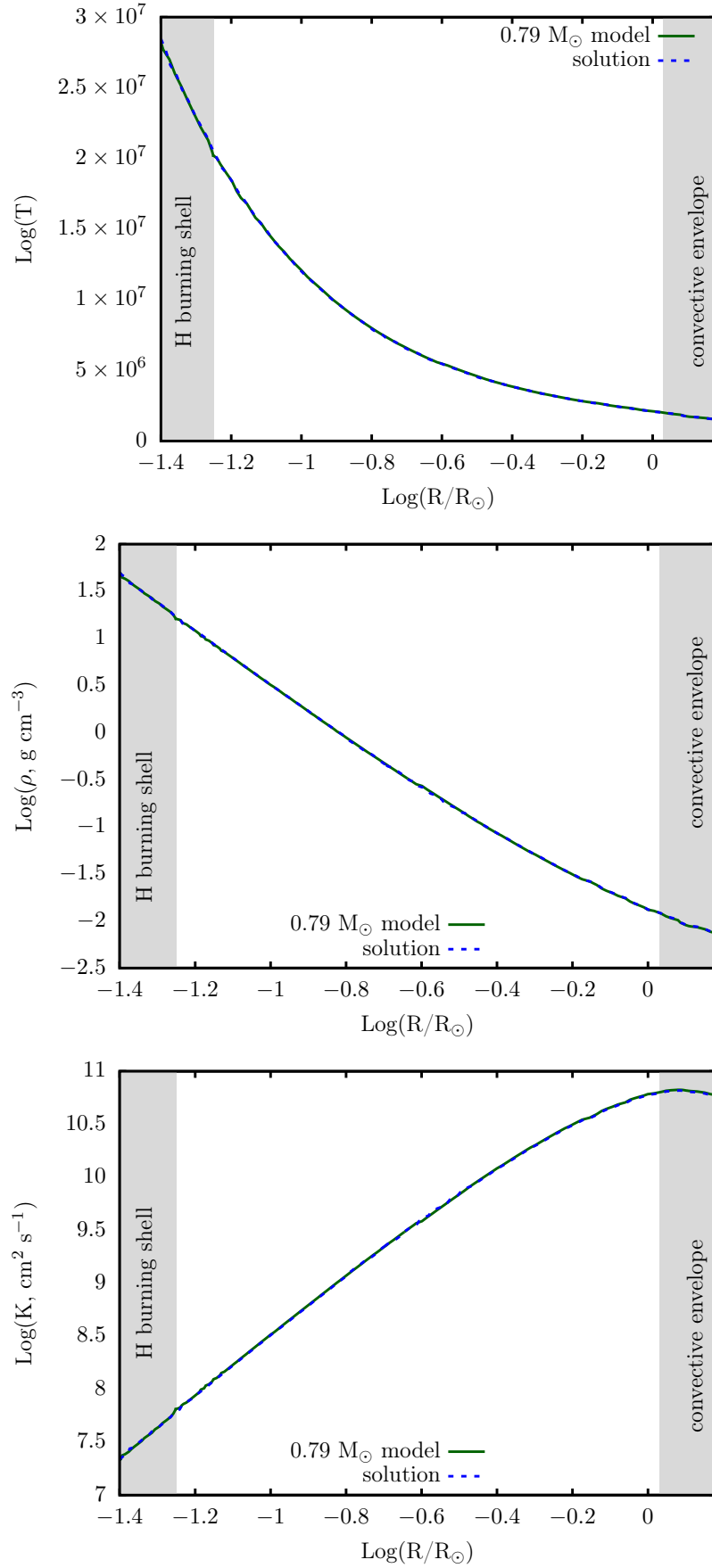


FIGURE 3.8: Temperature (top panel), density (middle panel), and thermal diffusivity (bottom panel) in the thermohaline region of our $0.79 M_{\odot}$ model (dark green curve) compared to our modified “solution” model (blue dashed curve) at the epoch “This study” in Fig. 3.1.

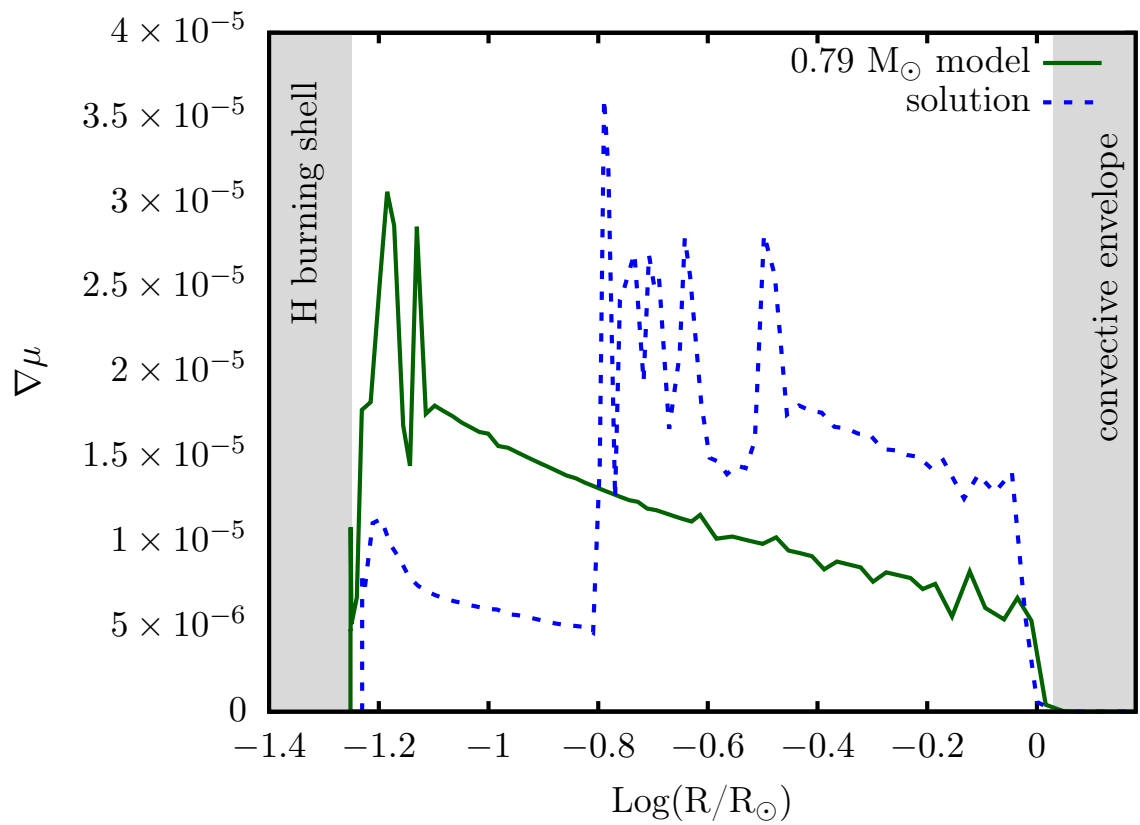


FIGURE 3.9: Molecular weight gradient in the thermohaline region of our 0.79 M_\odot model (dark green curve) compared to our modified “solution” model (blue dashed curve) at the epoch “This study” in Fig. 3.1.

Chapter 4

The Nucleosynthesis code MONSOON

The following content was published in Henkel, K., Karakas, A.I., and Lattanzio, J.C. (2017), “A phenomenological modification of thermohaline mixing in globular cluster red giants”, *The Monthly Notices of the Royal Astronomical Society*, 469, 4, 4600-4612:

- Sentence 1 in §4.1,
- §4.2,
- §4.3.2,
- §4.3.3, and
- Fig. 4.2.

4.1 Introduction

Our stellar models have been constructed using MONSTAR and then processed by the Monash post-processing nucleosynthesis code MONSOON (Cannon, 1993; Campbell and Lattanzio, 2008; Karakas and Lattanzio, 2014; Karakas and Lugaro, 2016). Other than the study in Chapter 5, the studies in this thesis do not utilise the nucleosynthesis code, therefore we keep this chapter brief.

There are myriad reasons why one would use a post-processing code. We use MONSTAR to calculate the structure of the star, and use MONSOON to calculate detailed abundances of specific nucleic species and associated changes of these abundances due to burning and mixing (most of the elements in MONSOON are not included in MONSTAR). We also use MONSOON to calculate detailed mixing properties and can implement more complex mixing formalisms, however we note that this can decouple MONSOON and MONSTAR, as was the case in Chapter 5. MONSOON does not affect the structure of the star calculated by MONSTAR, but requires as input the radius, temperature, density, mixing length, and velocity as a function of interior mass and time.

There are many advantages to having a post-processing code to calculate abundances, which can include reduced computation time, and increased flexibility and variety in modelling (e.g. nucleosynthetic network, mixing

processes, etc). To elaborate, for example, we have the opportunity to easily follow nucleic species without the need to recalculate the star's structure at every timestep. Alternatively, we need not even use MONSOON if MONSTAR adequately covers the necessary aspects of evolution.

4.2 Reaction rates

The version of MONSOON that we use reads in the 86 species in its network, being:

g, n, p, d, ³He, ⁴He, ⁷Li, ⁷Be, ⁸B, ¹²C, ¹³C, ¹⁴C, ¹³N, ¹⁴N, ¹⁵N, ¹⁴O, ¹⁵O, ¹⁶O, ¹⁷O, ¹⁸O, ¹⁹O, ¹⁷F, ¹⁸F, ¹⁹F, ²⁰F, ²⁰Ne, ²¹Ne, ²²Ne, ²³Ne, ²¹Na, ²²Na, ²³Na, ²⁴Na, ²³Mg, ²⁴Mg, ²⁵Mg, ²⁶Mg, ²⁷Mg, ²⁵Al, ²⁶Al, ²⁷Al, ²⁸Al, ²⁷Si, ²⁸Si, ²⁹Si, ³⁰Si, ³¹Si, ²⁹P, ³⁰P, ³¹P, ³²P, ³²S, ³³S, ³⁴S, ³⁵S, ³⁶S, ³⁷S, ³³Cl, ³⁴Cl, ³⁵Cl, ³⁶Cl, ³⁷Cl, ³⁸Cl, ³⁶Ar, ³⁷Ar, ³⁸Ar, ³⁹Ar, ⁴⁰Ar, ⁴¹Ar, ³⁷K, ³⁸K, ³⁹K, ⁴⁰K, ⁴¹K, ⁴²K, ⁴⁰Ca, ⁴¹Ca, ⁴²Ca, ⁴³Ca, ⁴⁴Ca, ⁴⁵Ca, ⁴¹Sc, ⁴²Sc, ⁴³Sc, ⁴⁴Sc

and associated reaction rates.

The reaction rates used in MONSOON are from the JINA REACLIB database (Caughlan and Fowler, 1988; Cyburt et al., 2010) and are in REACLIB format:

$$\lambda = \exp[a_0 + a_1 T_9^{-1} + a_2 T_9^{-1/3} + a_3 T_9^{1/3} + a_4 T_9 + a_5 T_9^{5/3} + a_6 \ln T_9] \quad (4.1)$$

where $\lambda = N_A \langle \sigma v \rangle \text{ cm}^3 \text{ mole}^{-1} \text{ s}^{-1}$ is the reaction rate coefficient, often simply referred to as the reaction rate, $N_A = 6.023 \times 10^{23} \text{ mole}^{-1}$ is Avogadro's number, σ is the cross section of the reaction in cm^2 , v is the velocity of particles in cm s^{-1} , $a_x \{x = 0, 6\}$ are the reaction coefficients provided in the REACLIB database, and T_9 is temperature in units of 10^9 K .

4.3 Solution method

MONSOON calculates detailed mixing and nucleosynthesis using the structure provided by MONSTAR. This includes compositions (including s-process elements), changes in composition over a single timestep, advective and diffusive flow rates, and reaction rates.

4.3.1 Meshing routine

MONSOON uses a combination of Lagrangian and non-Lagrangian mesh points. In addition to this, MONSOON employs different meshing algorithms for different evolutionary phases, and it is often necessary to add (and remove) mesh points to resolve certain mixing or burning characteristics.

Mixing and mesh moving

As alluded to above, a combination of mesh point types is employed in MONSOON. Geometrically-spaced mesh points are employed during the main sequence (from the core to the surface). This is in contrast to shell-burning evolutionary phases such as the RGB and AGB, where intershell regions contain Lagrangian points and the burning shells are a combination of tightly-spaced Lagrangian and non-Lagrangian points.

As a shell advances during RGB or AGB evolution, Lagrangian points from the region above the shell, which may be either the envelope or inter-shell region depending upon the shell considered, are converted to non-Lagrangian points as they become part of the shell. Furthermore, mesh points in the shell can also be released below the shell (and converted to Lagrangian) if no longer required, e.g. from the movement of mesh regions with extra resolution. To avoid numerical diffusion, all mesh points consumed in a timestep are either removed completely by the code, or recycled (more detail on this below).

In the case of thermohaline mixing occurring during RGB evolution, it is necessary to add extra mesh points above the hydrogen burning region to resolve the resultant mixing near the molecular weight inversion. This is because the region that thermohaline mixing is operating over is very thin and the molecular weight inversion is very small in magnitude. A recent modification to the code recycles unnecessary non-Lagrangian points below the H shell to the top of the thermohaline region. This modification ensures adequate resolution in these burning regions while limiting the number of mesh points and consequently computation time required (Angelou, 2014).

The movement of the burning shells is traced by three points, fixed by the abundances of hydrogen or helium depending upon the shell being considered. As well as adding mesh points near the burning shells, a region with additional mesh points is added at the expected location of first dredge-up for improved resolution purposes. Abundances that are defined on mesh boundaries are interpolated to determine the abundances in the centre of the mass shell.

Mixing is then calculated depending upon the type of transport mechanism in a given mesh point at a particular time. There are two forms of mixing calculated in MONSOON, and they are:

- Diffusive mixing (discussed in §4.3.3), and
- Advective mixing (two stream mixing, discussed in §4.3.2).

Calculating compositions

MONSOON calculates the burning, reaction rates, compositions, and changes in composition, and converges on solutions depending upon how the mesh is moving. It does this by setting a guess on the composition and iterating towards a solution within allowed errors. The steps that MONSOON takes are briefly summarised below.

1. The reaction rates are determined at each mesh point. The star is divided into segments of consecutive radiative or convective mesh points. The mesh segments are solved depending upon if the mesh is moving in or stationary/out.
2. A vector is filled with equations (composition, change in composition, rates, mesh points), then a matrix with derivatives of these wrt composition is populated (burning terms only).
3. The reaction rates, composition, and change in composition populate a tridiagonal matrix, which is easily solved via Gaussian elimination.
4. Corrections are determined.
5. These corrections are applied to converge the stellar model, and the model is considered converged for the timestep.
6. Reaction rates and changes in composition are determined to ensure the size of the next timestep is not too large.
7. The mixing is calculated again before determining a new model at the next timestep, and the process repeats.

4.3.2 Thermohaline mixing and convection: Two stream advective mixing

Note that in each code we employ different mixing algorithms for thermohaline mixing. In MONSTAR we employ a diffusive mixing scheme as outlined in §2.6. In MONSOON we employ an advective mixing scheme as outlined below.

Our two stream phenomenological advective mixing approach is shown in Figs. 4.1 and 4.2 (Cannon, 1993). We set the value of the diffusion coefficient D_t in MONSTAR according to Equation 2.36 and calculate v and l for use in MONSOON using

$$l = \alpha H_P, \quad (4.2)$$

where $\alpha = 1.69$ and is the same as used in MONSTAR, H_P is the pressure scale height, and from Equation 2.29

$$v = \frac{3D}{l}. \quad (4.3)$$

The total mass flux F across radius r is zero in accordance with mass conservation. Using this information the mass fluxes in the up and down streams are calculated using

$$F_u = F_d = \frac{4\pi r^2 \rho v}{2}. \quad (4.4)$$

Fig. 4.2 schematically shows the two streams in this mixing regime, with each stream being divided by horizontal levels k . The thermohaline mixing velocities according to Equation 4.3 are calculated at the boundaries of each horizontal level. From the structure model, the density and radius are also known at the boundary of each level. To determine the velocity of material in each stream at each level k , $v_{u,k}$ and $v_{d,k}$ for the up and down stream

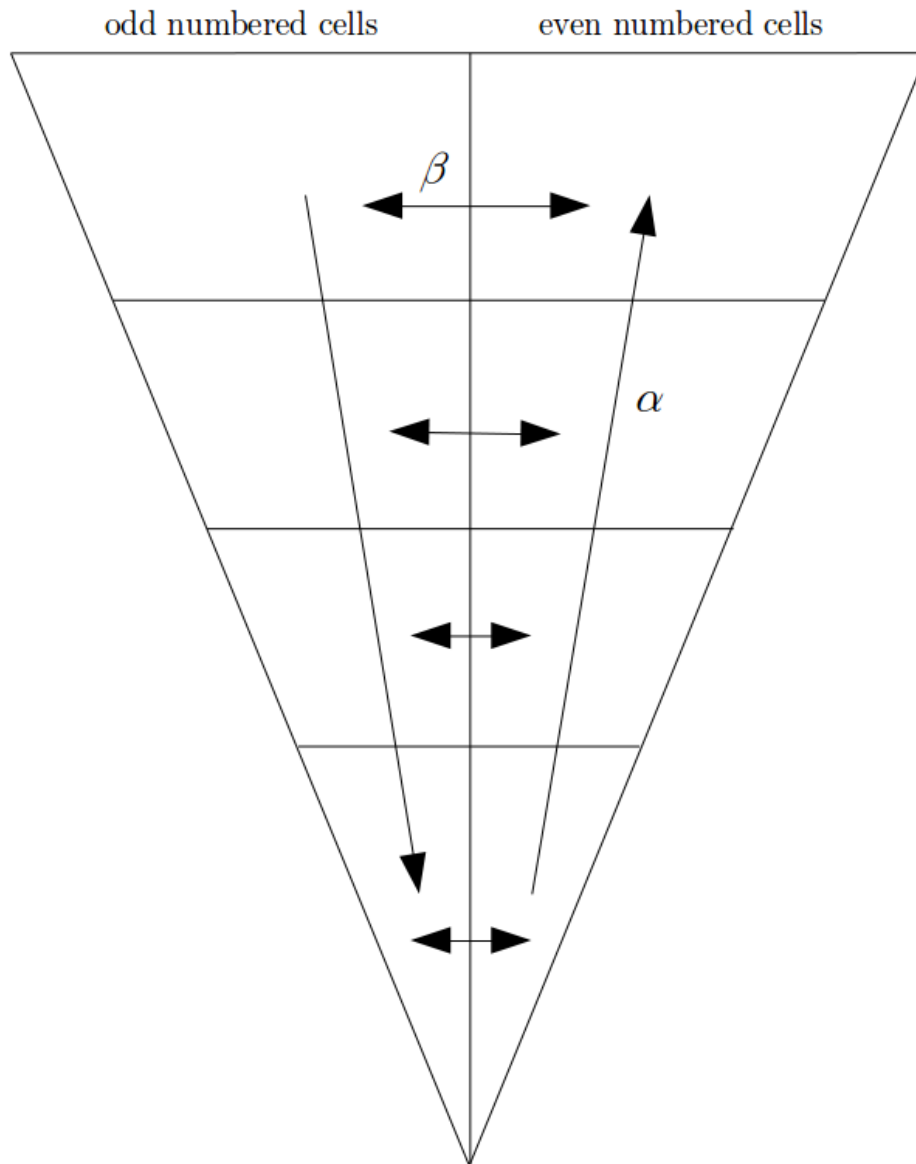


FIGURE 4.1: The two stream mixing regime, where α indicates vertical mass flow, and β represents horizontal mass flow between streams to conserve mass.

respectively, we denote the fractional cross-sectional areas of the downstream, f_d , and the upstream, f_u , for the thermohaline region (and other regions where mixing is done via the two stream mechanism). The values of f_d and f_u also satisfy $f_d + f_u = 1$. To conserve mass it is required that up and down mass fluxes are equal, therefore the flux in each stream is

$$4\pi r_k^2 \rho_k v_{u,k} f_u = 4\pi r_k^2 \rho_k v_{d,k} f_d. \quad (4.5)$$

The velocities $v_{u,k}$ and $v_{d,k}$ are determined from the thermohaline velocity in Equation 4.3 by

$$v_{u,k} f_u = v_{d,k} f_d = \frac{v}{2}. \quad (4.6)$$

The factor of $1/2$ in the right-hand side of Equation 4.6 is a direct result of the mass flux equalling zero according to mass conservation. From this condition it is necessary that the flux in each stream must be equal as shown in Equations 4.4 and 4.5, therefore the total mass flux is split *evenly* between the two streams regardless of the cross-sectional area of each stream. A wider stream will consist of material travelling at a slower velocity and vice versa for a thin stream in accordance with Equation 4.6.

Showing the derivation for the downstream only (similar equations can be derived for the upstream), an equation for α , the fraction of mass replaced in a downstream cell moving vertically per second on a level k , is given by

$$\alpha_{2i-1} = \frac{1}{2f_d m_{2i-1}} 4\pi r_k^2 v_{d,k} \rho_k, \quad (4.7)$$

where m_{2i-1} is the mass of cell $2i - 1$.

4.3.3 Diffusive mixing

The difference between the vertical mass flow into and out of a given cell must move horizontally if mass is to be conserved. This flow rate is denoted by b and shown below for level k

$$b_k = \frac{1}{2} [4\pi (r_{k+1})^2 v_{d,k+1} \rho_{k+1} - 4\pi (r_k)^2 v_{d,k} \rho_k]. \quad (4.8)$$

If $b = 0$ we still allow for horizontal mass flow. This is calculated using standard mixing length concepts where a blob of material will travel a vertical mixing length l with velocity v before losing its identity. Let β be the fraction of mass replaced in each cell moving horizontally per second. The equation for β must also take into consideration the mass flow according to b (Equation 4.8). For each cell on level k , we define equations for the fraction of mass replaced in an upstream cell per second, say β_{2i} , and a downstream cell per second, say β_{2i-1} , in relation to b

$$\left. \begin{aligned} \beta_{2i} &= \frac{v_k}{f_u l_k} + b \\ \beta_{2i-1} &= \frac{v_k}{f_d l_k} \end{aligned} \right\} \text{if } b \text{ is negative,} \quad (4.9)$$

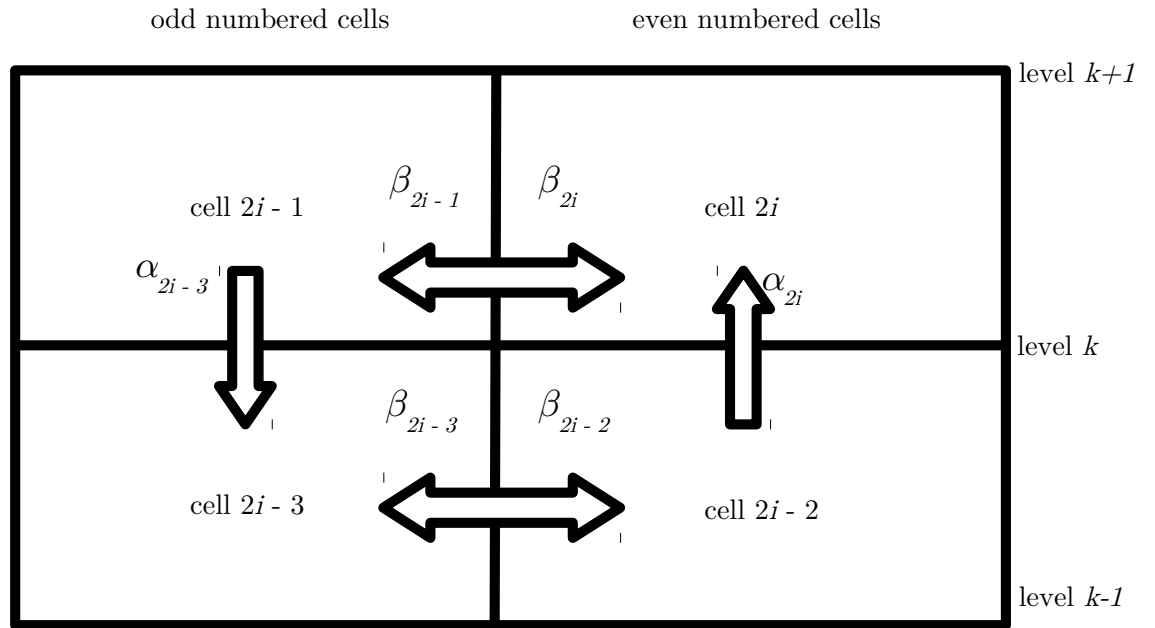


FIGURE 4.2: A set of four cells in the up and down streams of the two stream mixing regime.

$$\left. \begin{aligned} \beta_{2i} &= \frac{v_k}{f_u l_k} \\ \beta_{2i-1} &= \frac{v_k}{f_d l_k} - b \end{aligned} \right\} \text{if } b \text{ is positive.} \quad (4.10)$$

Equations 4.9 and 4.10 state that if b is negative, mass must flow from the upstream into the downstream. If b is positive, mass must flow from the downstream into the upstream. Unless otherwise stated, we take $f_u = f_d = 0.5$.

Chapter 5

A phenomenological modification of thermohaline mixing in globular cluster red giants

Most of the content in this chapter is published in Henkel, K., Karakas, A.I., and Lattanzio, J.C. (2017), “A phenomenological modification of thermohaline mixing in globular cluster red giants”, *The Monthly Notices of the Royal Astronomical Society*, 469, 4, 4600-4612.

Unpublished content is included in the *Evolution code vs nucleosynthesis code* section in §5.3.4 (including associated figures), which was completed in response to the reviewer’s comments but deemed unnecessary for the final manuscript. Additionally, the final paragraph of §5.1 was not in the final manuscript but added to the thesis to put the research into context.

5.1 Introduction

Thermohaline mixing is a favoured mechanism for the so-called “extra mixing” on the red giant branch of low-mass stars. The mixing is triggered by the molecular weight inversion created above the hydrogen shell during first dredge-up when helium-3 burns via ${}^3\text{He}({}^3\text{He}, 2\text{p}){}^4\text{He}$. The standard 1D diffusive mixing scheme cannot simultaneously match carbon and lithium abundances to NGC6397 red giants. We investigate two modifications to the standard scheme: (1) an advective two stream mixing algorithm, and (2) modifications to the standard 1D thermohaline mixing formalism. We cannot simultaneously match carbon and lithium abundances using our two stream mixing approach. However we develop a modified diffusive scheme with an explicit temperature dependence that can simultaneously fit carbon and lithium abundances to NGC6397 stars. Our modified diffusive scheme induces mixing that is faster than the standard theory predicts in the hotter part of the thermohaline region and mixing that is slower in the cooler part. Our results infer that the extra mixing mechanism needs further investigation and more observations are required, particularly for stars in different clusters spanning a range in metallicity.

This study follows on from the work done by Angelou et al. (2015) who found that they could not simultaneously fit carbon and lithium abundances to NGC6397 giant stars using the same diffusion coefficient. To elaborate further, to match carbon abundances to observations a diffusion coefficient of ~ 1000 is required, yet a value closer to ~ 150 is needed for lithium. We extend this work by constructing four tests in an attempt to match carbon and lithium abundances as a function of absolute visual magnitude to NGC6397 red giants using a single diffusion coefficient value. These four tests are:

1. Modifying the vertical velocity v and mixing length l independently in the two stream advective scheme in MONSOON,
2. Modifying v and l to maintain a constant diffusion coefficient in the two stream advective scheme,
3. Modifying the cross-sectional areas of the up and down streams in the two stream advective scheme, and
4. Invoking an artificial temperature dependence in our diffusive scheme in MONSTAR.

5.2 Stellar models

Using MONSTAR and MONSOON, discussed in Chapters 2 and 4 respectively, we evolve our stellar models from the zero-age main sequence (ZAMS) to the helium flash, which terminates RGB evolution. To allow meaningful comparisons with observations we fit our stellar models to the globular cluster NGC6397 because it is the only globular cluster to date that has observations for both carbon (Briley et al., 1990) and lithium (Lind et al., 2009) along the RGB. It is imperative to have observations of both elements because carbon and lithium burn at different temperatures and are therefore independent indicators of extra mixing.

5.2.1 Fitting stellar parameters

We test two metallicities that span the range of observed metallicities for NGC6397. We test $[\text{Fe}/\text{H}] = -2.03$ (Gratton et al., 2003) and -1.82 (Reid and Gizis, 1998). The metallicity given in Gratton et al. (2003) is very close to the Harris (1996, 2010 edition) value of -2.02 . Lind et al. (2009) find $[\text{Fe}/\text{H}] = -2.10$, which is similar to results found by Castilho et al. (2000) ($[\text{Fe}/\text{H}] = -2.0 \pm 0.05$), Gratton et al. (2001) ($[\text{Fe}/\text{H}] = -2.03 \pm 0.02 \pm 0.04$)¹, Korn et al. (2007) ($[\text{Fe}/\text{H}] = -2.12 \pm 0.03$), and Husser et al. (2016) ($[\text{Fe}/\text{H}] = -2.120 \pm 0.002$). The Reid and Gizis (1998) value of -1.82 is the upper bound of NGC6397 published metallicities.

We use $[\alpha/\text{Fe}] = 0.34$ according to Gratton et al. (2003). We determine $Z = 0.000246$ using $[\text{Fe}/\text{H}] = -2.0$ according to Gratton et al. (2003) and $Z = 0.00039$ using $[\text{Fe}/\text{H}] = -1.8$ according to Reid and Gizis (1998).

¹Where the first set of error bars are internal errors and the second set are systematic errors within the abundance scale of the 25 subdwarfs analysed by Gratton et al. (2001).

We construct stellar models with masses $0.79M_{\odot}$ and $0.8M_{\odot}$ and $Y = 0.24$ (this Y value is within observational uncertainties of the inferred primordial abundance, Mucciarelli et al., 2014; Cooke and Fumagalli, 2018). These produce main sequence turn-off (MSTO) ages of 13.8 Gyr and 13.2 Gyr respectively, and RGB tip ages of 15.1 Gyr and 14.4 Gyr respectively with $[\text{Fe}/\text{H}] = -2.0$, which are good matches for the age of NGC6397 found by Gratton et al. (2003) of 13.9 ± 1.1 Gyr. A $0.8M_{\odot}$ stellar model with $[\text{Fe}/\text{H}] = -1.8$ produces a MSTO age of 13.3 Gyr and an RGB tip age of 14.6 Gyr.

FDU and RGB bump magnitudes

The FDU and RGB bump absolute visual magnitudes of NGC6397 giants are $M_V = 3.3$ and 0.16 respectively (Lind et al., 2009) using the bolometric corrections of Alonso, Arribas, and Martínez-Roger (1999). Lind et al. (2009) do not report uncertainties in their magnitude estimates. Nataf et al. (2013) find the V -band magnitude of the bump to be 12.533 ± 0.046 . We apply this uncertainty to the bump magnitude of Lind et al. (2009) and find the values of the FDU and bump magnitudes to be 3.3 ± 0.046 and 0.16 ± 0.046 respectively.

The value of the overshoot factor f_{OS} , Equation 2.34 in §2.5.1, affects the predicted magnitude of the bump. We test a range of f_{OS} values from 0.02 to 0.15 to match the magnitudes of FDU and RGB bump, with results shown in Fig. 5.1 for our $0.8M_{\odot}$, $Z = 0.000246$, $[\text{Fe}/\text{H}] = -2.0$ stellar model.

We find the stellar models that best match the FDU and bump magnitudes observed for NGC6397 using our two chosen metallicities are a $0.79M_{\odot}$ star with $Z = 0.000246$ using $[\text{Fe}/\text{H}] = -2.0$ (Gratton et al., 2003), $Y = 0.24$ and $f_{OS} = 0.14$ (henceforth our $0.79M_{\odot}$ model), and a $0.80M_{\odot}$ star with $Z = 0.00039$ using $[\text{Fe}/\text{H}] = -1.8$ (Gratton et al., 2003), $Y = 0.24$ and $f_{OS} = 0.10$ (henceforth our $0.80M_{\odot}$ model). In Fig. 5.2 we show a range of f_{OS} values for our $0.80M_{\odot}$ model (as we did in Fig. 5.1 for our $0.79M_{\odot}$ model).

Hertzsprung-Russell diagram

We plot the giant branch of our best-fit models according to our overshoot results (Fig. 5.1) on a HR diagram in Fig. 5.3 compared to the observational HR diagram of NGC6397 (Lind et al., 2009).

In Fig. 5.3 we see that the model that best matches the giant branch of NGC6397 is our $0.79M_{\odot}$ model. This is also the best fit for FDU and the LFB. The difference in metallicities between our $0.79M_{\odot}$ model and $0.80M_{\odot}$ model (along with initial stellar mass) likely contributes to the HR diagram discrepancies in Fig. 5.3, though this does not change our results or conclusions.

To allow analysis of burning timescales and composition changes in our model, we choose an epoch just after surface abundance changes due to thermohaline mixing have occurred. The epoch chosen is shown in Fig. 5.4. All analysis of internal stellar properties is done at this epoch.

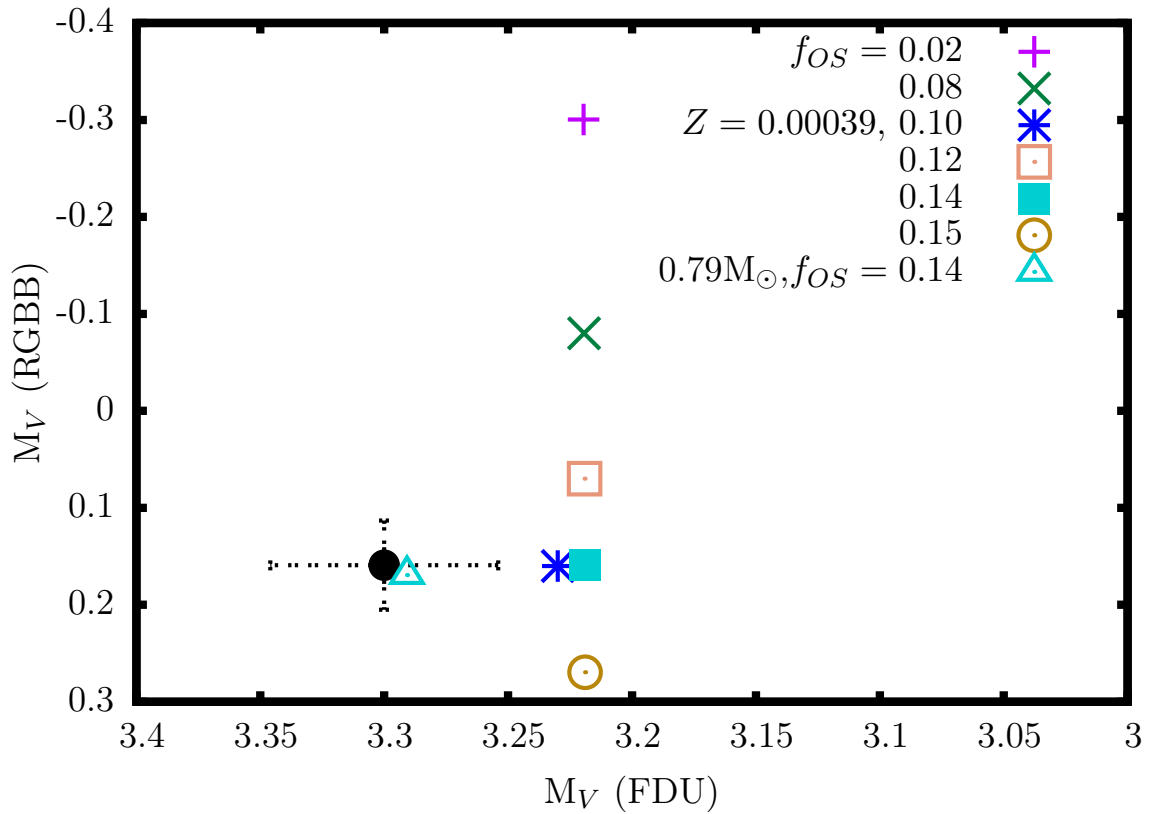


FIGURE 5.1: FDU and RGB bump magnitudes for our $0.8M_{\odot}$, $Z = 0.000246$, $[\text{Fe}/\text{H}] = -2.0$ stellar model where we vary f_{OS} , with values given in the legend. Also given in the legend are the best-fit models of $0.8M_{\odot}$, $Z = 0.00039$, $[\text{Fe}/\text{H}] = -1.8$ and $f_{OS} = 0.10$ (labelled with Z), and $0.79M_{\odot}$, $Z = 0.000246$, $[\text{Fe}/\text{H}] = -2.0$ and $f_{OS} = 0.14$. FDU and RGB bump magnitudes of Lind et al. (2009) with the observational uncertainty of Nataf et al. (2013) is black.

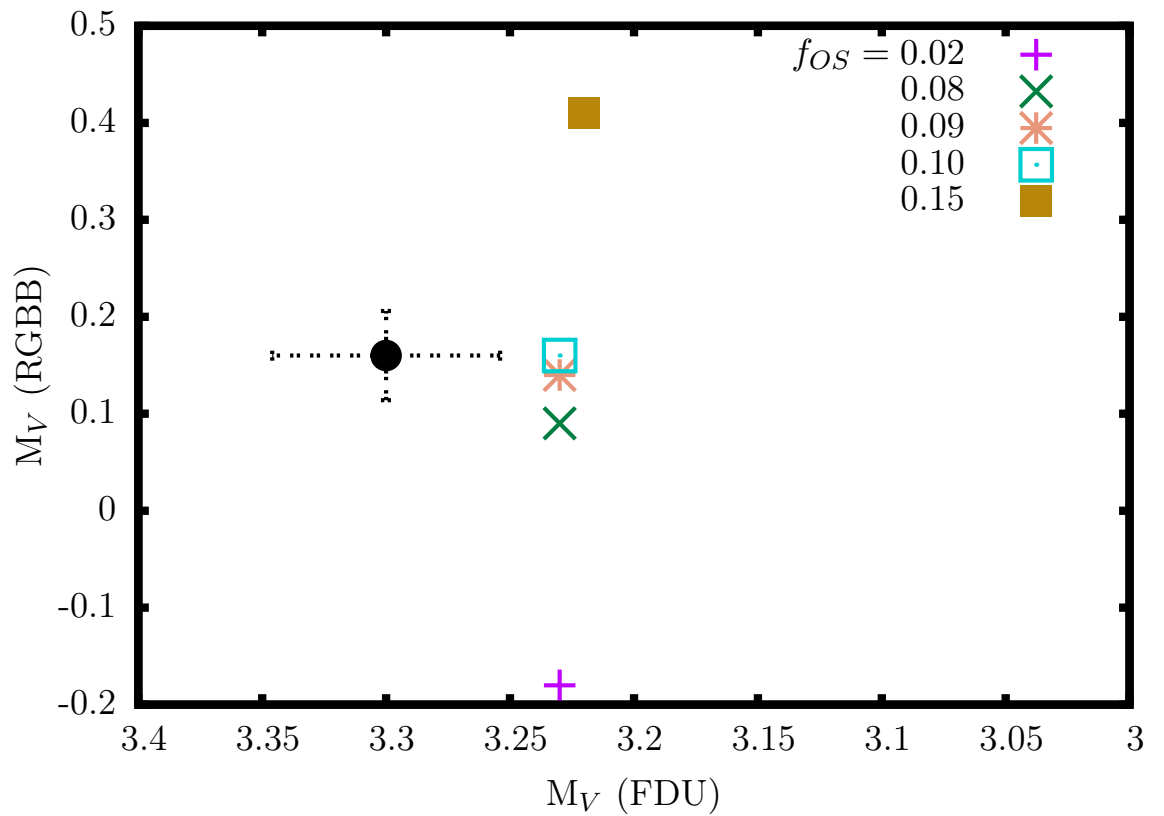


FIGURE 5.2: FDU and RGB bump magnitudes for our $0.8M_{\odot}$, $Z = 0.000390$, $[\text{Fe}/\text{H}] = -1.8$ stellar model where we vary f_{OS} , with values given in the legend. FDU and RGB bump magnitudes of Lind et al. (2009) with the observational uncertainty of Nataf et al. (2013) is black.

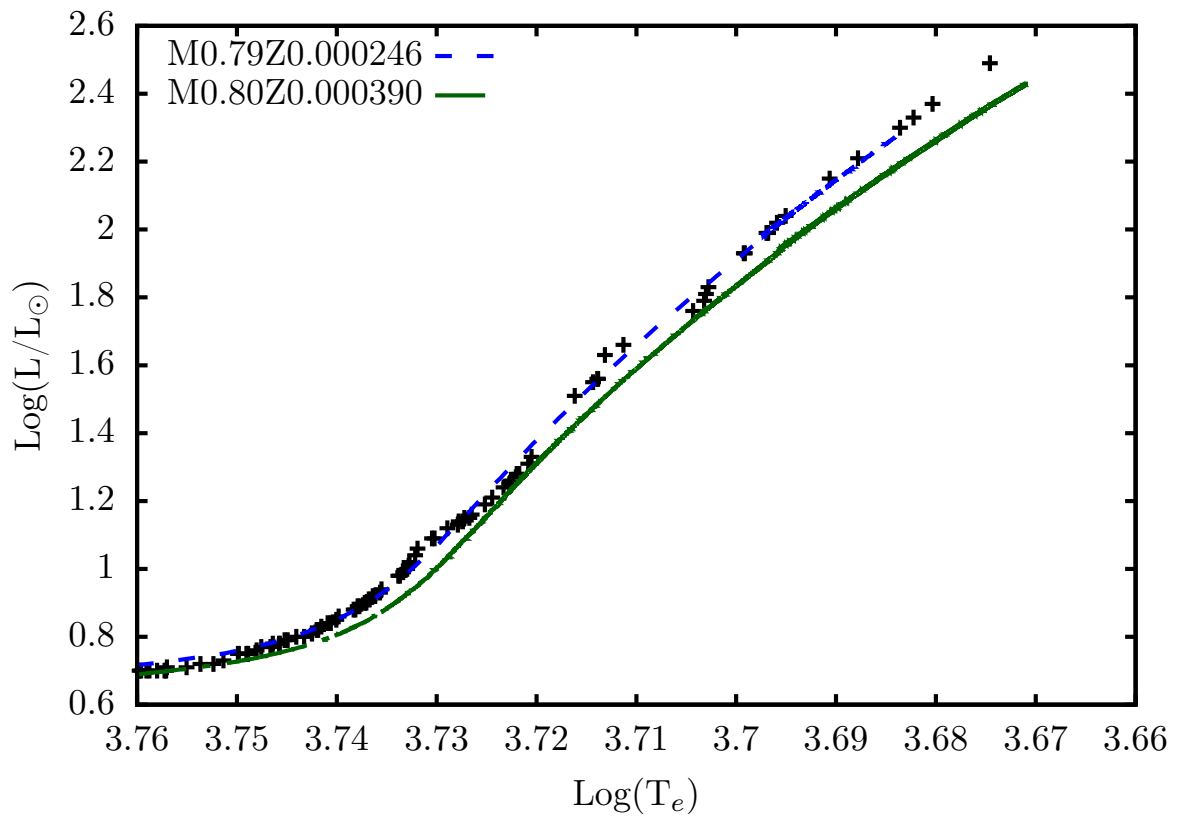


FIGURE 5.3: The giant branch of the Hertzsprung-Russell diagram of our models compared to observations of NGC6397 (Lind et al., 2009). Our $0.79M_{\odot}$ model, denoted M0.79Z0.000246 in the legend, is the blue dashed curve. Our $0.80M_{\odot}$ model, denoted M0.8Z0.00390, is the green solid curve.

The locations of FDU and thermohaline mixing (“Thm”) on the HR diagram are when abundance changes on the surface are observed due to these events. Interestingly we see from the inset of Fig. 5.4 that abundance changes due to thermohaline mixing first appear on the surface at a lower luminosity than the LFB. Generally it is thought that thermohaline mixing coincides with the LFB on the HR diagram but this is not necessarily the case according to Fig. 5.4 and is also found by other groups² (Charbonnel and Lagarde, 2010). Extra mixing is governed by ^3He fusion inverting the μ gradient whereas the LFB is due to the structural change in the star as the H shell passes through the hydrogen discontinuity caused by FDU. These events need not coincide with each other because they occur at different temperatures and time is required to build a molecular weight version after the hydrogen burning shell enters the region that was previously homogenised by the convective envelope. The lithium abundance changes at lower temperatures before the H shell reaches the discontinuity. Hence abundance changes caused by thermohaline mixing occur slightly before the reversal in the HR diagram, which requires the H shell to have reached the discontinuity. There is also a delay between when thermohaline mixing begins and when it connects to the convective envelope as Fig 5.5 shows in more detail. The amount of time elapsed is dependent upon timestepping and spatial resolution in the stellar evolution code (for a detailed discussion of this, see Lattanzio et al., 2015). In Fig. 5.5 we can see that thermohaline mixing begins prior to the H shell connecting with the hydrogen abundance discontinuity.

5.2.2 Nuclear burning timescales in our standard model

The timescales discussed below have been determined using MONSTAR. We denote D_0 as the thermohaline coefficient for the standard case with $C_t = 1000$ and test three variations of D_t according to $D_t = f \times D_0$ where $f = 1/3, 1, 3$. We show the results in Figs. 5.6 and 5.7. The case of $f = 3$ is mixing that is faster than the standard $f = 1$ case, and $f = 1/3$ is mixing that is slower. Timescales are plotted as a function of radius. The nuclear burning timescales depend upon temperature and density, and are independent of f .

Lithium and carbon burning timescales in the thermohaline region

Lithium-7, which burns at around 2×10^6 K, is a useful tracer of mixing and burning. This is especially the case for low-mass RGB stars that have extensive convective envelopes. Beryllium-7, which captures an electron to form ^7Li as part of the ppII chain, is an integral isotope in the Cameron-Fowler mechanism (a means for producing ^7Li in stellar interiors; Cameron and Fowler, 1971). Beryllium-7 has a short half-life and is destroyed via electron capture (ppII chain) and/or proton capture (ppIII chain). It is produced via alpha capture on ^3He as the first reaction in the ppII and ppIII chains.

²As shown in Fig. 5.4 the difference in $\log(L/L_\odot)$ between thermohaline mixing and the LFB is only ~ 0.01 . Observationally this is extremely difficult to distinguish, hence it is sufficient to approximate that the LFB and extra mixing occur at the same time.

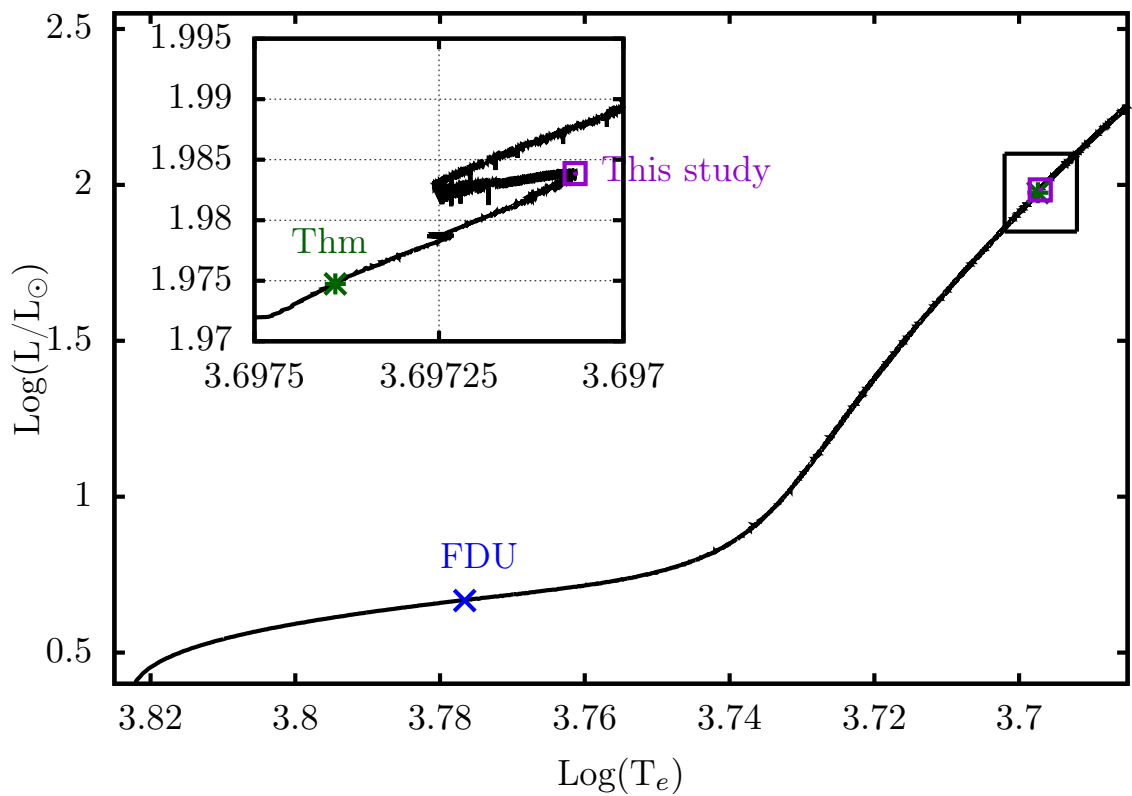


FIGURE 5.4: Hertzsprung-Russell diagram of our $0.79M_{\odot}$ model. The points on the plot denote the location on the HR diagram where abundance changes occur in our models. First dredge-up (“FDU”, blue cross), thermohaline mixing (“Thm”, green asterisk), and the luminosity we have chosen to take snapshots of our mixing mechanism (“This study”, purple square) are indicated. The region of the LFB is shown in the inset.

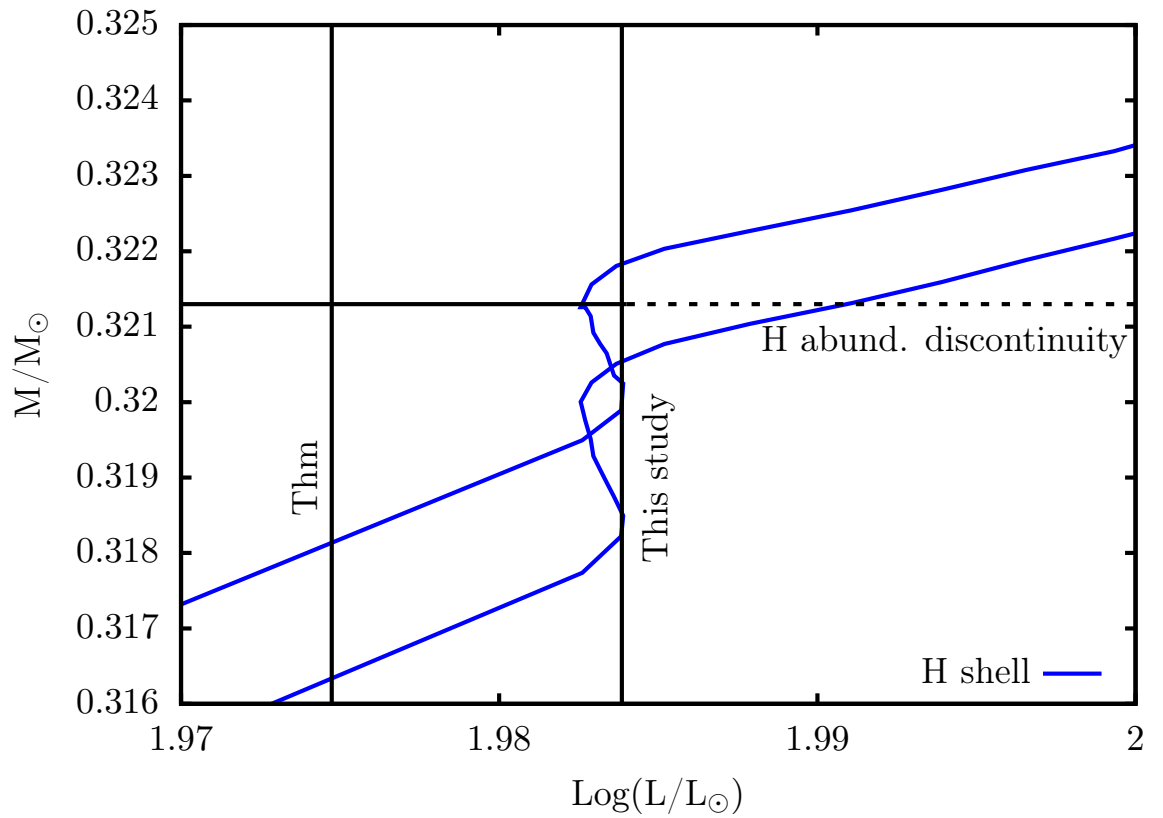


FIGURE 5.5: Upper and lower mass boundaries of the H shell (in blue) of our $0.79M_{\odot}$ model as it is nearing the LFB. These mass boundaries are defined as the mass where $X = 0.05$ and $X = 0.66$. The luminosity location of surface abundance changes due to thermohaline mixing (“Thm”) and the epoch chosen for this study (“This study”) are indicated and are the same as in Fig. 5.4. The initial mass location of the hydrogen abundance discontinuity is also shown as a solid line until it is smoothed at the LFB where it becomes a dashed line.

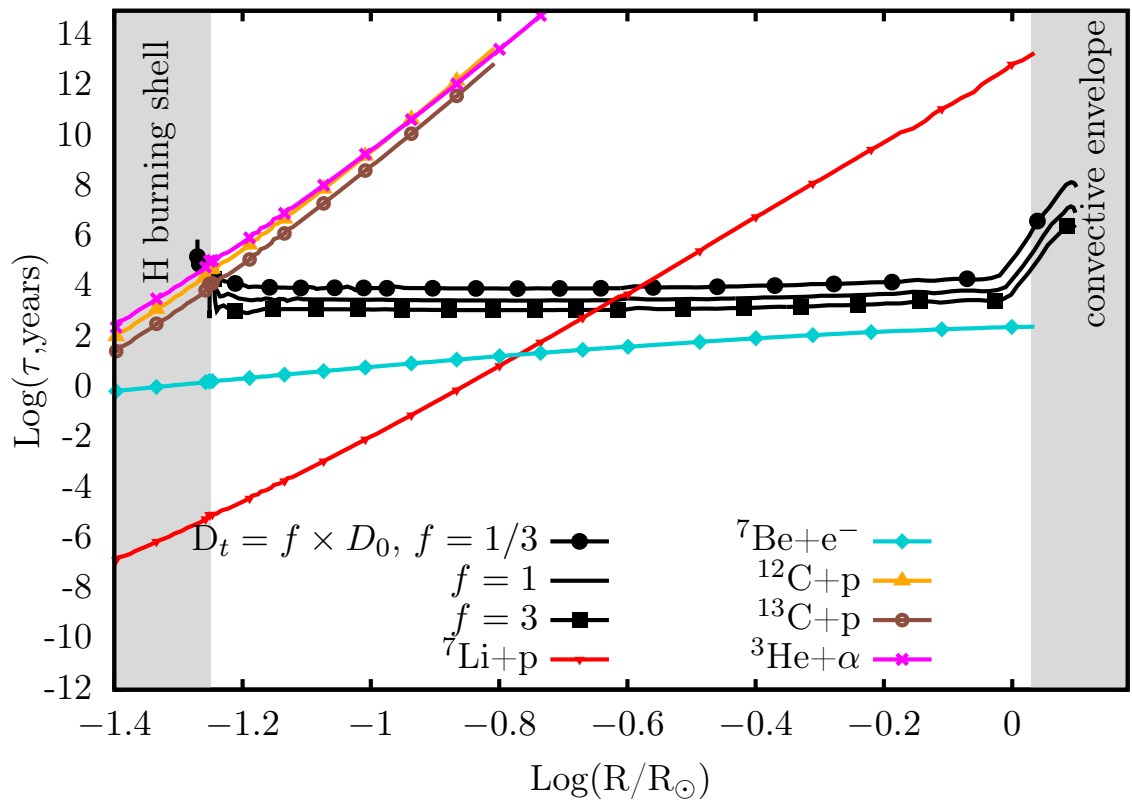


FIGURE 5.6: The log of mixing timescales (years; black curves) and nuclear burning timescales of ${}^7\text{Li}$ (red), ${}^7\text{Be}$ (turquoise), ${}^{12}\text{C}$ (orange), ${}^{13}\text{C}$ (burgundy), and ${}^3\text{He}$ (magenta) in our $0.79M_{\odot}$ model at the point labelled “This study” in Fig. 5.4.

Helium-3 itself is important because destruction of ${}^3\text{He}$ via ${}^3\text{He}({}^3\text{He}, 2p){}^4\text{He}$ is the reaction that sets a thermohaline-suitable environment just above the H shell by producing a local decrease in μ .

There are two limiting cases for the mixing: if it is infinitely fast then all abundances are homogeneous; if there is no mixing the shapes of the abundance profiles are due to burning alone (decreasing with increasing depth/temperature). Although not dominant at the temperatures in the thermohaline region³ as shown in Fig. 5.8, the ppII chain is still operating, destroying ${}^3\text{He}$ by alpha capture via ${}^3\text{He}(\alpha, \gamma){}^7\text{Be}$ and producing ${}^7\text{Be}$. As stated previously, faster mixing ($f = 3$ in Figs. 5.6 and 5.7) produces a more homogeneous ${}^3\text{He}$ profile than slower mixing ($f = 1/3$). The timescale for ${}^3\text{He}$ alpha capture is longer than the mixing timescale regardless of f , producing a ${}^3\text{He}$ abundance that does not vary dramatically with f as shown in the middle panel of Fig. 5.7.

Alpha capture on ${}^3\text{He}$ produces ${}^7\text{Be}$ and this occurs predominantly in the interior where ${}^3\text{He}$ burns fastest. A fast rate of mixing will bring ${}^3\text{He}$ from the interior (where temperatures are higher) towards the surface faster. Therefore less ${}^3\text{He}$ will burn, producing less ${}^7\text{Be}$. However, the ${}^7\text{Be}$ will also be brought from the interior faster, and although it will be destroyed via electron capture at nearly the same rate at all temperatures, the amount of ${}^7\text{Be}$ destroyed is less than when mixing is slower.

The rate of ${}^7\text{Be}$ destruction is always faster than the rate of mixing for all tested f , therefore over the entire thermohaline zone the ${}^7\text{Be}$ abundance does not become homogeneous. In the interior (from the base of the thermohaline zone to $\log(R/R_\odot) \sim -0.8$), ${}^7\text{Li}$ destruction is much faster than mixing by several orders of magnitude, therefore the ${}^7\text{Li}$ profile is not homogeneous with position. The ${}^7\text{Li}$ profile is complicated because both destruction (by proton capture) and production (by electron capture on ${}^7\text{Be}$) timescales are of similar orders of magnitude, particularly around $\log(R/R_\odot) \sim -0.8$. This produces the variation of around 3 orders of magnitude that is dependent upon f and shown in the top panel of Fig. 5.7. Beyond $\log(R/R_\odot) \sim -0.8$ the rate of ${}^7\text{Li}$ destruction is slower than the rate of mixing and the profile is approximately homogeneous.

Faster mixing means that the timescale of ${}^{12}\text{C}$ destruction is slower than the mixing timescale over the entire thermohaline region and the abundance profile is (almost) homogeneous. When f is reduced and the rate of mixing is slower, the timescale of ${}^{12}\text{C}$ destruction can be faster than the mixing timescale for a thin region at the base of the thermohaline zone. More ${}^{12}\text{C}$ destruction occurs because ${}^{12}\text{C}$ is allowed to burn at the base of the thermohaline zone.

Destruction of ${}^{13}\text{C}$ via proton capture is slower than both the rates of mixing and ${}^{12}\text{C}$ destruction. When mixing is fast, ${}^{13}\text{C}$ is essentially homogenised over the region. When mixing is slower, ${}^{13}\text{C}$ is destroyed slower than it is produced, resulting in net production of ${}^{13}\text{C}$. The combination of increased ${}^{12}\text{C}$ destruction and increased ${}^{13}\text{C}$ production results in a ${}^{12}\text{C}$ abundance

³At a time just after the initiation of thermohaline mixing, temperatures range from ~ 20 MK at the base of the thermohaline region to ~ 2 MK at the base of the convective envelope (Fig. 5.8).

that is lower and a ^{13}C abundance that is higher in the thermohaline region when $f = 1/3$ compared to the $f = 1$ and $f = 3$ cases.

5.2.3 Motivation for studies and observational limitations

The data we use for NGC6397 are from Lind et al. (2009) for lithium and Briley et al. (1990) for carbon. Angelou et al. (2015) found that the decrease in the carbon abundances due to thermohaline mixing occurred prior to the RGB bump whereas lithium declined at the bump, as predicted. We have found that this is related to the distance modulus and note that Lind et al. (2009) and Briley et al. (1990) used different values of the distance modulus for NGC6397; Lind et al. (2009) used 12.57 and Briley et al. (1990) used 11.8. By adjusting the distance modulus of the stars observed by Briley et al. (1990) to match that of Lind et al. (2009), we resolve the issue found by Angelou et al. (2015) and find that carbon and lithium begin their decrease at the same magnitude.

To match lithium abundances to observations, a C_t value of around 150 is required but a value closer to 1000 is needed to match carbon as shown in Fig. 5.9 (as also found by Angelou et al., 2015). To elaborate on this, if $C_t = 1000$ is used and carbon matches observations then the models deplete lithium too much. Converse to this, if we use $C_t = 150$ to match lithium observations then we require an increased depletion of carbon.

The spread of the observational data is a complication when comparing to our theoretical models (Fig. 5.9). The spread of the carbon abundances is of the order of 0.2 dex at a given magnitude. This spread is most likely due to the different stellar populations present in NGC6397. Angelou et al. (2012) showed that observations of carbon and nitrogen in the intermediate-metallicity clusters M3 and M13 were best represented by separate models with initially different carbon and nitrogen compositions. The stars with an essentially normal composition are the CN-weak population, which form the upper envelope of the carbon distribution. It is these stars that we try to fit here. Errors of individual star carbon abundances are around 0.1 dex (Briley et al., 1990), as shown in the bottom panel of Fig. 5.9. The 0.1 dex error we use for the carbon observations is based upon the discussion and values given (in their Table 11) in Briley et al. (1990) and is a conservative value for the upper-RGB stars. In fact, the errors given in Briley et al. (1990) show their coolest stars towards the tip of the RGB have errors larger than their hotter stars, which makes sense given that the strength of the carbon molecular bands decreases with temperature. The model with $C_t = 150$ can match the lower RGB stars within errors but cannot match the most carbon-depleted upper RGB stars as shown in Fig. 5.9.

The observations of lithium are more tightly constrained with smaller errors (Lind et al., 2009) but again there are very few observations near the RGB tip and the coolest few stars do not have associated errors⁴ as shown in the top panel of Fig. 5.9. When $C_t = 150$ we can match the lithium abundances of all of the RGB stars in NGC6397 but when $C_t = 1000$ we cannot match any RGB stars after the start of extra mixing.

⁴The observed abundances for the coolest RGB stars are upper limits only.

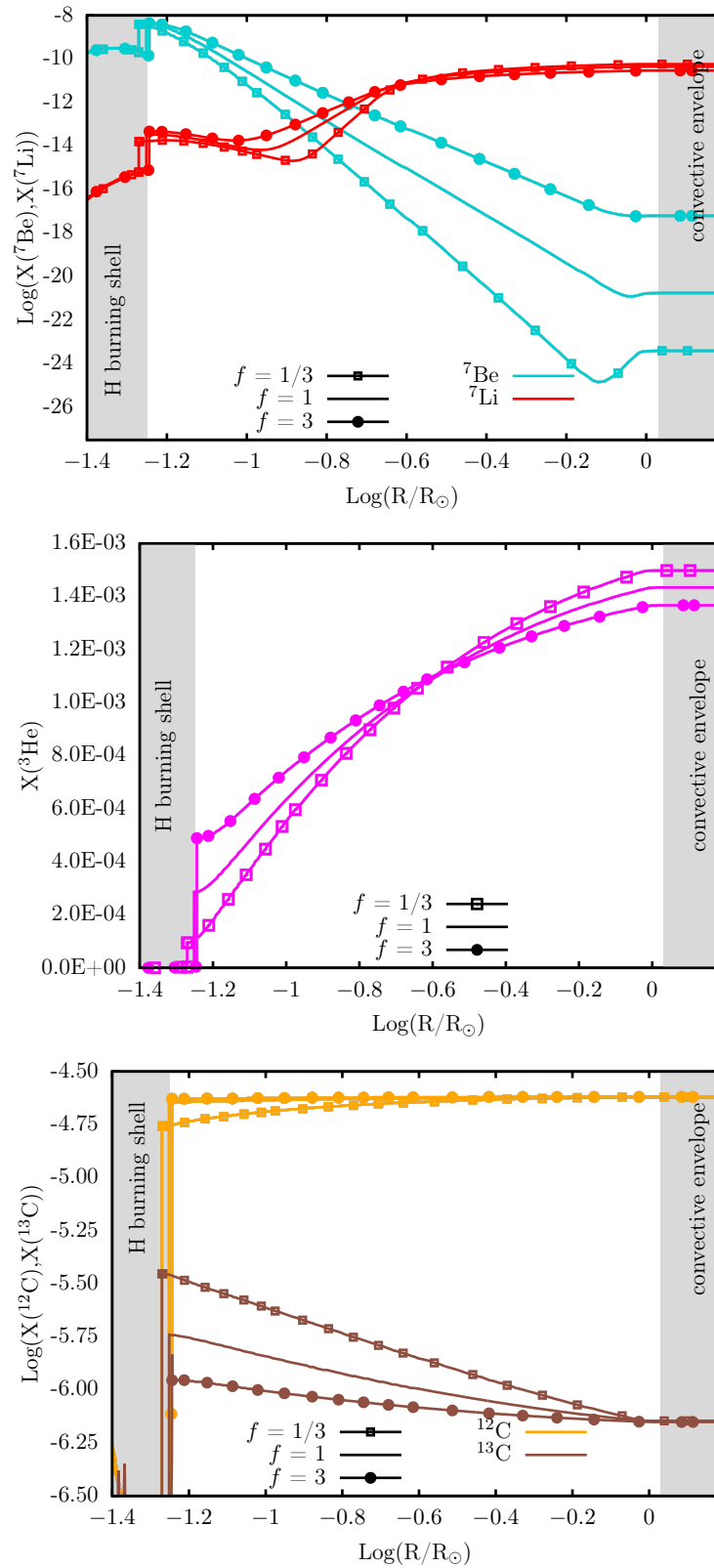


FIGURE 5.7: Abundance profiles for $f = 1/3$ (open squares), 1 (solid curves), and 3 (filled circles). Top panel: ${}^7\text{Li}$ (red) and ${}^7\text{Be}$ (turquoise). Middle panel: ${}^3\text{He}$. Bottom panel: ${}^{12}\text{C}$ (orange) and ${}^{13}\text{C}$ (burgundy) in our $0.79M_{\odot}$ model at the point labelled “This study” in Fig. 5.4.

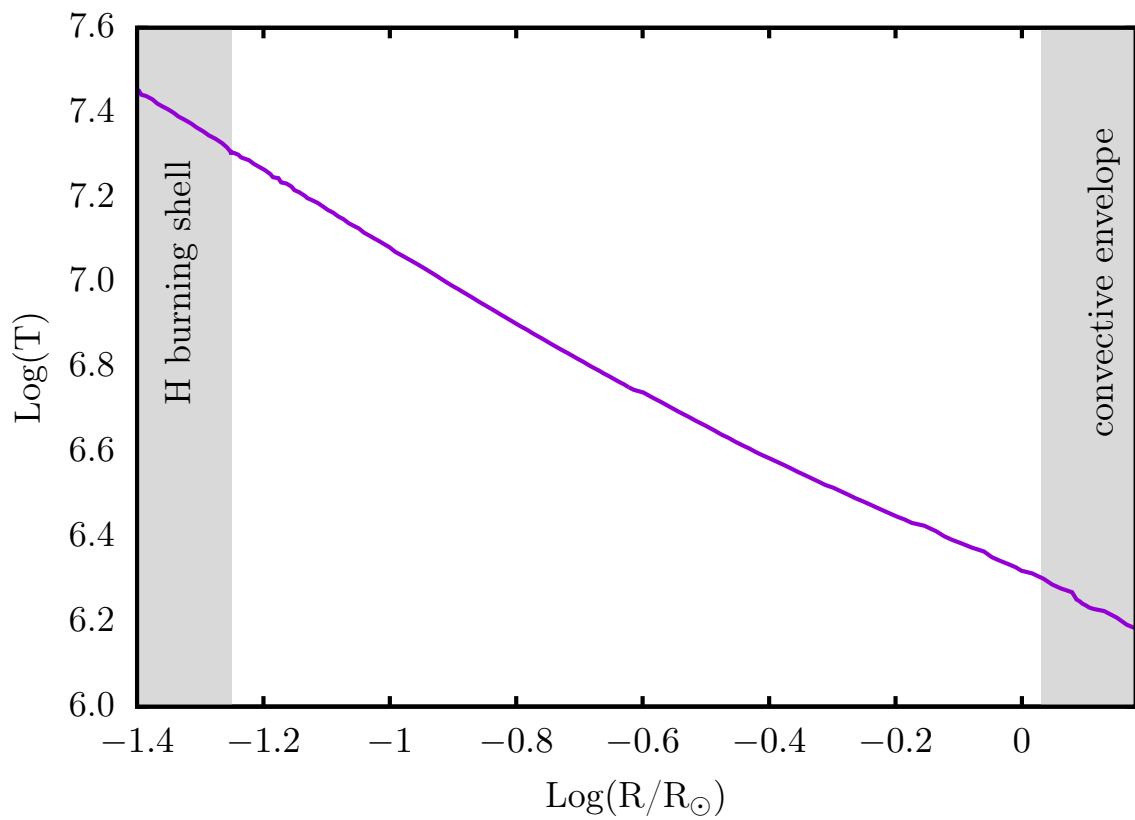


FIGURE 5.8: Temperature as a function of radius in the thermohaline region for our $0.79M_{\odot}$ stellar model. The stage of evolution is shown in Fig. 5.4 as the point “This study”.

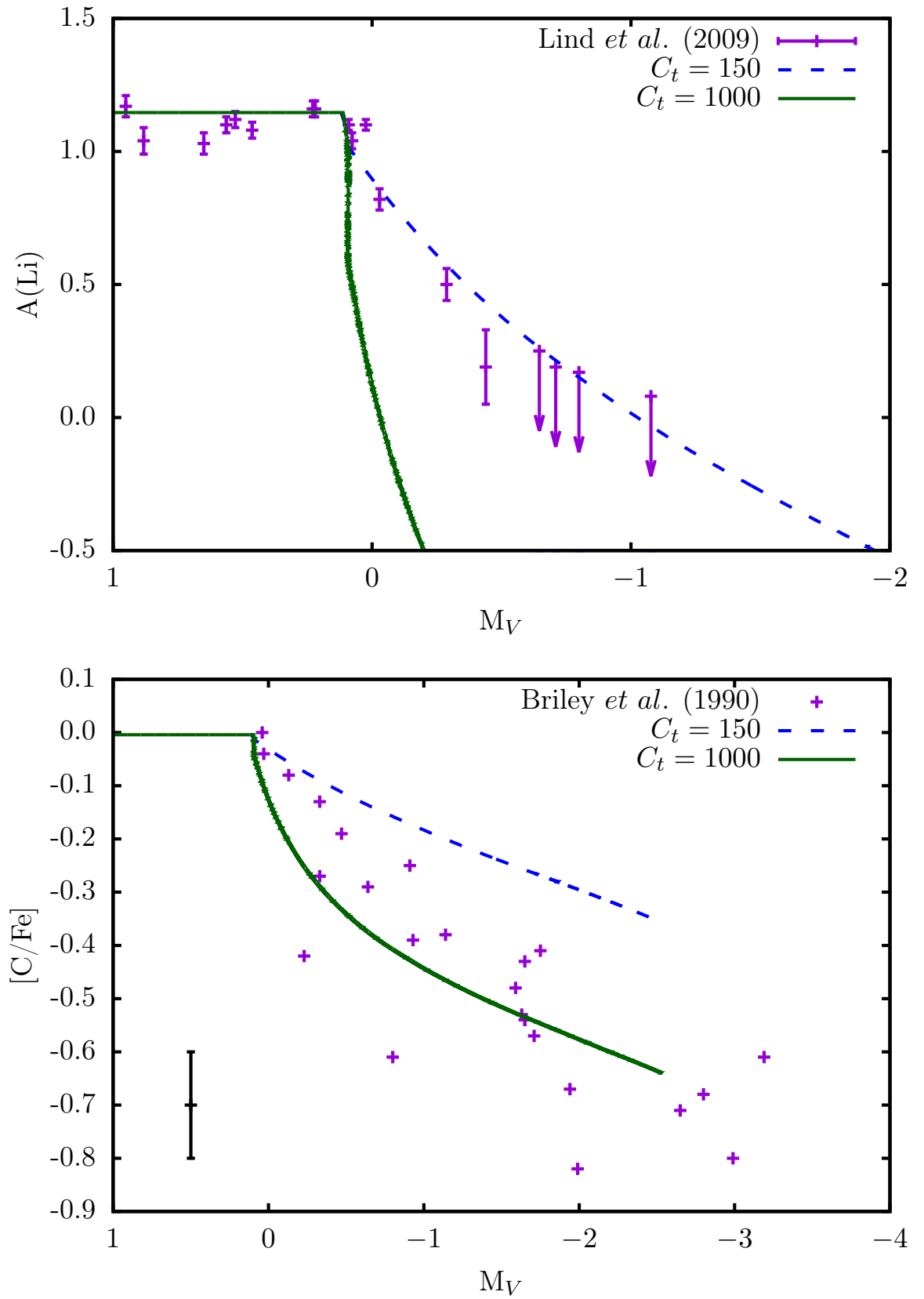


FIGURE 5.9: Top panel: Theoretical surface lithium abundances (curves) compared to observations (purple points, arrows indicate upper limits, Lind *et al.*, 2009). Bottom panel: Theoretical carbon abundances (curves) compared to observations with a 0.1 dex error bar (purple points, Briley *et al.*, 1990). In each panel the dark green curve is when the thermohaline mixing free parameter $C_t = 1000$. The blue dashed curve is for $C_t = 150$.

5.3 Test Cases and Results

5.3.1 Case 1: Independently changing v and l in the two stream advective mixing scheme

We explore the advective two stream model implemented in MONSOON, detailed in Chapter 4, by varying v and l in Equation 2.29. We invoke “mixing factors” to modify the mixing length and velocity according to

$$\begin{aligned} v_{\text{new}} &= f_v \times v_{\text{std}}, \\ l_{\text{new}} &= f_l \times l_{\text{std}}, \end{aligned} \tag{5.1}$$

where the subscript “std” indicates the parameter value for a given C_t (as defined by Equation 2.37). Looking at the value of β for horizontal mixing in Equations 4.9 and 4.10, we see that the only place in our two stream mixing model where l appears is in these equations. Therefore it is straightforward to show that $\beta \propto 1/l$. Hence varying f_l is the same as varying $1/\beta$.

It is important to note that when f_v and f_l are varied independently we change the effective value of D_t in MONSOON by a factor of f_v or f_l despite setting a value of D_t in MONSTAR according to the Ulrich/Kippenhahn formula. Therefore D_t in MONSTAR and D_t in MONSOON will be inconsistent. Indeed, as soon as we use a different mixing algorithm (in MONSOON) to the diffusion equation (in MONSTAR) then the results are technically inconsistent. We accept this inconsistency because there is negligible feedback on the underlying stellar structure.

Table 5.1 summarises the models calculated for Case 1. When referring to specific tests in Table 5.1 we first refer to the case letter and then the value of the variable. For example, when referencing the test where f_v is being changed independently and we wish to refer to the $f_v = 0.10$ test, we say $V0.10$.

Single parameter results

The effect of changing f_v and f_l independently on the surface lithium and carbon abundances is shown in Fig. 5.10 (for f_v) and Fig. 5.11 (for f_l).

Fast mixing and long mixing lengths (high f_v and f_l respectively) result in increased depletion of both carbon and lithium on the surface. Independently changing f_v and f_l cannot simultaneously match the lithium and the (upper envelope of the) carbon abundances to observations for a single value of C_t .

For the case of changing f_v and f_l independently when $C_t = 1000$ the models that best match lithium abundances to observations are $V0.50$ or $L0.33$ (corresponding to “effective” C_t values of 500 and 333 respectively). The models that best match carbon abundances to observations are $V1.00$ or $L1.00$ (corresponding to an “effective” C_t value of 1000). These results are consistent with the motivation for this study where if C_t is chosen to match

Case	f_v	f_l	Name
V	0.10	1	V0.10
	0.33	1	V0.33
	0.50	1	V0.50
	2.00	1	V2.00
	3.00	1	V3.00
	10.0	1	V10.0
L	1	0.10	L0.10
	1	0.33	L0.33
	1	0.50	L0.50
	1	2.00	L2.00
	1	3.00	L3.00
	1	10.0	L10.0

TABLE 5.1: Models tested in Case 1: Independently changing v and l in the two stream advective mixing scheme.

carbon to observations we deplete lithium too much even when uncertainties/errors of the observations are taken into account.

5.3.2 Case 2: Changing v and l to maintain constant D in the two stream advective mixing scheme

Table 5.2 summarises the models tested for Case 2. Here both f_v and f_l are changed to maintain the selected value of D_t . We refer to the case letter and then the value of f_v (remembering that in this case $f_l = 1/f_v$). For example, $DV0.10$ refers to the test where $f_v = 0.10$ and $f_l = 10$.

Results

Fig. 5.12 shows the effect on the surface abundances of lithium (top panel) and carbon (bottom panel). The effect of changing f_v is much more significant than changing f_l . To elaborate, varying the velocity of the material has a greater effect on abundances than does varying the mixing length and this is why we see a similar result to changing f_v independently (as in Fig. 5.10).

The model that best matches models to observations of lithium is $DV0.33$ and the model that best matches carbon is $DV1.00$. This is consistent with the results of independently changing f_v and f_l discussed in §5.3.1. In the single parameter tests it was found that models matched observations when $f_v, f_l \sim 0.33 - 0.5$ for lithium and when $f_v, f_l \sim 1 - 2$ for carbon. We find the same result here. It is evident no solution can be found by modifying f_v and f_l to maintain D_t using our two stream mixing algorithm.

5.3.3 Case 3: Changing f_u and f_d in the two stream advective mixing scheme

An important point to consider is that the cross-sectional areas of the streams are unknown; they can and may indeed be unequal in real stars

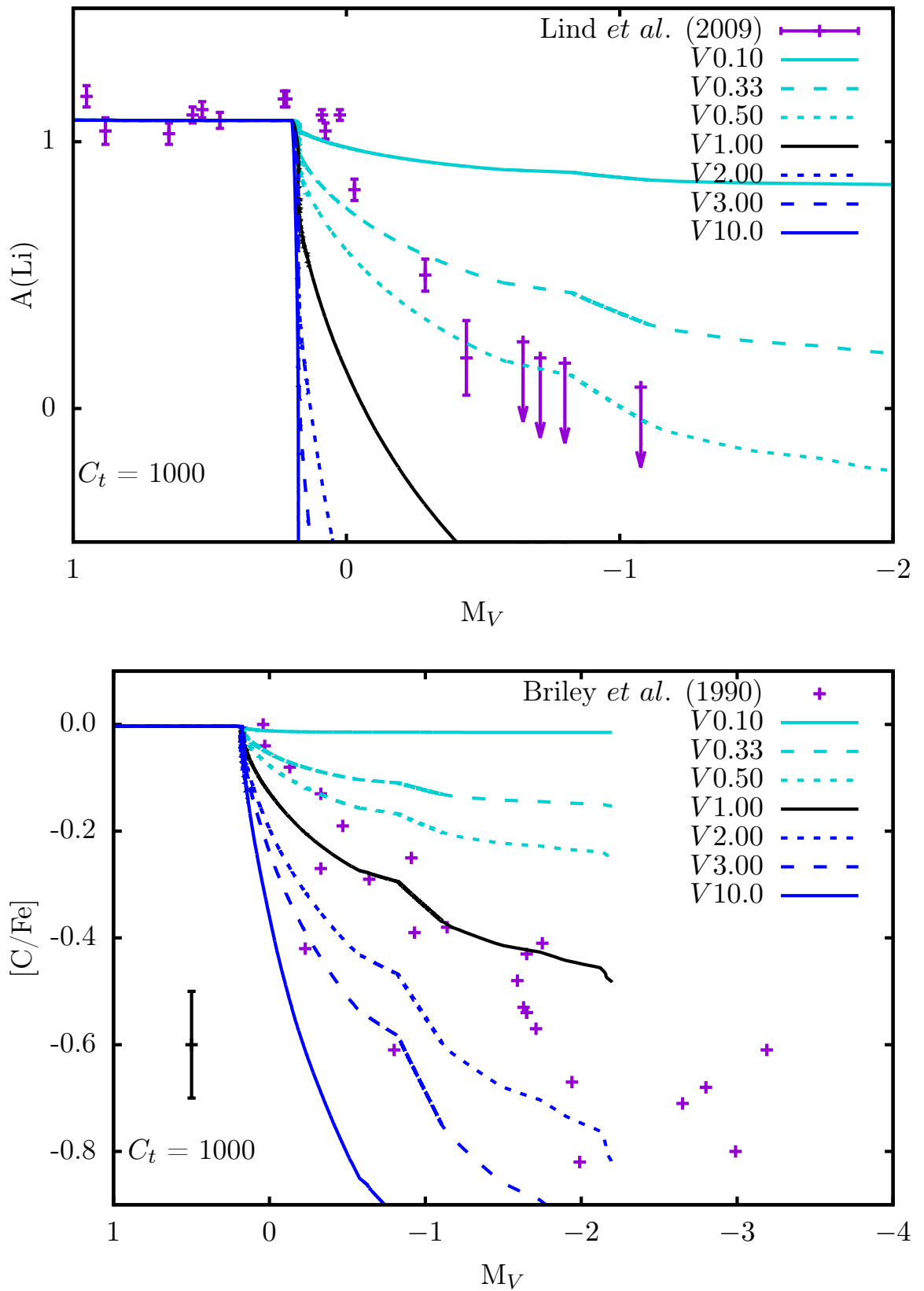


FIGURE 5.10: The effect of changing f_v on the surface abundance profiles of $A(\text{Li})$ (top panel) and $[\text{C}/\text{Fe}]$ with a 0.1 dex error bar (bottom panel) and $C_t = 1000$. The values of f_v and colour key of the curves are in the legend of the plots. Observations are purple points, with upper limits denoted by arrows (Briley *et al.*, 1990; Lind *et al.*, 2009).

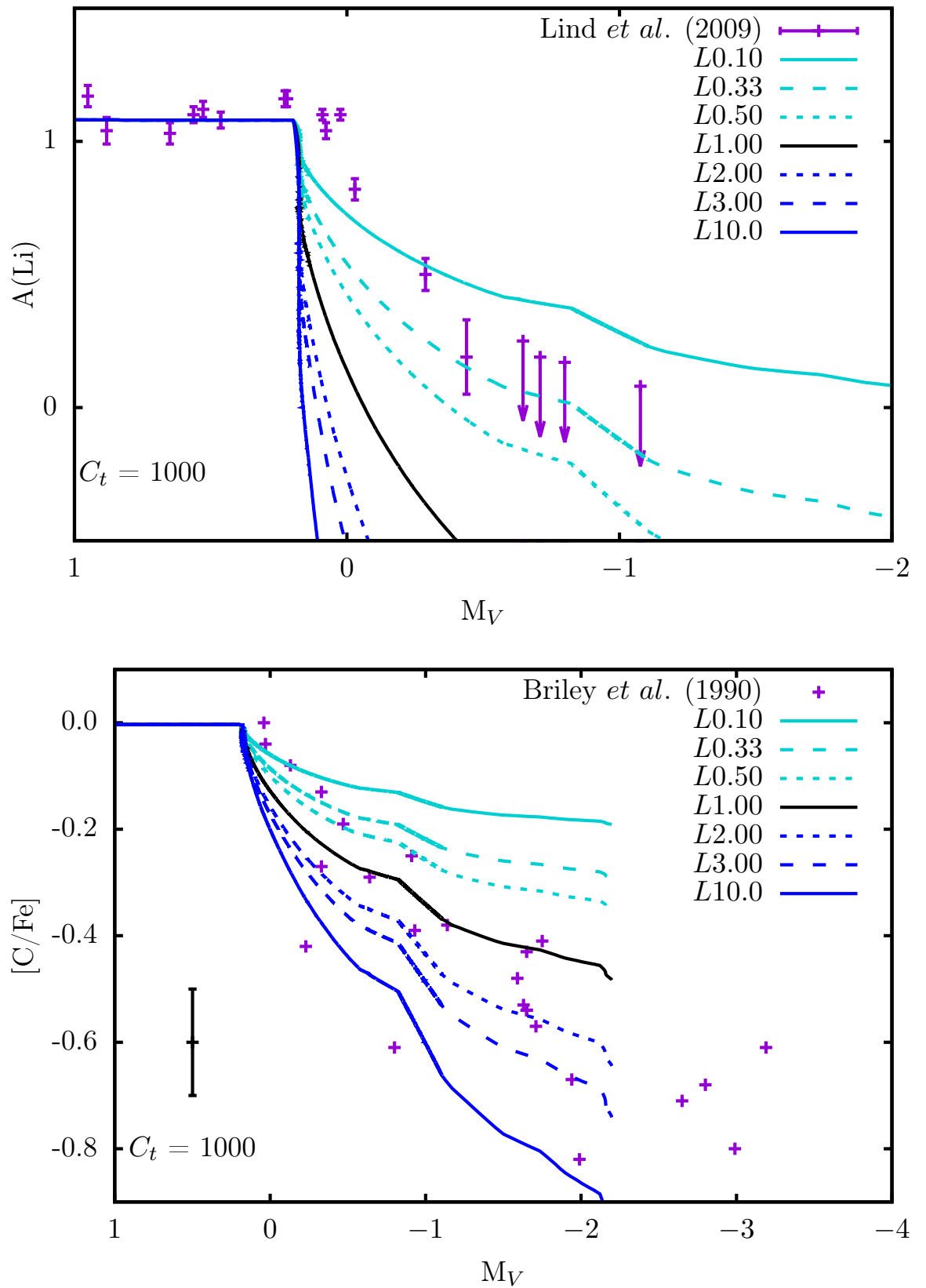


FIGURE 5.11: The effect of changing f_l on the surface abundance profiles of $A(\text{Li})$ (top panel) and $[\text{C}/\text{Fe}]$ with a 0.1 dex error bar (bottom panel) and $C_t = 1000$. The values of f_l and colour key of the curves are in the legend of the plots. Observations are purple points, with upper limits denoted by arrows (Briley et al., 1990; Lind et al., 2009).

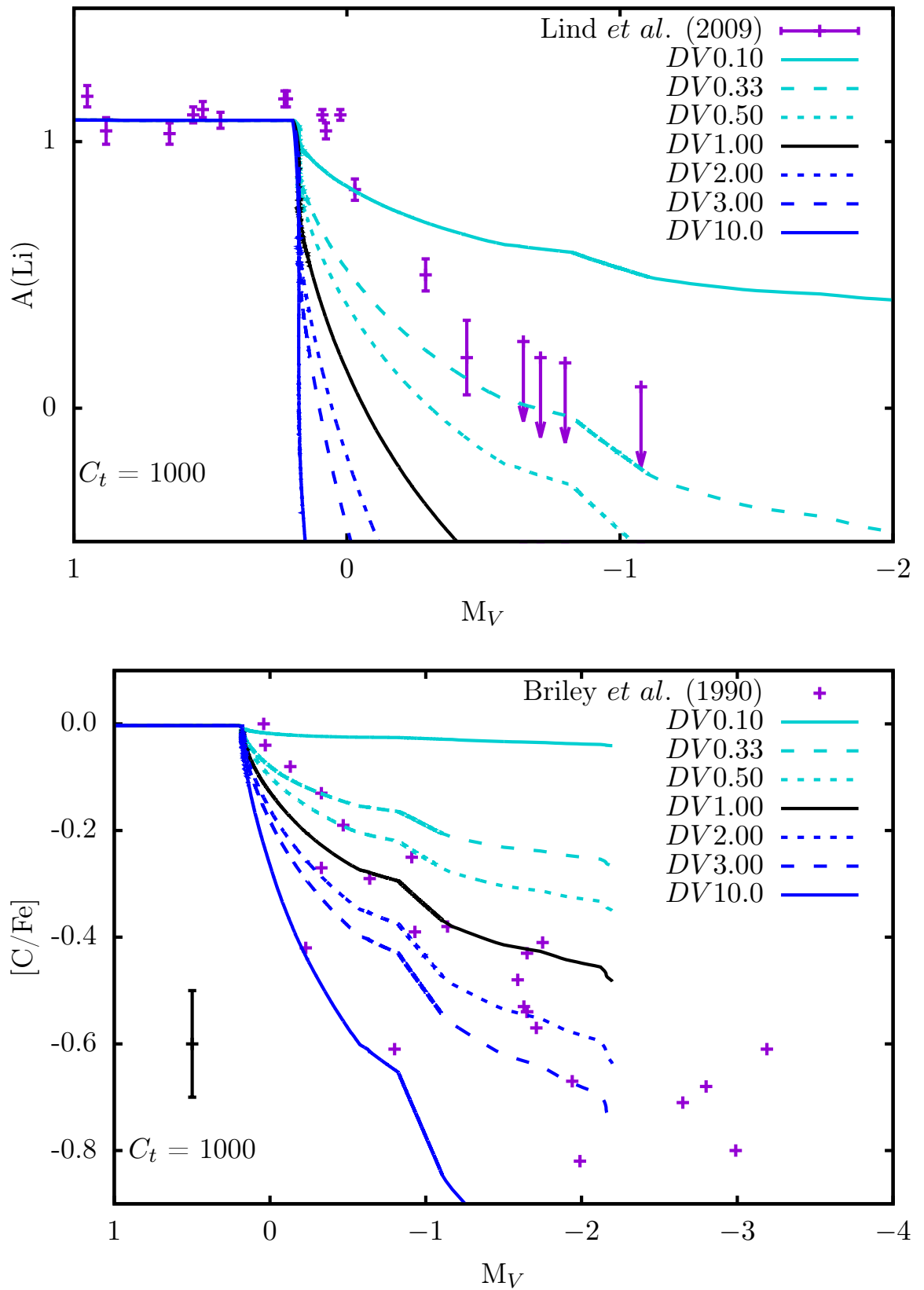


FIGURE 5.12: The effect of changing f_l and f_v to maintain constant D_t on the surface abundance profiles of $A(\text{Li})$ (top panel) and $[\text{C}/\text{Fe}]$ with a 0.1 dex error bar (bottom panel) with $C_t = 1000$. The values of f_l and f_v and colour key of the curves are in the legend of the plots. Observations are purple points, with upper limits denoted by arrows (Briley et al., 1990; Lind et al., 2009).

Case	f_v	f_l	Name
<i>DV</i>	0.10	10.0	<i>DV0.10</i>
	0.33	3.00	<i>DV0.33</i>
	0.50	2.00	<i>DV0.50</i>
	2.00	0.50	<i>DV2.00</i>
	3.00	0.33	<i>DV3.00</i>
	10.0	0.10	<i>DV10.0</i>

TABLE 5.2: Models tested in Case 2: Changing v and l to maintain constant D_t in the two stream advective mixing scheme.

Case	f_d	f_v, f_l	Name
<i>FD</i>	0.01	1,1	<i>FD0.01</i>
	0.50	1,1	<i>FD0.50</i>
	0.99	1,1	<i>FD0.99</i>

TABLE 5.3: Models tested in Case 3: Changing f_u and f_d in the two stream advective mixing scheme.

(as opposed to $f_u = f_d = 0.5$). The f_u and f_d values we tested are given in Table 5.3.

Results

Fig. 5.13 shows that modifying the up and down stream cross-sectional areas does not significantly affect the results. Indeed, only for the test *FD0.99* do we see an effect on the lithium abundance, and only towards the end of RGB evolution.

We do no further tests of modifying f_v and f_l (either independently or to maintain D_t) for varying f_d because Fig. 5.13 shows that modifying f_d does not have a significant effect on the results and we expect the same result as seen in Figs. 5.10, 5.11, and 5.12 regardless of the value of f_d .

5.3.4 Case 4: Changing the thermohaline coefficient in the diffusive mixing scheme

The results from §5.3.1, §5.3.2 and §5.3.3 show that changing the mixing length/velocity in the advective scheme cannot match our models to observations. In Chapter 3 we develop a method that can “target” (in a sense) different elements depending upon their destruction/production timescales.

Results

The number of combinations of D_t , T_{crit} , i , and o available mean that we expect a family of solutions that can simultaneously match carbon and lithium abundances to observations. An analytic multi-dimensional theory of thermohaline mixing is not available and beyond the scope of this thesis. Hence

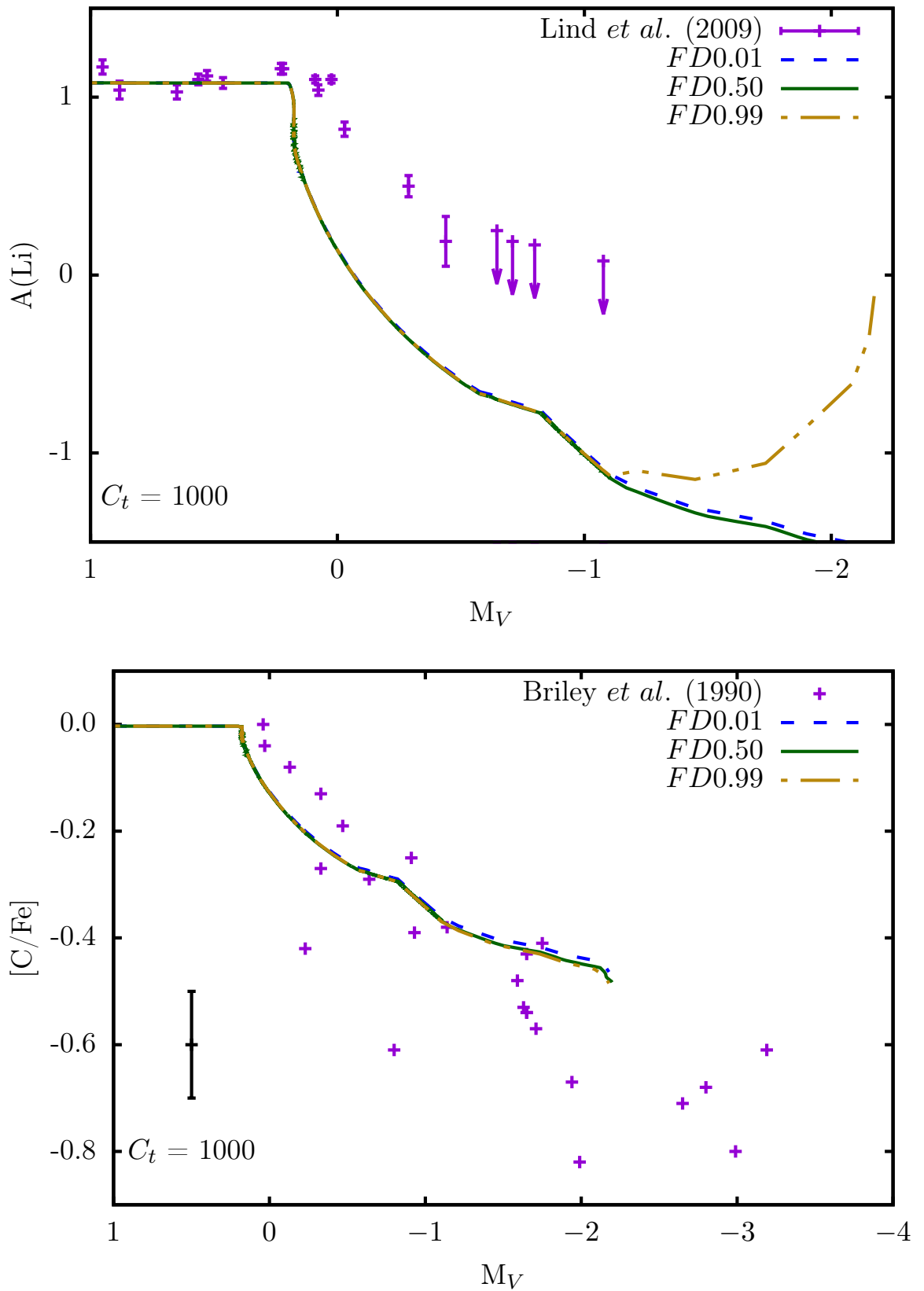


FIGURE 5.13: The effect of changing f_d on the surface abundance profiles of $A(\text{Li})$ (top panel) and $[\text{C}/\text{Fe}]$ with a 0.1 dex error bar (bottom panel) and $C_t = 1000$. The values of f_d and colour key of the curves are in the legend of the plots. Observations are purple points, with upper limits denoted by arrows (Briley *et al.*, 1990; Lind *et al.*, 2009).

in the first instance we seek solutions that are within one order of magnitude of the diffusion coefficient as found by the Ulrich/Kippenhahn 1D theory. In Figs. 5.14 and 5.15 we show one solution where $T_{\text{crit}} = 8\text{MK}$, $i = 3.0$ and $o = 0.1$. We could certainly generate a better fit, but since the modification we used is purely phenomenological we feel that this would not add any insights. The present result tells us that to match both carbon and lithium simultaneously we need faster mixing in hot regions and slower mixing in cooler regions.

Evolution code vs nucleosynthesis code

We now briefly discuss the different mixing formalisms employed in MONSTAR and MONSOON and the effect that this has on the results presented thus far.

We remind the reader that the main purpose of MONSTAR is to compute the structure of the star and to only determine abundances of elements that are associated with predominant nucleosynthetic processes (i.e., pp chain and CNO cycling). MONSOON however uses the stellar structure calculated by MONSTAR and performs more detailed calculations of mixing and burning using a reaction network that is much more comprehensive than the network included in MONSTAR. This causes small differences in the calculated abundances of elements when all properties of the stellar model (e.g., mass) are equal.

The stellar models in Cases 1-3 (investigating changes to f_v , f_l , and f_d) were run using MONSTAR and then post-processed using MONSOON whereas Case 4 (adding an additional temperature dependence) was not post-processed with MONSOON. Therefore Cases 1-3 were investigating the advective thermohaline mixing scheme, unlike Case 4, which was investigating the diffusive scheme. To explain this further, the mixing schemes in each code are different therefore the evolution of the surface abundances is different (as explained above). A comparison between the evolution and nucleosynthesis codes is shown in Fig. 5.16 and shows that the diffusive scheme in MONSTAR is more efficient at destroying carbon and lithium than the advective scheme in MONSOON. This does not affect the conclusions of this study, but we ask the reader to note these differences.

5.4 Discussion and Conclusions

We have modified the thermohaline mixing model to be able to match lithium and carbon abundances to observations of NGC6397 red giants. We do this by adding an additional temperature dependence to the thermohaline diffusion coefficient. The final conclusions of the analysis are that our successful model proposes mixing that is faster in hotter regions and slower in cooler.

The effect of our modification to the standard theory is to facilitate the Cameron-Fowler mechanism thus reducing the decline of the lithium surface abundance. Our model achieves this by removing beryllium faster

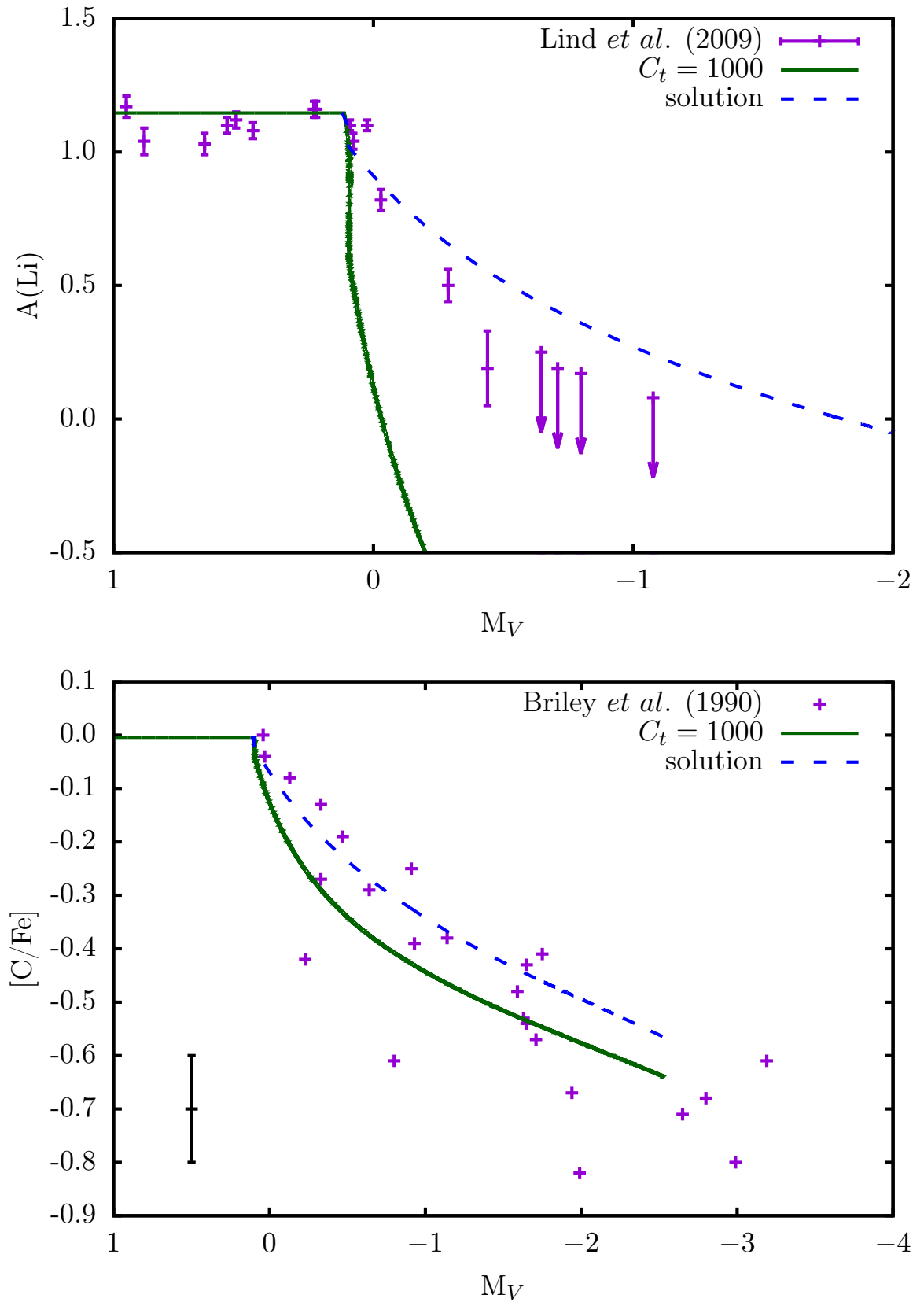


FIGURE 5.14: Top panel: Theoretical surface lithium abundances (curves) compared to observations with errors (purple points, Lind *et al.*, 2009). Bottom panel: Theoretical carbon abundances (curves) compared to observations with a 0.1 dex error bar (purple points, Briley *et al.*, 1990). In each panel the dark green curve is when the thermohaline mixing free parameter C_t is 1000. The blue curve is one solution with $T_{\text{crit}} = 8\text{MK}$, $i = 3.0$, and $o = 0.1$.

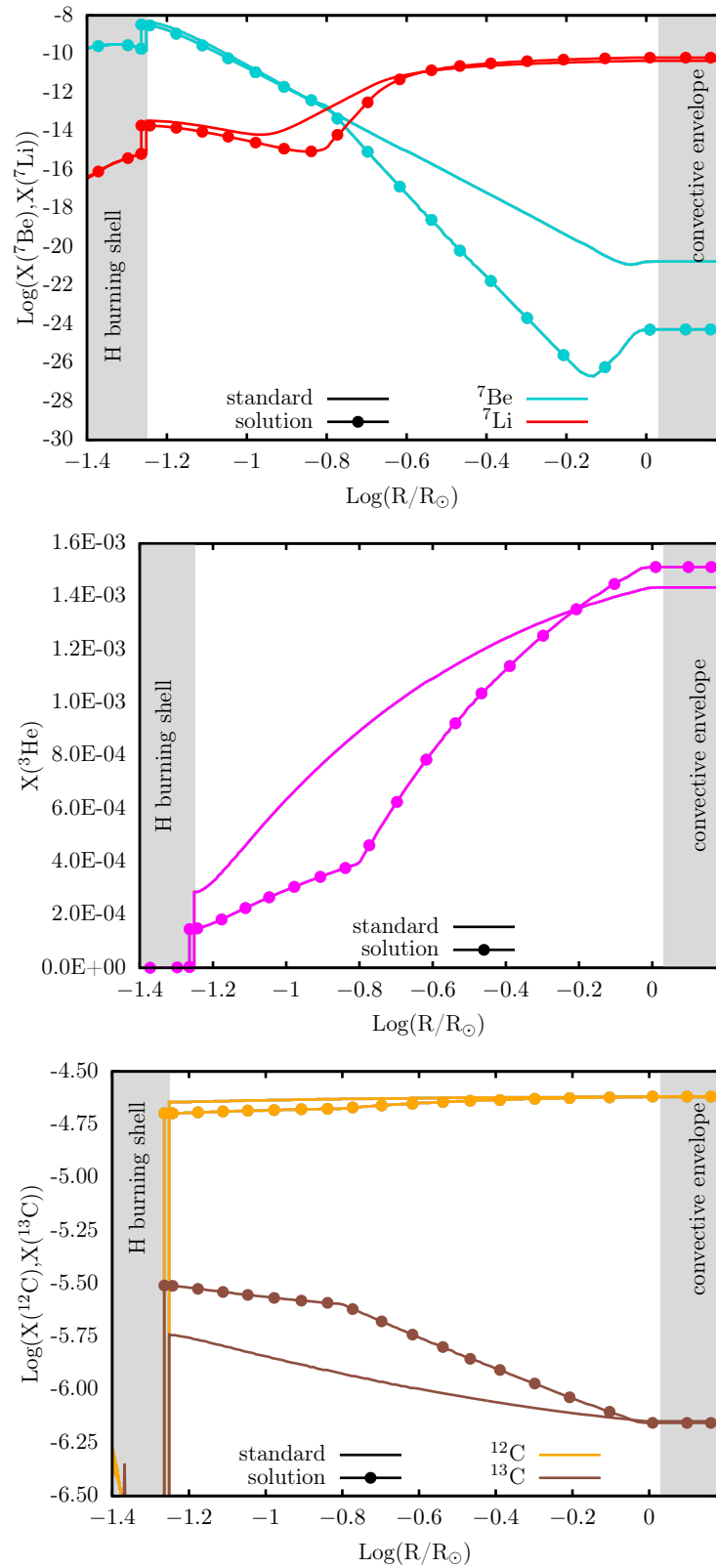


FIGURE 5.15: Abundance profiles for $f = 1$ standard case (solid curves), and one solution where $T_{\text{crit}} = 8\text{MK}$, $i = 3.0$ and $o = 0.1$ (filled circles). Top panel: ^7Li (red) and ^7Be (turquoise). Bottom panel: ^{12}C (orange) and ^{13}C (burundy).

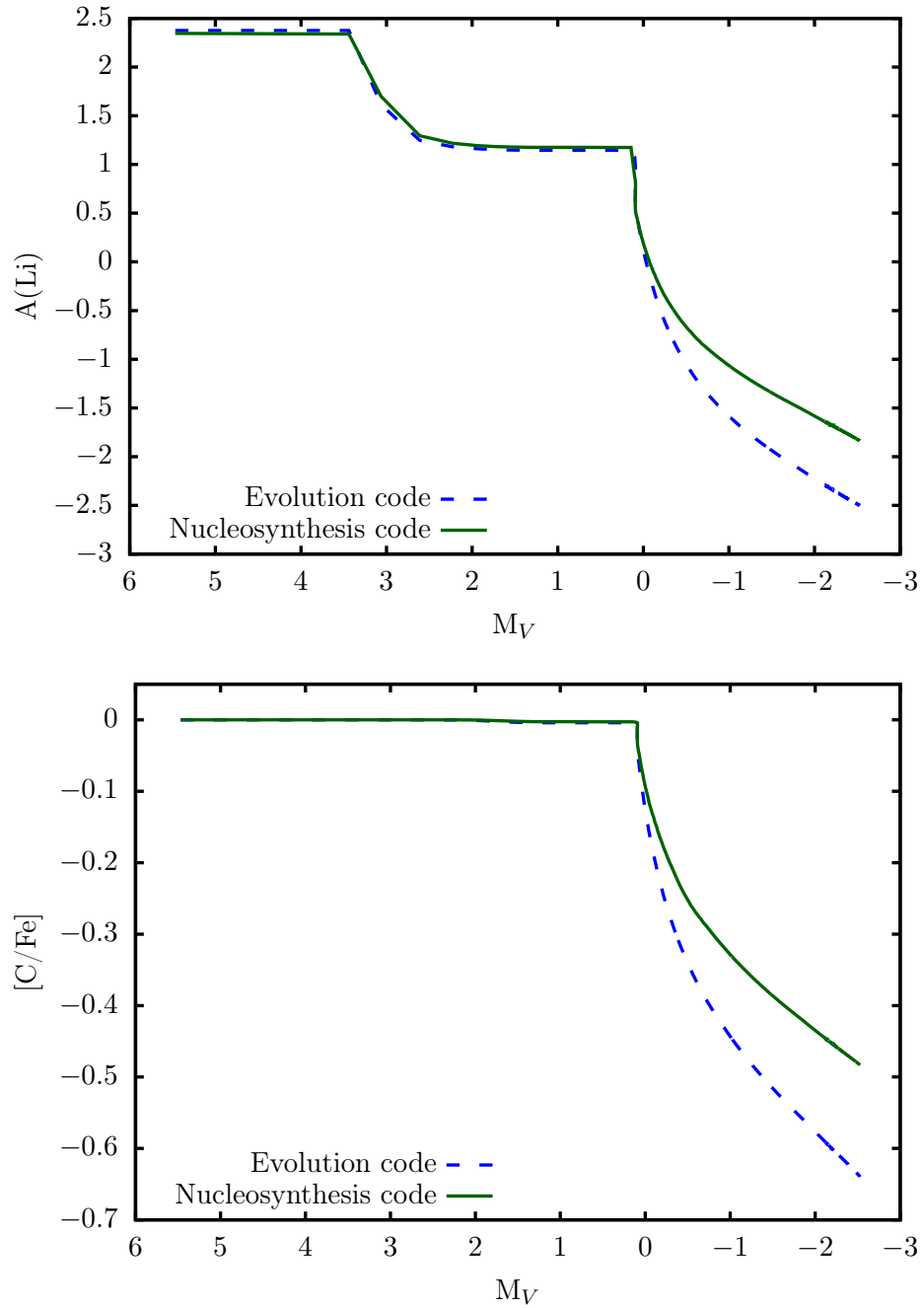


FIGURE 5.16: Theoretical surface lithium (top panel) and carbon (bottom panel) abundances vs absolute visual magnitude. In each panel the blue dashed curve is the surface value from the evolution code MONSTAR and the dark green curve is the surface value from the nucleosynthesis code MONSOON. The model is a $0.79 M_{\odot}$, $Z = 0.000246$ star with $C_t = 1000$, $f_v = f_l = 1$, and $f_d = 0.5$.

from the vicinity of the H shell and allowing it to remain longer in the outer part of the radiative zone (where it captures an electron to produce lithium). A similar effect can be obtained when one uses a constant diffusion coefficient, which was shown by Denissenkov and Vandenberg (2003).

Our successful method presumably results in a number of non-unique solutions because of the size of the parameter space available. Despite this success, there are caveats that must be noted. Our model is 1D and subject to the uncertainties and limitations that are inherent in all stellar evolution modelling (e.g., Karakas and Lattanzio, 2014). Also, we are adding an additional temperature dependence that is not yet driven by physics. There may be physics in the 1D theory derived by Ulrich (1972) and Kippenhahn, Ruschenplatt, and Thomas (1980) that could drive such an extra temperature dependence that has not been identified. This is an avenue for further research and beyond the scope of this thesis.

Modifying our advective scheme mixing length and velocity parameters independently (producing a change in D_t) and dependently (maintaining constant D_t) could not simultaneously match carbon and lithium for the same set of parameters. Our advective regime, unlike a diffusion equation, does not mix along a composition gradient and all elements present in the mixing regions are carried in the streams with the same velocity as the streams themselves. Fast mixing and long mixing lengths (high f_v and f_l respectively) result in increased depletion of both carbon and lithium on the surface because they, and all other elements in the mixing region, are brought down more quickly to high-temperature regions where they are burnt. Changing the velocity of the streams and/or the mixing length does not affect certain elements differently to others, therefore carbon and lithium are depleted more when the velocity and mixing length are increased (and vice versa when the mixing velocity and length are decreased). This is the limitation of this method and is the main reason why it is unsuccessful. Indeed, the standard diffusion implementation also fails because it shows these characteristics.

We look to results from multi-dimensional studies to inform 1D stellar modelling. The theory derived by Ulrich (1972) is one-dimensional. Further, it cannot adequately constrain the aspect ratio (α in Equation 2.37) of the fingers. Studies using 3D simulations of surface (Robinson et al., 2003; Steffen, Freytag, and Ludwig, 2005; Collet, Asplund, and Trampedach, 2007) and interior (Stancliffe et al., 2011; Ohlmann et al., 2017) convection zones in stars have found that the upstream velocity is slower and the cross-sectional area of the upstream flow is larger than the respective values for the downstream, i.e. $v_u < v_d$ and $f_u > f_d$. These effects do not appear in the standard theory.

Multi-dimensional simulations of thermohaline mixing have also been performed. The 2D simulations of Denissenkov (2010) show that fingers (corresponding to $\alpha \sim 7$) of material arise in the oceanic thermohaline environment but blobs with $\alpha \sim 0.5$ occur in the RGB case. Denissenkov (2010) achieved fingers of material (with $\alpha > 1$) in their RGB case only for highly viscous environments (viscosities that are 4 orders of magnitude higher than in real RGB stars). Garaud and Brummell (2015) found shearing in

their 2D simulations when the Prandtl number⁵ was less than 0.5 that was not seen in their 3D simulations, and concluded that for sufficiently low Prandtl numbers, 3D models are necessary to resolve the thermohaline environment.

Several other 3D simulations of thermohaline mixing have been conducted in recent years (Denissenkov and Merryfield, 2011; Traxler, Garaud, and Stellmach, 2011a; Brown, Garaud, and Stellmach, 2013; Medrano, Garaud, and Stellmach, 2014; Garaud and Brummell, 2015). Denissenkov and Merryfield (2011) compared their 3D work to the 2D simulations of Denissenkov (2010) and confirmed the results from the 2D simulations, as well as finding the excitation of gravity waves in their oceanic case but not their RGB case. Secondary instabilities (e.g., gravity waves) triggered by thermohaline mixing have been found by other groups (Traxler, Garaud, and Stellmach, 2011a; Garaud and Brummell, 2015). Three-dimensional simulations show that the shape of the thermohaline fingers changes as conditions come closer to representing real stellar conditions (i.e. as the Prandtl number decreases), with the thermohaline fingers becoming more like blobs (Traxler, Garaud, and Stellmach, 2011a). Subsequent studies found that thermohaline fingers became blobs over time (Brown, Garaud, and Stellmach, 2013; Medrano, Garaud, and Stellmach, 2014; Garaud and Brummell, 2015).

In all of the multi-dimensional thermohaline mixing simulations above, the sizes of the down and upstreams were approximately equal to each other, and we found from our 1D study no significant effect when the stream size was altered. However, the simulated stellar environments are not entirely representative of the conditions in real stars. Real stars are likely to be much more turbulent because the Prandtl number is extremely small in reality ($\sim 10^{-6}$) compared to simulations, which typically have Prandtl numbers $\sim 0.1 - 0.01$ (Traxler, Garaud, and Stellmach, 2011a; Brown, Garaud, and Stellmach, 2013; Garaud and Brummell, 2015). Additionally, the density ratio, the ratio of the (stabilising) entropy gradient to the (destabilising) compositional gradient, in simulations is generally ~ 1.1 and much lower than the RGB value of 1.7×10^3 (Traxler, Garaud, and Stellmach, 2011a; Brown, Garaud, and Stellmach, 2013; Garaud and Brummell, 2015). Brown, Garaud, and Stellmach (2013) found that a density ratio of 1.1 resulted in larger, convective-like plumes, whereas a more turbulent environment with a density ratio of 3 was more finger-like, indicating that the density ratio in real RGB stars could produce fingers of material as opposed to blobs.

It is clear that we do not yet adequately understand the thermohaline mechanism. Additionally, to provide theoretical stellar models sufficient (observational) constraints, more observations of both carbon and lithium in globular cluster red giants are needed for stars in the same cluster (other than NGC6397) covering a range in metallicity. This will help us to determine what the implementation we used to match models to NGC6397 is telling us about necessary modifications to the standard theory.

⁵The Prandtl number is defined as the ratio of the viscosity and the thermal diffusivity of a fluid, and is typically given by the formula $Pr = \nu/k_T$ (Garaud and Brummell, 2015).

Chapter 6

Thermohaline mixing in extremely metal-poor stars

The content in this chapter is published in Henkel, K., Karakas, A.I., Casey, A.R., Church, R.P., and Lattanzio, J.C. (2018), “Thermohaline mixing in extremely metal-poor stars”, *Astrophysical Journal Letters*, 863, 1.

This study follows on directly from the study in Chapter 5, which investigated the evolution of the surface abundances of carbon and lithium in the globular cluster NGC6397. We compared our stellar models to observations of NGC6397 giants and found that a minor modification of the standard thermohaline theory could simultaneously match carbon and lithium abundances for the same set of parameters. In this chapter, we detail our investigation into thermohaline mixing in extremely metal-poor (EMP) stars.

EMP stars are an integral piece in the puzzle that is the early Universe, and although anomalous subclasses of EMP stars such as carbon-enhanced metal-poor (CEMP) stars are well-studied, they make up less than half of all EMP stars with $[\text{Fe}/\text{H}] \sim -3.0$. The amount of carbon depletion occurring on the red giant branch (carbon offset) is used to determine the evolutionary status of EMP stars, and this offset will differ between CEMP and normal EMP stars. The depletion mechanism employed in stellar models (from which carbon offsets are derived) is very important, however the only widely available carbon offsets in the literature are derived from stellar models using a thermohaline mixing mechanism that cannot simultaneously match carbon and lithium abundances to observations for a single diffusion coefficient. Our stellar evolution models utilise a modified thermohaline mixing model that can match carbon and lithium in the metal-poor globular cluster NGC6397. We compare our models to the bulk of the EMP star sample at $[\text{Fe}/\text{H}] = -3$ and show that our modified models follow the trend of the observations and deplete less carbon compared to the standard thermohaline mixing theory. We conclude that stellar models that employ the standard thermohaline mixing formalism overestimate carbon offsets and hence CEMP star frequencies, particularly at metallicities where carbon-normal stars dominate the EMP star population.

6.1 Introduction

EMP stars tell us about the origin and evolution of the Galaxy at the earliest times and consequently the origins of the heavy elements we see today. Studies of EMP stars are particularly useful with regards to chemical evolution and determining the progenitors of early supernovae, and allow astronomers to gain a better understanding of the nature of elusive population III stars (Placco et al., 2014). Therefore EMP star studies are very useful for understanding both stellar and galactic evolution.

EMP stars can be further categorised based upon their abundances. Carbon enhanced metal-poor (CEMP) stars have an elemental carbon abundance of $[C/Fe] > +0.7$ (Aoki et al., 2007) and comprise 10-20% of all EMP stars with $[Fe/H] \lesssim -2.0$ (Norris et al., 2013). Placco et al. (2014) find this frequency increases to 43% for stars with $[Fe/H] \leq -3.0$ and 100% for stars with $[Fe/H] \leq -5.0$. The dominant subclass of CEMP stars are CEMP-s stars (enriched in *s*-process elements), which comprise around 80% of all CEMP stars (Aoki et al., 2007). Another category of EMP stars is that of nitrogen enhanced metal-poor (NEMP) stars (Pols et al., 2009).

On the Red Giant Branch (RGB), low-mass stars ($LMS, \lesssim 2.5 M_{\odot}$) exhibit signs of mixing beyond the inner boundaries of their convective envelopes. This produces a decline in the surface abundance of carbon ($[C/Fe]$) and $^{12}C/^{13}C$ (Briley et al., 1990; Gilroy and Brown, 1991; Gratton et al., 2000; Smith and Martell, 2003; Martell, Smith, and Briley, 2008) and lithium (Lind et al., 2009), and an increase in the nitrogen abundance (Gratton et al., 2000). The effects of extra mixing are observed in LMS in open and globular clusters, though the decline of surface abundances is steeper at lower metallicity (Gratton et al., 2000; Aoki et al., 2007).

There are a number of postulated explanations for extra mixing, and thermohaline mixing (Ulrich, 1972; Kippenhahn, Ruschenplatt, and Thomas, 1980) is one popular theory (for others see Denissenkov, Pinsonneault, and MacGregor, 2009; Denissenkov, 2012; Lagarde et al., 2012b; Karakas and Lattanzio, 2014). Thermohaline mixing is driven by the molecular weight inversion created by the reaction ${}^3\text{He}({}^3\text{He}, 2p){}^4\text{He}$ reaction that occurs just above the hydrogen shell, where temperatures are sufficient for ${}^3\text{He}$ destruction but are too low for significant contributions from the p+p or CNO cycle reactions (Denissenkov and Herwig, 2004; Eggleton, Dearborn, and Lattanzio, 2006; Charbonnel and Zahn, 2007). The decrease in molecular weight is so small that it can only drive mixing in a region that has been completely homogenised, e.g. by first dredge-up (FDU). The depth of FDU reduces as metallicity decreases, therefore the location of the molecular weight inversion is further out in mass in low-metallicity stars but at similar temperatures to stars of higher metallicity (Church et al., 2014). However the temperature gradient in low-metallicity stars is not as steep as in stars of higher metallicity, and temperatures are consequently higher in the thermohaline region at low metallicities. This produces a steeper decline in abundances, which matches observational trends (an effect also seen in other theoretical stellar models, e.g. Charbonnel and Zahn, 2007).

A problem encountered when invoking thermohaline mixing as the extra mixing mechanism on the RGB is the inability to simultaneously match carbon and lithium abundances for a single diffusion coefficient value (Angelou et al., 2015). Although observations of both carbon and lithium abundances strongly constrain the extra mixing mechanism occurring on the RGB, due to their different burning temperatures, many previous studies analysed only one of these abundances. Henkel, Karakas, and Lattanzio (2017) overcome this problem for the first time by using a phenomenological modification of thermohaline mixing that invokes faster mixing in the hotter part of the thermohaline region and slower mixing in the cooler part. They match their stellar models to observations of the metal-poor ($[\text{Fe}/\text{H}] \sim -2.0$) globular cluster NGC6397 (Gratton et al., 2003).

The amount of carbon depletion due to extra mixing, also called the “carbon offset”, increases as a star evolves up the RGB and is therefore a function of evolutionary stage (Placco et al., 2014). Theoretical offsets, the magnitude of which are dependent upon evolutionary status ($\log g$), are applied to red giant surface abundances to recover initial (pre-RGB) carbon abundances. Applying offsets to a population of stars allows us to derive the frequency of stars that were born with carbon abundances high enough to be classified as CEMP stars, even though the star’s current carbon abundance may not be in the CEMP star range. Offsets at a given $\log g$ are determined according to $[\text{C}/\text{Fe}] = [\text{C}/\text{Fe}]_{\text{initial}} - \text{offset}$. Observers therefore require theoretical models for information on these offsets, yet there are few low-metallicity, low-mass stellar models that include a thorough study of the effects of extra mixing. Existing low-metallicity stellar model grids include Stancliffe et al. (2009), Lagarde et al. (2012b), and Placco et al. (2014).

The models of Stancliffe et al. (2009) were computed using the STARS evolution code and include the thermohaline prescription of Ulrich (1972) and Kippenhahn, Ruschenplatt, and Thomas (1980). The equation for the thermohaline diffusion coefficient is given by

$$D_t = C_t K(\phi/\delta) \frac{-\nabla_\mu}{(\nabla_{\text{ad}} - \nabla)}, \quad (6.1)$$

where all variables have their usual meaning, and the dimensionless parameter, C_t , is treated as a free parameter. Stancliffe et al. (2009) use $C_t = 1000$, following Charbonnel and Zahn (2007). Placco et al. (2014) also use the STARS code and include thermohaline mixing according to Stancliffe et al. (2009). Although Stancliffe et al. (2009) acknowledge that surface lithium decreases due to extra mixing, both Stancliffe et al. (2009) and Placco et al. (2014) focus their discussions on CEMP stars and consequently perform analyses of carbon and nitrogen abundances only. Additionally, Placco et al. (2014) shift their theoretical models by $\log g = 0.5$ to make the observed and theoretical locations of extra mixing coincide. Lagarde et al. (2012b) utilise the Ulrich/Kippenhahn thermohaline mixing implementation described in Charbonnel and Zahn (2007) with $C_t = 1000$. Although Lagarde et al. (2012b) do not discuss surface abundance changes, Charbonnel and Zahn (2007) analyse their theoretical surface abundances of lithium, carbon, and nitrogen and compare to field stars (Gratton et al.,

2000). Their models match carbon but other elements are not well explained, e.g. lithium, which is depleted too much in stellar models compared to the observations.

Although available, large grids of metal-poor stellar models are often coarse in metallicity and fail to adequately model the bulk of the EMP star sample at relevant metallicities. Consequently, observers must either derive empirical relations to determine the carbon offset for low-metallicity stars or use online resources such as the tool developed by Placco et al. (2014). This tool for determining carbon offsets for a given set of stellar parameters is based on stellar evolution models that employ the standard thermohaline mixing mechanism. It has been shown that the standard formalism cannot simultaneously match carbon and lithium abundances at metallicities where “normal” EMP stars dominate the population (i.e. stars that show no carbon or nitrogen enhancement with $[\text{Fe}/\text{H}] > -3$, Norris et al., 2013; Placco et al., 2014; Henkel, Karakas, and Lattanzio, 2017). This will affect the carbon offsets and hence the inferred frequency of CEMP stars in the Galaxy.

We apply the methodology of Henkel, Karakas, and Lattanzio (2017) to a subsample of EMP stars from the Stellar Abundances for Galactic Archeology (SAGA) database (Suda et al., 2008). The SAGA database includes thousands of EMP stars, many of which have carbon, nitrogen, and lithium abundances.

6.2 Theoretical models

We compute our stellar models using MONSTAR, the Monash version of the Mt. Stromlo stellar evolution code, and refer to Henkel, Karakas, and Lattanzio (2017) for a detailed description of the code and input physics. Stellar models are evolved from before the zero-age main sequence (Hayashi track) to the helium flash.

We select carbon-normal EMP dwarfs and giants from the SAGA database that have both carbon and lithium observations and find that they have an average metallicity of $[\text{Fe}/\text{H}] \sim -3$ (metallicity range of sample is -3.5 to -2.5). Therefore to allow meaningful comparisons with these observations we adopt $[\text{Fe}/\text{H}] = -3$. We use Asplund et al. (2009) scaled solar abundances (with the exception of initial $[\text{C}/\text{Fe}]$) and an alpha-element enhancement $[\alpha/\text{Fe}] = 0.4$ according to the $[\alpha/\text{Fe}]$ - $[\text{Fe}/\text{H}]$ observational trend shown in Fig. 1 of Yong et al. (2016).

We construct stellar models with mass $0.8M_{\odot}$ and $Y = 0.24$, which produces main sequence turn-off (MSTO) and RGB tip ages of 13.2 and 14.1 Gyrs respectively. Following Henkel, Karakas, and Lattanzio (2017) we include convective overshoot according to Herwig et al. (1997) and adopt an overshoot factor $f_{\text{OS}} = 0.14$ at the formal border of convective regions (defined by the Schwarzschild criterion).

To adequately cover the spread of carbon abundances in the stellar subsample, we test four initial $[\text{C}/\text{Fe}]$ abundances: $[\text{C}/\text{Fe}] = -0.5, 0, +0.3,$ and $+0.5$. For each initial carbon abundance, we compare our modified

thermohaline mixing scheme that includes a phenomenological temperature dependence (Henkel, Karakas, and Lattanzio, 2017) to a standard case using the unmodified thermohaline diffusion coefficient equation as derived by Ulrich (1972) and Kippenhahn, Ruschenplatt, and Thomas (1980) with $C_t = 1000$. By implementing the modification to the standard formalism detailed in Henkel, Karakas, and Lattanzio (2017), we facilitate the Cameron-Fowler mechanism (Cameron and Fowler, 1971) for producing ${}^7\text{Li}$ in stars by bringing ${}^7\text{Be}$ from hotter to cooler regions. This is why our modified models deplete less lithium than the standard thermohaline models but still deplete carbon as required by the observations.

6.3 Results

The standard thermohaline mixing model cannot reproduce the downturn in $[\text{C}/\text{Fe}]$ as shown in Fig. 6.1 (we discuss the stars in red in §6.4). Our modified models do not evolve to the low lithium abundances that the standard models do, and do not match the observed stars with $A(\text{Li}) < 0$. Stars with abundances as low as the standard models with $A(\text{Li}) \lesssim -1$ are not seen in the observed data, however this could be a selection effect or bias towards stars with higher lithium abundances.

Fig. 6.2 shows that the models with the highest initial carbon abundances are a better match to the observations, and this is expected due to the population being enhanced in α -elements. However we limited our selection of stars to those from Fig. 6.1 with carbon isotopic observations. Due to the limited number of stars with carbon isotopic observations and a possible bias towards stars with higher $[\text{C}/\text{Fe}]$, it is difficult to confidently conclude which model best matches the data.

Although the nitrogen abundances of our solution models do not differ from the standard models significantly, as shown in Fig 6.3, they cover the range of nitrogen observations (when NEMP stars are not considered). The difference between the modified and standard models (for a given initial carbon) is indistinguishable because nitrogen reaches saturation and is unaffected by differences in the mixing mechanism. Indeed, we can achieve a better fit to the nitrogen observations if initial nitrogen is decreased from 0 to -0.5 (shown by the green curve in Fig. 6.3), but this does not alter our conclusions.

6.4 Discussion

Our modified thermohaline mixing models match the observed rate of carbon depletion in metal-poor stars in the $[\text{C}/\text{Fe}]-A(\text{Li})$ plane (Fig. 6.1). This is because our modified models induce mixing that is faster in the hotter region of the thermohaline zone and slower in the cooler part (for more details, see Henkel, Karakas, and Lattanzio, 2017).

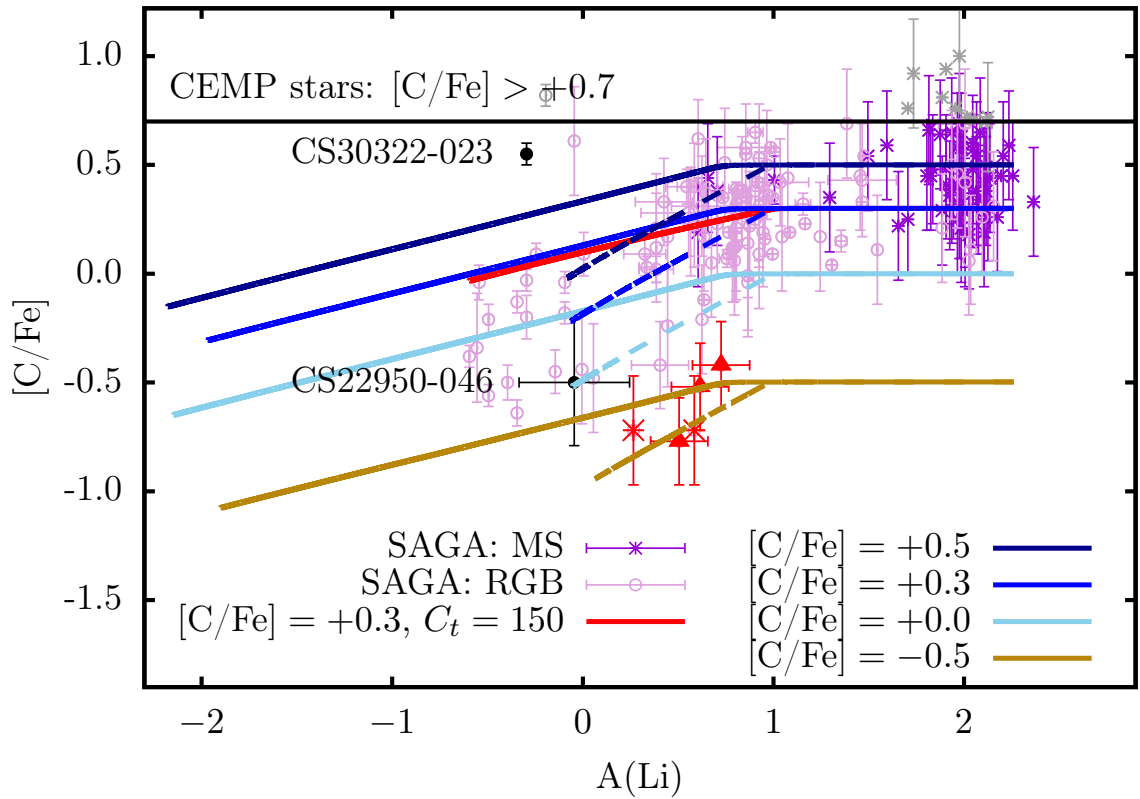


FIGURE 6.1: $[C/Fe]$ as a function of $A(Li)$ for our standard and modified thermohaline mixing models with four initial carbon abundances. Observations are from the SAGA database (Suda et al., 2008) with the exception of CS22950-046 (Johnson et al., 2007) and CS30322-023 (the strength of the CN band is due to an overabundance of nitrogen according to Masseron et al., 2006, and should therefore be classified as a NEMP star). The stars in red are discussed further in the text. The criterion for CEMP stars (Placco et al., 2014) is indicated, and stars that satisfy the criterion are shown in grey. For all models, the thermohaline mixing free parameter $C_t = 1000$ except for the red curve where $C_t = 150$ and initial $[C/Fe] = 0.3$. Standard thermohaline models are shown with solid lines, and results with the modified algorithm of Henkel, Karakas, and Lattanzio (2017) are shown with dashed lines.

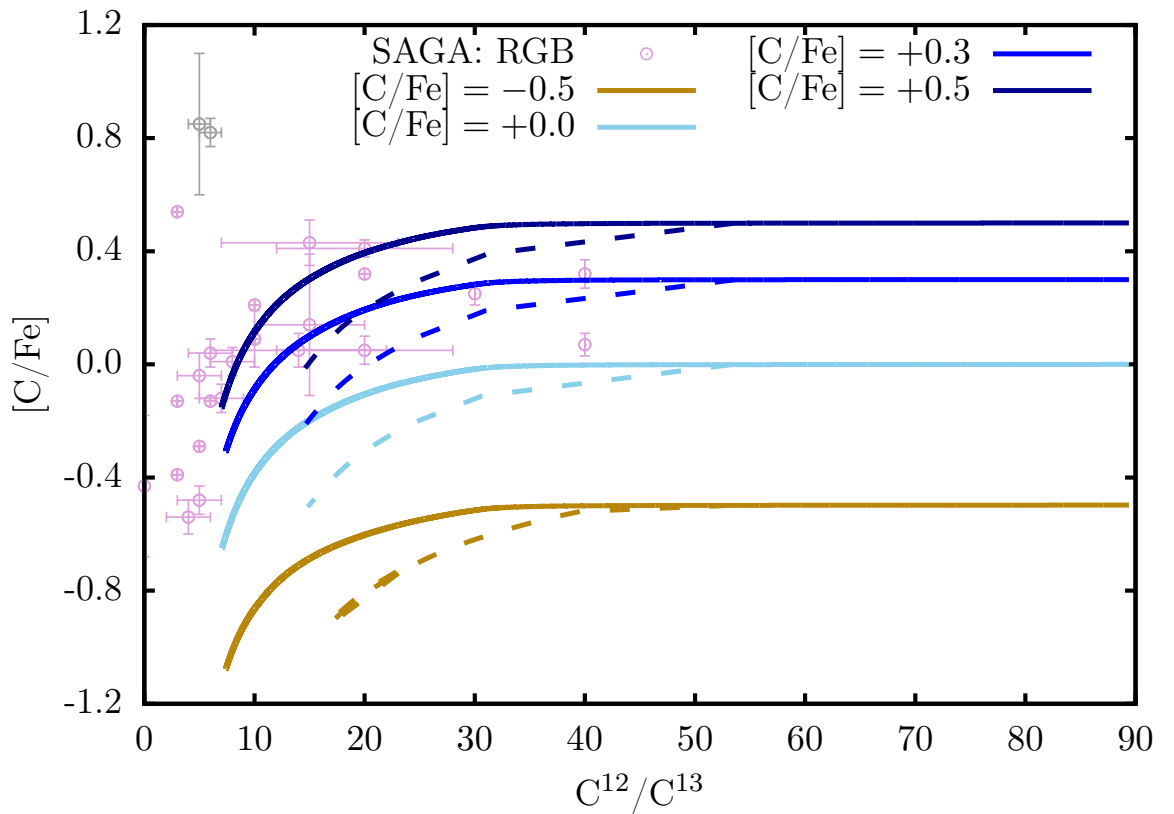


FIGURE 6.2: $[C/Fe]$ as a function of $^{12}C/^{13}C$ for our standard and modified thermohaline mixing models with four initial carbon abundances (details are given in the legend). The stars are those in Fig. 6.1 that have carbon isotopic observations in the SAGA database (Suda et al., 2008). The stars that satisfy the CEMP star criterion (Placco et al., 2014) are shown in grey. Standard thermohaline models are shown with solid lines, and results with the modified algorithm of Henkel, Karakas, and Lattanzio (2017) are shown with dashed lines.

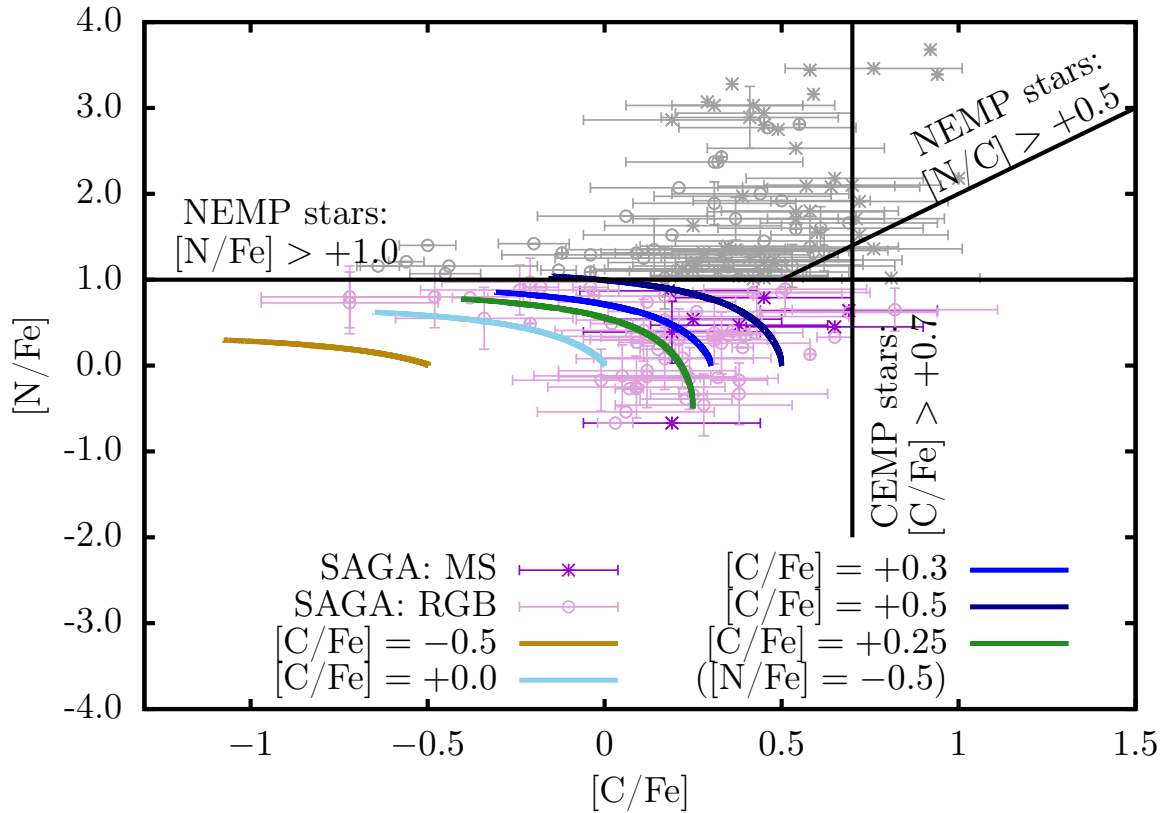


FIGURE 6.3: $[N/Fe]$ as a function of $[C/Fe]$ for our standard (solid lines) and modified (dashed lines) thermohaline mixing models with four initial carbon abundances (details are given in the legend). Initial $[N/Fe] = 0$ for all models except where indicated in the legend. The standard and modified models overlap because nitrogen has reached saturation. Observations are from the SAGA database (Suda et al., 2008). The criteria for NEMP (Pols et al., 2009) and CEMP (Placco et al., 2014) stars are shown by the solid lines, and stars that satisfy either criterion are shown in grey.

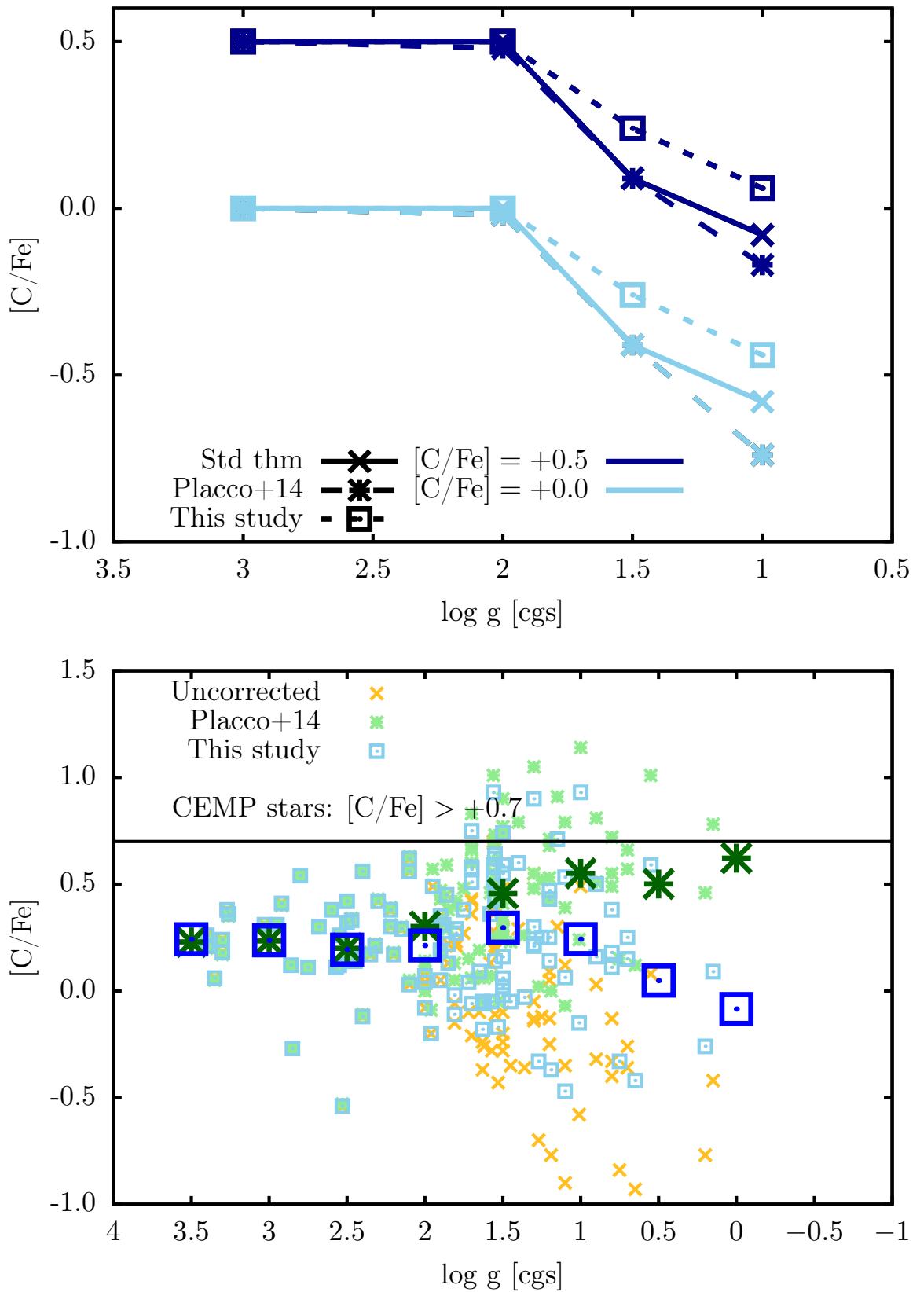


FIGURE 6.4: Top panel: The predicted carbon abundance after applying the carbon offsets from the models used in this paper and those of (Placco et al., 2014) for two of our initial carbon abundances (details are given in the legend). Bottom panel: Carbon as a function of $\log g$ of the giant stars in Fig. 6.1 where the uncorrected carbon abundances are orange crosses, carbon abundances with the offset of Placco et al. (2014) are green asterisks, and the abundances with the offsets from this study are blue squares. The large symbols are averages in $\log g$ bins (at the $\log g$ value of the symbol ± 0.25) and the symbol colour and shape correspond to the observations in the legend. The CEMP star criterion is indicated (Placco et al., 2014).

An issue with implementing thermohaline mixing as the extra mixing mechanism is the requirement for different diffusion coefficient (or C_t) values to match carbon and lithium abundances (Angelou et al., 2015; Henkel, Karakas, and Lattanzio, 2017). Henkel, Karakas, and Lattanzio (2017) match carbon and lithium abundances for a single value of C_t ($C_t = 1000$) for NGC6397 giants with $[\text{Fe}/\text{H}] \sim -2$, however there is no theoretical or observational indication as to whether this is a suitable value of C_t for this sample of EMP stars. Ideally, to determine if a single value of C_t is suitable, we require carbon and lithium abundances as a function of luminosity or absolute magnitude, which are not available for these EMP stars. However Gaia will provide further data (e.g. magnitudes) in the near future. As a test, we determine the surface carbon and lithium abundances of a model that includes the standard thermohaline mixing formalism with $C_t = 150$ and $[\text{C}/\text{Fe}] = +0.3$ and show the results in Fig. 6.1. The model with $C_t = 150$ matches the amount of lithium depletion (unlike our modified models) but only covers the upper envelope of carbon abundances.

6.4.1 Carbon-poor/lithium rich giants

There are five metal-poor stars that have unusually low carbon for a given lithium abundance, or high lithium abundances for a given carbon abundance. These are represented by the red symbols in Fig. 6.1, namely HE1317-0407, HE2253-0849, HE2148-1105A (red filled triangles in Fig. 6.1, observed by Hollek et al., 2011), CS22956-114, and HE1320-1339 (red stars in Fig. 6.1, observed by Roederer et al., 2014). Compared to the dominant trend in the observed stars and our stellar models, these stars appear to have either (1) depleted carbon faster or (2) experienced lithium production.

There are several possible theoretical explanations for these anomalous stars:

1. The stars had lower initial carbon, say $[\text{C}/\text{Fe}] = -0.5$ (shown by the golden curves in Fig. 6.1). No dwarfs have been observed with such a low carbon composition in *this* sample. The lack of observed carbon-poor dwarfs could be explained by selection effects due to the difficulty of measuring low abundances of carbon in dwarfs that have much hotter atmospheres than their cool giant counterparts, and the bias towards observing giants that are much brighter and more numerous than dwarfs.
2. Thermohaline mixing begins on the RGB and continues during AGB evolution. For this explanation to be explicable with what we observe (i.e. normal lithium and low carbon), we require lithium production by either internal mechanisms such as deep mixing (e.g. Stancliffe, 2010; Lattanzio et al., 2015) or external mechanisms such as binary interactions.

After taking into consideration the sources of error that are inherent in deriving abundances from cool evolved stars, we are satisfied that our models match the upper envelope of these anomalous stars. Although beyond the scope of this letter, these stars should be the subject of further investigation.

[C/Fe]	0.5	0.00 0.00 (0.00)	0.00 0.00 (0.02)	0.26 0.41 (0.39)	0.44 0.58 (0.67)
	0.3	0.00 0.00 (0.00)	0.00 0.00 (0.02)	0.26 0.41 (0.41)	0.44 0.58 (0.69)
	0.0	0.00 0.00 (0.00)	0.00 0.00 (0.02)	0.26 0.41 (0.41)	0.44 0.58 (0.74)
	-0.5	0.00 0.00	0.00 0.00	0.25 0.40	0.43 0.57
		3.0	2.0	1.5	1.0
log g [cgs]					

TABLE 6.1: Carbon abundance offsets in $\log g$ -[C/Fe] space with $[\text{Fe}/\text{H}] = -3$ and $[\text{N}/\text{Fe}] = 0.0$. The bolded values are from our modified models, the unbolded values are from our standard models, and the corresponding theoretical offsets from Fig. 10 of Placco et al. (2014) are in brackets. Placco et al. (2014) do not show results for an initial carbon abundance of $[\text{C}/\text{Fe}] = -0.5$ in their Fig. 10 therefore we do not show their results for this initial [C/Fe] value.

6.4.2 Theoretical carbon offsets

We now compare the offsets from our models to the theoretical carbon offsets determined by Placco et al. (2014, detailed in their Fig. 10). The carbon offsets of Placco et al. (2014) are derived from a grid of 210 models varying in metallicity, initial [C/Fe], and initial [N/Fe], with $C_t = 1000$, and we refer to their paper for a detailed description of their method for determining offsets. Our models in comparison do not vary in metallicity or initial [N/Fe], therefore we only compare to the models of Placco et al. (2014) that match our initial stellar parameters. We note that Placco et al. (2014) compute models at $[\text{Fe}/\text{H}] = -1.3, -2.3, -3.3,$ and -4.3 , not at our chosen metallicity ($[\text{Fe}/\text{H}] = -3$). The results for initial $[\text{C}/\text{Fe}] = +0.0$ and $+0.5$ are shown in the top panel of Fig. 6.4, and results for all initial carbon abundances are in Table 6.1.

Our carbon offsets become larger in magnitude with decreasing $\log g$ (evolution up the giant branch), which is a trend also seen by Placco et al. (2014) and expected from normal RGB evolution. Additionally, our offsets are typically lower than those of Placco et al. (2014). This is because our modified models destroy less carbon on the RGB than models with the standard thermohaline mixing formalism. As our models are a better fit to the observations, we infer that carbon-normal EMP stars at this metallicity destroy less carbon than predicted by the standard theory. Therefore, our offsets should be preferred when inferring the initial carbon abundance of an individual observed star at relevant metallicities.

6.4.3 CEMP star frequency

Finally, we apply our carbon offsets and the offsets of Placco et al. (2014) to the data in Fig. 6.1 and determine the frequency of CEMP stars. To do this, we linearly interpolate in $[C/Fe]$ and $\log g$, and apply the offset to the observed data to yield “corrected” abundances (i.e. inferred birth abundances). We then take the average of the abundances in $\log g$ bins, and in the bottom panel of Fig. 6.4 we plot the uncorrected and corrected abundances as well as the averages as functions of $\log g$. The corrected distribution should be relatively flat over all $\log g$ if the correct initial carbon abundances were recovered.

The bottom panel of Fig. 6.4 shows that the data with our offsets produce a flatter trend than the offsets of Placco et al. (2014) because our carbon corrections are smaller at low surface gravities. Using the definition of CEMP as stars with $[C/Fe] > +0.7$ (Aoki et al., 2007), our offsets imply that this sample initially contained $\sim 5.2\%$ CEMP stars, whereas the offsets of Placco et al. (2014) yield $\sim 14.7\%$. Offsets derived from stellar models that include the standard formalism of thermohaline mixing overestimate the amount the carbon depletion in stars at metallicities not dominated by CEMP stars (i.e. $[Fe/H] \geq -3$), and applying such offsets will consequently yield overestimated CEMP star frequencies at these metallicities. We acknowledge however theoretical and observational CEMP star frequencies are uncertain (for more on this, see Cohen et al., 2005; Frebel et al., 2006; Collet, Asplund, and Trampedach, 2007; Pols et al., 2009; Izzard et al., 2009).

6.5 Conclusions

We have produced stellar models that employ a modification to the standard thermohaline mixing formalism on the RGB and compare our models to a subsample of EMP dwarfs and giants from the SAGA database with $[Fe/H] \sim -3$. Our modified models match observations of both the carbon and lithium abundances of the EMP stars considered.

We determine the amount of carbon depletion (carbon offset) for our theoretical models and find that our carbon offsets are lower than those of Placco et al. (2014). This suggests that the offsets suitable for this sample of EMP stars are not as large as the offsets predicted by models that include a standard thermohaline mixing implementation.

We conclude that analysis of EMP stars requires updated carbon offsets, because currently available offsets overestimate the amount of carbon depletion on the RGB and observers using such offsets will overestimate evolutionary burning and mixing. An updated CEMP star frequency has direct implications for Galactic chemical evolution and requires further investigation at varying metallicities, particularly metallicities where CEMP stars are not the dominant class of EMP stars. We also emphasise that a more statistically complete sample of low-metallicity stars is required to gain further insights into this problem.

Chapter 7

Thermohaline mixing in the Galactic disc

This chapter uses Gaia-ESO data from internal data release (iDR) 4, obtained from our collaborator Dr. Andrew Casey.

7.1 Introduction

Concurrent with a new wave of technological advancements is the prevalence of large surveys that produce extensive homogeneous data for Galactic field and cluster stars.

Large homogeneous data sets, especially chemical abundances, provide insights into many aspects of stellar evolution. This is particularly the case for the non-canonical mixing mechanism occurring after first dredge-up (FDU, Iben, 1964) on the red giant branch (RGB) of low- to intermediate-mass stars. This “extra” mixing mechanism is characterised by changes to the surface abundances of particular elements (e.g., decrease of ^{12}C and ^7Li , and an increase of ^{14}N and ^{13}C). The magnitudes of the abundance changes are dependent upon stellar mass, metallicity, and α element enhancement (discussed in Chapters 1 and 2, and in further detail below).

7.1.1 Extra mixing

The favoured mechanism adopted for this extra mixing is thermohaline mixing, which is driven by the molecular weight inversion created above the H shell by the $^3\text{He}(^3\text{He},2\text{p})^4\text{He}$ reaction (Ulrich, 1972; Kippenhahn, Ruschenplatt, and Thomas, 1980; Denissenkov and Herwig, 2004; Eggleton, Dearborn, and Lattanzio, 2006; Charbonnel and Zahn, 2007). The thermohaline diffusion coefficient is given by:

$$D_t = C_t K(\theta/\delta) \frac{-\nabla_\mu}{(\nabla_{\text{ad}} - \nabla)}, \quad (7.1)$$

where we remind the reader that K is the thermal conductivity, $\phi = (\partial \ln \rho / \partial \ln \mu)_{P,T}$, $\delta = (\partial \ln \rho / \partial \ln T)_{P,\rho}$ ($\phi = \delta = 1$ for an ideal gas), and all other symbols have their usual meanings. The dimensionless parameter

C_t is given by the formula

$$C_t = (8/3)\pi^2\alpha^2, \quad (7.2)$$

where α is formally the aspect ratio of the thermohaline mixing blobs (Ulrich, 1972; Kippenhahn, Ruschenplatt, and Thomas, 1980).

Using a single diffusion coefficient, Angelou et al. (2015) found that they could not simultaneously fit carbon and lithium observations of giants in NGC6397. In their stellar models, Henkel, Karakas, and Lattanzio (2017) overcame the problem encountered by Angelou et al. (2015) by implementing a modified thermohaline mixing scheme that increases the mixing speed of material in the hottest part of the thermohaline region and decreases the speed in the cooler part. By using this modification, Henkel, Karakas, and Lattanzio (2017) could simultaneously match the carbon and lithium abundances in NGC6397 giants for a single set of parameters (including a single value of C_t).

We have previously investigated the effectiveness and robustness of this modified scheme for the low-metallicity globular cluster NGC6397 (Henkel, Karakas, and Lattanzio, 2017) and extremely metal-poor stars in the halo field (Henkel et al., 2018). The next obvious test for this scheme is for stars with higher metallicities, i.e., the Galactic thick and thin discs.

Two examples of large, recent, ongoing surveys that provide insights into the extra mixing mechanism are the Apache Point Observatory Galactic Evolution Experiment (APOGEE, Allende Prieto et al., 2008) and the Gaia-ESO survey (GES, Gilmore et al., 2012; Randich, Gilmore, and Gaia-ESO Consortium, 2013).

7.1.2 APOGEE

APOGEE is using high-resolution, high signal-to-noise infrared (H-band) spectroscopy to survey over 100,000 red giants across the full range of the Galactic bulge, halo, and disc to a magnitude limit of $H \approx 13.5$. A recent data release, Data Release 12 (DR12), revealed that of the 146,000 surveyed stars, approximately 10.4% (15,000) are located in the bulge, 19.2% (28,000) are in the halo, and 37.7% (55,000) are in the disc (the remaining stars are located in other survey fields, including the Kepler/CoRoT fields, halo stream fields, star cluster fields, and the Sagittarius Dwarf Spheroidal Galaxy field). APOGEE measures the abundances of 15 chemical species to 0.1 dex precision, where the elements are C, N, O, Na, Mg, Al, Si, S, K, Ca, Ti, V, Cr, Fe, and Ni for most surveyed stars. The accuracy of abundances of elements measured from molecular lines (i.e., C, N, and O) are very sensitive to temperature, therefore the error inherent in the abundances of such species should be considered. This is particularly the case for stars with low metallicities ($[\text{Fe}/\text{H}] < -1$) or higher surface temperatures ($T_{\text{eff}} > 5250$ K), where the strength of molecular lines is significantly reduced (Allende Prieto et al., 2008).

We now discuss the results of recent papers that use APOGEE data that are relevant to this thesis. Using data from DR12, Masseron and Gilmore (2015)

analysed the carbon and nitrogen abundances for ~ 81000 stars that fit their criteria (signal-to-noise ratio $\text{SNR} > 100$, $T_{\text{eff}} > 4000$ K). The program stars cover the thick and thin discs (i.e., a range in $[\alpha/\text{Fe}]$ enhancement) as well as stars from the subgiant branch (pre-FDU) to the upper RGB (post-FDU and extra mixing). Alpha element ratios ($[\alpha/\text{Fe}]$), as explained in Chapter 2, are an indicator of the contribution of supernovae to the initial composition of the protostellar gas. These α element ratios do not change during stellar evolution and can therefore constrain star formation histories, where stars with higher $[\alpha/\text{Fe}]$ are predicted to have formed before stars with lower $[\alpha/\text{Fe}]$. This assumption is made because the contribution of Type II supernovae to the interstellar medium occurs before the contribution of Type Ia supernovae. This is important because the thick and thin discs are separated in $[\alpha/\text{Fe}]$, having $[\alpha/\text{Fe}] > 0.15$ and < 0.15 respectively, meaning that the thick disc theoretically formed before the thin disc. Masseron and Gilmore (2015) use the fact that the program stars cover a wide range of evolutionary stages to determine features of the discs via the $[\text{C}/\text{N}]$ and $[\alpha/\text{Fe}]$ ratios.

Theory and observations confirm that while mass, metallicity, and to a lesser degree $[\alpha/\text{Fe}]$ (discussed in more detail below), all play a role in governing a star's $[\text{C}/\text{N}]$ value, for stars with mass $< 3 M_{\odot}$, initial stellar mass is the dominant factor that governs the $[\text{C}/\text{N}]$ abundance (metallicity and α enhancement are not as significant, Charbonnel, 1994; Masseron and Gilmore, 2015; Martig et al., 2016). Masseron and Gilmore (2015) find that a gradient exists in $[\text{C}/\text{N}]$ that is proportional to α enhancement in the younger, lower- $[\alpha/\text{Fe}]$ thin disc stars, i.e., at a given metallicity, thin disc stars with lower $[\alpha/\text{Fe}]$ also have a lower $[\text{C}/\text{N}]$ as shown in Fig. 7.1. No such trend is present in the α -enhanced thick disc stars, which are observed to have a lower $[\text{C}/\text{N}]$ than their thin disc counterparts. This is not in agreement with other studies that have shown that canonical extra mixing is more efficient in lower metallicity, α -enhanced populations (Gratton et al., 2000; Spite et al., 2005). Masseron and Gilmore (2015) conclude that α enhancement plays a role in the observed “inhibition” of extra mixing in the older thick disc stars, particularly because both thin and thick disc populations are of masses and metallicities where extra mixing is predicted to be observable and the most significant difference between the discs is their α enhancement. An offset in metallicity is also present in the data, with the thick disc having an average metallicity that is lower than the thin disc as shown in Fig. 7.1. Masseron and Gilmore (2015) state that selection bias is significant in metal-poor APOGEE data but do not discuss in detail.

In a more recent study, Souto et al. (2016) analysed the abundances of 12 stars from the metal-rich open cluster NGC2420, which has a mean metallicity $[\text{Fe}/\text{H}] = -0.16 \pm 0.04$ and main sequence turn-off mass $M_{\text{MSTO}} \sim 1.6 M_{\odot}$. They find (which was also found in previous studies by Spite et al., 2005; Masseron and Gilmore, 2015; Salaris et al., 2015; Martig et al., 2016) that extra mixing seems to be inhibited in higher-metallicity stars. Although the results of Souto et al. (2016) are not statistically significant and they draw no conclusions, Souto et al. (2016) state that differences between the RGB and red clump C/N values (i.e., the effects of extra mixing) have been reported for the approximately solar metallicity open clusters Collinder 261 ($[\text{Fe}/\text{H}] \approx -0.03 \pm 0.05$, De Silva et al., 2007; Mikolaitis et al.,

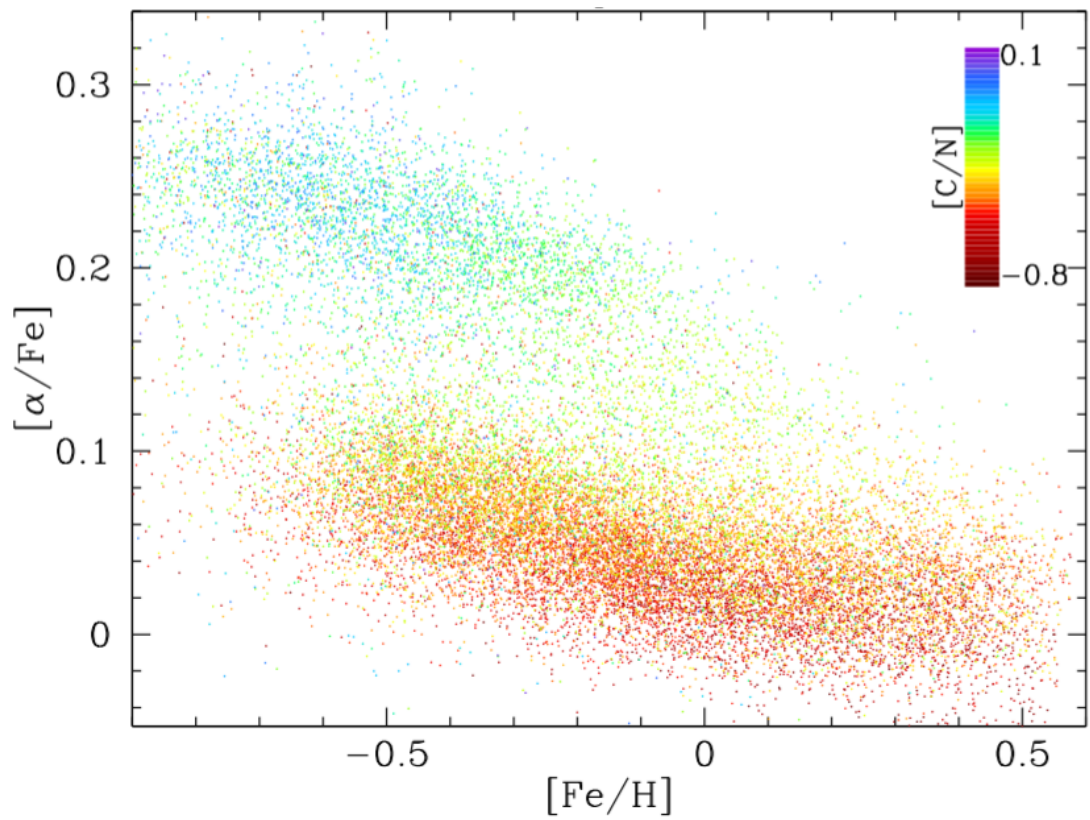


FIGURE 7.1: $[\alpha/Fe]$ as a function of metallicity for post-FDU RGB stars in the APOGEE sample used by Masseron and Gilmore (2015). The C/N ratios are colour coded. Figure is Fig. 12 from Masseron and Gilmore (2015).

2012; Drazdauskas et al., 2016b) and M67 ($[\text{Fe}/\text{H}] \approx -0.03 \pm 0.03$, Tautvaišienė et al., 2000). This implies that extra mixing would most likely be observable in the cluster NGC2420 with more observations (Souto et al., 2016).

Another study by Bertelli Motta et al. (2017) using stars in M67 find that while the $[\text{C}/\text{N}]$ value actually increases (as opposed to decreases if extra mixing were operating as predicted) on the upper RGB, there are too few observations of upper RGB stars to draw any statistically-significant conclusions, and that more high-resolution spectroscopic observations of upper RGB stars in M67 are required.

7.1.3 Gaia-ESO

GES uses the Fibre Large Array Multi-Element Spectrograph (FLAMES) multi-fiber facility on the Very Large Telescope (VLT, Pasquini et al., 2002) to target more than 10^5 stars in the Milky Way. FLAMES covers the visual spectral range by feeding two spectrographs, GIRAFFE (intermediate to high resolution, $R \sim 5000$ to ~ 30000) and UVES (high resolution, $R \sim 47000$), to measure abundances for at least 12 elements (including Na, Mg, Si, Ca, Ti, V, Cr, Mn, Fe, Co, Sr, Zr, Ba) for field stars, and additional elements (e.g., Li) for metal-rich clusters (Gilmore et al., 2012).

Studies using GES data have focused on carbon abundances, namely $[\text{C}/\text{N}]$, $[\text{C}/\text{Fe}]$, and $^{12}\text{C}/^{13}\text{C}$, and show mixed results in relation to the importance (or presence) of an extra mixing mechanism in the observations (Tautvaišienė et al., 2015; Drazdauskas et al., 2016a; Drazdauskas et al., 2016b; Tautvaišienė et al., 2016). In these studies, the thermohaline mixing models of Charbonnel and Lagarde (2010), Lagarde et al. (2012b, which also include rotation) and Eggleton, Dearborn, and Lattanzio (2008) are used for comparison to observations.

Thermohaline mixing (with $C_t = 1000$) overestimates the depletion of the C/N ratio of GES stars in the solar metallicity clusters Trumpler 20 ($[\text{Fe}/\text{H}] = +0.09 \pm 0.10$, Carraro et al., 2014), NGC4815 ($[\text{Fe}/\text{H}] = -0.19 \pm 0.10$, Tadross, 2003; Paunzen et al., 2010), and NGC6705 (average $[\text{Fe}/\text{H}] = +0.07 \pm 0.01$ from our sample), yet models that include thermohaline mixing and rotation¹ “agree quite well” with the C/N and $^{12}\text{C}/^{13}\text{C}$ ratios in NGC4609 ($[\text{Fe}/\text{H}] = +0.05 \pm 0.13$, Drazdauskas et al., 2016a) and NGC5316 ($[\text{Fe}/\text{H}] = +0.05 \pm 0.13$, Drazdauskas et al., 2016a). The authors of that study note that models without thermohaline mixing also match within standard errors (Tautvaišienė et al., 2015; Drazdauskas et al., 2016a). The results of Drazdauskas et al. (2016a) for NGC4609 and NGC5316 are shown in Fig. 7.2.

In another recent study, Drazdauskas et al. (2016b) found that the C/N ratio in Collinder 261 ($[\text{Fe}/\text{H}] = +0.13 \pm 0.05$) and Melotte 66 ($[\text{Fe}/\text{H}] = -0.33 \pm 0.03$) red clump stars agree (within standard errors) with all of the stellar models they considered, regardless of whether thermohaline

¹The value of the initial rotation rate is 30% of the critical velocity, which is given by the formula $V_{\text{crit}} = \left(\frac{2}{3}\right)^{\frac{3}{2}} \left(\frac{GM}{R}\right)^{\frac{1}{2}}$, as outlined in Lagarde et al. (2012b).

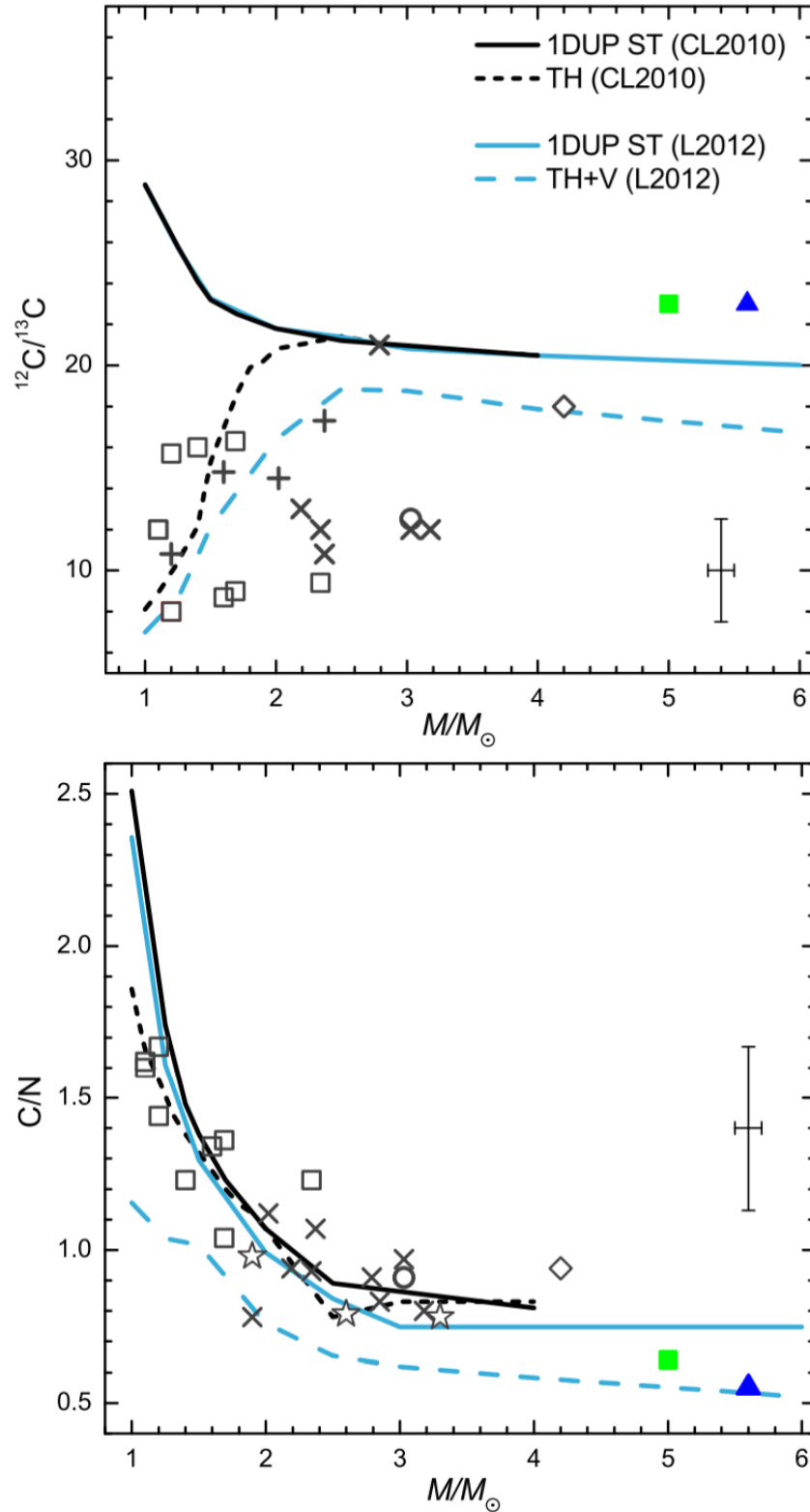


FIGURE 7.2: $^{12}\text{C}/^{13}\text{C}$ (top panel) and C/N (bottom panel) as a function of initial stellar mass. Filled square is the value for NGC5316, and the filled triangle is for NGC4609. Grey open squares are results from Tautvaišienė et al. (2000), Tautvaišienė et al. (2005), Mikolaitis et al. (2010), Mikolaitis et al. (2011a), Mikolaitis et al. (2011b), Mikolaitis et al. (2012), and Drazdauskas et al. (2016b), grey plus symbols are from Gilroy (1989), grey open circles are from Luck (1994), grey crosses are from Smiljanic et al. (2009), and grey open diamonds are from Santrich, Pereira, and Drake (2013). Solid curves are values predicted for stars at first dredge-up using the solar metallicity models of Charbonnel and Lagarde (2010, solid black curve) and Lagarde et al. (2012b, solid blue curve). Typical error bars are shown (Charbonnel and Lagarde, 2010; Smiljanic et al., 2009; Gilroy, 1989). Figure is Figs. 8 (top panel) and 9 (bottom panel) from Drazdauskas et al. (2016a).

mixing was included or not, as shown in the bottom panel of Fig. 7.3. Their thermohaline mixing models (regardless of the inclusion of rotation) agree with the $^{12}\text{C}/^{13}\text{C}$ ratio as a function of turn-off stellar mass from open cluster studies as shown in the top panel of Fig. 7.3, and the authors draw no further conclusions. These results are in agreement with other studies that show that thermohaline models agree well with observations of the C/N and $^{12}\text{C}/^{13}\text{C}$ ratios for stars in NGC2324 ([Fe/H] = -0.163 , Paunzen et al., 2010) and NGC2477 ([Fe/H] = -0.008 , Paunzen et al., 2010; Tautvaišienė et al., 2016). Tautvaišienė et al. (2016) also found that for stars in NGC3960 ([Fe/H] = -0.68 ± 0.28 , Paunzen et al., 2010), the C/N ratio agrees well with stellar models that include only thermohaline mixing (no rotation), whereas the carbon isotopic ratio for the same cluster agrees well with models that include both thermohaline mixing and rotation.

Lagarde et al. (2018) use data from the second, fourth, and fifth GES internal data releases (iDR2, iDR4, iDR5) to compare to their Besançon Galaxy models (Lagarde et al., 2017). Through a comprehensive analysis of the [C/N] ratio in GES stars spanning a sizeable metallicity range ([Fe/H] ~ -1.3 to $+0.4$), they found that it is important to include thermohaline mixing in stellar models of giants in order to understand the observed chemical trends at low metallicities ([Fe/H] < -0.5), as shown in Fig. 7.4.

The results of the above studies suggest that the thermohaline mixing mechanism appears to be a necessary inclusion in stellar models of red giants at solar metallicity. However it is clear that as long as large uncertainties exist in observational data, it will be difficult to draw specific conclusions regarding the extra mixing mechanism and we require further understanding in this area, namely:

1. The magnitude of the effect (or presence) of extra mixing observationally, particularly at higher (i.e., solar and above) metallicities, which would allow us to better constrain our models.
2. The effect of α enhancement on the surface abundances of elements related to extra mixing.
3. The physical mechanism of extra mixing.
4. If thermohaline mixing is the extra mixing mechanism, the value of the parameters in the theory that can match observations of multiple elements (i.e., carbon and lithium) simultaneously.

To place appropriate constraints on models of extra mixing, observations of multiple elements are required. We therefore use GES data because it has observations of lithium *and* carbon, whereas APOGEE only has carbon.

7.2 Observations

We use data from the GES fourth internal data release (iDR4).

GES abundances are given in the form

$$A(X) = \log_{10}(X/H) + 12, \quad (7.3)$$

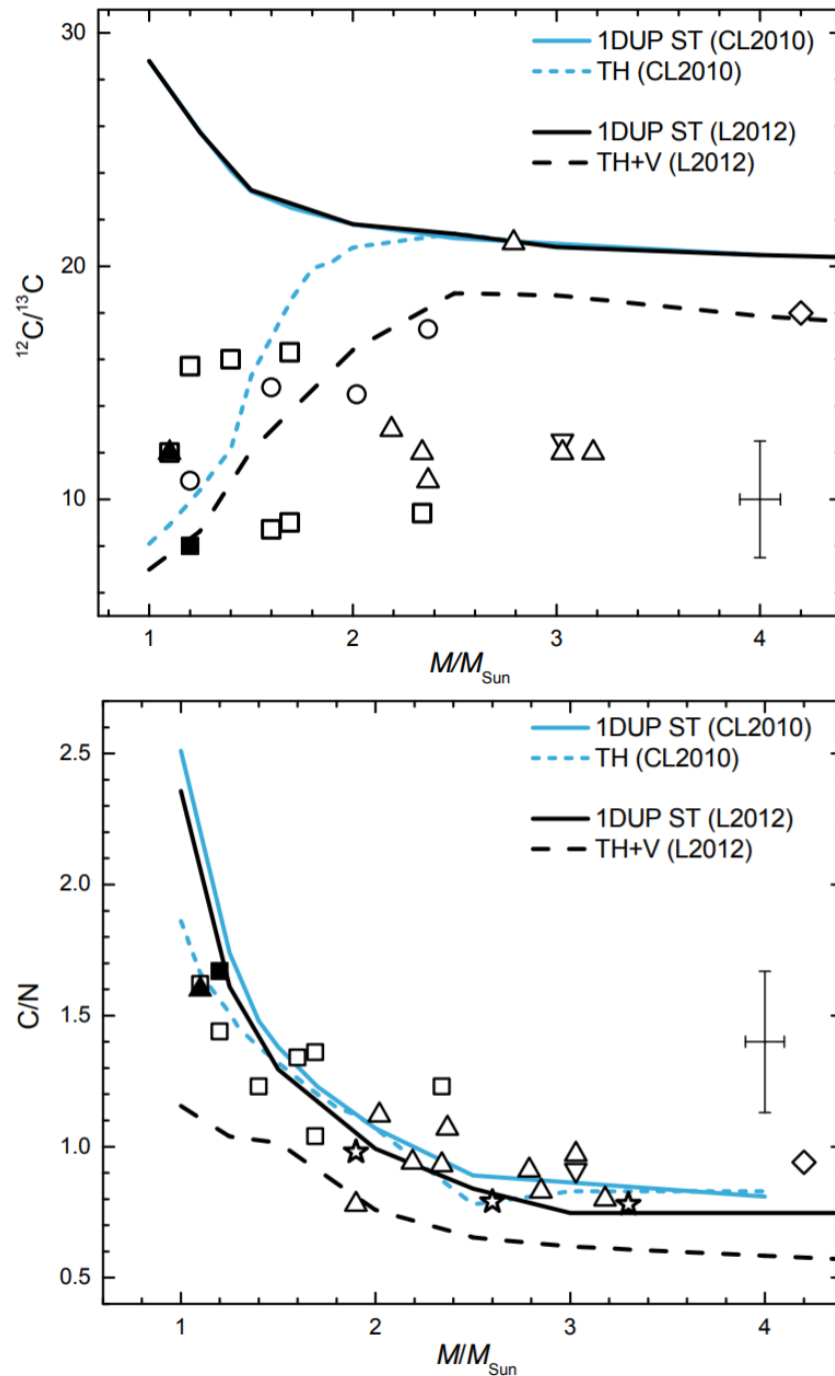


FIGURE 7.3: $^{12}\text{C}/^{13}\text{C}$ (top panel) and C/N (bottom panel) as a function of initial stellar mass. Filled square is the value for Melotte 66, and the filled triangle is for Collinder 261. Grey open squares are results from Tautvaišienė et al. (2000), Tautvaišienė et al. (2005), Mikolaitis et al. (2010), Mikolaitis et al. (2011a), Mikolaitis et al. (2011b), and Mikolaitis et al. (2012), grey open circles are from Gilroy (1989), grey reverse open triangles are from Luck (1994), grey open triangles are from Smiljanic et al. (2009), and grey open diamonds are from Santrich, Pereira, and Drake (2013). Solid curves are values predicted for stars at first dredge-up using the solar metallicity models of Charbonnel and Lagarde (2010, upper blue curve) and Lagarde et al. (2012b, lower black curve). Typical error bars are shown (Charbonnel and Lagarde, 2010; Smiljanic et al., 2009; Gilroy, 1989). Figure is Figs. 7 (top panel) and 8 (bottom panel) from Drazdauskas et al. (2016b).

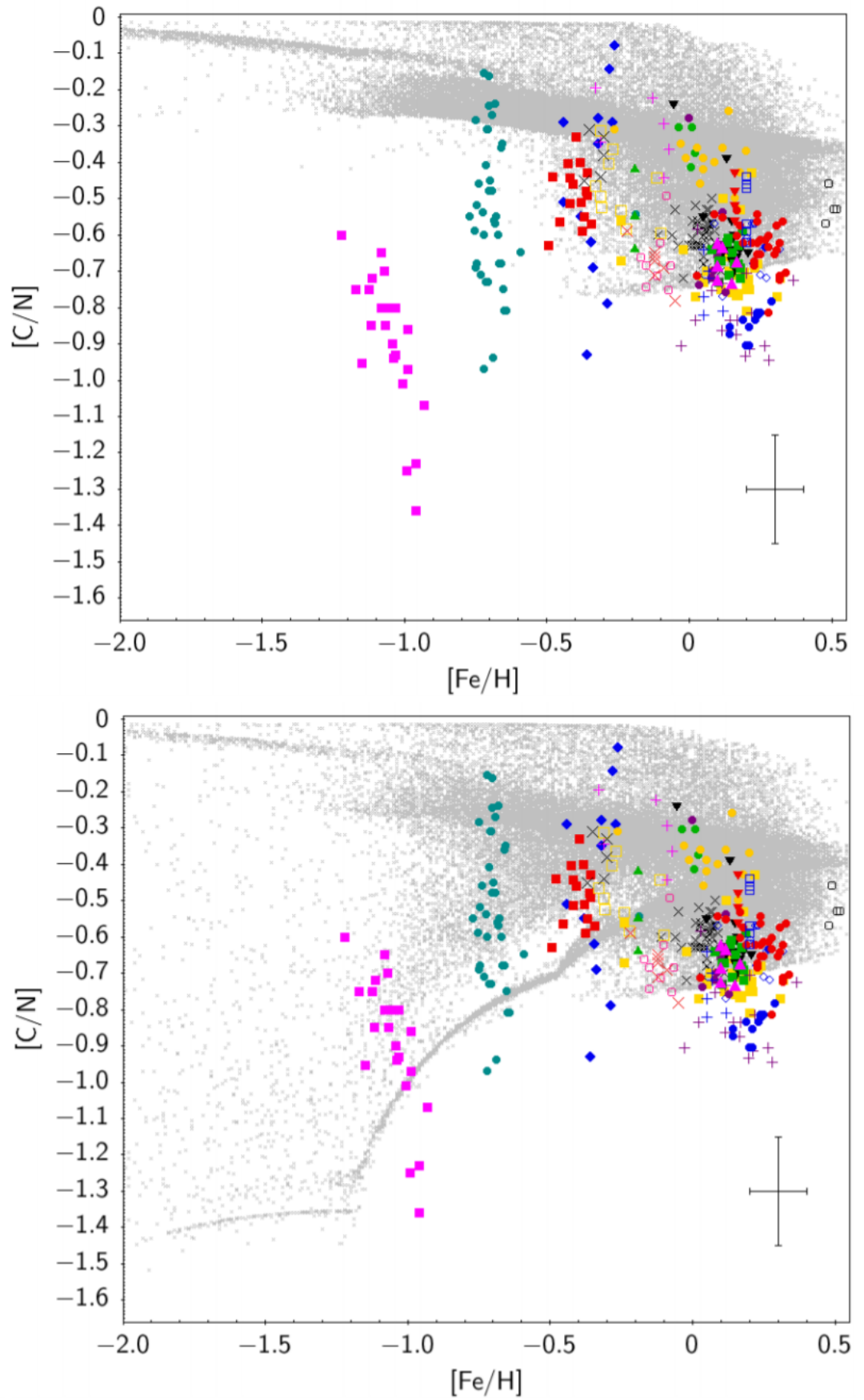


FIGURE 7.4: $[C/N]$ as a function of $[Fe/H]$. Grey dots are synthetic populations with the Besançon Galaxy model (Lagarde et al., 2017) with (bottom panel) and without (top panel) thermohaline mixing. Coloured symbols represent different globular and open cluster stars from the Lagarde et al. (2018) UVES sample (refer to the original manuscript for details on the observations). Figure is Fig. 8 from Lagarde et al. (2018).

where X is the abundance of an element by number (Bertelli Motta et al., 2018). We keep lithium abundances in the above $A(X)$ form and convert carbon abundances to the usual spectroscopic notation according to

$$[X/A] = \log_{10}(X/A) - \log_{10}(X/A)_{\odot}. \quad (7.4)$$

where we use the solar abundances as detailed in Tautvaišienė et al. (2015). Namely, we use $A(C)_{\odot} = 8.39$ and $A(\text{Fe})_{\odot} = 7.45$.

7.2.1 Clusters

As stated above, GES is observing more than 10^5 stars in the Galaxy to discover more about the history, and the chemical and dynamical evolution, of the Milky Way. To do this, globular and open clusters spanning a range in metallicity are observed. We now briefly discuss each of the clusters used in this study and related properties, e.g., age and metallicity. Additionally, we detail the number of members of each cluster included in our sample after appropriate metallicity, radial velocity (as determined by the GES team), and abundance criteria have been met (the details of the metallicity and abundance criteria are in §7.3). In Table 7.1 we summarise the data for the clusters.

Cluster	[Fe/H]	Age	Main sequence turn-off mass (M(MSTO))
NGC6752	[Fe/H] $\sim -1.43 \pm 0.04$ Gratton et al. (2003)	13.8 ± 1.1 Gyr Gratton et al. (2003)	-
NGC2808	[Fe/H] $\sim -1.104 \pm 0.006 \pm 0.046$ Carretta et al. (2009a)	12.5 Gyr Piotto et al. (2007)	-
NGC1851	[Fe/H] $\sim -1.02 \pm 0.01$ Carretta and Gratton (1997), Schiavon et al. (2005), and Koleva et al. (2008)	9.2 Gyr Carretta and Gratton (1997), Schiavon et al. (2005), and Koleva et al. (2008)	-
47 Tucanae (NGC104)	[Fe/H] $\sim -0.768 \pm 0.016 \pm 0.031$ Gratton et al. (2003)	10.8 ± 1.1 Gyr Gratton et al. (2003)	$0.86 M_{\odot}$ Thompson et al. (2009)
NGC5927	[Fe/H] $\sim -0.487 \pm 0.011$ Koleva et al. (2008)	10 Gyr Koleva et al. (2008)	-
NGC2516	[Fe/H] ~ -0.422 Cameron (1985)	158 ± 40 Myr Sung et al. (2002)	-
NGC2243	[Fe/H] $\sim -0.54 \pm 0.10$ Cameron (1985)	3.1 – 5 Gyr Sung et al. (2002)	$1.2 M_{\odot}$ Smiljanic et al. (2016)
NGC4815	[Fe/H] $\sim -0.19 \pm 0.10$	0.5 – 0.63 Gyr	2.6 ± 0.1

	Tadross (2003) and Paunzen et al. (2010)	Friel et al. (2014)	Tautvaišienė et al. (2015)
NGC2547	[Fe/H] $\sim -0.16 \pm 0.04$ Paunzen et al. (2010)	55 ± 25 Myr Chabrier and Baraffe (1997), D'Antona and Mazzitelli (1997), Siess, Dufour, and Forestini (2000), and Oliveira et al. (2003)	-
NGC6005	[Fe/H] ~ -0.1 Piatti et al. (1998)	1.2 ± 0.3 Gyr Piatti et al. (1998)	-
M67 (NGC2682)	[Fe/H] $\sim -0.04 \pm 0.03$ Paunzen et al. (2010)	$3.8 - 4.3$ Gyr Sarajedini (1999) and Giampapa et al. (2006)	$1.22 M_{\odot}$ Pols et al. (1998)
NGC2264	[Fe/H] $\sim -0.02 \pm 0.04$ Claria (1985), Tadross (2003), and Paunzen et al. (2010)	~ 3 Myr Dahm (2008)	-
NGC6633	[Fe/H] $\sim -0.06 \pm 0.02$ Jacobson et al. (2016), Magrini et al. (2017), and Spina et al. (2017)	$0.425 - 0.575$ Gyr Randich et al. (2018)	$2.74 M_{\odot}$ Smiljanic et al. (2009)
NGC2451	[Fe/H] $\sim -0.01 \pm 0.01$ Hünsch et al. (2004), Jacobson et al. (2016), and Spina et al. (2017)	$50 - 80$ Myr Hünsch et al. (2004), Jacobson et al. (2016), and Spina et al. (2017)	$\sim 5 M_{\odot}$ Reimers and Koester (1988)
NGC6705	[Fe/H] $\sim +0.07 \pm 0.01$ (Cantat-Gaudin et al., 2014; Tautvaišienė et al., 2015)	$0.25 - 0.32$ Gyr Tautvaišienė et al. (2015)	$3.2 M_{\odot}$ Cantat-Gaudin et al. (2014), Tautvaišienė et al. (2015), and Smiljanic et al. (2016)

TABLE 7.1: Metallicity, age, and main sequence turn-off mass of the clusters used in this study. Where multiple values are reported for a cluster characteristic, we give the most recent value.

NGC6752

NGC6752 is an old metal-poor globular cluster approximately 13.8 ± 1.1 Gyr old with metallicity $[\text{Fe}/\text{H}] \sim -1.43 \pm 0.04$ (Gratton et al., 2003). Our sample consists of 42 NGC6752 stars with average $[\text{Fe}/\text{H}] \sim -1.45 \pm 0.04$.

NGC2808

Analysis of NGC2808 has revealed that there are at least three populations present in the main sequence (D'Antona et al., 2002; Milone et al., 2015). Piotto et al. (2007) compared data of NGC2808 stars with isochrones and found that the age of NGC2808 is ~ 12.5 Gyr (however the age could be as low as 10 Gyr depending upon the models and parameters adopted, e.g., the helium abundance, Milone et al., 2015). Measurements of the metallicity of NGC2808 include $[\text{Fe}/\text{H}] \sim -1.104 \pm 0.006 \pm 0.046$ (Carretta et al., 2009a) and $-1.151 \pm 0.022 \pm 0.050$ (from GIRAFFE and UVES data, determined by Carretta, 2006; Carretta et al., 2009c, respectively), where metallicities are reported as $[\text{Fe}/\text{H}] \pm \text{statistical error} \pm \text{systematic error}$ (Carretta et al., 2009a). We find 20 members for NGC2808 with average $[\text{Fe}/\text{H}] \sim -1.01 \pm 0.02$.

NGC1851

There are known multiple populations in the globular cluster NGC1851 that differ in age by around 1 Gyr (Milone et al., 2008; Carretta et al., 2011). The cluster is ~ 9.2 Gyr old with a metallicity of approximately -1.21 (Carretta and Gratton, 1997; Schiavon et al., 2005; Koleva et al., 2008). We have 43 NGC1851 members with an average $[\text{Fe}/\text{H}] \sim -1.02 \pm 0.01$.

47 Tucanae (NGC104)

NGC104 (or 47 Tucanae) is a globular cluster that is $\sim 10.8 \pm 1.1$ Gyr old (Gratton et al., 2003) with an average metallicity that was measured as -0.70 (Reid and Gizis, 1998; Kraft and Ivans, 2003) and -0.66 ± 0.04 (Gratton et al., 2003). Additionally, data from UVES and GIRAFFE find the average metallicity of NGC104 to be $-0.768 \pm 0.016 \pm 0.031$ (Carretta et al., 2009b; Carretta et al., 2009a; Carretta et al., 2009c). We have 50 members with an average metallicity of approximately -0.70 ± 0.01 .

NGC5927

The globular clusters NGC5927a and b are approximately 10 Gyr old (Koleva et al., 2008) with an average metallicity that was measured as -0.64 (Carretta and Gratton, 1997) and -0.439 ± 0.011 for NGC5927a, and -0.487 ± 0.011 for NGC5927b (Koleva et al., 2008). We have 9 confirmed members that have an average metallicity of -0.34 ± 0.02 . The differences in metallicity for this cluster can be attributed to a number of factors, including different observations, small number statistics, and analysis methods (Koleva et al., 2008).

NGC2516

The average metallicity of NGC2516 has varied in the literature, with values that are typical of sub-solar (-0.422) and super-solar ($+0.06$). However

many of these values are derived from samples with fewer than 10 stars except for the study of Cameron (1985), which found an average $[\text{Fe}/\text{H}] \sim -0.422$ using 67 NGC2516 members (Lynga and Wramdemark, 1984; Nissen, 1988; Claria, Lapasset, and Minniti, 1989; Piatti, Claria, and Abadi, 1995; Twarog, Ashman, and Anthony-Twarog, 1997; Sung et al., 2002; Paunzen et al., 2010). Our sample contains 36 members with average $[\text{Fe}/\text{H}] \sim -0.17 \pm 0.06$. Sung et al. (2002) estimate the age of NGC2516 to be between 125.9 Myr and 199.5 Myr.

NGC2243

NGC2243 is a relatively old open cluster with age estimates that have been measured between 3.1 and 5 Gyr (Bonifazi et al., 1990; Bergbusch, Vandenberg, and Infante, 1991; Gratton and Contarini, 1994; Vandenberg, Bergbusch, and Dowler, 2006; Kaluzny et al., 2006) and an average metallicity $[\text{Fe}/\text{H}] \sim -0.54 \pm 0.10$ (François et al., 2013). We have 22 members with an average metallicity $[\text{Fe}/\text{H}] = -0.40 \pm 0.02$.

NGC4815

There are limited recorded observations of the open cluster NGC4815, with the average metallicity found by Tadross (2003) and Paunzen et al. (2010) to be -0.19 ± 0.10 from one observation. We have 12 members with an average $[\text{Fe}/\text{H}] \sim -0.68 \pm 0.07$. Friel et al. (2014) used Gaia-ESO data and concluded that the age of NGC4815 was 0.5 - 0.63 Gyr.

NGC2547

NGC2547 is a metal-rich, young open cluster with age determinations that yield differing results, ranging from 55 ± 25 Myr (Chabrier and Baraffe, 1997; D’Antona and Mazzitelli, 1997; Siess, Dufour, and Forestini, 2000; Oliveira et al., 2003) from isochrone fitting, to 37.1 ± 2.1 Myr and 48.1 ± 3.1 Myr using the lithium depletion boundary² (Chabrier and Baraffe, 1997; D’Antona and Mazzitelli, 1997; Siess, Dufour, and Forestini, 2000; Oliveira et al., 2003). The metallicity of NGC2547 is not well-studied, with several studies analysing only 1 member star finding values of $[\text{Fe}/\text{H}]$ to be between ~ -0.21 and -0.13 (Claria, 1982; Piatti, Claria, and Abadi, 1995; Twarog, Ashman, and Anthony-Twarog, 1997). A study by Cameron (1985) had a sample of 43 stars and found the average metallicity to be -0.121 , and Paunzen et al. (2010) found a cluster metallicity of -0.16 ± 0.04 with 5 members. In our sample, we have 24 NGC2547 members that have an average $[\text{Fe}/\text{H}] \sim -0.01 \pm 0.03$. This is significantly higher than previous studies, even when taking errors and uncertainties into account. However we note that higher quality observations yield more accurate data, therefore

²The lithium depletion boundary is a method of determining the age of a cluster of coeval stars. Lithium is a very short-lived element in stellar interiors, and its depletion is highly dependent upon stellar mass. Therefore, observations of lithium abundances that have decreased from their initial cluster value can give astronomers an indication of the star’s mass and, by extension, the age of the cluster (Oliveira et al., 2003).

our average metallicity is (probably) more indicative of the real metallicity of NGC2547.

NGC6005

There is a lack of data for the open cluster NGC6005 in the literature. The most comprehensive work done was by Piatti et al. (1998), who determined that NGC6005 is 1.2 ± 0.3 Gyr old with an average metallicity of -0.1 . We have 24 members with average $[\text{Fe}/\text{H}] \sim -0.19 \pm 0.06$.

M67 (NGC2682)

M67 (or NGC2682) is an open cluster with an average metallicity that is slightly sub-solar. Metallicity values determined in the mid-1980's to the early 2000's are within the values of -0.11 and -0.01 using 14 to 58 members (Janes and Smith, 1984; Cameron, 1985; Nissen, Twarog, and Crawford, 1987; Piatti, Claria, and Abadi, 1995; Noriega-Mendoza and Ruelas-Mayorgo, 1997; Twarog, Ashman, and Anthony-Twarog, 1997; Tadross, 2003), with a more recent study finding the average metallicity of 7 M67 members is -0.04 ± 0.03 (Paunzen et al., 2010). We have 22 M67 members with average $[\text{Fe}/\text{H}] \sim -0.03 \pm 0.02$. Age estimates of M67 range from 3.8 - 4.3 Gyr (Sarajedini, 1999; Giampapa et al., 2006).

NGC2264

NGC2264 is a slightly sub-solar open cluster with average metallicities in the literature that are between -0.16 and 0.00 (Claria, 1985; Tadross, 2003; Paunzen et al., 2010), however the sample sizes for these determinations are very small (fewer than 5). We have 28 members with average $[\text{Fe}/\text{H}] \sim -0.02 \pm 0.04$. Using pre-main sequence isochrone fitting, Dahm (2008) estimates the median age to be ~ 3 Myr with a dispersion of ~ 5 Myr. This age dispersion may be related to the cluster formation timescale, as proposed by Sung and Bessell (2010), because this is a cluster with many star-forming regions that vary in age. Earlier studies of this cluster also found the age to be ~ 3 Myr (Lynga, 1981; Pérez, 1991).

NGC6633

Studies using Gaia data of the open cluster NGC6633 use various ages that include 0.63 ± 0.10 Gyr as determined by Jeffries et al. (2002) and adopted in the analyses of Jacobson et al. (2016) and Magrini et al. (2017), and $0.425 - 0.575$ Gyr as determined by Dias et al. (2002), Williams and Bolte (2007), and van Leeuwen (2009) and adopted by Randich et al. (2018). We have 65 members with an average metallicity of $+0.01 \pm 0.02$. This metallicity is consistent (within errors) with other published values (Jacobson et al., 2016; Magrini et al., 2017; Spina et al., 2017).

NGC2451

NGC2451 consists of two young open clusters (a and b) with an age range from $\sim 50 - 80$ Myr and an average metallicity of -0.05 ± 0.02 and -0.01 ± 0.01 for the NGC2451a and NGC2451b clusters respectively (Hünsch et al., 2004; Jacobson et al., 2016; Spina et al., 2017). We have 68 members that have an average metallicity of 0.02 ± 0.02 .

NGC6705

NGC6705 is a young open cluster with an estimated age that is between 0.25 and 0.32 Gyr and respective main sequence turn-off masses of 3.47 to $3.2 M_{\odot}$ (Cantat-Gaudin et al., 2014; Tautvaišienė et al., 2015). After removing non-members based on radial velocity measurements and abundance criteria, we have 35 members with an average $[\text{Fe}/\text{H}] \sim +0.07 \pm 0.01$, which is consistent (within errors) with the average metallicity found by Tautvaišienė et al. (2015).

7.3 Models

We construct our stellar models using MONSTAR, the Monash version of the Mt. Stromlo stellar evolution code (for more details, see Henkel, Karakas, and Lattanzio, 2017). To allow appropriate comparisons between our models and the available data, we create a grid of models varying in mass, metallicity, and α element enhancement as detailed in Table 7.2.

We use Asplund et al. (2009) solar abundances, and $A(\text{C})_{\odot} = 8.39$ and $A(\text{Fe})_{\odot} = 7.45$ according to Tautvaišienė et al. (2015). Additionally, we set α enhancement according to Fig. 1 in Yong et al. (2016). Metal-poor populations are observed to be enhanced in α elements, which is discussed in more detail in §2.2.1.

After selecting our desired $[\text{Fe}/\text{H}]$ for each model, we calculate Z (including α enhancement) according to

$$[\text{M}/\text{H}] \simeq [\text{Fe}/\text{H}] + \log(0.638f_{\alpha} + 0.362) \quad (7.5)$$

where f_{α} is related to the α enhancement according to $\log_{10}(f_{\alpha}) = [\alpha/\text{Fe}]$ and satisfies $Z = f_{\alpha}Z_0$ (Z_0 is scaled solar for given $[\text{Fe}/\text{H}]$) as given by Salaris, Chieffi, and Straniero (1993). We then scale the helium mass fraction Y according to the formula

$$Y = Y_p + \frac{\Delta Y}{\Delta Z}Z, \quad (7.6)$$

where we take primordial helium $Y_p = 0.2485$ (which is within error of standard estimates, e.g. Tsivilev et al., 2013; Peimbert, Peimbert, and Luridiana, 2016). We also take $\frac{\Delta Y}{\Delta Z} = 2.1$ for metal-rich populations (above solar), however this relation fails to model low-metallicity populations, therefore

for metal-poor populations we take $\frac{\Delta Y}{\Delta Z} = 1.45$ ($Z \geq 0.0001$, Casagrande et al., 2011).

For each model with the standard implementation of thermohaline mixing, we have another model identical in every parameter except for the treatment of thermohaline mixing. We model thermohaline mixing as detailed in Henkel, Karakas, and Lattanzio (2017). Briefly, we modify the thermohaline mixing diffusion coefficient according to

$$D_{\text{new}} = \begin{cases} i \times D_t & \text{if } T > T_{\text{crit}}, \\ o \times D_t & \text{if } T < T_{\text{crit}}, \end{cases} \quad (7.7)$$

where T_{crit} is what we call the “critical temperature”, i is the “inner” factor that modifies the diffusion coefficient from the base of the thermohaline region to the location of T_{crit} , and o is the “outer” factor that modifies the diffusion coefficient from the location of T_{crit} to the top of the thermohaline region. The effect that modifying i , o , and T_{crit} has on surface abundances is detailed in Chapter 3.

We then compare our models to the appropriate data. To do this, we firstly group clusters into metallicity bins based upon the approximate average metallicity of the stars in that cluster. The metallicity bins we use are: $[\text{Fe}/\text{H}] = -1.5 \pm 0.25$, -1.0 ± 0.25 , -0.5 ± 0.25 , $+0.0 \pm 0.25$, and $+0.3 \pm 0.25$. We then make further cuts to the stars we have in each cluster according to the metallicity bins above. We do this so we can make appropriate comparisons to our models and group clusters of similar metallicity for analysis. We group the clusters according to Table 7.2. Finally, we only include stars that have observations of both carbon and lithium abundances. This is because both elements burn at different temperatures and are therefore tracers of mixing and burning in stellar interiors (this is discussed in more detail in Chapter 1).

7.4 Results

In Figs. 7.5 - 7.9 we show $A(\text{Li})$ (top panels) and $[\text{C}/\text{Fe}]$ (bottom panels) as a function of surface gravity. Figs. 7.5, 7.6, 7.7, 7.8, and 7.9 are for $[\text{Fe}/\text{H}] = 0.0, +0.3, -0.5, -1.0$ and -1.5 respectively. In each panel, we overlay our stellar models on the observations with various initial masses (shown in the legend of each figure). For each mass we show a model that includes the standard implementation of thermohaline mixing and a model that includes our modification to the standard implementation according to the work of Henkel, Karakas, and Lattanzio (2017).

7.4.1 Solar and super-solar metallicities ($[\text{Fe}/\text{H}] = 0.0, +0.3$)

Lithium

The top panels of Figs. 7.5 and 7.6 show that FDU occurs at lower surface gravities in our models compared to the observations. This means that in

Model parameters			Observations	
[Fe/H]	[α /Fe]	Mass (M_{\odot})	Cluster [Fe/H] range	Cluster/s
-1.5	+0.3	0.80, 1.00, 1.30	-1.5 ± 0.25	NGC6752
-1.0	+0.3	0.80, 1.00, 1.30	-1.0 ± 0.25	NGC2808 NGC1851
-0.5	+0.2	1.00, 1.30, 1.50	-0.5 ± 0.25	NGC104 NGC2243 NGC5927 NGC4815
0.0	0.0	1.00, 1.30, 1.50, 1.70, 2.00	0.0 ± 0.25	NGC2547 NGC2451 NGC6633 M67 NGC2516 NGC2264 NGC6005
+0.3	0.0	1.30, 1.50, 2.00	$+0.3 \pm 0.25$	NGC6705

TABLE 7.2: Grid of stellar models. The three leftmost columns (*Model parameters*) describe the stellar model parameters adopted. The two rightmost columns (*Observations*) outline the range of average cluster metallicities (*Cluster [Fe/H] range*) that can be appropriately compared to the stellar models of a given metallicity, and the clusters that have an average metallicity within this range that are used for comparison (*Cluster/s*).

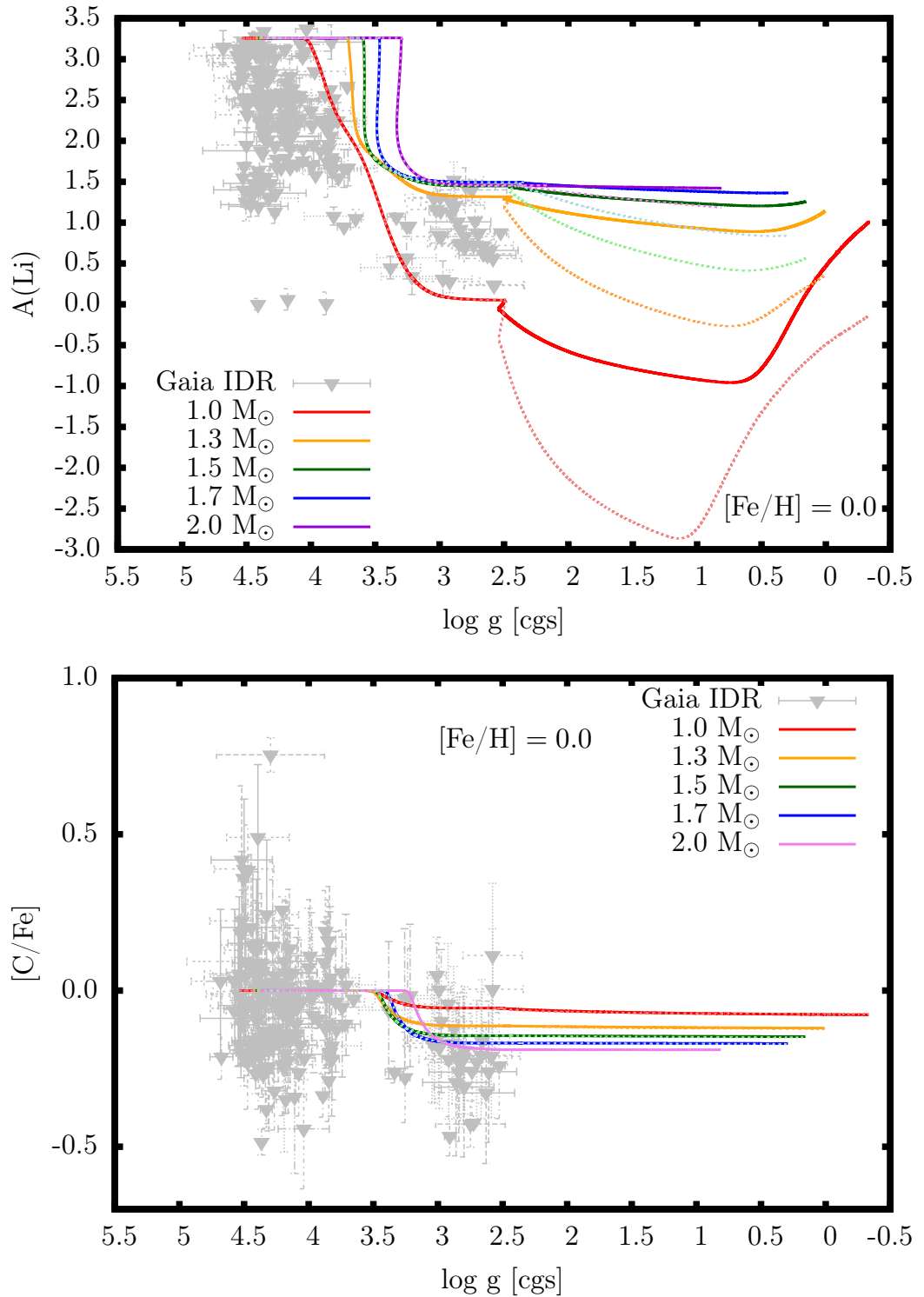


FIGURE 7.5: Lithium ($A(\text{Li})$, top panel) and carbon ($[\text{C}/\text{Fe}]$, bottom panel) abundances as a function of surface gravity. The curves are our models with $[\text{Fe}/\text{H}] = 0$, colours represent different masses (refer to key for details). For each curve, solid lines represent the modified thermohaline mechanism and dashed lines represent the standard implementation. Filled triangles are GES abundances from NGC2547 ($[\text{Fe}/\text{H}] \sim -0.16 \pm 0.04$, Paunzen et al., 2010), NGC2451 ($[\text{Fe}/\text{H}] \sim -0.01 \pm 0.01$, Hünsch et al., 2004; Jacobson et al., 2016; Spina et al., 2017), NGC6633 ($[\text{Fe}/\text{H}] \sim -0.06 \pm 0.02$, Jacobson et al., 2016; Magrini et al., 2017; Spina et al., 2017), M67 ($[\text{Fe}/\text{H}] \sim -0.04 \pm 0.03$, Paunzen et al., 2010), NGC2516 ($[\text{Fe}/\text{H}] \sim -0.422$, Cameron, 1985), NGC2264 ($[\text{Fe}/\text{H}] \sim -0.02 \pm 0.04$, Claria, 1985; Tadross, 2003; Paunzen et al., 2010), and NGC6005 ($[\text{Fe}/\text{H}] \sim -0.1$, Piatti et al., 1998).

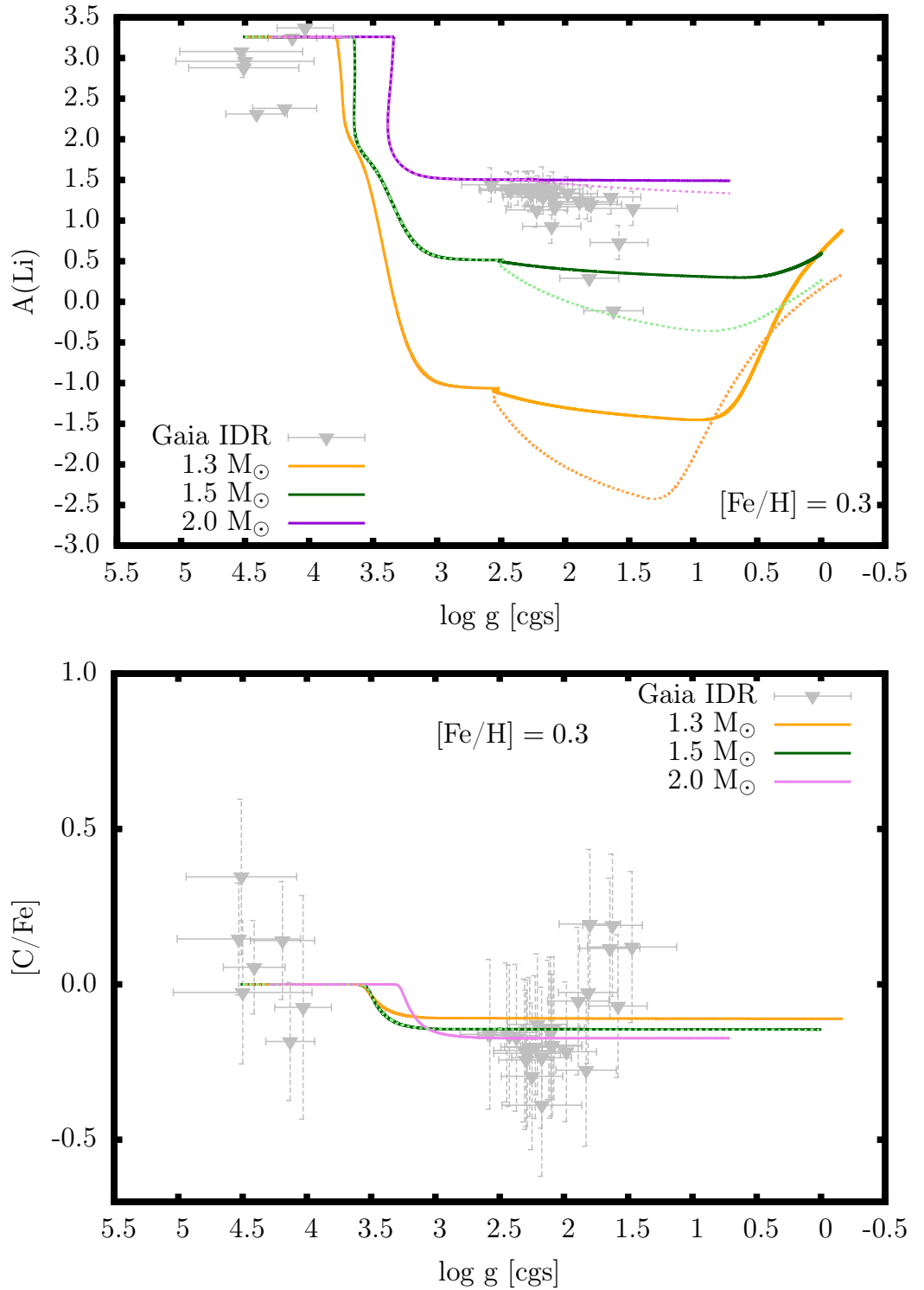


FIGURE 7.6: Lithium ($A(\text{Li})$, top panel) and carbon ($[\text{C}/\text{Fe}]$, bottom panel) abundances as a function of surface gravity. The curves are our models with $[\text{Fe}/\text{H}] = +0.3$, colours represent different masses (refer to key for details). For each curve, solid lines represent the modified thermohaline mechanism and dashed lines represent the standard implementation. Filled triangles are GES abundances from NGC6705 ($[\text{Fe}/\text{H}] \sim +0.07 \pm 0.01$, Cantat-Gaudin et al., 2014; Tautvaišienė et al., 2015).

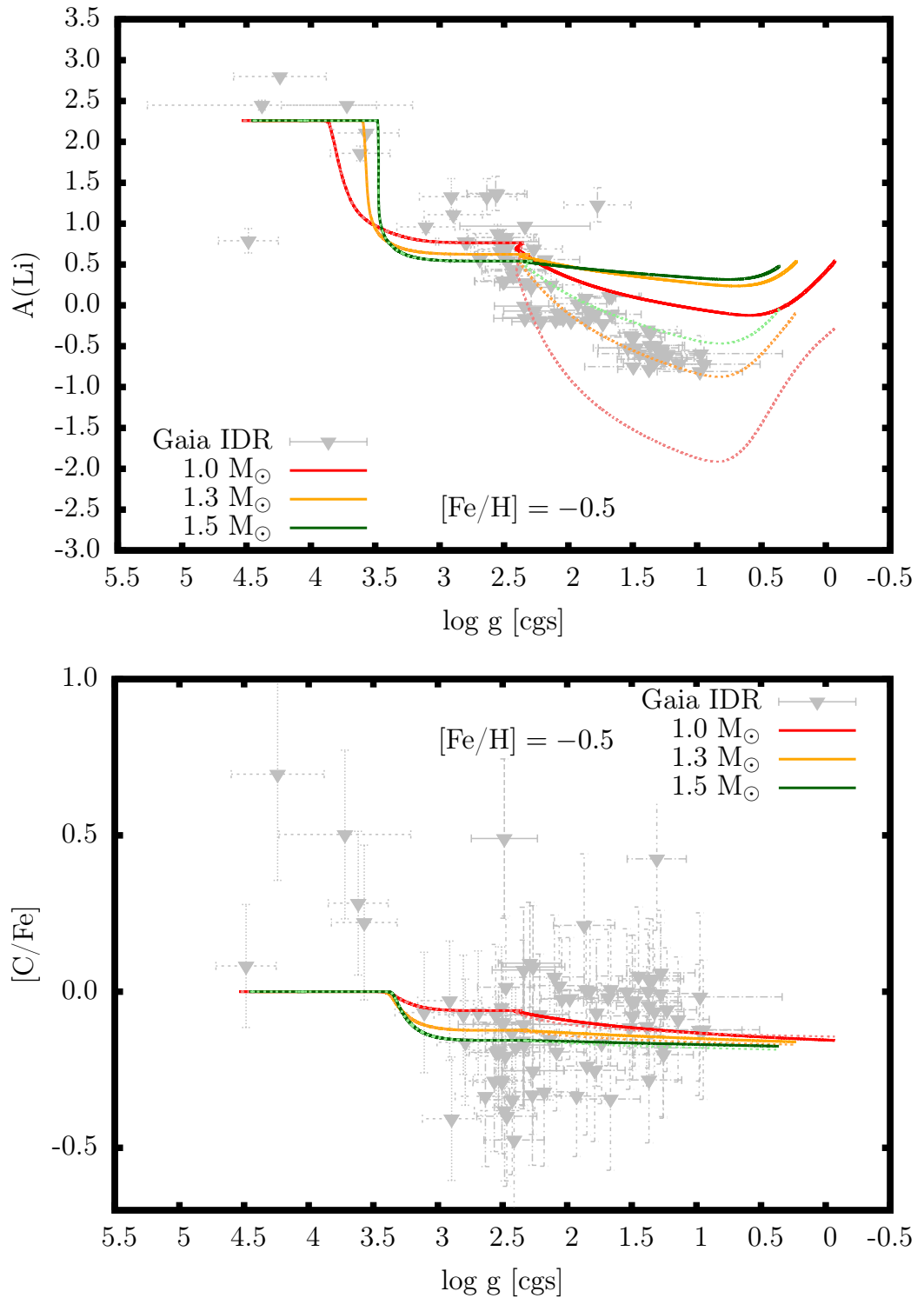


FIGURE 7.7: Lithium ($A(\text{Li})$, top panel) and carbon ($[\text{C}/\text{Fe}]$, bottom panel) abundances as a function of surface gravity. The curves are our models with $[\text{Fe}/\text{H}] = -0.5$, colours represent different masses (refer to key for details). For each curve, solid lines represent the modified thermohaline mechanism and dashed lines represent the standard implementation. Filled triangles are GES abundances from NGC104 ($[\text{Fe}/\text{H}] \sim -0.768 \pm 0.016 \pm 0.031$, Gratton et al., 2003), NGC2243 ($[\text{Fe}/\text{H}] \sim -0.54 \pm 0.10$, Cameron, 1985), NGC5927 ($[\text{Fe}/\text{H}] \sim -0.487 \pm 0.011$, Koleva et al., 2008), and NGC4815 ($[\text{Fe}/\text{H}] \sim -0.19 \pm 0.10$, Tadross, 2003; Paunzen et al., 2010).

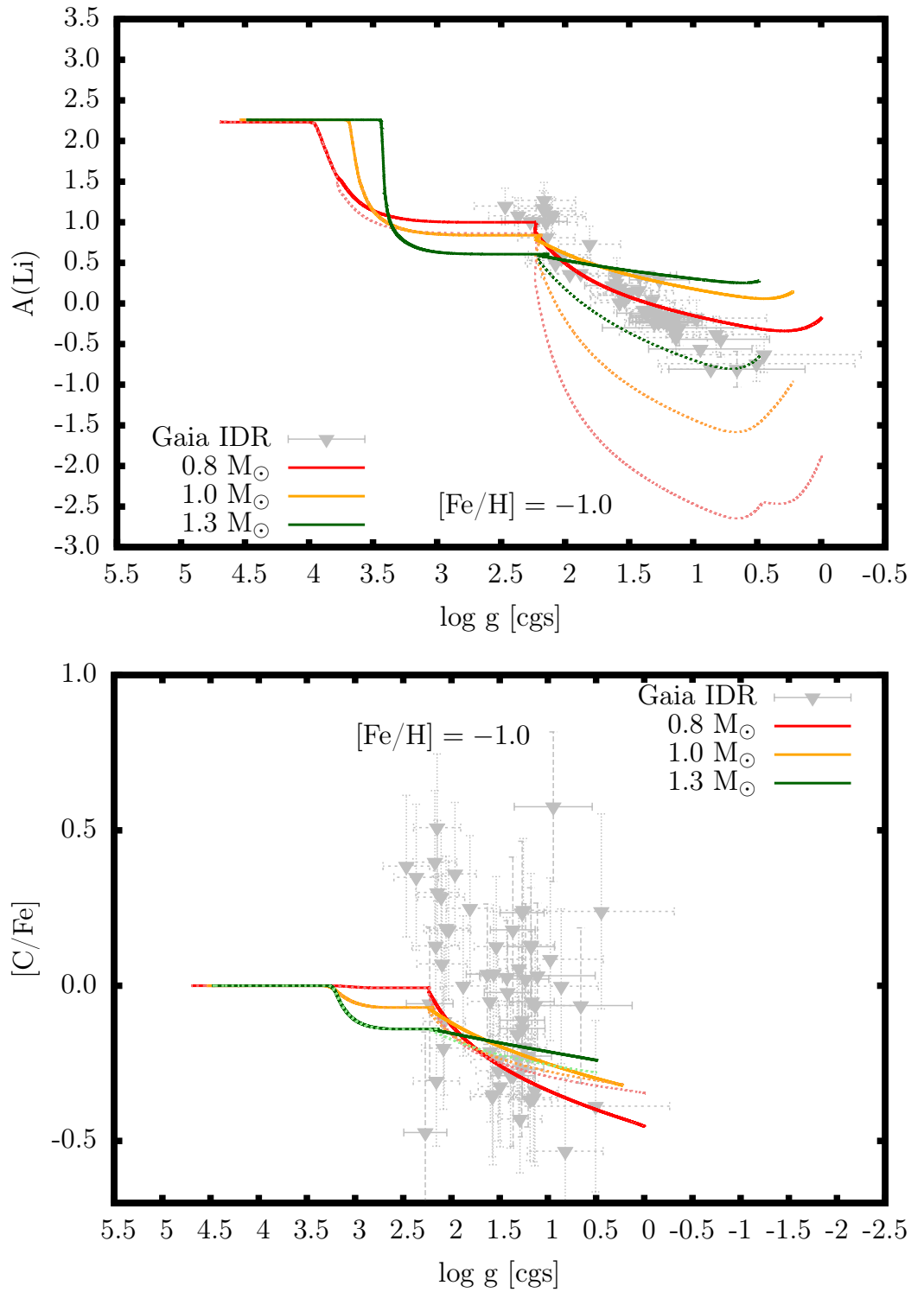


FIGURE 7.8: Lithium ($A(\text{Li})$, top panel) and carbon ($[\text{C}/\text{Fe}]$, bottom panel) abundances as a function of surface gravity. The curves are our models with $[\text{Fe}/\text{H}] = -1.0$, colours represent different masses (refer to key for details). For each curve, solid lines represent the modified thermohaline mechanism and dashed lines represent the standard implementation. Filled triangles are GES abundances from NGC2808 ($[\text{Fe}/\text{H}] \sim -1.104 \pm 0.006 \pm 0.046$, Carretta et al., 2009a) and NGC1851 ($[\text{Fe}/\text{H}] \sim -1.02 \pm 0.01$, Carretta and Gratton, 1997; Schiavon et al., 2005; Koleva et al., 2008).

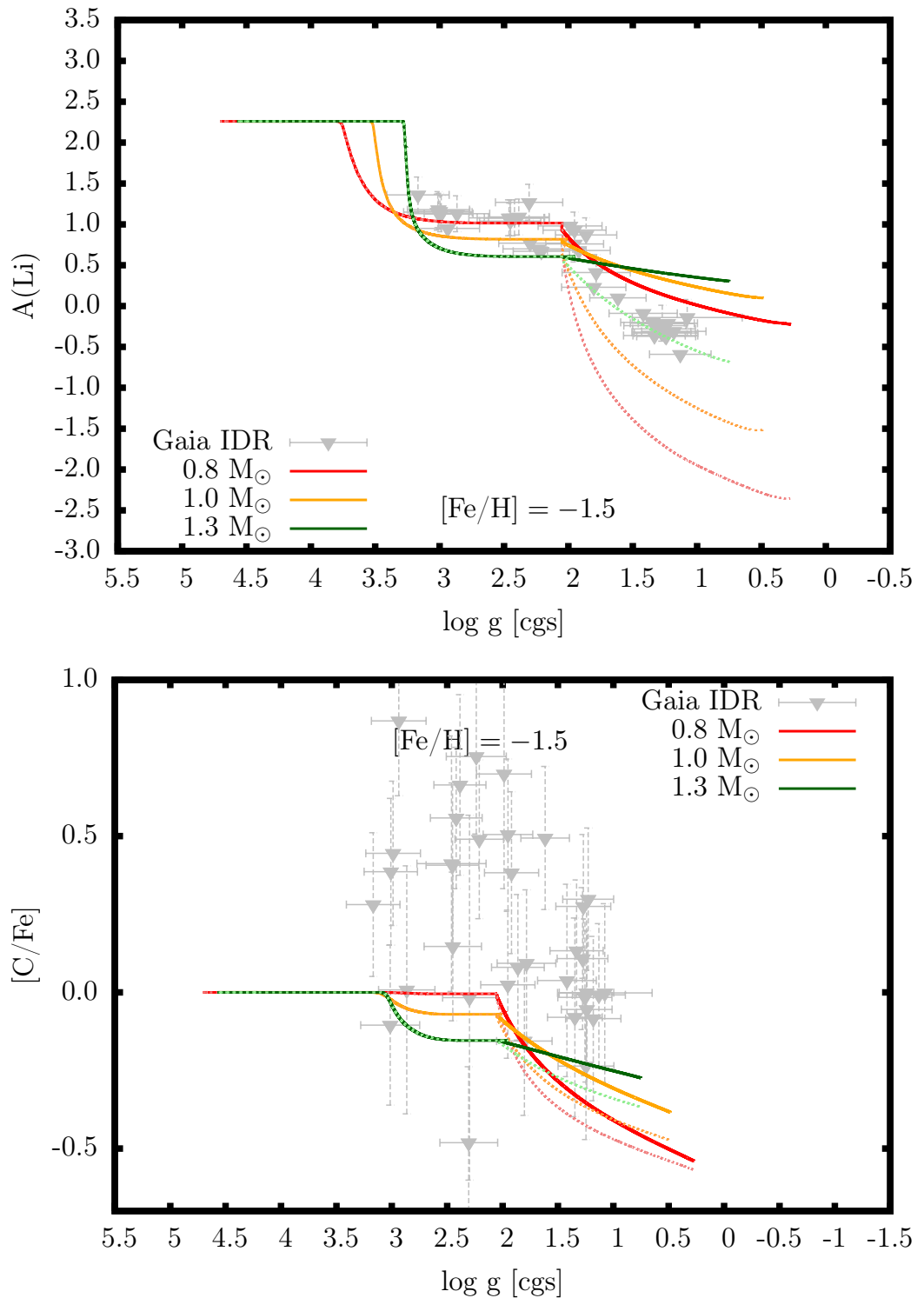


FIGURE 7.9: Lithium ($A(\text{Li})$, top panel) and carbon ($[\text{C}/\text{Fe}]$, bottom panel) abundances as a function of surface gravity. The curves are our models with $[\text{Fe}/\text{H}] = -1.5$, colours represent different masses (refer to key for details). For each curve, solid lines represent the modified thermohaline mechanism and dashed lines represent the standard implementation. Filled triangles are GES abundances from NGC6752 ($[\text{Fe}/\text{H}] \sim -1.43 \pm 0.04$, Gratton et al., 2003).

our models, FDU occurs at higher luminosities than the observations (or further up the RGB). The consequence of this is that surface abundance changes due to extra mixing will be offset in $\log g$ compared to the observations, therefore it is more meaningful to compare the shape of the model curves to the observations, i.e., how rapid the declines due to FDU and thermohaline mixing are, rather than the surface gravity value at which these events occur. We note however that this issue could be alleviated by the inclusion of rotation in our stellar models. Rotation on the main sequence causes a reduction in surface lithium abundances that is qualitatively similar to first dredge-up (Palacios et al., 2003).

From the top panel of Fig. 7.5 it is evident that both the $1 M_{\odot}$ standard and modified thermohaline mixing models do not match the data at solar metallicity, as the models deplete too much lithium during FDU compared to the observations. Therefore it can be concluded that a model with an initial mass between 1 and $1.3 M_{\odot}$ would agree better with the observations. These initial masses correspond to RGB-tip ages of 11.67 and 4.42 Gyr respectively. The clusters at this metallicity (NGC2547, NGC2451, NGC6633, M67, NGC2516, NGC2264, and NGC6005) all have ages in the literature that are significantly less than this, ranging from 3 Myr (NGC2264) to 575 Myr (NGC6633), with the exceptions of M67 and NGC6005, which have age estimates of 3.8 - 4.3 and 1.2 Gyr respectively. This suggests that the clusters younger than our predictions have RGB stars that are significantly more massive than our models. This is confirmed when we consider the main-sequence turn-off mass estimates for these clusters (although not all of the clusters have mass estimates, detailed in Table 7.1). The main sequence turn-off mass estimates for M67 ($1.22 M_{\odot}$) match the model masses that best match the data (1 and $1.3 M_{\odot}$) however the turn-off masses of NGC6633 ($2.74 M_{\odot}$) and NGC2451 ($\sim 5 M_{\odot}$) are too large, as expected.

There is a lack of observed giants at solar metallicity, therefore it is difficult to confidently conclude which thermohaline mixing mechanism (modified or standard) is an appropriate match to the data, however we suggest that the standard implementation appears to deplete lithium too fast and a slower decline of lithium during RGB ascent (as per our modified model) is a better match for the data.

For $[\text{Fe}/\text{H}] = +0.3$, as shown in the top panel of Fig. 7.6, the $1.3 M_{\odot}$ model depletes too much lithium after FDU, yet a model with initial mass between 1.5 and $2 M_{\odot}$ would sufficiently agree with the observations. These initial masses correspond to RGB-tip ages of 1.02 and 1.14 Gyr respectively. NGC6705 is considerably younger than this (0.25 - 0.32 Gyr old) and consequently has main sequence turn-off mass estimates that are more massive than our stellar models suggest (3.47 - $3.2 M_{\odot}$).

There are more giants observed at this metallicity compared to solar, however constraining the thermohaline mixing parameters is still difficult due to the spread of the observations, which is (most likely) due to rotation on the main sequence that mimics first dredge-up.

Carbon

In the bottom panel of Fig. 7.5, we first note that there is a very large spread of initial carbon on the main sequence of at least an order of magnitude (0.0 ± 0.5). We note that this spread is larger than the (approximately) solar metallicity Galactic Archaeology with HERMES (GALAH) survey sample of Buder et al. (2018), shown in Fig. 7.10. Furthermore, most of the observed giants have carbon abundances that are lower than the models predict on the RGB. As discussed above, the analysis of surface lithium abundances at this metallicity suggests that a stellar model with initial mass of around $1.2 M_{\odot}$ best matches the data, therefore if we assume that this solution is unique, the same model matches the carbon abundances, and that the observational uncertainties are correct, we can conclude that

1. There must be a significant spread of initial carbon in this population because carbon abundances do not change significantly as a result of extra mixing at this metallicity (according to our theoretical predictions), and;
2. Following on from the above point, carbon abundances observed in giant branch stars are approximately unchanged from the amount that the stars were born with (within 0.2 dex) at this metallicity.

For the higher metallicity of $[\text{Fe}/\text{H}] = +0.3$ (bottom panel of Fig. 7.6), the situation is similar to that at solar metallicity. The spread in carbon on the main sequence is not as large as for solar at around 0.5 dex (0.0 ± 0.25) compared to 1 dex at solar, however the number of observed stars is significantly less. Again, the change in carbon due to FDU is only around 0.2 dex in our models (there is no significant change due to thermohaline mixing), indicating that it is reasonable to assume that giant branch carbon abundances can predict initial carbon on the main sequence. Due to the spread in carbon observations on the main sequence and giant branch, it is difficult to constrain or compare with the thermohaline mixing implementation parameters.

In Figs. 7.11 - 7.25 (in the Appendix of this chapter), we show that the spread in initial carbon is not a consequence of combining observations of multiple clusters and cannot be traced back to a particular cluster.

7.4.2 Sub-solar metallicities ($[\text{Fe}/\text{H}] = -0.5, -1.0, -1.5$)

The observed sample stars at solar and super-solar metallicities predominantly consist of stars that are on the main sequence, making it difficult to constrain the parameters of the thermohaline mixing mechanism at those metallicities. At sub-solar metallicities where the stellar populations are older, there are few observed main sequence stars and the majority of the observations are giants or sub-giants.

The spread in the carbon data is too large to constrain the best-fit model initial mass and thermohaline mixing implementation, therefore at these low metallicities we use the observed lithium abundances. It is likely that the

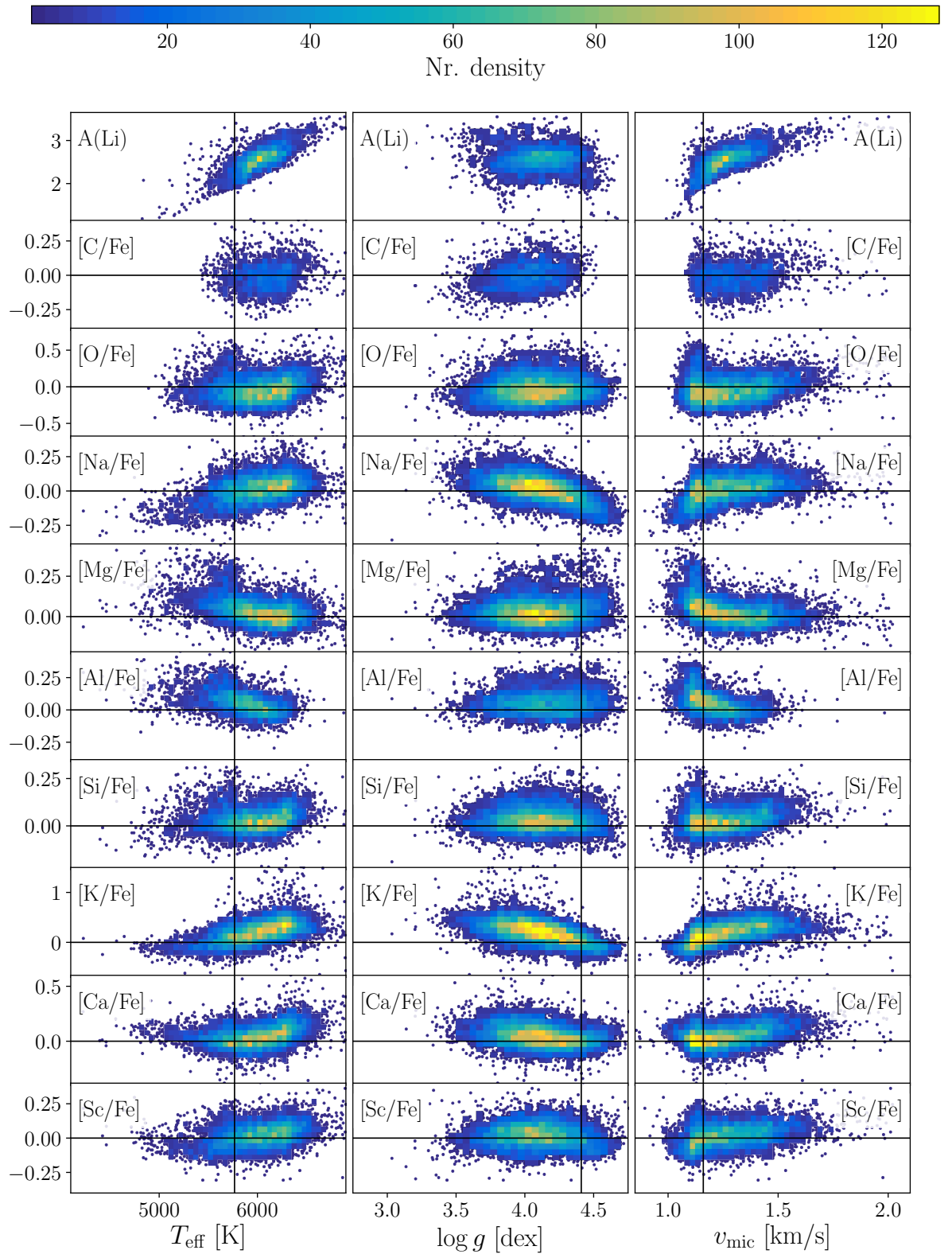


FIGURE 7.10: Elemental abundances relative to iron (except for lithium) for dwarf, turn-off and subgiant stars in the GALAH survey sample used by Buder et al. (2018) as a function of T_{eff} (left panels), $\log g$ (middle panels), and microturbulence velocity (v_{mic} , right panels). Colour indicates the number of stars in each bin. Of relevance to this section is the carbon abundances (second row of panels). Figure is Fig. A.5 from Buder et al. (2018).

spread in carbon is due to a spread in initial carbon abundances (as suggested for the solar/super-solar metallicity data above and the extremely metal-poor sample discussed in Chapter 6, Henkel et al., 2018) as well as varying $[\alpha/\text{Fe}]$ enhancement (discussed in §7.5). Large star-to-star variations in the abundances of carbon and nitrogen have also been observed in globular clusters (e.g., see Gratton, Sneden, and Carretta, 2004; Lardo et al., 2012, and references therein).

Observations of the Milky Way infer that stars at sub-solar metallicities are likely to be older than our Sun and are therefore of lower mass than our Sun, as shown by age-metallicity distributions and associated isochrone modelling (we note that age-metallicity distributions also show a large spread, Bergemann et al., 2014; Mackereth et al., 2017). At $[\text{Fe}/\text{H}] = -0.5$, the top panel of Fig. 7.7 shows that a stellar model with mass $< 1 M_{\odot}$ with our modified thermohaline mixing mechanism agrees with the data. The figure also shows that a $1.3 M_{\odot}$ stellar model with the standard thermohaline implementation matches reasonably well, however such an initial mass does not make sense for the reasons stated above. A $0.8 M_{\odot}$ model with $[\text{Fe}/\text{H}] = -0.5$ has an RGB-tip age of 9.42 Gyr, which is considerably older than two of the GES clusters at this metallicity (NGC4815 and NGC2243) but is within age estimate uncertainties for the other two GES clusters (NGC5927 and 47 Tuc).

The top panels of Figs. 7.8 and 7.9 for $[\text{Fe}/\text{H}] = -1.0$ and -1.5 respectively both show that our $0.8 M_{\odot}$ model (or slightly less massive than this) with our modified implementation is the best match to the data. At $[\text{Fe}/\text{H}] = -1.0$ and -1.5 , the $0.8 M_{\odot}$ stellar model has RGB-tip ages of 17.25 and 15.07 Gyr respectively and main sequence turn-off ages of 15.21 and 13.54 Gyr respectively. The RGB-tip ages are longer than the estimated ages for the clusters at these metallicities (NGC6752, NGC2808, and NGC1851), which range from 9.2 to 13.8 Gyr, but the main sequence turn-off age for the model at $[\text{Fe}/\text{H}] = -1.5$ is within uncertainties.

7.5 Discussion

As described briefly in §7.1.2, the study by Masseron and Gilmore (2015) using APOGEE data of the Galactic thick and thin discs revealed trends in RGB stellar abundances in terms of $[\text{C}/\text{N}]$ and $[\alpha/\text{Fe}]$. We make comparisons to that study because our models are analogous to the thick and thin disc populations (our solar and super-solar metallicity models with no $[\alpha/\text{Fe}]$ enhancement represent some of the thin disc population and our sub-solar metallicity models with $[\alpha/\text{Fe}]$ enhancement represent part of the thick disc/halo population). We also make comparisons to studies that use GES data.

7.5.1 Solar and super-solar metallicities ($[\text{Fe}/\text{H}] = 0.0, +0.3$)

The Lagarde et al. (2012b) stellar models used by Masseron and Gilmore (2015) show that for stars at solar metallicity (i.e., thin disc stars with no

α element enhancement), the [C/N] ratio does not change significantly on the upper RGB *post-FDU*. This is in agreement with the results found for other approximately solar metallicity clusters using GES data (i.e., Trumpler 20, NGC4815, NGC6705, Collinder 261, and Melotte 66, Tautvaišienė et al., 2015; Drazdauskas et al., 2016a), but exceptions exist where thermohaline mixing models agree with observations (e.g., NGC4609, NGC531, NGC2324, NGC2477, and NGC3960, Drazdauskas et al., 2016b; Tautvaišienė et al., 2016). Our models show that carbon does not change significantly on the upper RGB. This is because higher-metallicity stars have a steeper temperature gradient than their lower-metallicity counterparts. Church et al. (2014) show that the thermohaline instability occurs at a similar temperature in both solar- and low-metallicity stars, therefore the cooler thermoahline region is cooler in high-metallicity stars and the decline in surface abundances is not as steep. We can hypothesise, as stated in §7.4, that the spread of carbon abundances observed on the RGB is a result of a spread in initial carbon on the main sequence.

Masseron and Gilmore (2015) calculate that stars in the thin disc with $[\text{Fe}/\text{H}] = 0$ are best modelled with initial masses of $1.06 - 1.38 M_{\odot}$, which is consistent with our findings using the lithium abundances in the top panel of Fig. 7.5. We note that the match found by Masseron and Gilmore (2015) is not perfect, particularly on the upper RGB and for stars with $-0.3 < [\text{C}/\text{N}] < -0.1$. Current understanding of stellar evolution predicts that a unique solution must match both carbon and lithium, and because we find a model that agrees well with the observed lithium abundances but no single model for carbon, this provides further support to the conclusion that the spread of carbon observed on the RGB is due to a spread in initial carbon. The spread in initial carbon could also be affected by a chemical inhomogeneity in the Galaxy and/or the contribution from low- to intermediate-mass AGB stars.

Another factor that may contribute to the spread in carbon on the upper RGB is the value of the $[\alpha/\text{Fe}]$ enhancement. Masseron and Gilmore (2015) found that there is a gradient in C/N for thin disc stars, including those with solar and super-solar metallicities. Indeed a variation in $[\alpha/\text{Fe}]$ between 0 and 0.1, which is possible for thin disc stars, is found to be correlated with a significant change in the C/N ratio and could therefore also contribute to the spread in RGB carbon abundances seen in the bottom panels of Figs. 7.5 and 7.6.

7.5.2 Sub-solar metallicities ($[\text{Fe}/\text{H}] = -0.5, -1.0, -1.5$)

The models used by Masseron and Gilmore (2015) underestimate the C/N ratio for thick disc stars on the upper RGB. This indicates that there is either too much surface nitrogen or not enough surface carbon in their models, implying that perhaps too much CN-cycled material is dredged up (which would increase nitrogen and decrease carbon) or the thermohaline mixing mechanism employed is not appropriate (extra mixing is important at these metallicities, for reasons discussed many times previously). Our modified thermohaline mixing mechanism results in higher abundances of surface

carbon compared to the standard implementation, and this difference becomes more significant with decreasing metallicity. However, even for our lowest metallicity models with $[\text{Fe}/\text{H}] = -1.5$, the difference is not large enough to account for the discrepancy between the models and observations found by Masseron and Gilmore (2015).

Additionally, unlike for the thin disc stars, Masseron and Gilmore (2015) do not find any trend of $[\alpha/\text{Fe}]$ and $[\text{C}/\text{N}]$ for the thick disc stars. This indicates that the spread in carbon is not influenced strongly by variations in $[\alpha/\text{Fe}]$ enhancement and is mainly driven by a spread in initial carbon.

The lithium abundances at these metallicities are observed for most of the RGB evolution, and observations are particularly numerous after the luminosity function bump (predicted start of extra mixing). Therefore the lithium abundances provide a much tighter constraint on our stellar model masses and preferred thermohaline mixing scheme. The standard thermohaline implementation depletes lithium too quickly, therefore our modified scheme is a better fit to the data at these metallicities.

7.5.3 Conclusions

The spread in carbon data (particularly at metallicities below solar) is too large to provide constraints on the best-fit model and thermohaline mixing implementation. This spread however suggests that there is likely a significant variation in initial carbon in these populations and that the low-metallicity populations are most likely also affected by a variation in $[\alpha/\text{Fe}]$ enhancement. The effect of thermohaline mixing becomes more apparent in stellar populations and theoretical stellar models as mass and metallicity decrease, therefore for populations where $[\text{Fe}/\text{H}] \geq -0.5$, our results suggest that observed carbon abundances of giants remain relatively unchanged from main sequence abundances. The magnitude of the decrease in carbon on the RGB due to FDU is within the uncertainty of the observations.

Lithium observations in this sample provide a much better constraint for our stellar models than the carbon abundances. The solar and super-solar metallicity samples show a spread in lithium abundances on the main sequence and giant branch (most likely due to rotation, Palacios et al., 2003), making it difficult to determine which model (in terms of mass and thermohaline mixing implementation) agrees with the data. The most metal-rich sample (with $[\text{Fe}/\text{H}] = +0.3$) would be well-matched by a model with initial mass between 1.5 and $2 M_{\odot}$, however it is unclear whether our modified thermohaline mixing mechanism or the standard implementation is best due to the spread in the data. For the solar metallicity sample, our modified thermohaline mixing model with an initial mass of between 1.0 and $1.3 M_{\odot}$ would agree with the data and the main sequence turn-off mass of M67 ($1.22 M_{\odot}$). Models with the standard thermohaline mixing mechanism and these initial masses deplete lithium too fast.

The lower-metallicity samples contain more observations on the giant branch, which provide a better constraint for the thermohaline mixing implementation and the best-fit stellar model. The two lowest metallicity samples ($[\text{Fe}/\text{H}] = -1.5$ and -1.0) would be well-matched by a stellar model with our modified thermohaline mixing mechanism and an initial stellar mass of $< 0.8 M_{\odot}$, however due to the spread in the data and taking into account the uncertainties in the observations, our $0.8 M_{\odot}$ model is a reasonable match. The slightly sub-solar metallicity sample with $[\text{Fe}/\text{H}] = -0.5$ would agree with a model the modified thermohaline mixing mechanism and an initial stellar mass of $< 1.0 M_{\odot}$.

To draw more absolute conclusions and constrain our stellar models, more observations are required, particularly of carbon at low metallicities and lithium in solar and super-solar metallicity giants.

Finally, we reiterate what the results of this chapter reveal about the thermohaline mixing mechanism, particularly with regards to the research questions identified in §7.1. We conclude that extra mixing is observable in the surface lithium abundances of the solar and super-solar metallicity samples and more accurate observations are required to reveal the extra mixing signature in the carbon abundances. As discussed above, it is difficult to constrain stellar models using carbon observations due to the spread in initial abundances. We reason that this spread is most likely a consequence of carbon abundance variation in the protostellar material and α element enhancement. Finally, although the physical mechanism of extra mixing is not clear, our results for the low metallicity sample show that the standard thermohaline mixing theory cannot sufficiently match observations, which indicates that modifications to the standard implementation (or a new theory altogether) is required.

7.6 Acknowledgements

This work has made use of data from the European Space Agency (ESA) mission *Gaia* (<https://www.cosmos.esa.int/gaia>), processed by the *Gaia* Data Processing and Analysis Consortium (DPAC, <https://www.cosmos.esa.int/web/gaia/dpac/consortium>). Funding for the DPAC has been provided by national institutions, in particular the institutions participating in the *Gaia* Multilateral Agreement.

7.7 Appendix

The following figures are identical to Figs. 7.5- 7.9, however here we distinguish observations of each individual cluster.

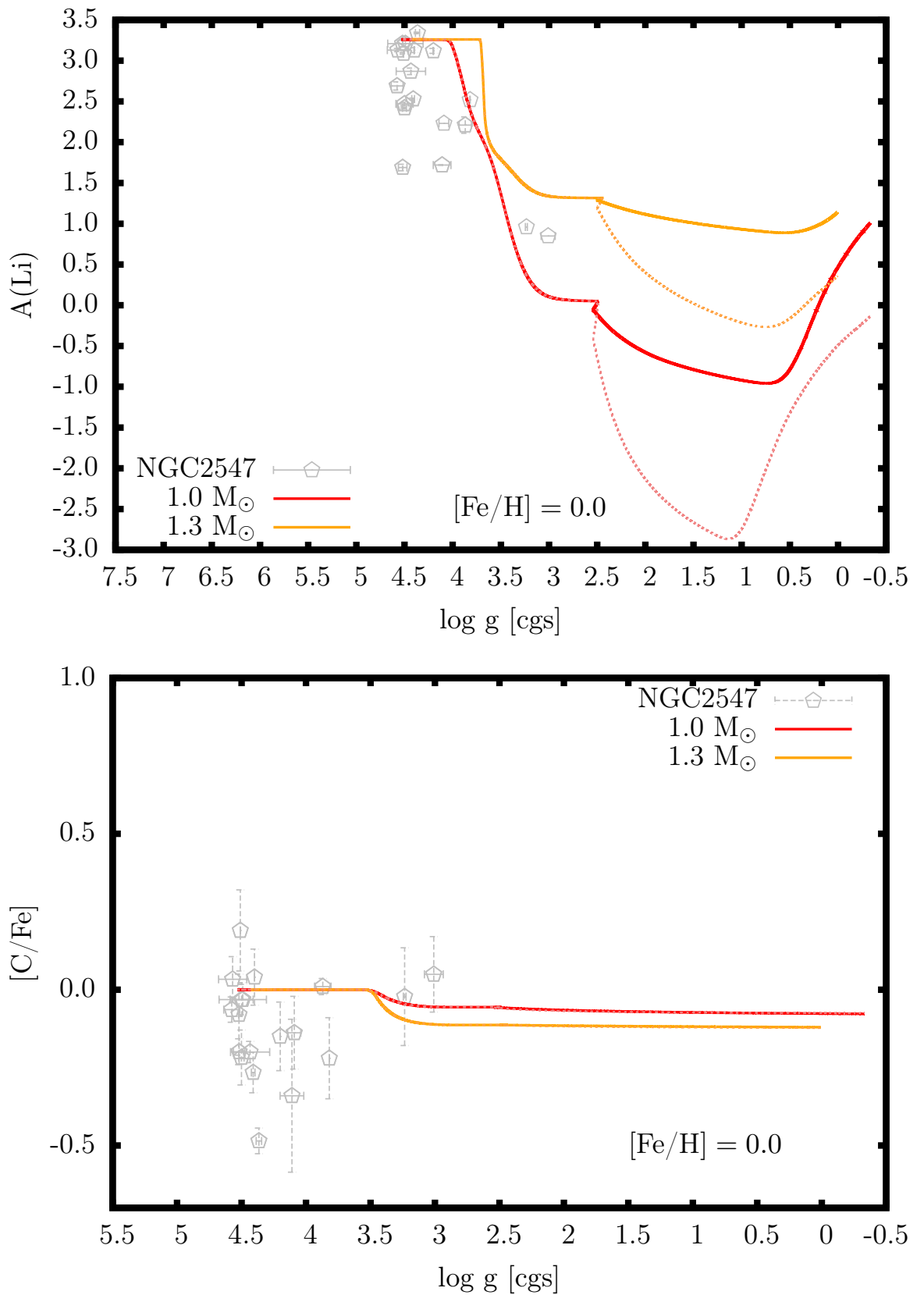


FIGURE 7.11: Lithium ($A(\text{Li})$, top panel) and carbon ($[\text{C}/\text{Fe}]$, bottom panel) abundances as a function of surface gravity. The curves are our models with $[\text{Fe}/\text{H}] = 0$, colours represent different masses (refer to key for details). For each curve, solid lines represent the modified thermohaline mechanism and dashed lines represent the standard implementation. Filled triangles are GES abundances from NGC2547.

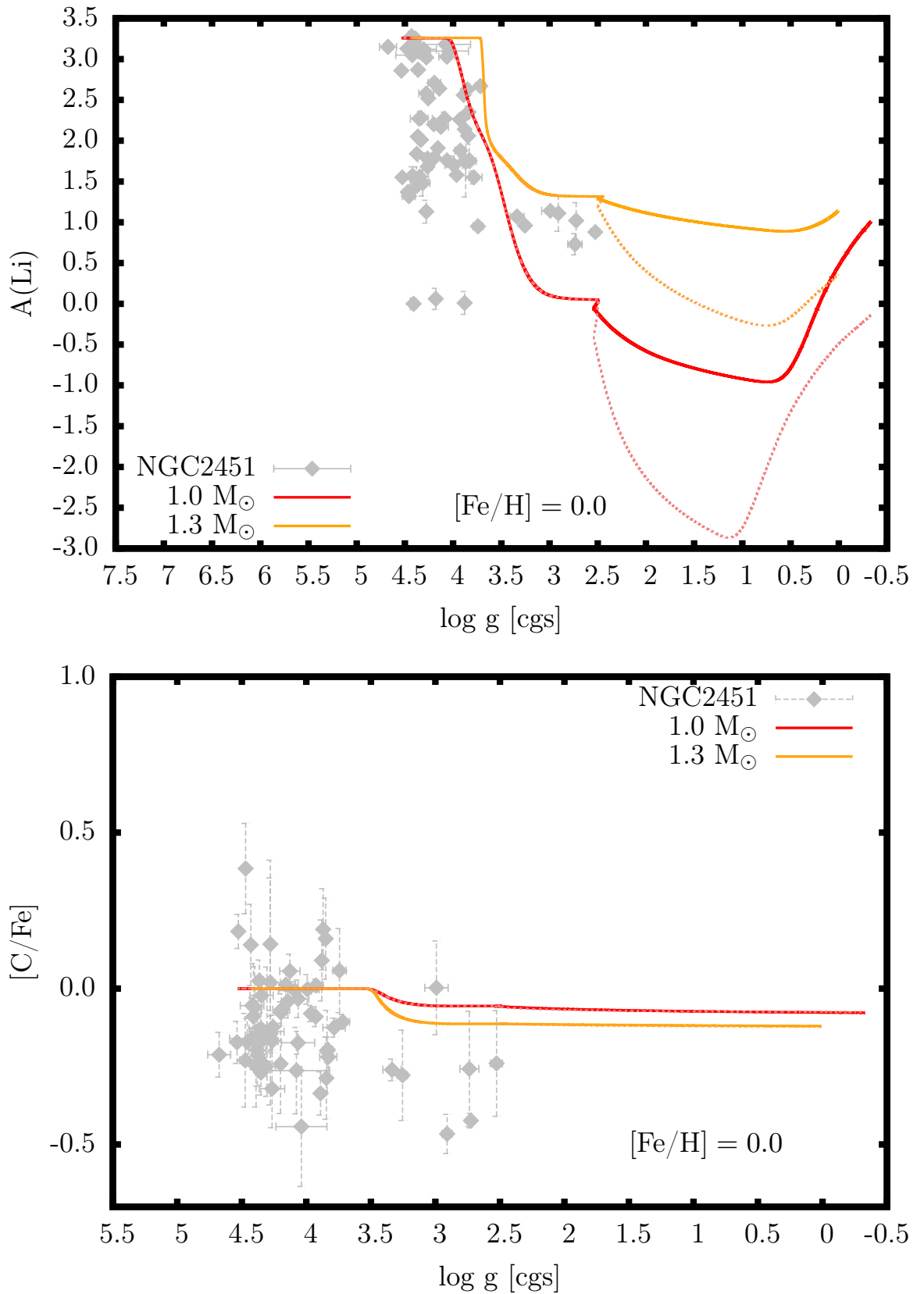


FIGURE 7.12: Lithium ($A(\text{Li})$, top panel) and carbon ($[\text{C}/\text{Fe}]$, bottom panel) abundances as a function of surface gravity. The curves are our models with $[\text{Fe}/\text{H}] = 0$, colours represent different masses (refer to key for details). For each curve, solid lines represent the modified thermohaline mechanism and dashed lines represent the standard implementation. Filled triangles are GES abundances from NGC2451.

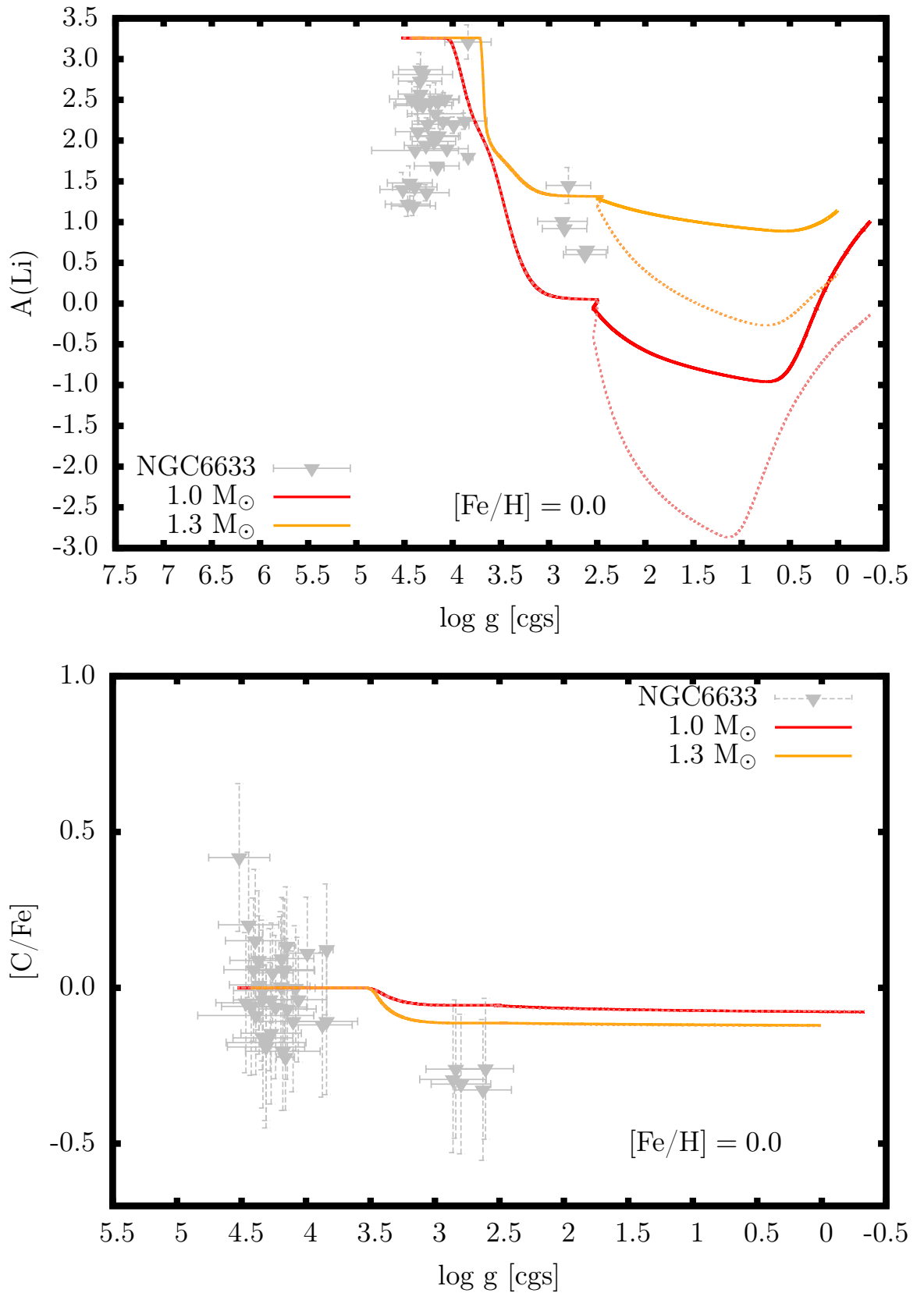


FIGURE 7.13: Lithium ($A(\text{Li})$, top panel) and carbon ($[\text{C}/\text{Fe}]$, bottom panel) abundances as a function of surface gravity. The curves are our models with $[\text{Fe}/\text{H}] = 0$, colours represent different masses (refer to key for details). For each curve, solid lines represent the modified thermohaline mechanism and dashed lines represent the standard implementation. Filled triangles are GES abundances from NGC6633.

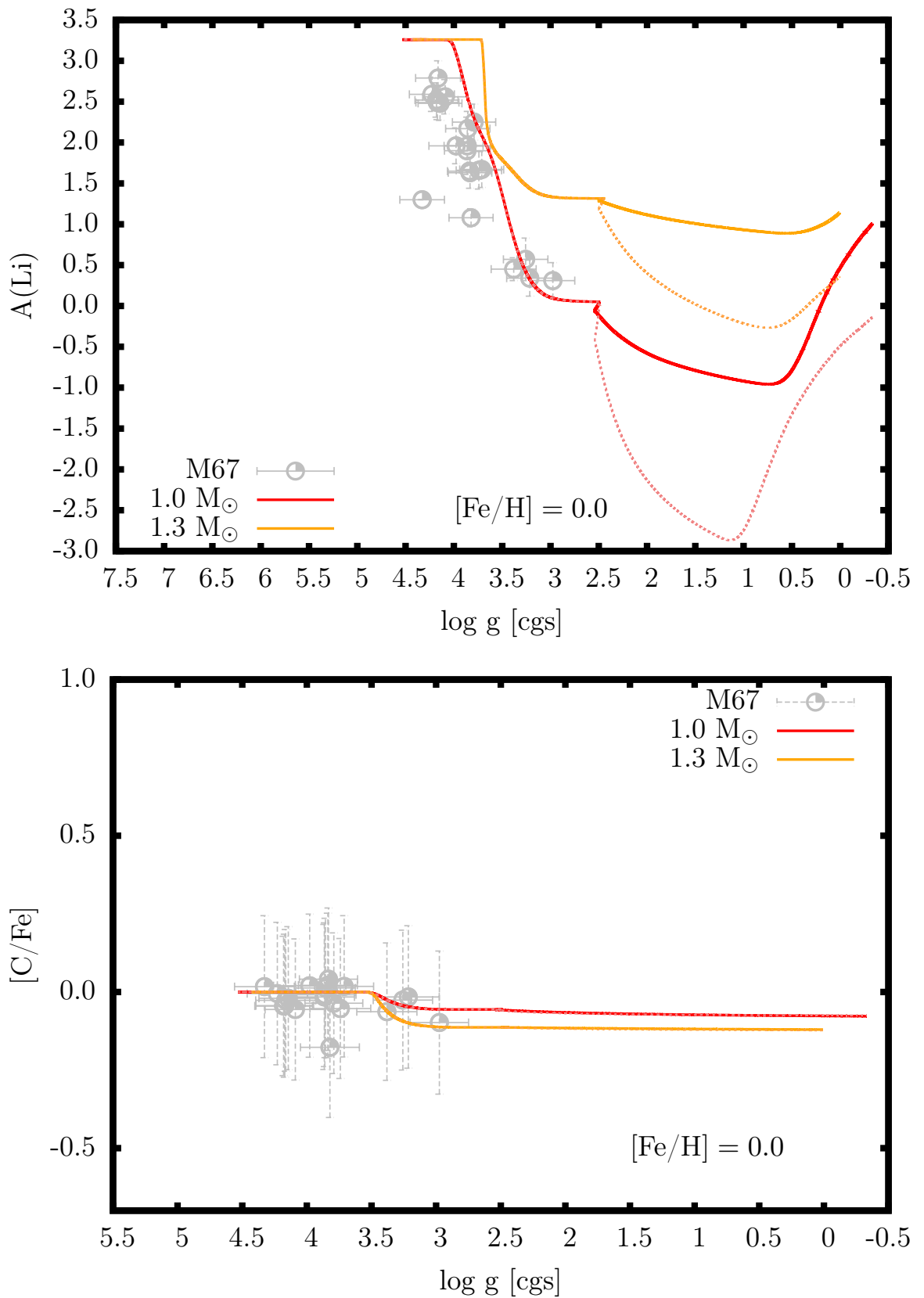


FIGURE 7.14: Lithium ($A(\text{Li})$, top panel) and carbon ($[\text{C}/\text{Fe}]$, bottom panel) abundances as a function of surface gravity. The curves are our models with $[\text{Fe}/\text{H}] = 0$, colours represent different masses (refer to key for details). For each curve, solid lines represent the modified thermohaline mechanism and dashed lines represent the standard implementation. Filled triangles are GES abundances from M67.

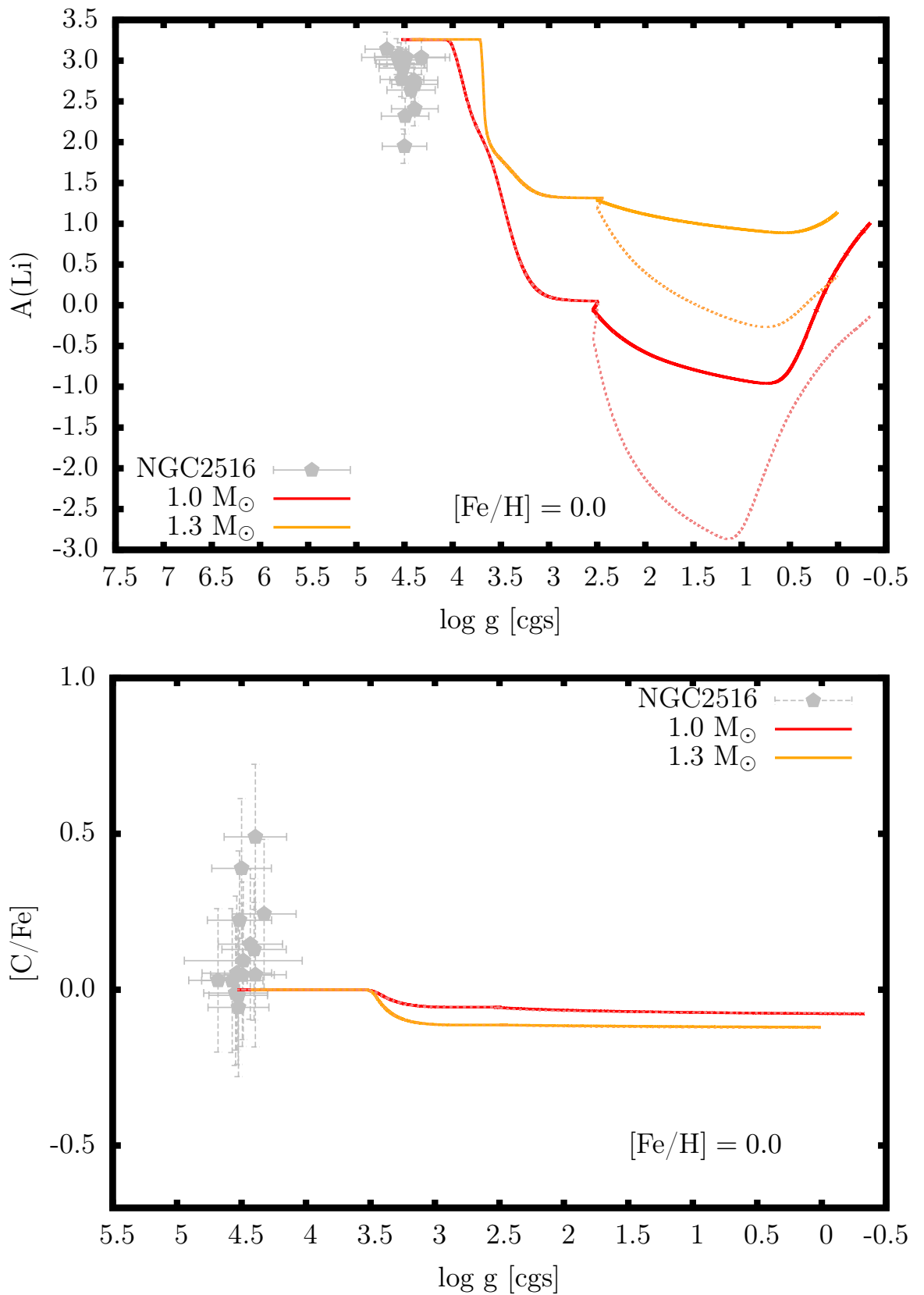


FIGURE 7.15: Lithium ($A(\text{Li})$, top panel) and carbon ($[\text{C}/\text{Fe}]$, bottom panel) abundances as a function of surface gravity. The curves are our models with $[\text{Fe}/\text{H}] = 0$, colours represent different masses (refer to key for details). For each curve, solid lines represent the modified thermohaline mechanism and dashed lines represent the standard implementation. Filled triangles are GES abundances from NGC2516.

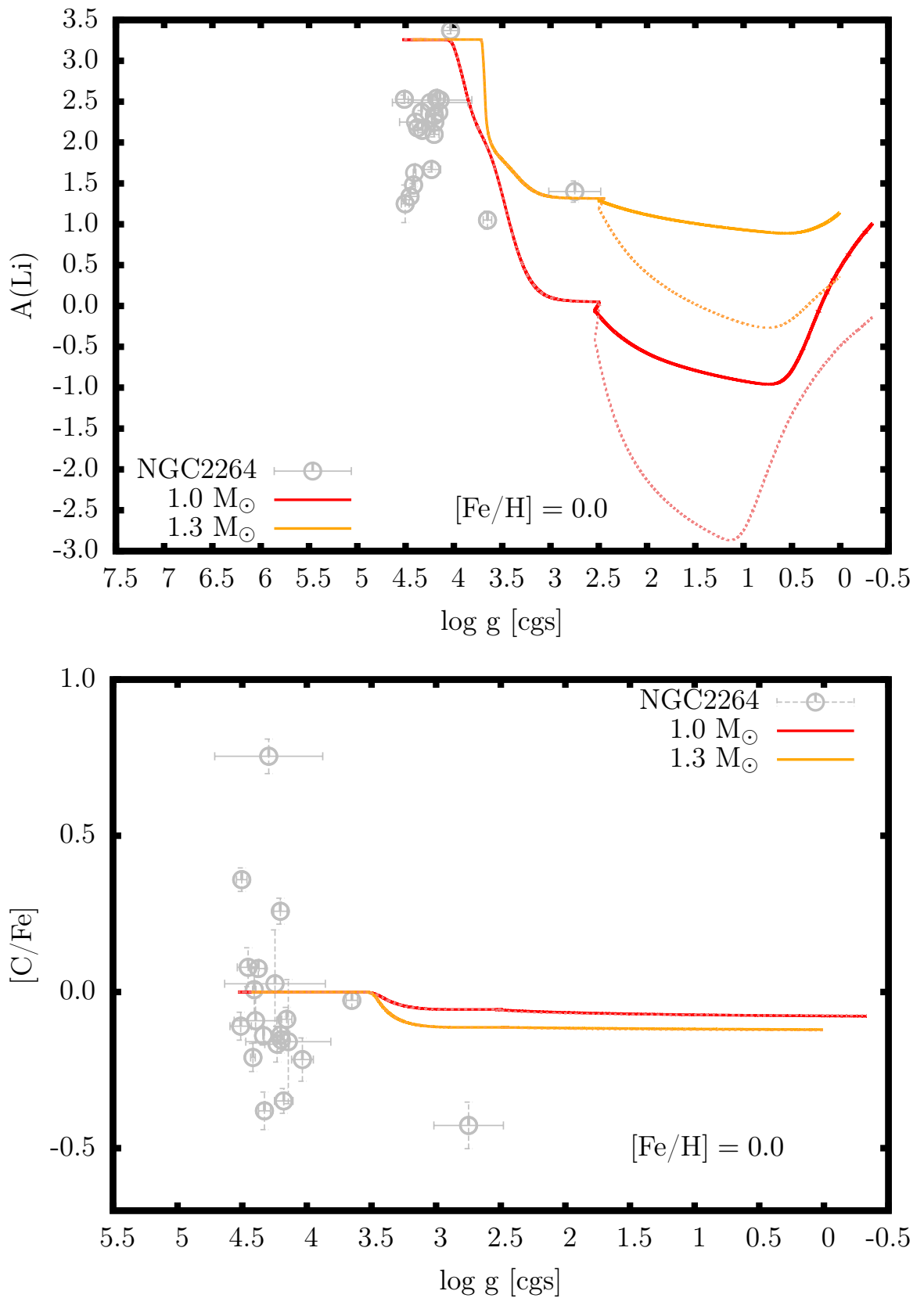


FIGURE 7.16: Lithium ($A(\text{Li})$, top panel) and carbon ($[\text{C}/\text{Fe}]$, bottom panel) abundances as a function of surface gravity. The curves are our models with $[\text{Fe}/\text{H}] = 0$, colours represent different masses (refer to key for details). For each curve, solid lines represent the modified thermohaline mechanism and dashed lines represent the standard implementation. Filled triangles are GES abundances from NGC2264.

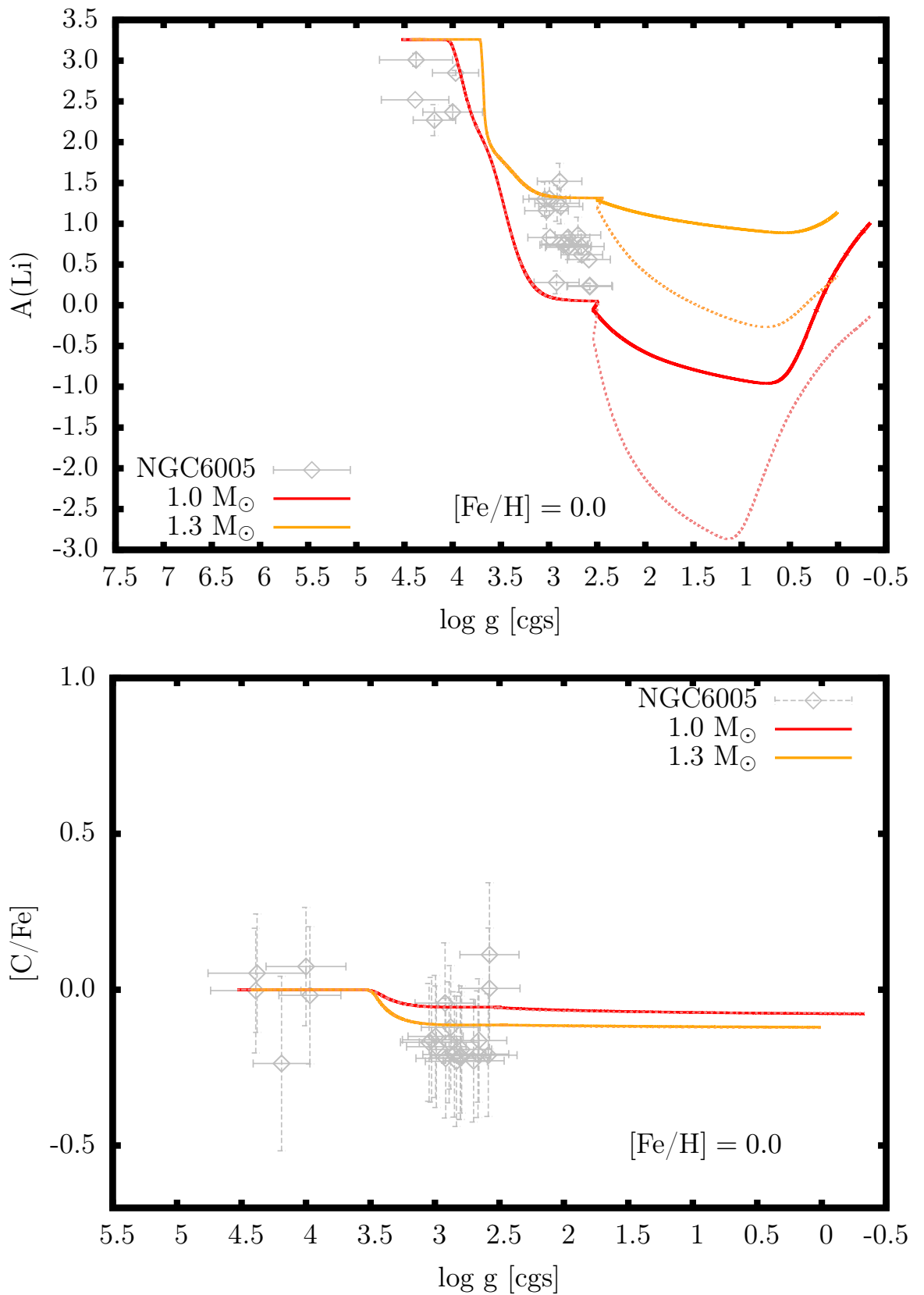


FIGURE 7.17: Lithium ($A(\text{Li})$, top panel) and carbon ($[\text{C}/\text{Fe}]$, bottom panel) abundances as a function of surface gravity. The curves are our models with $[\text{Fe}/\text{H}] = 0$, colours represent different masses (refer to key for details). For each curve, solid lines represent the modified thermohaline mechanism and dashed lines represent the standard implementation. Filled triangles are GES abundances from NGC6005.

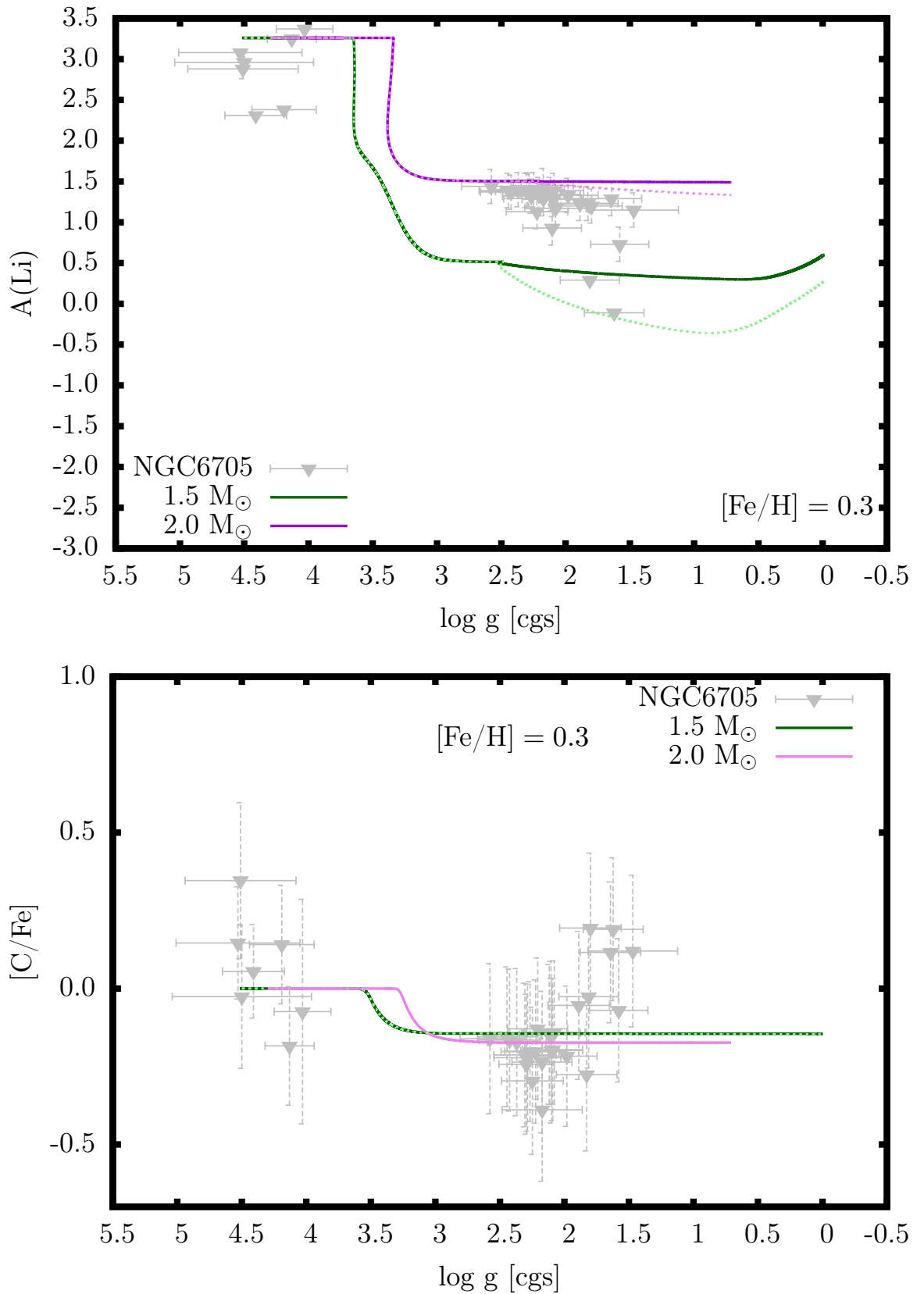


FIGURE 7.18: Lithium ($A(\text{Li})$, top panel) and carbon ($[\text{C}/\text{Fe}]$, bottom panel) abundances as a function of surface gravity. The curves are our models with $[\text{Fe}/\text{H}] = +0.3$, colours represent different masses (refer to key for details). For each curve, solid lines represent the modified thermohaline mechanism and dashed lines represent the standard implementation. Filled triangles are GES abundances from NGC6705 (detailed in key).

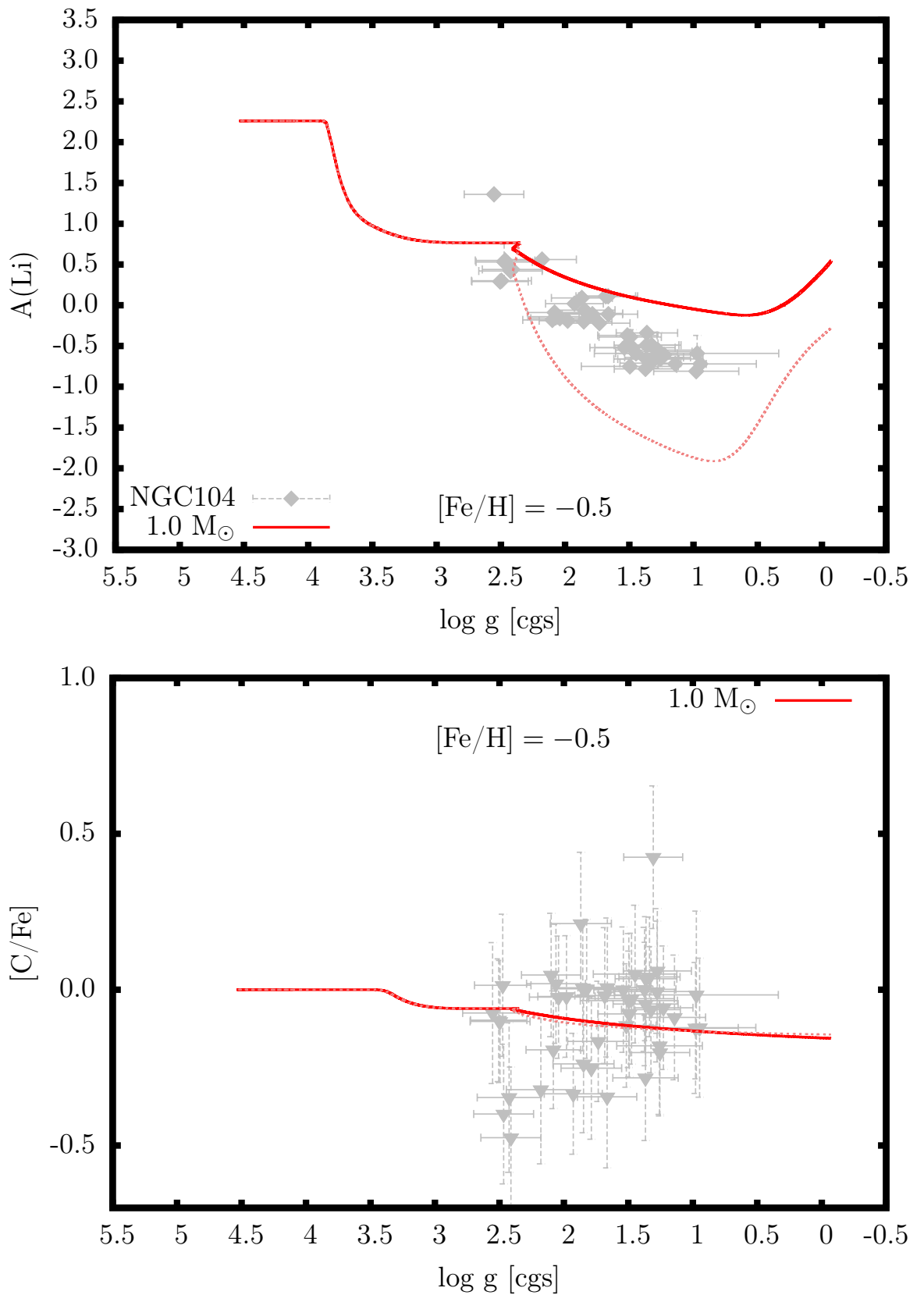


FIGURE 7.19: Lithium ($A(\text{Li})$, top panel) and carbon ($[\text{C}/\text{Fe}]$, bottom panel) abundances as a function of surface gravity. The curves are our models with $[\text{Fe}/\text{H}] = -0.5$, colours represent different masses (refer to key for details). For each curve, solid lines represent the modified thermohaline mechanism and dashed lines represent the standard implementation. Filled triangles are GES abundances from NGC104.

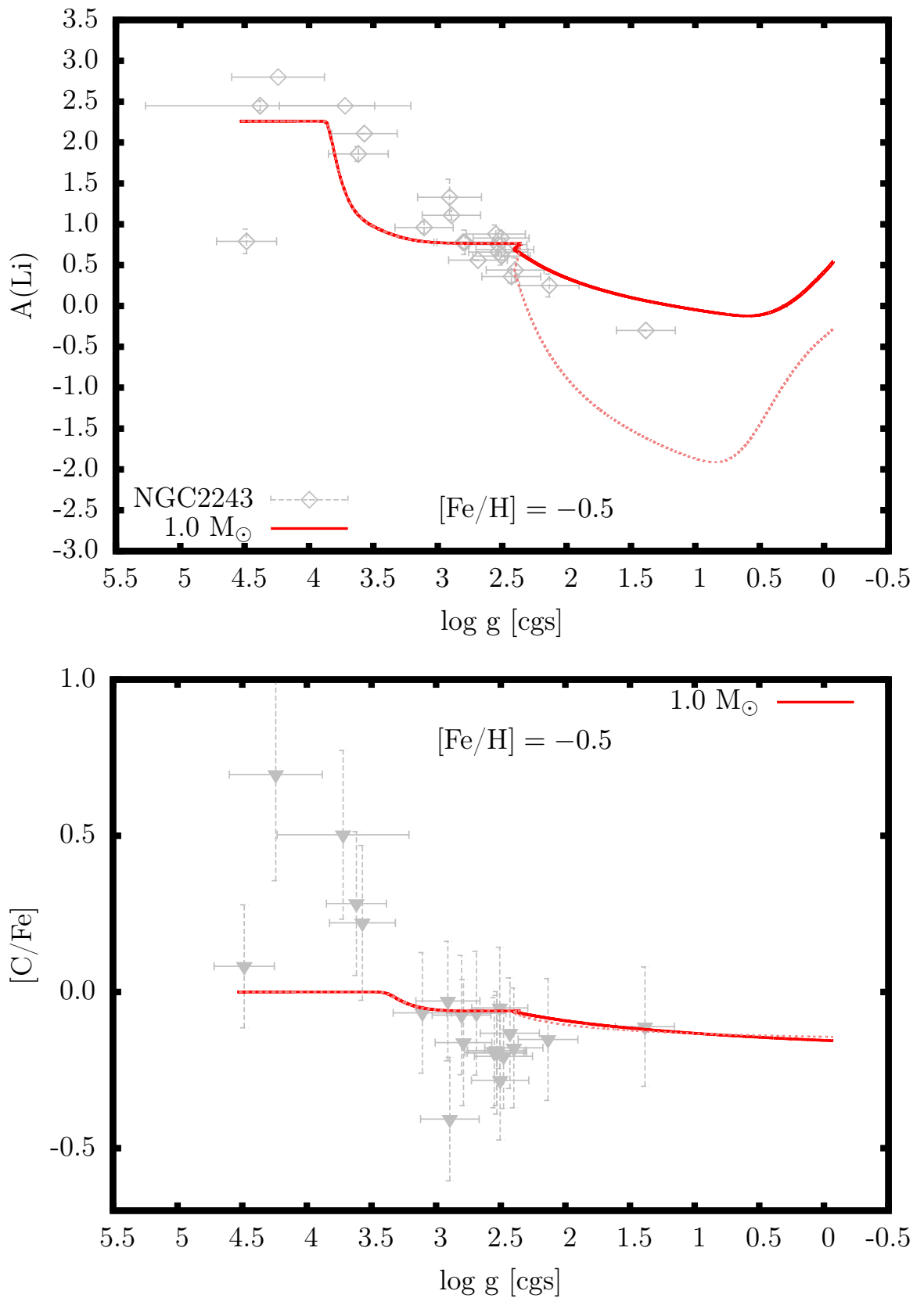


FIGURE 7.20: Lithium ($A(\text{Li})$, top panel) and carbon ($[\text{C}/\text{Fe}]$, bottom panel) abundances as a function of surface gravity. The curves are our models with $[\text{Fe}/\text{H}] = -0.5$, colours represent different masses (refer to key for details). For each curve, solid lines represent the modified thermohaline mechanism and dashed lines represent the standard implementation. Filled triangles are GES abundances from NGC2243.

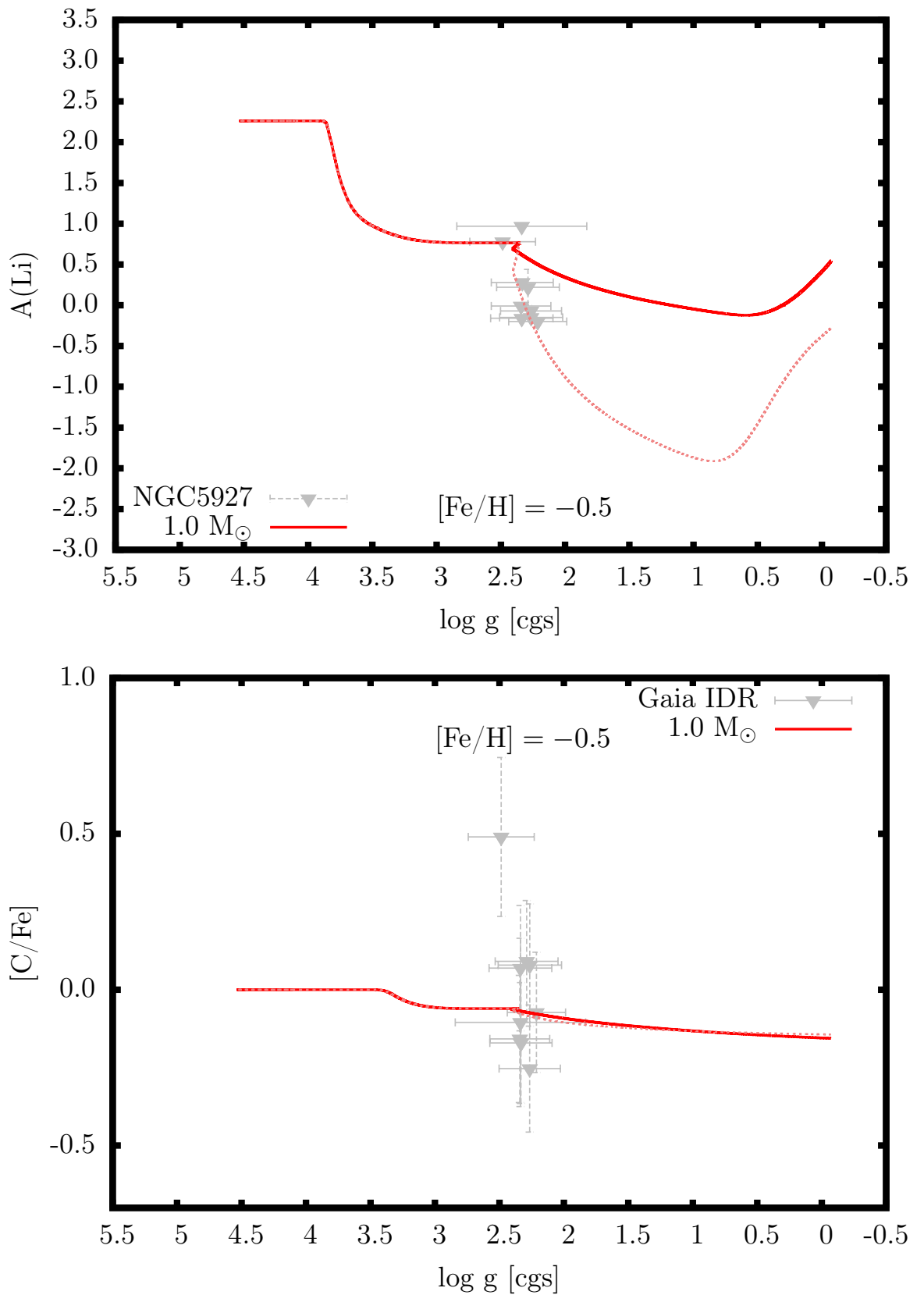


FIGURE 7.21: Lithium ($A(\text{Li})$, top panel) and carbon ($[\text{C}/\text{Fe}]$, bottom panel) abundances as a function of surface gravity. The curves are our models with $[\text{Fe}/\text{H}] = -0.5$, colours represent different masses (refer to key for details). For each curve, solid lines represent the modified thermohaline mechanism and dashed lines represent the standard implementation. Filled triangles are GES abundances from NGC5927.

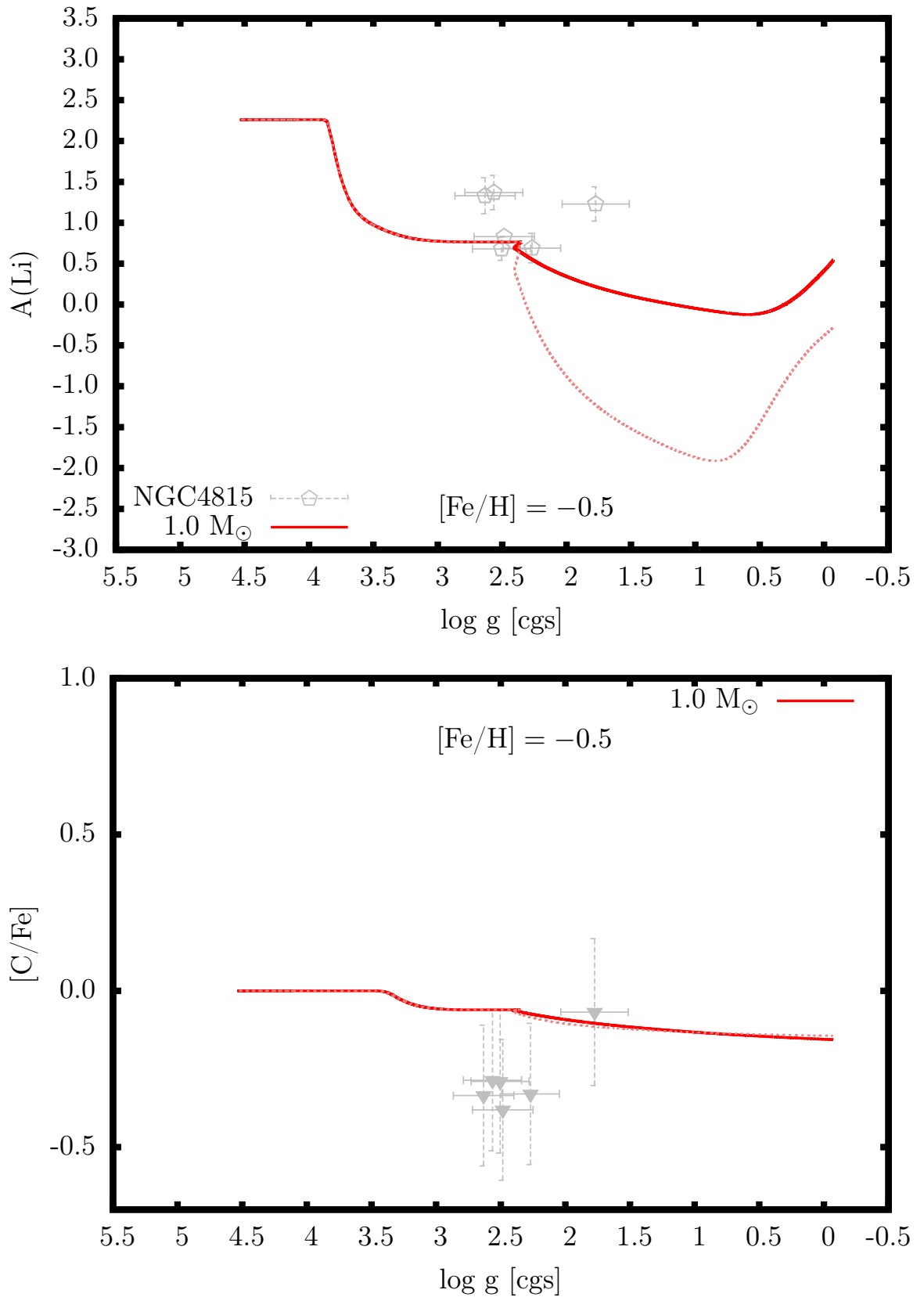


FIGURE 7.22: Lithium ($A(\text{Li})$, top panel) and carbon ($[\text{C}/\text{Fe}]$, bottom panel) abundances as a function of surface gravity. The curves are our models with $[\text{Fe}/\text{H}] = -0.5$, colours represent different masses (refer to key for details). For each curve, solid lines represent the modified thermohaline mechanism and dashed lines represent the standard implementation. Filled triangles are GES abundances from NGC4815.

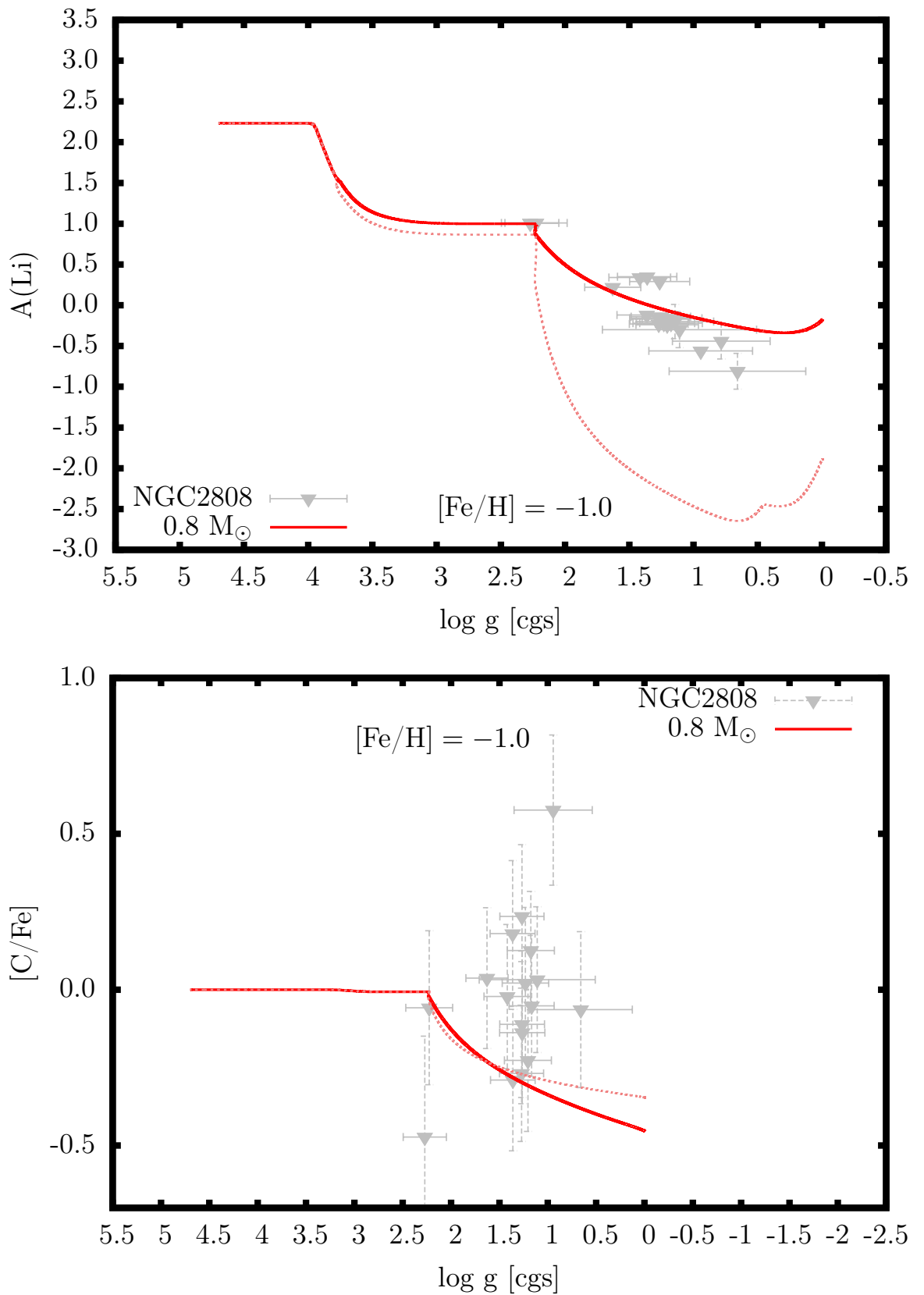


FIGURE 7.23: Lithium ($A(\text{Li})$, top panel) and carbon ($[\text{C}/\text{Fe}]$, bottom panel) abundances as a function of surface gravity. The curves are our models with $[\text{Fe}/\text{H}] = -1.0$, colours represent different masses (refer to key for details). For each curve, solid lines represent the modified thermohaline mechanism and dashed lines represent the standard implementation. Filled triangles are GES abundances from NGC2808.

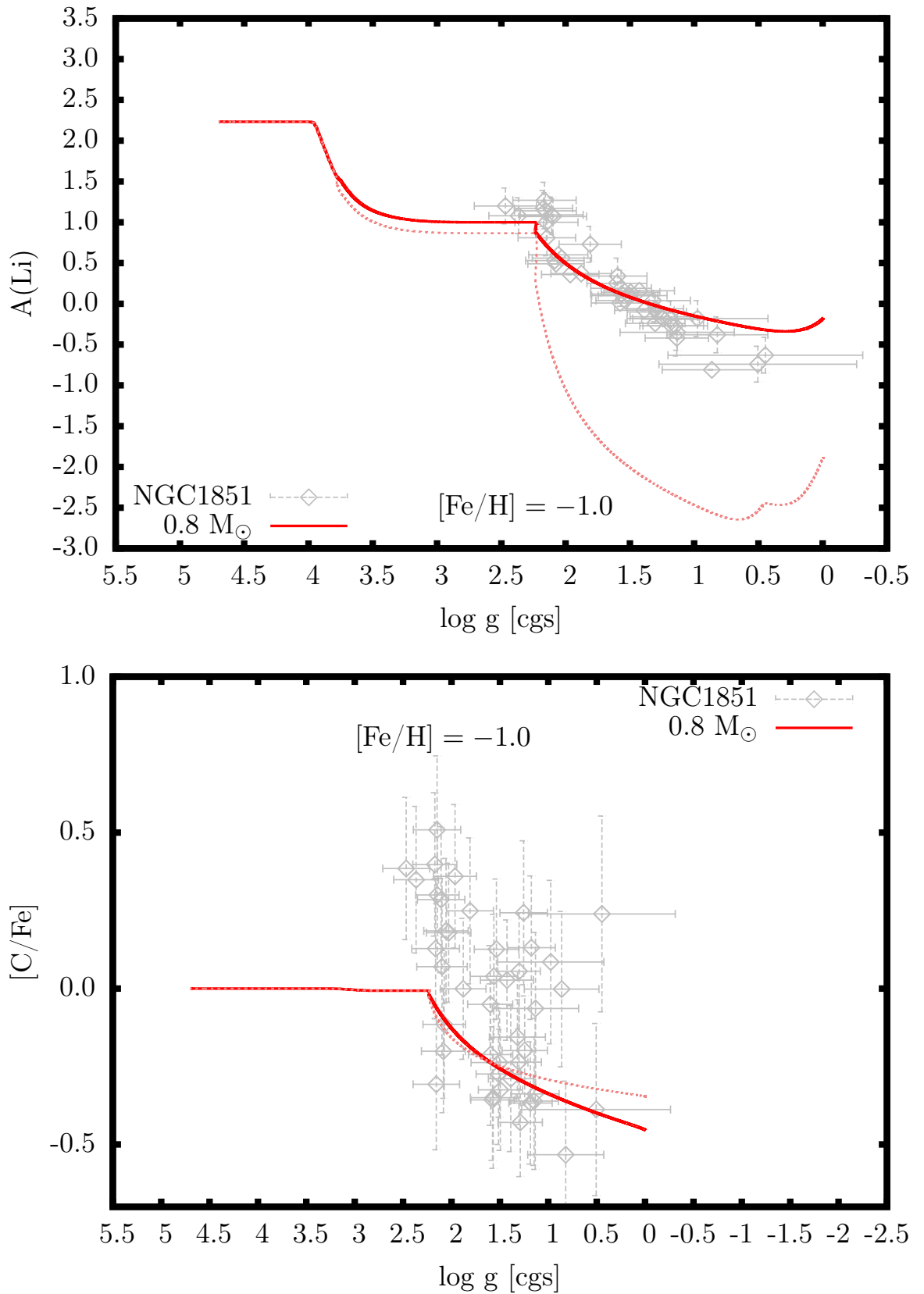


FIGURE 7.24: Lithium ($A(\text{Li})$, top panel) and carbon ($[\text{C}/\text{Fe}]$, bottom panel) abundances as a function of surface gravity. The curves are our models with $[\text{Fe}/\text{H}] = -1.0$, colours represent different masses (refer to key for details). For each curve, solid lines represent the modified thermohaline mechanism and dashed lines represent the standard implementation. Filled triangles are GES abundances from NGC1851.

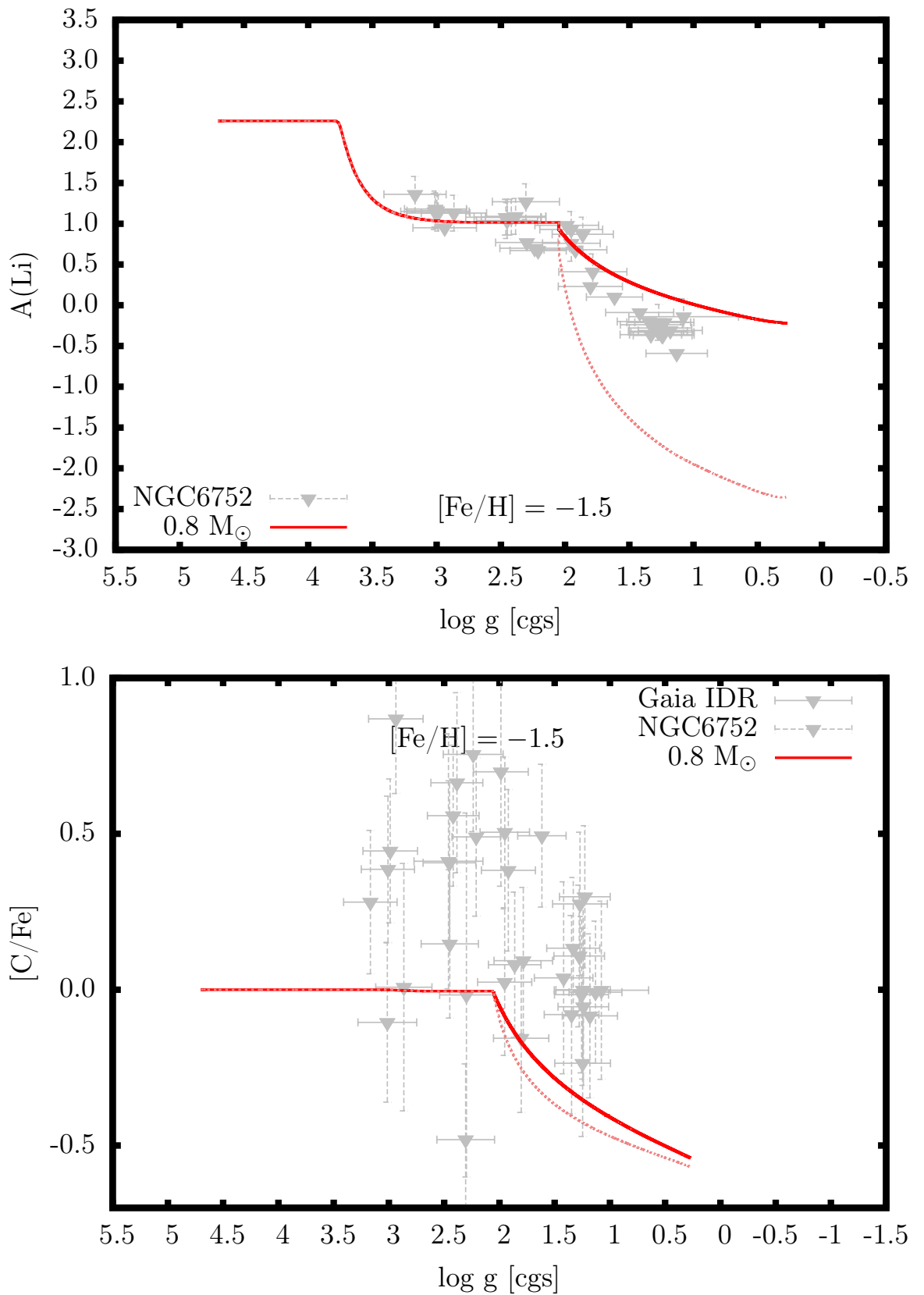


FIGURE 7.25: Lithium ($A(\text{Li})$, top panel) and carbon ($[\text{C}/\text{Fe}]$, bottom panel) abundances as a function of surface gravity. The curves are our models with $[\text{Fe}/\text{H}] = -1.5$, colours represent different masses (refer to key for details). For each curve, solid lines represent the modified thermohaline mechanism and dashed lines represent the standard implementation. Filled triangles are GES abundances from NGC6752.

Chapter 8

Conclusions and Future work

8.1 Concluding remarks

In this thesis our general aim was to further investigate the non-canonical mixing occurring in red giant branch stars. This “extra” mixing is characterised by surface abundance changes of particular pp chain and CNO-cycle elements including carbon, lithium, and nitrogen (see Lambert and Ries, 1977; Gilroy and Brown, 1991; Charbonnel, Brown, and Wallerstein, 1998; Gratton et al., 2000; Smith and Martell, 2003; Shetrone, 2003; Weiss et al., 2004; Martell, Smith, and Briley, 2008; Smiljanic et al., 2009; Lind et al., 2009, and references therein).

The physical mechanism of extra mixing is unknown and several explanations have been postulated in the literature, including meridional circulation (von Zeipel, 1924a; von Zeipel, 1924b; Eddington, 1925; Vogt, 1925; Paczyński, 1973; Sweigart and Mengel, 1979) and rotation (Chanamé, Pinsonneault, and Terndrup, 2005; Palacios et al., 2006; Denissenkov, Pinsonneault, and MacGregor, 2009; Denissenkov, 2012). Stellar models show however that meridional circulation and rotation do not affect surface abundances in a significant way and therefore cannot explain the abundances changes caused by extra mixing (Sweigart and Mengel, 1979; Chanamé, Pinsonneault, and Terndrup, 2005; Palacios et al., 2006).

One popular solution to extra mixing is thermohaline mixing. Thermohaline mixing is a doubly-diffusive process and operates as finger-/blob-like structures across layers that differ in temperature and molecular weight (traditionally temperature and salinity, as the process was first discovered in the oceans). An environment suitable for thermohaline mixing occurs naturally in stellar interiors after first-dredge up, where the molecular weight changes above the hydrogen burning shell due to helium-3 fusion via ${}^3\text{He}({}^3\text{He}, 2p){}^4\text{He}$ (Ulrich, 1972; Kippenhahn, Ruschenplatt, and Thomas, 1980; Eggleton, Dearborn, and Lattanzio, 2006; Charbonnel and Zahn, 2007; Eggleton, Dearborn, and Lattanzio, 2008).

The thermohaline mixing theory is included in stellar evolution codes according to the prescription given by Ulrich (1972) and Kippenhahn, Ruschenplatt, and Thomas (1980), and includes a dimensionless parameter C that is dependent upon the aspect ratio α of the thermohaline mixing blobs/fingers. Stellar models that include thermohaline mixing according to the theory cannot match observations of carbon and lithium abundances to observations, as shown by Angelou et al. (2015) and in Fig. 8.1.

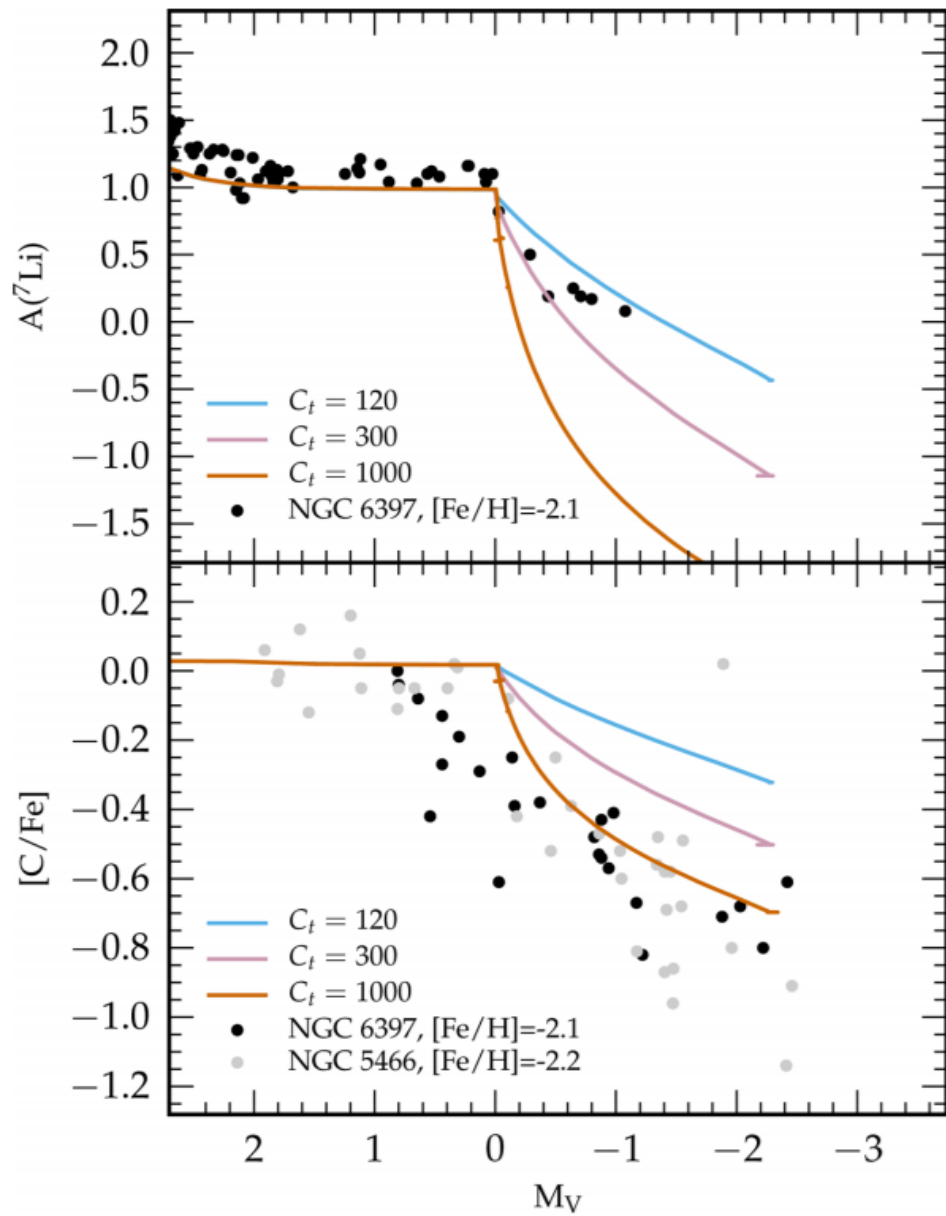


FIGURE 8.1: $A(\text{Li})$ (top panel) and $[\text{C}/\text{Fe}]$ (bottom panel) as functions of magnitude for stars in NGC6397 (black points) and NGC5466 (grey points). Curves are for a $0.8 M_{\odot}$, $Z = 0.00011$ model with $C = 120$ (blue curves), $C = 300$ (pink curves), and $C = 1000$ (orange curves). Observations of NGC6397 are from Lind et al. (2009) and observations of NGC5466 are from Shetrone et al. (2010). Figure is Fig. 10 from Angelou et al. (2015).

Henkel, Karakas, and Lattanzio (2017) extend the work of Angelou et al. (2015, and references therein) and further investigate the non-canonical mixing occurring in red giant branch stars.

As shown in Fig. 8.1, Angelou et al. (2015) found that to match observations of carbon and lithium in NGC6397, different C values (or thermohaline diffusion coefficients) were required. Current theoretical understanding of the thermohaline mixing mechanism does not support different coefficients for individual elements/molecules, therefore Angelou et al. (2015) concluded that modifications to the standard thermohaline theory, or a new mixing theory, were required.

This thesis extends the work of Angelou et al. (2015, and references therein) to further investigate possible solutions to this problem. Our investigations initially focused on the two stream advective scheme employed in our post-processing nucleosynthesis code (described in Chapter 4). We attempted to simultaneously match carbon and lithium abundances in NGC6397 by modifying the vertical velocity and the relative size of the up and down streams, however the changes to the surface abundances due to our modifications were not sufficient to explain the observations and no unique solution could be found.

We then proceeded to investigate modifications to the standard theory as implemented in the evolution code (described in Chapter 3). Although purely phenomenological, our results show that by invoking a phenomenological temperature dependence on the mixing scheme in the thermohaline region, we can match giants in NGC6397 using a single set of parameters (Henkel, Karakas, and Lattanzio, 2017). This result had not been achieved previously and highlighted the requirement for modifications to the standard theory if it is to be applied as the mechanism altering abundances on the RGB after first dredge-up.

The next step in our investigations of thermohaline mixing was to study different populations of stars in the Galactic disc and halo, including extremely metal-poor (EMP, $[\text{Fe}/\text{H}] = -3.0$, Chapter 6), solar (Chapter 7), and super-solar ($[\text{Fe}/\text{H}] = +0.3$, Chapter 7) metallicity populations. We begin with the EMP population. In Chapter 6 we show that our stellar models with the modified thermohaline regime are a better match to the observations than the models with the standard implementation. Additionally, EMP stars are important in regards to understanding the evolution of the Milky Way therefore we can draw further conclusions from our results. Provided that the initial carbon abundance of a star/stellar population is known (or can be inferred from stellar modelling), a common tool used to estimate evolutionary stage of an EMP star is the amount of carbon depletion due to extra mixing on the RGB, often called the “carbon offset” (FDU in these stars does not change surface carbon). Applying appropriate offsets to stellar populations can allow the frequency of stars that were enhanced in carbon at birth to be determined, knowledge of which is important for Galactic evolution.

We find that currently available offsets overestimate the carbon offset by approximately 9.5% at $[\text{Fe}/\text{H}] \sim -3$ and will therefore overestimate the carbon-enhanced star frequency at metallicities where the effect of extra

mixing on stellar abundances is observable (Henkel et al., 2018). Furthermore, we also briefly note that studying the frequency of EMP stars is important for understanding the initial mass function, the formation and evolution of dwarf galaxies, as well as the first (population III) stars (see Helmi et al., 2006; Aoki et al., 2009; Frebel, Simon, and Kirby, 2014; Beers, 2018, and references therein).

The final study in this thesis (Chapter 7) investigates the application of the modified thermohaline mechanism in populations that are more metal-rich than those analysed previously, being the sub- to super-solar metallicity ranges ($-1.5 < [\text{Fe}/\text{H}] < +0.3$). Although extra mixing is theoretically observable at solar metallicity, there have been recent claims that the extra mixing signature is not present in solar metallicity stars (Souto et al., 2016) or is “suppressed” in α element enhanced populations (Masseron and Gilmore, 2015). We note that these results are from studies using data from the APOGEE survey, which measures carbon but not lithium.

Using Gaia-ESO survey internal data release 4 data that includes both carbon *and* lithium observations, we find from the lithium data that while it is unclear which version of the thermohaline implementation (standard or modified) is the best match to the super-solar sample ($[\text{Fe}/\text{H}] = +0.3$), the modified thermohaline models are good matches to the samples at lower metallicities ($[\text{Fe}/\text{H}] = 0, -0.5, -1.0, \text{ and } -1.5$). The spread in carbon is too large to constrain the stellar model parameters. This spread is most likely a combination of a spread in initial carbon of the population and $[\alpha/\text{Fe}]$ enhancement. We conclude that more accurate observations of carbon are needed to provide sufficient constraints to stellar models and further understand the spread in initial carbon.

At the time of publication/completion of the studies in this thesis, no physical mechanism had been identified that could justify the temperature dependence required. However, very recently, Sengupta and Garaud (2018) presented a physical phenomena that occurs in their simulations, which could explain the “enhanced efficiency” of fingering convection (i.e., thermohaline mixing) in RGB stars after the luminosity function bump. They perform direct numerical simulations using their code PADDI (Stellmach and Hansen, 2008; Traxler, Garaud, and Stellmach, 2011a; Stellmach et al., 2011) and find that the shear instability between thermohaline fingers is stabilised by rotation (a result also found by Medrano, Garaud, and Stellmach, 2014) and that an increase in the rotation rate does not significantly alter the thermohaline mixing rate. Interestingly, for their longer period simulations with lower resolution (the authors note that the resolution is still high enough to resolve mixing fingers), they find that large scale vortices can occur. These vortices show enhanced core concentrations of high molecular weight material and an increase in the downward vertical velocity component that results in enhanced chemical transport (i.e., more efficient fingering mixing). Fig. 8.2 shows the development of a vortex in one of their simulations.

However there are still caveats with this phenomenon. The vortices found in the simulations by Sengupta and Garaud (2018) may not frequently form under realistic stellar conditions. Sufficient rotation is required to trigger the formation of a vortex, however rotation that is too strong will decay

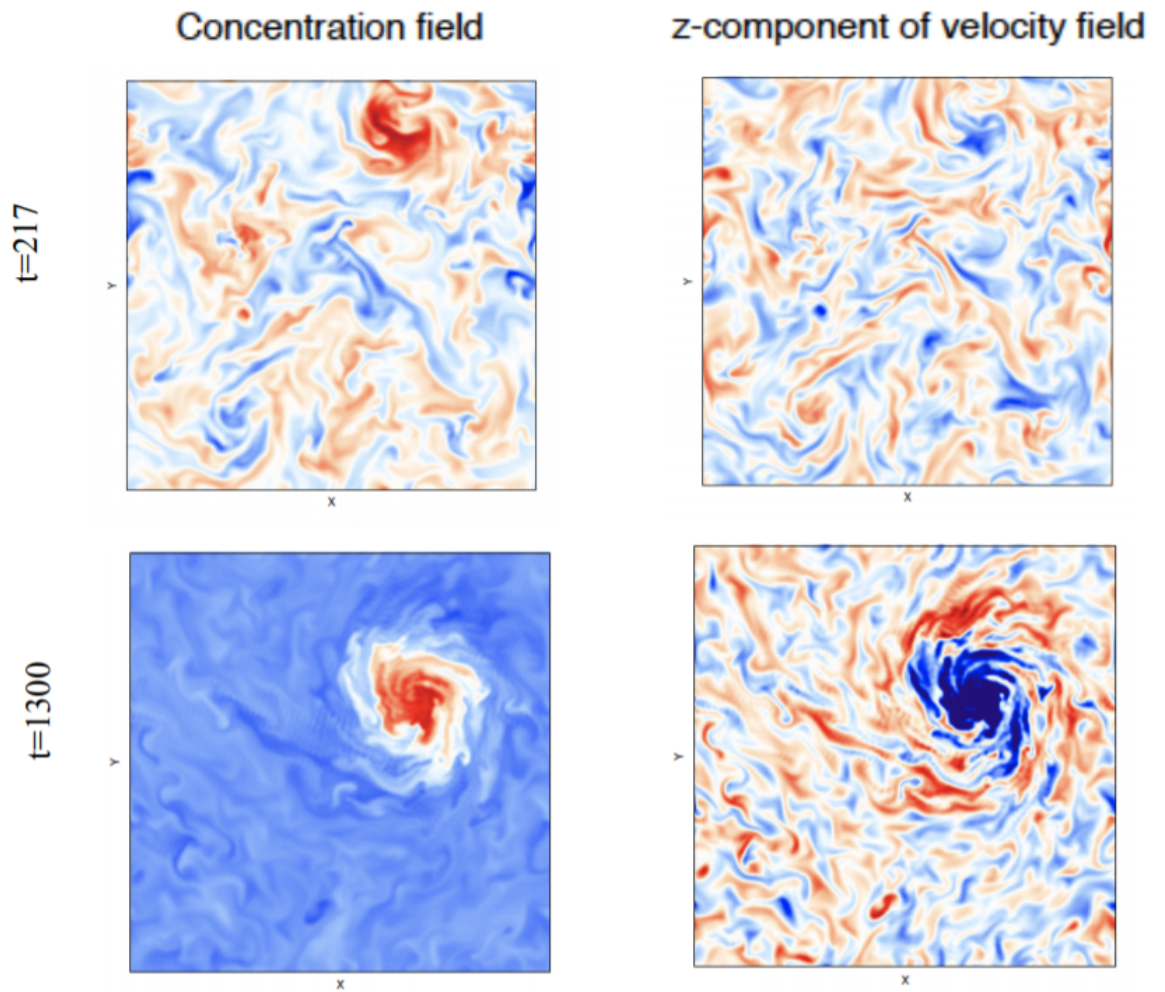


FIGURE 8.2: Chemical (left) and vertical velocity (right) horizontal snapshots at two time steps (refer to panels for details). The model run is detailed in Sengupta and Garaud (2018). Red and blue indicate positive and negative values respectively of the quantities. Figure is Fig. 9 from Sengupta and Garaud (2018).

all horizontal motion in the vortex. These conditions may be present near the poles of RGB stars yet is unlikely to occur at lower latitudes (Moll and Garaud, 2017; Sengupta and Garaud, 2018). Large-scale horizontal jets (as opposed to vortices) may form towards the equator though further research is required to determine if this scenario is likely (or indeed possible) and whether chemical transport via thermohaline fingers would be enhanced in such conditions (Sengupta and Garaud, 2018).

We conclude by stating that our phenomenological modification to the standard thermohaline mixing formalism demonstrates the need for further research (outlined briefly below) and more detailed observations, despite the fact that no confirmed physical mechanism currently exists. We reiterate however that there is promising research into a possible physical mechanism, as discussed above.

8.2 Future work

As was stated in the discussion and conclusions of the studies in this thesis, there are several predominant topics for future work that can follow on from this work.

1. *More observations of carbon (including isotopic carbon) and lithium are required for stars across all evolutionary stages and metallicities, particularly for stars along the red giant branch at solar metallicity.* This would assist in constraining and informing stellar evolution and modelling.
2. *Modelling rotation and thermohaline mixing in such a way that includes the interactive effect between other instabilities.* This direction of research has been started by Maeder et al. (2013) but requires implementation into stellar evolution codes (and parameterisation for 1D codes).
3. *Further development of multi-dimensional codes.* One-dimensional stellar codes have an important place in research and provide a fast, computationally cheap way of analysing mixing and burning in stars. However for simulations of (more) realistic stellar interiors, multiple dimensions are required. The results of such simulations can further inform and constrain 1D codes. For example, using their 1D stellar code, Henkel, Karakas, and Lattanzio (2017) concluded that the standard thermohaline mixing theory was insufficient, and found that a phenomenological modification (faster mixing in hot regions and slower mixing in cool regions) was required to match models to observations. The results of multi-dimensional simulations by Sengupta and Garaud (2018) show that vortices may form that have velocity profiles (refer to Fig. 8.2) that support the findings of Henkel, Karakas, and Lattanzio (2017).
4. *Applications to other areas of astrophysics.* This is a broad point, but may include applications to:
 - Dwarf galaxy studies, with regards to EMP stars and the frequency of carbon-enhanced metal-poor EMP stars at low metallicities (e.g., Helmi et al., 2006; Aoki et al., 2009; Frebel, Simon,

and Kirby, 2014; Beers, 2018, and references therein). The frequency of carbon-enhanced to carbon-normal stars (such as the updated determinations of Henkel et al., 2018) at low metallicities (the early epochs of our Galaxy's history) is vital to understanding the first stars, with further implications for the stellar and galactic formation history of the early Universe (Placco et al., 2014; Salvadori, Skúladóttir, and Tolstoy, 2015);

- Planetary nebulae/post-AGB studies, regarding whether thermohaline mixing (or rather, the RGB extra mixing mechanism in general) continues on the AGB and how this affects the abundances of AGB stars and planetary nebulae (e.g., see Siess, 2009; Cantiello and Langer, 2010; Stancliffe, 2010; Lagarde et al., 2013, and references therein), and;
- White dwarf accretion, regarding the mixing mechanism occurring on the surface of white dwarfs as material of a different molecular weight to that of the surface material is accreted (e.g., see Deal, Vauclair, and Vauclair, 2013; Koester, 2015, and references therein).

Bibliography

- Alexander, D. R. (1975). “Low-Temperature Rosseland Opacity Tables”. In: *ApJS* 29, p. 363.
- Alexander, D. R., R. L. Rypma, and H. R. Johnson (1983). “Effect of molecules and grains on Rosseland mean opacities”. In: *ApJ* 272, pp. 773–780.
- Allende Prieto, C. et al. (2008). “APOGEE: The Apache Point Observatory Galactic Evolution Experiment”. In: *Astronomische Nachrichten* 329, p. 1018. DOI: [10.1002/asna.200811080](https://doi.org/10.1002/asna.200811080). arXiv: [0809.2362](https://arxiv.org/abs/0809.2362).
- Alonso, A., S. Arribas, and C. Martínez-Roger (1999). “The effective temperature scale of giant stars (F0-K5). II. Empirical calibration of T_{eff} versus colours and [Fe/H]”. In: *A&AS* 140, pp. 261–277.
- Anders, F. et al. (2017). “Galactic archaeology with asteroseismology and spectroscopy: Red giants observed by CoRoT and APOGEE”. In: *A&A* 597, A30, A30. DOI: [10.1051/0004-6361/201527204](https://doi.org/10.1051/0004-6361/201527204). arXiv: [1604.07763](https://arxiv.org/abs/1604.07763).
- Angelou, G. C. (2014). “On the Role of Doubly-Diffusive Mixing in Low-Mass Red Giant Branch Stars”. PhD thesis. Monash University.
- Angelou, G. C. et al. (2012). “The Role of Thermohaline Mixing in Intermediate- and Low-metallicity Globular Clusters”. In: *ApJ* 749, 128, p. 128.
- Angelou, G. C. et al. (2015). “Diagnostics of stellar modelling from spectroscopy and photometry of globular clusters”. In: *MNRAS* 450, pp. 2423–2440. DOI: [10.1093/mnras/stv770](https://doi.org/10.1093/mnras/stv770). arXiv: [1504.01739](https://arxiv.org/abs/1504.01739) [astro-ph.SR].
- Angulo, C. et al. (1999). “A compilation of charged-particle induced thermonuclear reaction rates”. In: *Nucl. Phys. A* 656, pp. 3–183.
- Aoki, W. et al. (2007). “Carbon-enhanced Metal-poor Stars. I. Chemical Compositions of 26 Stars”. In: *ApJ* 655, pp. 492–521. DOI: [10.1086/509817](https://doi.org/10.1086/509817). eprint: [astro-ph/0609702](https://arxiv.org/abs/astro-ph/0609702).
- Aoki, W. et al. (2009). “Chemical composition of extremely metal-poor stars in the Sextans dwarf spheroidal galaxy”. In: *A&A* 502, pp. 569–578. DOI: [10.1051/0004-6361/200911959](https://doi.org/10.1051/0004-6361/200911959). arXiv: [0904.4307](https://arxiv.org/abs/0904.4307).
- Arnett, D. (1996). *Supernovae and Nucleosynthesis: An Investigation of the History of Matter from the Big Bang to the Present*.
- Asplund, M. et al. (2009). “The Chemical Composition of the Sun”. In: *ARA&A* 47, pp. 481–522.
- Bascoul, G. P. (2007). “Numerical simulations of semiconvection”. In: *Convection in Astrophysics*. Ed. by F. Kupka, I. Roxburgh, and K. L. Chan. Vol. 239. IAU Symposium, pp. 317–319. DOI: [10.1017/S1743921307000658](https://doi.org/10.1017/S1743921307000658).
- Bastian, N. and C. Lardo (2018). “Multiple Stellar Populations in Globular Clusters”. In: *ARA&A* 56, pp. 83–136. DOI: [10.1146/annurev-astro-081817-051839](https://doi.org/10.1146/annurev-astro-081817-051839). arXiv: [1712.01286](https://arxiv.org/abs/1712.01286) [astro-ph.SR].

- Beaudet, G. and M. Tassoul (1971). "Fitting Formulae for a Relativistic and/or Degenerate Electron Gas". In: *A&A* 13, p. 209.
- Beers, T. C. (2018). "CEMP Stars in the Halo and Their Origin in Ultra-Faint Dwarf Galaxies". In: *American Astronomical Society Meeting Abstracts* #232. Vol. 232. American Astronomical Society Meeting Abstracts, p. 114.05.
- Bellman, S. et al. (2001). "Carbon Abundances of M92 Red Giant Branch Stars". In: *Publ. Astron. Soc. Pac.* 113, pp. 326–334.
- Bergbusch, P. A., D. A. Vandenberg, and L. Infante (1991). "BV CCD photometry of the old open cluster NGC 2243". In: *AJ* 101, pp. 2102–2125. DOI: [10.1086/115832](https://doi.org/10.1086/115832).
- Bergemann, M. et al. (2014). "The Gaia-ESO Survey: radial metallicity gradients and age-metallicity relation of stars in the Milky Way disk". In: *A&A* 565, A89, A89. DOI: [10.1051/0004-6361/201423456](https://doi.org/10.1051/0004-6361/201423456). arXiv: [1401.4437](https://arxiv.org/abs/1401.4437).
- Bertelli Motta, C. et al. (2017). "Observing the products of stellar evolution in the old open cluster M67 with APOGEE". In: *ArXiv e-prints*. arXiv: [1701.00979](https://arxiv.org/abs/1701.00979) [[astro-ph.SR](https://arxiv.org/abs/1701.00979)].
- Bertelli Motta, C. et al. (2018). "The Gaia-ESO Survey: evidence of atomic diffusion in M67?" In: *MNRAS* 478, pp. 425–438. DOI: [10.1093/mnras/sty1011](https://doi.org/10.1093/mnras/sty1011). arXiv: [1804.06293](https://arxiv.org/abs/1804.06293) [[astro-ph.SR](https://arxiv.org/abs/1804.06293)].
- Bland-Hawthorn, J., M. R. Krumholz, and K. Freeman (2010). "The Long-term Evolution of the Galactic Disk Traced by Dissolving Star Clusters". In: *ApJ* 713, pp. 166–179. DOI: [10.1088/0004-637X/713/1/166](https://doi.org/10.1088/0004-637X/713/1/166). arXiv: [1002.4357](https://arxiv.org/abs/1002.4357).
- Bland-Hawthorn, J., S. Sharma, and K. Freeman (2014). "GALAH survey: chemically tagging the thick disk". In: *EAS Publications Series*. Vol. 67. EAS Publications Series, pp. 219–226. DOI: [10.1051/eas/1567039](https://doi.org/10.1051/eas/1567039). arXiv: [1504.01765](https://arxiv.org/abs/1504.01765).
- Böhm-Vitense, E. (1958). "Über die Wasserstoffkonvektionszone in Sternen verschiedener Effektivtemperaturen und Leuchtkräfte. Mit 5 Textabbildungen". In: *Zeitschrift für Astrophysik* 46, p. 108.
- Bonifazi, A. et al. (1990). "CCD photometry of Galactic open clusters. II - NGC 2243". In: *MNRAS* 245, pp. 15–29.
- Briley, M. M. et al. (1990). "An analysis of G-band strengths in NGC 6397 and M55 red giants". In: *ApJ* 359, pp. 307–318. DOI: [10.1086/169066](https://doi.org/10.1086/169066).
- Brown, J. A. (1987). "Carbon-to-nitrogen ratios along the evolutionary sequence of M67". In: *ApJ* 317, pp. 701–709. DOI: [10.1086/165316](https://doi.org/10.1086/165316).
- Brown, J. M., P. Garaud, and S. Stellmach (2013). "Chemical Transport and Spontaneous Layer Formation in Fingering Convection in Astrophysics". In: *ApJ* 768, 34, p. 34.
- Buder, S. et al. (2018). "The GALAH survey: An abundance, age, and kinematic inventory of the solar neighbourhood made with TGAS". In: *arXiv e-prints*. arXiv: [1804.05869](https://arxiv.org/abs/1804.05869) [[astro-ph.SR](https://arxiv.org/abs/1804.05869)].
- Busse, F. H. (1978). "Non-linear properties of thermal convection". In: *Reports on Progress in Physics* 41, pp. 1929–1967. DOI: [10.1088/0034-4885/41/12/003](https://doi.org/10.1088/0034-4885/41/12/003).
- Cameron, A. G. W. and W. A. Fowler (1971). "Lithium and the s-process in Red-Giant Stars". In: *ApJ* 164, pp. 111–114.
- Cameron, L. M. (1985). "Metallicities and distances of galactic clusters as determined from UBV-data. II - The metallicities and distances of 38 open

- clusters. III - Ages and abundance gradients of open clusters". In: *A&A* 147, pp. 39–53.
- Campbell, S. W. (2007). "Low-metallicity AGB stars". PhD thesis. Monash University.
- Campbell, S. W. and J. C. Lattanzio (2008). "Evolution and nucleosynthesis of extremely metal-poor and metal-free low- and intermediate-mass stars. I. Stellar yield tables and the CEMPs". In: *A&A* 490, pp. 769–776.
- Cannon, R. C. (1993). "Massive Thorne-Zytkow Objects - Structure and Nucleosynthesis". In: *MNRAS* 263, p. 817.
- Cantat-Gaudin, T. et al. (2014). "The Gaia-ESO Survey: Stellar content and elemental abundances in the massive cluster NGC 6705". In: *A&A* 569, A17, A17. DOI: [10.1051/0004-6361/201423851](https://doi.org/10.1051/0004-6361/201423851). arXiv: [1407.1510](https://arxiv.org/abs/1407.1510) [[astro-ph.SR](https://arxiv.org/abs/1407.1510)].
- Cantiello, M. and N. Langer (2010). "Thermohaline mixing in evolved low-mass stars". In: *A&A* 521, A9, A9.
- Canuto, V. M. (1999). "Turbulence in Stars. III. Unified Treatment of Diffusion, Convection, Semiconvection, Salt Fingers, and Differential Rotation". In: *ApJ* 524, pp. 311–340. DOI: [10.1086/307783](https://doi.org/10.1086/307783).
- Carbon, D. F. et al. (1982). "Carbon and nitrogen abundances in giant stars of the metal-poor globular cluster M92". In: *ApJS* 49, pp. 207–258. DOI: [10.1086/190796](https://doi.org/10.1086/190796).
- Carraro, G. et al. (2014). "Chemical abundance analysis of the old, rich open cluster Trumpler 20". In: *A&A* 562, A39, A39. DOI: [10.1051/0004-6361/201322783](https://doi.org/10.1051/0004-6361/201322783). arXiv: [1401.1563](https://arxiv.org/abs/1401.1563).
- Carretta, E. (2006). "Abundances in Red Giant Stars of NGC 2808 and Correlations between Chemical Anomalies and Global Parameters in Globular Clusters". In: *AJ* 131, pp. 1766–1783.
- Carretta, E. and R. G. Gratton (1997). "Abundances for globular cluster giants. I. Homogeneous metallicities for 24 clusters". In: *A&AS* 121, pp. 95–112. DOI: [10.1051/aas:1997116](https://doi.org/10.1051/aas:1997116). eprint: [astro-ph/9607078](https://arxiv.org/abs/astro-ph/9607078).
- Carretta, E. et al. (2009a). "Intrinsic iron spread and a new metallicity scale for globular clusters". In: *A&A* 508, pp. 695–706. DOI: [10.1051/0004-6361/200913003](https://doi.org/10.1051/0004-6361/200913003). arXiv: [0910.0675](https://arxiv.org/abs/0910.0675).
- Carretta, E. et al. (2009b). "Na-O anticorrelation and HB. VII. The chemical composition of first and second-generation stars in 15 globular clusters from GIRAFFE spectra". In: *A&A* 505, pp. 117–138. DOI: [10.1051/0004-6361/200912096](https://doi.org/10.1051/0004-6361/200912096). arXiv: [0909.2938](https://arxiv.org/abs/0909.2938).
- Carretta, E. et al. (2009c). "Na-O anticorrelation and HB. VIII. Proton-capture elements and metallicities in 17 globular clusters from UVES spectra". In: *A&A* 505, pp. 139–155. DOI: [10.1051/0004-6361/200912097](https://doi.org/10.1051/0004-6361/200912097). arXiv: [0909.2941](https://arxiv.org/abs/0909.2941).
- Carretta, E. et al. (2011). "Multiple stellar populations in the globular cluster NGC 1851". In: *A&A* 533, A69, A69. DOI: [10.1051/0004-6361/201117269](https://doi.org/10.1051/0004-6361/201117269). arXiv: [1106.3174](https://arxiv.org/abs/1106.3174) [[astro-ph.SR](https://arxiv.org/abs/1106.3174)].
- Casagrande, L. et al. (2011). "New constraints on the chemical evolution of the solar neighbourhood and Galactic disc(s). Improved astrophysical parameters for the Geneva-Copenhagen Survey". In: *A&A* 530, A138, A138.
- Cassisi, S. and M. Salaris (2013). *Old Stellar Populations: How to Study the Fossil Record of Galaxy Formation*.

- Castilho, B. V. et al. (2000). "High resolution abundance analysis of 16 giants and subgiants in the metal-poor globular cluster NGC 6397". In: *A&A* 361, pp. 92–100.
- Caughlan, G. R. and W. A. Fowler (1988). "Thermonuclear Reaction Rates V". In: *Atomic Data and Nuclear Data Tables* 40, p. 283.
- Chabrier, G. and I. Baraffe (1997). "Structure and evolution of low-mass stars". In: *A&A* 327, pp. 1039–1053. eprint: [astro-ph/9704118](https://arxiv.org/abs/astro-ph/9704118).
- Chanamé, J., M. Pinsonneault, and D. M. Terndrup (2005). "Abundance Anomalies and Rotational Evolution of Low-Mass Red Giants: A Maximal Mixing Approach". In: *ApJ* 631, pp. 540–571.
- Charbonneau, P. and G. Michaud (1991). "Meridional circulation and diffusion in A and early F stars". In: *ApJ* 370, pp. 693–708. DOI: [10.1086/169853](https://doi.org/10.1086/169853).
- Charbonnel, C. (1994). "Clues for non-standard mixing on the red giant branch from C-12/C-13 and C-12/N-14 ratios in evolved stars". In: *A&A* 282, pp. 811–820.
- Charbonnel, C., J. A. Brown, and G. Wallerstein (1998). "Mixing processes during the evolution of red giants with moderate metal deficiencies: the role of molecular-weight barriers". In: *A&A* 332, pp. 204–214.
- Charbonnel, C. and N. Lagarde (2010). "Thermohaline instability and rotation-induced mixing. I. Low- and intermediate-mass solar metallicity stars up to the end of the AGB". In: *A&A* 522, A10.
- Charbonnel, C. and J.-P. Zahn (2007). "Thermohaline mixing: a physical mechanism governing the photospheric composition of low-mass giants". In: *A&A* 467, pp. L15–L18.
- Church, R. P. et al. (2014). "Which physics determines the location of the mean molecular weight minimum in red giants?" In: *MNRAS* 443, pp. 977–984. DOI: [10.1093/mnras/stu1195](https://doi.org/10.1093/mnras/stu1195).
- Claria, J. J. (1982). "Membership Basic Parameters and Luminosity Function of the Southern Open Cluster NGC2547". In: *A&AS* 47, p. 323.
- (1985). "Membership and photometric abundances of red evolved stars in open clusters". In: *A&AS* 59, pp. 195–204.
- Claria, J. J., E. Lapasset, and D. Minniti (1989). "Photometric metal abundances of high-luminosity red stars in young and intermediate-age open clusters". In: *A&AS* 78, pp. 363–374.
- Clayton, D. D. (1983). *Principles of stellar evolution and nucleosynthesis*. University of Chicago Press.
- Cohen, J. G. et al. (2005). "The Frequency of Carbon Stars among Extremely Metal-poor Stars". In: *ApJ* 633, pp. L109–L112. DOI: [10.1086/498502](https://doi.org/10.1086/498502). eprint: [astro-ph/0510105](https://arxiv.org/abs/astro-ph/0510105).
- Collet, R., M. Asplund, and R. Trampedach (2007). "Three-dimensional hydrodynamical simulations of surface convection in red giant stars. Impact on spectral line formation and abundance analysis". In: *A&A* 469, pp. 687–706. DOI: [10.1051/0004-6361:20066321](https://doi.org/10.1051/0004-6361:20066321). eprint: [astro-ph/0703652](https://arxiv.org/abs/astro-ph/0703652).
- Constantino, T. et al. (2016). "The treatment of mixing in core helium burning models - II. Constraints from cluster star counts". In: *MNRAS* 456, pp. 3866–3885. DOI: [10.1093/mnras/stv2939](https://doi.org/10.1093/mnras/stv2939). arXiv: [1512.04845](https://arxiv.org/abs/1512.04845) [[astro-ph.SR](https://arxiv.org/abs/astro-ph.SR)].
- Cooke, R. J. and M. Fumagalli (2018). "Measurement of the primordial helium abundance from the intergalactic medium". In: *Nature Astronomy*

- 2, pp. 957–961. DOI: [10.1038/s41550-018-0584-z](https://doi.org/10.1038/s41550-018-0584-z). arXiv: [1810.06561](https://arxiv.org/abs/1810.06561).
- Cottrell, P. L. and G. S. Da Costa (1981). “Correlated cyanogen and sodium anomalies in the globular clusters 47 Tuc and NGC 6752”. In: *ApJ* 245, pp. L79–L82.
- Cyburt, R. H. et al. (2010). “The JINA REACLIB Database: Its Recent Updates and Impact on Type-I X-ray Bursts”. In: *ApJS* 189, pp. 240–252.
- Dahm, S. E. (2008). “The Young Cluster and Star Forming Region NGC 2264”. In: *Handbook of Star Forming Regions, Volume I*. Ed. by B. Reipurth, p. 966.
- D’Antona, F. and I. Mazzitelli (1997). “Evolution of low mass stars”. In: *Mem. Soc. Astron. Ital.* 68, p. 807.
- D’Antona, F. et al. (2002). “Helium variation due to self-pollution among Globular Cluster stars. Consequences on the horizontal branch morphology”. In: *A&A* 395, pp. 69–75.
- De Silva, G. M. et al. (2007). “Chemical Homogeneity in Collinder 261 and Implications for Chemical Tagging”. In: *AJ* 133, pp. 1161–1175. DOI: [10.1086/511182](https://doi.org/10.1086/511182). eprint: [astro-ph/0611832](https://arxiv.org/abs/astro-ph/0611832).
- Deal, M., S. Vauclair, and G. Vauclair (2013). “Thermohaline Instabilities Induced by Heavy Element Accretion onto White Dwarfs: Consequences on the Derived Accretion Rates”. In: *18th European White Dwarf Workshop*. Vol. 469. Astronomical Society of the Pacific Conference Series, p. 435. arXiv: [1210.5349](https://arxiv.org/abs/1210.5349) [[astro-ph](https://arxiv.org/abs/astro-ph).SR].
- Dearborn, D. S. P., J. C. Lattanzio, and P. P. Eggleton (2006). “Three-dimensional Numerical Experimentation on the Core Helium Flash of Low-Mass Red Giants”. In: *ApJ* 639, pp. 405–415. eprint: [astro-ph/0512049](https://arxiv.org/abs/astro-ph/0512049).
- Demarque, P. and J. G. Mengel (1971). “Advanced Evolution of Population II Stars. I. Red Giants and the Helium Flash”. In: *ApJ* 164, p. 317.
- Denissenkov, P. A. (2010). “Numerical Simulations of Thermohaline Convection: Implications for Extra-mixing in Low-mass RGB Stars”. In: *ApJ* 723, pp. 563–579.
- (2012). “A New Twist in the Evolution of Low-mass Stars”. In: *ApJ* 753, L3, p. L3.
- Denissenkov, P. A. and F. Herwig (2004). “Enhanced Extra Mixing in Low-Mass Red Giants: Lithium Production and Thermal Stability”. In: *ApJ* 612, pp. 1081–1091. DOI: [10.1086/422575](https://doi.org/10.1086/422575).
- Denissenkov, P. A. and W. J. Merryfield (2011). “Thermohaline Mixing: Does it Really Govern the Atmospheric Chemical Composition of Low-mass Red Giants?” In: *ApJ* 727, L8, p. L8.
- Denissenkov, P. A., M. Pinsonneault, and K. B. MacGregor (2009). “Magneto-Thermohaline Mixing in Red Giants”. In: *ApJ* 696, pp. 1823–1833.
- Denissenkov, P. A. and D. A. Vandenberg (2003). “Canonical Extra Mixing in Low-Mass Red Giants”. In: *ApJ* 593, pp. 509–523. DOI: [10.1086/376410](https://doi.org/10.1086/376410).
- Descouvemont, P. et al. (2004). “Compilation and R-matrix analysis of Big Bang nuclear reaction rates”. In: *Atomic Data and Nuclear Data Tables* 88, pp. 203–236. DOI: [10.1016/j.adt.2004.08.001](https://doi.org/10.1016/j.adt.2004.08.001). eprint: [astro-ph/0407101](https://arxiv.org/abs/astro-ph/0407101).

- Despain, K. H. (1981). "Low-mass evolution - Zero-age main sequence to asymptotic giant branch". In: *ApJ* 251, pp. 639–653.
- Deupree, R. G. (1984). "Two- and three-dimensional numerical simulations of the hydrodynamic phase of the core helium flash". In: *ApJ* 287, pp. 268–281.
- Dias, W. S. et al. (2002). "New catalogue of optically visible open clusters and candidates". In: *A&A* 389, pp. 871–873. DOI: [10.1051/0004-6361:200206668](https://doi.org/10.1051/0004-6361:200206668). eprint: [astro-ph/0203351](https://arxiv.org/abs/astro-ph/0203351).
- Doherty, C. L. et al. (2017). "Super-AGB Stars and their Role as Electron Capture Supernova Progenitors". In: *PASA* 34, e056, e056. DOI: [10.1017/pasa.2017.52](https://doi.org/10.1017/pasa.2017.52). arXiv: [1703.06895](https://arxiv.org/abs/1703.06895) [[astro-ph](https://arxiv.org/abs/astro-ph).SR].
- Drazdauskas, A. et al. (2016a). "Chemical composition of evolved stars in the young open clusters NGC 4609 and NGC 5316". In: *MNRAS* 462, pp. 794–803. DOI: [10.1093/mnras/stw1701](https://doi.org/10.1093/mnras/stw1701). arXiv: [1608.08375](https://arxiv.org/abs/1608.08375) [[astro-ph](https://arxiv.org/abs/astro-ph).SR].
- Drazdauskas, A. et al. (2016b). "The extent of mixing in stellar interiors: the open clusters Collinder 261 and Melotte 66". In: *A&A* 589, A50, A50. DOI: [10.1051/0004-6361/201628138](https://doi.org/10.1051/0004-6361/201628138). arXiv: [1603.09529](https://arxiv.org/abs/1603.09529) [[astro-ph](https://arxiv.org/abs/astro-ph).SR].
- Driebe, T. et al. (1998). "The evolution of helium white dwarfs. I. The companion of the millisecond pulsar PSR J1012+5307". In: *A&A* 339, pp. 123–133. eprint: [astro-ph/9809079](https://arxiv.org/abs/astro-ph/9809079).
- Dufour, P. et al. (2007). "White dwarf stars with carbon atmospheres". In: *Nature* 450, pp. 522–524. DOI: [10.1038/nature06318](https://doi.org/10.1038/nature06318). arXiv: [0711.3227](https://arxiv.org/abs/0711.3227).
- Eddington, A. S. (1925). "Circulating currents in rotating stars". In: *The Observatory* 48, pp. 73–75.
- Edelmann, P. V. F. et al. (2017). "Testing a one-dimensional prescription of dynamical shear mixing with a two-dimensional hydrodynamic simulation". In: *A&A* 604, A25, A25. DOI: [10.1051/0004-6361/201629873](https://doi.org/10.1051/0004-6361/201629873). arXiv: [1704.06261](https://arxiv.org/abs/1704.06261) [[astro-ph](https://arxiv.org/abs/astro-ph).SR].
- Eggleton, P. P., D. S. P. Dearborn, and J. C. Lattanzio (2006). "Deep Mixing of ^3He : Reconciling Big Bang and Stellar Nucleosynthesis". In: *Science* 314, p. 1580. eprint: [arXiv:astro-ph/0611039](https://arxiv.org/abs/astro-ph/0611039).
- (2008). "Compulsory Deep Mixing of ^3He and CNO Isotopes in the Envelopes of Low-Mass Red Giants". In: *ApJ* 677, pp. 581–592. eprint: [arXiv:0706.2710](https://arxiv.org/abs/0706.2710).
- Fernández-Alvar, E. et al. (2017). "Chemical trends in the Galactic halo from APOGEE data". In: *MNRAS* 465, pp. 1586–1600. DOI: [10.1093/mnras/stw2861](https://doi.org/10.1093/mnras/stw2861). arXiv: [1611.01249](https://arxiv.org/abs/1611.01249) [[astro-ph](https://arxiv.org/abs/astro-ph).SR].
- Forestini, M. and C. Charbonnel (1997). "Nucleosynthesis of light elements inside thermally pulsing AGB stars: I. The case of intermediate-mass stars". In: *A&AS* 123, pp. 241–272.
- François, P. et al. (2013). "Lithium abundance in the metal-poor open cluster NGC 2243". In: *A&A* 552, A136, A136. DOI: [10.1051/0004-6361/201220958](https://doi.org/10.1051/0004-6361/201220958). arXiv: [1303.3027](https://arxiv.org/abs/1303.3027) [[astro-ph](https://arxiv.org/abs/astro-ph).SR].
- Frebel, A., J. D. Simon, and E. N. Kirby (2014). "Segue 1: An Unevolved Fossil Galaxy from the Early Universe". In: *ApJ* 786, 74, p. 74. DOI: [10.1088/0004-637X/786/1/74](https://doi.org/10.1088/0004-637X/786/1/74). arXiv: [1403.6116](https://arxiv.org/abs/1403.6116).
- Frebel, A. et al. (2006). "Bright Metal-poor Stars from the Hamburg/ESO Survey. I. Selection and Follow-up Observations from 329 Fields". In:

- ApJ* 652, pp. 1585–1603. DOI: [10.1086/508506](https://doi.org/10.1086/508506). eprint: [astro-ph/0608332](https://arxiv.org/abs/astro-ph/0608332).
- Freeman, K. and J. Bland-Hawthorn (2002). “The New Galaxy: Signatures of Its Formation”. In: *ARA&A* 40, pp. 487–537. eprint: [arXiv:astro-ph/0208106](https://arxiv.org/abs/astro-ph/0208106).
- Friel, E. D. et al. (2014). “Gaia-ESO Survey: Properties of the intermediate age open cluster NGC 4815”. In: *A&A* 563, A117, A117. DOI: [10.1051/0004-6361/201323215](https://doi.org/10.1051/0004-6361/201323215). arXiv: [1403.7451](https://arxiv.org/abs/1403.7451) [[astro-ph.SR](https://arxiv.org/abs/astro-ph.SR)].
- Garaud, P. and N. Brummell (2015). “2D or Not 2D: The Effect of Dimensionality on the Dynamics of Fingering Convection at Low Prandtl Number”. In: *ApJ* 815, 42, p. 42. DOI: [10.1088/0004-637X/815/1/42](https://doi.org/10.1088/0004-637X/815/1/42). arXiv: [1508.07093](https://arxiv.org/abs/1508.07093) [[astro-ph.SR](https://arxiv.org/abs/astro-ph.SR)].
- Geiss, J. and G. Gloeckler (1998). “Abundances of Deuterium and Helium-3 in the Protosolar Cloud”. In: *Space Sci. Rev.* 84, pp. 239–250.
- Giampapa, M. S. et al. (2006). “A Survey of Chromospheric Activity in the Solar-Type Stars in the Open Cluster M67”. In: *ApJ* 651, pp. 444–461. DOI: [10.1086/507624](https://doi.org/10.1086/507624). eprint: [astro-ph/0607313](https://arxiv.org/abs/astro-ph/0607313).
- Gilmore, G. et al. (2012). “The Gaia-ESO Public Spectroscopic Survey”. In: *The Messenger* 147, pp. 25–31.
- Gilroy, K. K. (1989). “Carbon isotope ratios and lithium abundances in open cluster giants”. In: *ApJ* 347, pp. 835–848.
- Gilroy, K. K. and J. A. Brown (1991). “Carbon isotope ratios along the giant branch of M67”. In: *ApJ* 371, pp. 578–583.
- Gloeckler, G. and J. Geiss (1996). “Abundance of ^3He in the local interstellar cloud”. In: *Nature* 381, pp. 210–212.
- Gratton, R., C. Sneden, and E. Carretta (2004). “Abundance Variations Within Globular Clusters”. In: *ARA&A* 42, pp. 385–440.
- Gratton, R. G., E. Carretta, and A. Bragaglia (2012). “Multiple populations in globular clusters. Lessons learned from the Milky Way globular clusters”. In: *ARA&A* 20, p. 50.
- Gratton, R. G. and G. Contarini (1994). “Elemental Abundances in the Old Open Clusters NGC2243 and MELOTTE:66”. In: *A&A* 283, p. 911.
- Gratton, R. G. et al. (2000). “Mixing along the red giant branch in metal-poor field stars”. In: *A&A* 354, pp. 169–187.
- Gratton, R. G. et al. (2001). “The O-Na and Mg-Al anticorrelations in turn-off and early subgiants in globular clusters”. In: *A&A* 369, pp. 87–98.
- Gratton, R. G. et al. (2003). “Distances and ages of NGC 6397, NGC 6752 and 47 Tuc”. In: *A&A* 408, pp. 529–543. DOI: [10.1051/0004-6361:20031003](https://doi.org/10.1051/0004-6361:20031003). eprint: [astro-ph/0307016](https://arxiv.org/abs/astro-ph/0307016).
- Grevesse, N. and A. Noels (1993). “Cosmic abundances of the elements.” In: *Origin and Evolution of the Elements*. Ed. by N. Prantzos, E. Vangioni-Flam, and M. Casse, pp. 15–25.
- Grevesse, N. and A. J. Sauval (1998). “Standard Solar Composition”. In: *Space Sci. Rev.* 85, pp. 161–174. DOI: [10.1023/A:1005161325181](https://doi.org/10.1023/A:1005161325181).
- Harris, M. J. et al. (1983). “Thermonuclear reaction rates. III”. In: *ARA&A* 21, pp. 165–176.
- Harris, W. E. (1996). “A Catalog of Parameters for Globular Clusters in the Milky Way”. In: *AJ* 112, p. 1487.
- Hata, N. et al. (1995). “Big Bang nucleosynthesis in crisis?” In: *Physical Review Letters* 75, pp. 3977–3980. DOI: [10.1103/PhysRevLett.75.3977](https://doi.org/10.1103/PhysRevLett.75.3977). eprint: [hep-ph/9505319](https://arxiv.org/abs/hep-ph/9505319).

- Helmi, A. et al. (2006). "A New View of the Dwarf Spheroidal Satellites of the Milky Way from VLT FLAMES: Where Are the Very Metal-poor Stars?" In: *ApJ* 651, pp. L121–L124. DOI: [10.1086/509784](https://doi.org/10.1086/509784). eprint: [astro-ph/0611420](https://arxiv.org/abs/astro-ph/0611420).
- Henkel, K., A. I. Karakas, and J. C. Lattanzio (2017). "A phenomenological modification of thermohaline mixing in globular cluster red giants". In: *ArXiv e-prints*. arXiv: [1705.05550](https://arxiv.org/abs/1705.05550) [[astro-ph](https://arxiv.org/abs/astro-ph).SR].
- Henkel, K. et al. (2018). "Thermohaline mixing in extremely metal-poor stars". In: *ArXiv e-prints*. arXiv: [1808.02161](https://arxiv.org/abs/1808.02161) [[astro-ph](https://arxiv.org/abs/astro-ph).SR].
- Henyey, L. G., J. E. Forbes, and N. L. Gould (1964). "A New Method of Automatic Computation of Stellar Evolution." In: *ApJ* 139, p. 306. DOI: [10.1086/147754](https://doi.org/10.1086/147754).
- Herwig, F. et al. (1997). "Stellar evolution of low and intermediate-mass stars. IV. Hydrodynamically-based overshoot and nucleosynthesis in AGB stars." In: *A&A* 324, pp. L81–L84.
- Hollek, J. K. et al. (2011). "The Chemical Abundances of Stars in the Halo (CASH) Project. II. A Sample of 14 Extremely Metal-poor Stars". In: *ApJ* 742, 54, p. 54. DOI: [10.1088/0004-637X/742/1/54](https://doi.org/10.1088/0004-637X/742/1/54). arXiv: [1108.4422](https://arxiv.org/abs/1108.4422).
- Hubbard, W. B. and M. Lampe (1969). "Thermal Conduction by Electrons in Stellar Matter". In: *ApJS* 18, p. 297. DOI: [10.1086/190192](https://doi.org/10.1086/190192).
- Hünsch, M. et al. (2004). "Membership, rotation, and lithium abundances in the open clusters NGC 2451 A and B". In: *A&A* 418, pp. 539–549. DOI: [10.1051/0004-6361:20040043](https://doi.org/10.1051/0004-6361:20040043).
- Husser, T.-O. et al. (2016). "MUSE crowded field 3D spectroscopy of over 12 000 stars in the globular cluster NGC 6397. I. The first comprehensive HRD of a globular cluster". In: *A&A* 588, A148, A148. DOI: [10.1051/0004-6361/201526949](https://doi.org/10.1051/0004-6361/201526949). arXiv: [1602.01649](https://arxiv.org/abs/1602.01649) [[astro-ph](https://arxiv.org/abs/astro-ph).SR].
- Iben Jr., I. (1964). "The Surface Ration of N¹⁴ to C¹² during Helium Burning." In: *ApJ* 140, p. 1631. DOI: [10.1086/148077](https://doi.org/10.1086/148077).
- (1965). "Stellar Evolution. I. The Approach to the Main Sequence." In: *ApJ* 141, p. 993. DOI: [10.1086/148193](https://doi.org/10.1086/148193).
- (1975). "Thermal pulses; p-capture, alpha-capture, s-process nucleosynthesis; and convective mixing in a star of intermediate mass". In: *ApJ* 196, pp. 525–547. DOI: [10.1086/153433](https://doi.org/10.1086/153433).
- (2013). *Stellar Evolution Physics, Volume 1: Physical Processes in Stellar Interiors*.
- Iglesias, C. A. and F. J. Rogers (1996). "Updated Opal Opacities". In: *ApJ* 464, p. 943.
- Iliadis, C. (2007). *Nuclear Physics of Stars*. Wiley-VCH Verlag.
- Itoh, N. et al. (1983). "Electrical and thermal conductivities of dense matter in the liquid metal phase. I - High-temperature results". In: *ApJ* 273, pp. 774–782. DOI: [10.1086/161412](https://doi.org/10.1086/161412).
- Izzard, R. G. et al. (2009). "Population synthesis of binary carbon-enhanced metal-poor stars". In: *A&A* 508, pp. 1359–1374.
- Jacobson, H. R. et al. (2016). "The Gaia-ESO Survey: Probes of the inner disk abundance gradient". In: *A&A* 591, A37, A37. DOI: [10.1051/0004-6361/201527654](https://doi.org/10.1051/0004-6361/201527654). arXiv: [1605.04899](https://arxiv.org/abs/1605.04899).
- Janes, K. A. and G. H. Smith (1984). "The giant branch of the old open cluster M67". In: *AJ* 89, pp. 487–495. DOI: [10.1086/113539](https://doi.org/10.1086/113539).

- Jeffries, R. D. et al. (2002). "Membership, metallicity and lithium abundances for solar-type stars in NGC 6633". In: *MNRAS* 336, pp. 1109–1128. DOI: [10.1046/j.1365-8711.2002.05788.x](https://doi.org/10.1046/j.1365-8711.2002.05788.x). eprint: [astro-ph/0206367](https://arxiv.org/abs/astro-ph/0206367).
- Johnson, J. A. et al. (2007). "A Search for Nitrogen-enhanced Metal-poor Stars". In: *ApJ* 658, pp. 1203–1216. DOI: [10.1086/510114](https://doi.org/10.1086/510114). eprint: [astro-ph/0608666](https://arxiv.org/abs/astro-ph/0608666).
- Kaluzny, J. et al. (2006). "Eclipsing Binaries in the Open Cluster NGC2243. II. Absolute Properties of NVCMa". In: *Acta Astron.* 56, pp. 237–252. eprint: [astro-ph/0609380](https://arxiv.org/abs/astro-ph/0609380).
- Karakas, A. I., S. W. Campbell, and R. J. Stancliffe (2010). "Is Extra Mixing Really Needed in Asymptotic Giant Branch Stars?" In: *ApJ* 713, pp. 374–382.
- Karakas, A. I. and J. C. Lattanzio (2014). "The Dawes Review 2: Nucleosynthesis and Stellar Yields of Low- and Intermediate-Mass Single Stars". In: *PASA* 31, e030, e030. DOI: [10.1017/pasa.2014.21](https://doi.org/10.1017/pasa.2014.21). arXiv: [1405.0062](https://arxiv.org/abs/1405.0062) [[astro-ph.SR](https://arxiv.org/abs/astro-ph.SR)].
- Karakas, A. I., J. C. Lattanzio, and O. R. Pols (2002). "Parameterising the Third Dredge-up in Asymptotic Giant Branch Stars". In: *PASA* 19, pp. 515–526.
- Karakas, A. I. and M. Lugaro (2016). "Stellar Yields from Metal-rich Asymptotic Giant Branch Models". In: *ApJ* 825, 26, p. 26. DOI: [10.3847/0004-637X/825/1/26](https://doi.org/10.3847/0004-637X/825/1/26). arXiv: [1604.02178](https://arxiv.org/abs/1604.02178) [[astro-ph.SR](https://arxiv.org/abs/astro-ph.SR)].
- Kippenhahn, R., G. Ruschenplatt, and H.-C. Thomas (1980). "The time scale of thermohaline mixing in stars". In: *A&A* 91, pp. 175–180.
- Kippenhahn, R. and A. Weigert (1967). "Entwicklung in engen Doppeltsternsystemen I. Massenaustausch vor und nach Beendigung des zentralen Wasserstoff-Brennens". In: *Zeitschrift für Astrophysik* 65, p. 251.
- (1990). *Stellar Structure and Evolution*. Springer-Verlag.
- Kippenhahn, R., A. Weigert, and A. Weiss (2012). *Stellar Structure and Evolution*. DOI: [10.1007/978-3-642-30304-3](https://doi.org/10.1007/978-3-642-30304-3).
- Kitchatinov, L. L. (2016). "Meridional circulation in the sun and stars". In: *Geomagnetism and Aeronomy* 56, pp. 945–951. DOI: [10.1134/S0016793216080107](https://doi.org/10.1134/S0016793216080107). arXiv: [1603.07852](https://arxiv.org/abs/1603.07852) [[astro-ph.SR](https://arxiv.org/abs/astro-ph.SR)].
- Koester, D. (2015). "On Thermohaline Mixing in Accreting White Dwarfs". In: *19th European Workshop on White Dwarfs*. Ed. by P. Dufour, P. Bergeron, and G. Fontaine. Vol. 493. Astronomical Society of the Pacific Conference Series, p. 129. arXiv: [1408.6934](https://arxiv.org/abs/1408.6934) [[astro-ph.SR](https://arxiv.org/abs/astro-ph.SR)].
- Koleva, M. et al. (2008). "Spectroscopic ages and metallicities of stellar populations: validation of full spectrum fitting". In: *MNRAS* 385, pp. 1998–2010. DOI: [10.1111/j.1365-2966.2008.12908.x](https://doi.org/10.1111/j.1365-2966.2008.12908.x). arXiv: [0801.0871](https://arxiv.org/abs/0801.0871).
- Korn, A. J. et al. (2007). "Atomic Diffusion and Mixing in Old Stars. I. Very Large Telescope FLAMES-UVES Observations of Stars in NGC 6397". In: *ApJ* 671, pp. 402–419. DOI: [10.1086/523098](https://doi.org/10.1086/523098). arXiv: [0709.0639](https://arxiv.org/abs/0709.0639).
- Kraft, R. P. and I. I. Ivans (2003). "A Globular Cluster Metallicity Scale Based on the Abundance of Fe II". In: *Publ. Astron. Soc. Pac.* 115, pp. 143–169. DOI: [10.1086/345914](https://doi.org/10.1086/345914). eprint: [astro-ph/0210590](https://arxiv.org/abs/astro-ph/0210590).
- Lagarde, N. et al. (2011). "Thermohaline instability and rotation-induced mixing. II. Yields of ^3He for low- and intermediate-mass stars". In: *A&A* 536, A28, A28.

- Lagarde, N. et al. (2012a). “Effects of thermohaline instability and rotation-induced mixing on the evolution of light elements in the Galaxy: D, ^3He and ^4He ”. In: *A&A* 542, A62, A62.
- Lagarde, N. et al. (2012b). “Thermohaline instability and rotation-induced mixing. III. Grid of stellar models and asymptotic asteroseismic quantities from the pre-main sequence up to the AGB for low- and intermediate-mass stars of various metallicities”. In: *A&A* 543, A108.
- Lagarde, N. et al. (2013). “Thermohaline instability and rotation-induced mixing in low and intermediate mass stars: Consequences on global asteroseismic quantities”. In: *European Physical Journal Web of Conferences*. Vol. 43. European Physical Journal Web of Conferences, p. 01006. DOI: [10.1051/epjconf/20134301006](https://doi.org/10.1051/epjconf/20134301006).
- Lagarde, N. et al. (2017). “Population synthesis to constrain Galactic and stellar physics. I. Determining age and mass of thin-disc red-giant stars”. In: *A&A* 601, A27, A27. DOI: [10.1051/0004-6361/201630253](https://doi.org/10.1051/0004-6361/201630253). arXiv: [1702.01769](https://arxiv.org/abs/1702.01769) [[astro-ph.SR](#)].
- Lagarde, N. et al. (2018). “The Gaia-ESO survey: impact of extra-mixing on C- and N-abundances of giant stars”. In: *ArXiv e-prints*. arXiv: [1806.01868](https://arxiv.org/abs/1806.01868) [[astro-ph.SR](#)].
- Lambert, D. L. and L. M. Ries (1977). “Carbon, nitrogen, and oxygen abundances in 11 G and K giants”. In: *ApJ* 217, pp. 508–520. DOI: [10.1086/155599](https://doi.org/10.1086/155599).
- Langer, G. E. et al. (1986). “On the carbon abundance of subgiant stars in the globular cluster M 92”. In: *Publ. Astron. Soc. Pac.* 98, pp. 473–485. DOI: [10.1086/131781](https://doi.org/10.1086/131781).
- Lardo, C. et al. (2012). “C and N abundances of main sequence and subgiant branch stars in NGC 1851”. In: *A&A* 541, A141, A141.
- Lattanzio, J. C. and P. R. Wood (2003). “Evolution, Nucleosynthesis, and Pulsation of AGB Stars”. In: *Asymptotic giant branch stars, by Harm J. Habing and Hans Olofsson. Astronomy and astrophysics library, New York, Berlin: Springer, 2003, p. 23*. Ed. by H. J. Habing and H. Olofsson, p. 23.
- Lattanzio, J. C. et al. (2015). “On the numerical treatment and dependence of thermohaline mixing in red giants”. In: *MNRAS* 446, pp. 2673–2688. DOI: [10.1093/mnras/stu2238](https://doi.org/10.1093/mnras/stu2238). arXiv: [1410.6517](https://arxiv.org/abs/1410.6517) [[astro-ph.SR](#)].
- Lederer, M. T. and B. Aringer (2009). “Low temperature Rosseland opacities with varied abundances of carbon and nitrogen”. In: *A&A* 494, pp. 403–416.
- Lind, K. et al. (2009). “Signatures of intrinsic Li depletion and Li-Na anticorrelation in the metal-poor globular cluster NGC 6397”. In: *A&A* 503, pp. 545–557.
- Luck, R. E. (1994). “Open cluster chemical composition. 1: Later type stars in eight clusters”. In: *ApJS* 91, pp. 309–346. DOI: [10.1086/191940](https://doi.org/10.1086/191940).
- Lugaro, M. et al. (2017). “Stellar yields and abundances: new directions from planetary nebulae”. In: *ArXiv e-prints*. arXiv: [1703.00280](https://arxiv.org/abs/1703.00280) [[astro-ph.SR](#)].
- Lynga, G. (1981). “The Catalogue of Open Star Clusters”. In: *Astronomical Data Center Bulletin* 1, p. 90.
- Lynga, G. and S. Wrandemark (1984). “The common origin of some open clusters”. In: *A&A* 132, pp. 58–74.

- Mackereth, J. T. et al. (2017). “The age-metallicity structure of the Milky Way disc using APOGEE”. In: *MNRAS* 471, pp. 3057–3078. DOI: [10.1093/mnras/stx1774](https://doi.org/10.1093/mnras/stx1774). arXiv: [1706.00018](https://arxiv.org/abs/1706.00018).
- Maeder, A. and J.-P. Zahn (1998). “Stellar evolution with rotation. III. Meridional circulation with μ -gradients and non-stationarity”. In: *A&A* 334, pp. 1000–1006.
- Maeder, A. et al. (2013). “The thermohaline, Richardson, Rayleigh-Taylor, Solberg-Høiland, and GSF criteria in rotating stars”. In: *A&A* 553, A1, A1.
- Magrini, L. et al. (2017). “The Gaia-ESO Survey: radial distribution of abundances in the Galactic disc from open clusters and young-field stars”. In: *A&A* 603, A2, A2. DOI: [10.1051/0004-6361/201630294](https://doi.org/10.1051/0004-6361/201630294). arXiv: [1703.00762](https://arxiv.org/abs/1703.00762).
- Malmquist, K. G. (1922). “On some relations in stellar statistics”. In: *Meddelanden fran Lunds Astronomiska Observatorium Serie I* 100, pp. 1–52.
- Martell, S. L., G. H. Smith, and M. M. Briley (2008). “Deep Mixing and Metallicity: Carbon Depletion in Globular Cluster Giants”. In: *AJ* 136, pp. 2522–2532.
- Martig, M. et al. (2016). “Red giant masses and ages derived from carbon and nitrogen abundances”. In: *MNRAS* 456, pp. 3655–3670. DOI: [10.1093/mnras/stv2830](https://doi.org/10.1093/mnras/stv2830). arXiv: [1511.08203](https://arxiv.org/abs/1511.08203) [[astro-ph.SR](https://arxiv.org/abs/1511.08203)].
- Masseron, T. and G. Gilmore (2015). “Carbon, nitrogen and α -element abundances determine the formation sequence of the Galactic thick and thin discs”. In: *MNRAS* 453, pp. 1855–1866. DOI: [10.1093/mnras/stv1731](https://doi.org/10.1093/mnras/stv1731). arXiv: [1503.00537](https://arxiv.org/abs/1503.00537) [[astro-ph.SR](https://arxiv.org/abs/1503.00537)].
- Masseron, T. et al. (2006). “CS 30322-023: an ultra metal-poor TP-AGB star?” In: *A&A* 455, pp. 1059–1072.
- Mathis, S. et al. (2013). “Diagnoses to unravel secular hydrodynamical processes in rotating main sequence stars. II. The actions of internal gravity waves”. In: *A&A* 558, A11, A11. DOI: [10.1051/0004-6361/201321934](https://doi.org/10.1051/0004-6361/201321934).
- Mathis, S. et al. (2018). “Anisotropic turbulent transport in stably stratified rotating stellar radiation zones”. In: *A&A* 620, A22, A22. DOI: [10.1051/0004-6361/201629187](https://doi.org/10.1051/0004-6361/201629187). arXiv: [1808.01814](https://arxiv.org/abs/1808.01814) [[astro-ph.SR](https://arxiv.org/abs/1808.01814)].
- Medrano, M., P. Garaud, and S. Stellmach (2014). “Double-diffusive mixing in stellar interiors in the presence of horizontal gradients”. In: *ApJ* 792, L30, p. L30. DOI: [10.1088/2041-8205/792/2/L30](https://doi.org/10.1088/2041-8205/792/2/L30). arXiv: [1407.4648](https://arxiv.org/abs/1407.4648) [[astro-ph.SR](https://arxiv.org/abs/1407.4648)].
- Merryfield, W. J. (1995). “Hydrodynamics of semiconvection”. In: *ApJ* 444, pp. 318–337. DOI: [10.1086/175607](https://doi.org/10.1086/175607).
- Mestel, L. (1952). “On the theory of white dwarf stars. II. The accretion of interstellar matter by white dwarfs”. In: *MNRAS* 112, p. 598. DOI: [10.1093/mnras/112.6.598](https://doi.org/10.1093/mnras/112.6.598).
- (1953). “Rotation and stellar evolution”. In: *MNRAS* 113, p. 716.
- Meynet, G. and A. Maeder (2002). “Stellar evolution with rotation. VIII. Models at $Z = 10^{-5}$ and CNO yields for early galactic evolution”. In: *A&A* 390, pp. 561–583. DOI: [10.1051/0004-6361:20020755](https://doi.org/10.1051/0004-6361:20020755). eprint: [astro-ph/0205370](https://arxiv.org/abs/astro-ph/0205370).
- Meynet, G., A. Maeder, and N. Mowlavi (2004). “Diffusion in stellar interiors: Critical tests of three numerical methods”. In: *A&A* 416, pp. 1023–

1036. DOI: [10.1051/0004-6361:20031735](https://doi.org/10.1051/0004-6361:20031735). eprint: [astro-ph/0312368](https://arxiv.org/abs/astro-ph/0312368).
- Mikolaitis, Š. et al. (2010). “Chemical composition of clump stars in the open cluster NGC 6134”. In: *MNRAS* 407, pp. 1866–1874.
- (2011a). “Chemical composition of evolved stars in the open cluster IC 4651”. In: *MNRAS* 413, pp. 2199–2206. DOI: [10.1111/j.1365-2966.2011.18291.x](https://doi.org/10.1111/j.1365-2966.2011.18291.x). arXiv: [1101.0938](https://arxiv.org/abs/1101.0938) [[astro-ph.SR](https://arxiv.org/abs/astro-ph.SR)].
- (2011b). “Chemical composition of evolved stars in the open cluster NGC 2506”. In: *MNRAS* 416, pp. 1092–1098. DOI: [10.1111/j.1365-2966.2011.19106.x](https://doi.org/10.1111/j.1365-2966.2011.19106.x). arXiv: [1105.4047](https://arxiv.org/abs/1105.4047) [[astro-ph.SR](https://arxiv.org/abs/astro-ph.SR)].
- (2012). “C, N, O abundances and carbon isotope ratios in evolved stars of the open clusters Collinder 261 and NGC 6253”. In: *A&A* 541, A137, A137. DOI: [10.1051/0004-6361/201218831](https://doi.org/10.1051/0004-6361/201218831). arXiv: [1203.6514](https://arxiv.org/abs/1203.6514) [[astro-ph.SR](https://arxiv.org/abs/astro-ph.SR)].
- Milone, A. P. et al. (2008). “The ACS Survey of Galactic Globular Clusters. III. The Double Subgiant Branch of NGC 1851”. In: *ApJ* 673, pp. 241–250.
- Milone, A. P. et al. (2015). “The Hubble Space Telescope UV Legacy Survey of Galactic Globular Clusters. III. A Quintuple Stellar Population in NGC 2808”. In: *ApJ* 808, 51, p. 51. DOI: [10.1088/0004-637X/808/1/51](https://doi.org/10.1088/0004-637X/808/1/51). arXiv: [1505.05934](https://arxiv.org/abs/1505.05934) [[astro-ph.SR](https://arxiv.org/abs/astro-ph.SR)].
- Mitake, S., S. Ichimaru, and N. Itoh (1984). “Electrical and thermal conductivities of dense matter in the liquid metal phase. II - Low-temperature quantum corrections”. In: *ApJ* 277, pp. 375–378. DOI: [10.1086/161704](https://doi.org/10.1086/161704).
- Mocák, M. et al. (2009). “The core helium flash revisited. II. Two and three-dimensional hydrodynamic simulations”. In: *A&A* 501, pp. 659–677.
- Moll, R. and P. Garaud (2017). “The Effect of Rotation on Oscillatory Double-diffusive Convection (Semiconvection)”. In: *ApJ* 834, 44, p. 44. DOI: [10.3847/1538-4357/834/1/44](https://doi.org/10.3847/1538-4357/834/1/44). arXiv: [1610.03940](https://arxiv.org/abs/1610.03940) [[astro-ph.SR](https://arxiv.org/abs/astro-ph.SR)].
- Mucciarelli, A. et al. (2014). “The Helium Abundance in the Metal-poor Globular Clusters M30 and NGC 6397”. In: *ApJ* 786, 14, p. 14. DOI: [10.1088/0004-637X/786/1/14](https://doi.org/10.1088/0004-637X/786/1/14). arXiv: [1403.0595](https://arxiv.org/abs/1403.0595) [[astro-ph.SR](https://arxiv.org/abs/astro-ph.SR)].
- Nataf, D. M. et al. (2013). “Red Giant Branch Bump Brightness and Number Counts in 72 Galactic Globular Clusters Observed with the Hubble Space Telescope”. In: *ApJ* 766, 77, p. 77.
- Nissen, P. E. (1988). “The fourth-parameter problem in uvby-beta photometry of open clusters”. In: *A&A* 199, pp. 146–160.
- Nissen, P. E., B. A. Twarog, and D. L. Crawford (1987). “UvbyH-beta photometry of main-sequence stars in M67”. In: *AJ* 93, pp. 634–646. DOI: [10.1086/114345](https://doi.org/10.1086/114345).
- Noriega-Mendoza, H. and A. Ruelas-Mayorgo (1997). “A Technique for Simultaneous Determination of the Metallicity and Reddening of Old Open Clusters Using (V,B-V) Color-Magnitude Diagrams”. In: *AJ* 113, pp. 722–728. DOI: [10.1086/118291](https://doi.org/10.1086/118291).
- Norris, J. E. et al. (2013). “The Most Metal-poor Stars. IV. The Two Populations with $[Fe/H] \sim -3.0$ ”. In: *ApJ* 762, 28, p. 28. DOI: [10.1088/0004-637X/762/1/28](https://doi.org/10.1088/0004-637X/762/1/28). arXiv: [1211.3157](https://arxiv.org/abs/1211.3157).
- Ohlmann, S. T. et al. (2017). “Constructing stable 3D hydrodynamical models of giant stars”. In: *A&A* 599, A5, A5. DOI: [10.1051/0004-6361/201629692](https://doi.org/10.1051/0004-6361/201629692). arXiv: [1612.00008](https://arxiv.org/abs/1612.00008) [[astro-ph.SR](https://arxiv.org/abs/astro-ph.SR)].

- Olive, K. A. et al. (1995). "What is the problem with He-3". In: *ApJ* 444, pp. 680–685. DOI: [10.1086/175640](https://doi.org/10.1086/175640). eprint: [astro-ph/9410058](https://arxiv.org/abs/astro-ph/9410058).
- Oliveira, J. M. et al. (2003). "The lithium depletion boundary and the age of NGC 2547". In: *MNRAS* 342, pp. 651–663. DOI: [10.1046/j.1365-8711.2003.06592.x](https://doi.org/10.1046/j.1365-8711.2003.06592.x). eprint: [astro-ph/0303083](https://arxiv.org/abs/astro-ph/0303083).
- Paczynski, B. (1973). "Carbon Depletion in the Envelopes of Main Sequence Stars". In: *Acta Astronomica* 23, p. 191.
- Pagel, B. E. J. (1997). *Nucleosynthesis and Chemical Evolution of Galaxies*. Cambridge University Press.
- Palacios, A. et al. (2003). "Rotational mixing in low-mass stars. I Effect of the mu-gradients in main sequence and subgiant Pop I stars". In: *A&A* 399, pp. 603–616.
- Palacios, A. et al. (2006). "Rotational mixing in low-mass stars. II. Self-consistent models of Pop II RGB stars". In: *A&A* 453, pp. 261–278. eprint: [arXiv:astro-ph/0602389](https://arxiv.org/abs/astro-ph/0602389).
- Pasquini, L. et al. (2002). "Installation and commissioning of FLAMES, the VLT Multifibre Facility". In: *The Messenger* 110, pp. 1–9.
- Paunzen, E. et al. (2010). "On the metallicity of open clusters. I. Photometry". In: *A&A* 517, A32, A32. DOI: [10.1051/0004-6361/201014131](https://doi.org/10.1051/0004-6361/201014131). arXiv: [1008.3476 \[astro-ph.SR\]](https://arxiv.org/abs/1008.3476).
- Peimbert, A., M. Peimbert, and V. Luridiana (2016). "The primordial helium abundance and the number of neutrino families". In: *RMXAA* 52, pp. 419–424. arXiv: [1608.02062](https://arxiv.org/abs/1608.02062).
- Pérez, M. R. (1991). "The young open clusters NGC 2244 and NGC 2264, revisited." In: *Revista Mexicana de Astronomía y Astrofísica* 22, pp. 99–111.
- Phillips, A. C. (1999). *The Physics of Stars, 2nd Edition*, p. 262.
- Piatti, A. E., J. J. Claria, and M. G. Abadi (1995). "Chemical Evolution of the Galactic Disk: Evidence for a Gradient Perpendicular to the Galactic Plane". In: *AJ* 110, p. 2813. DOI: [10.1086/117731](https://doi.org/10.1086/117731).
- Piatti, A. E. et al. (1998). "A Photometric and Spectroscopic Study of the Southern Open Clusters PISMIS 18, PISMIS 19, NGC 6005, and NGC 6253". In: *AJ* 116, pp. 801–812. DOI: [10.1086/300443](https://doi.org/10.1086/300443).
- Piotto, G. et al. (2007). "A Triple Main Sequence in the Globular Cluster NGC 2808". In: *ApJ* 661, pp. L53–L56. DOI: [10.1086/518503](https://doi.org/10.1086/518503). eprint: [astro-ph/0703767](https://arxiv.org/abs/astro-ph/0703767).
- Placco, V. M. et al. (2014). "Carbon-enhanced Metal-poor Star Frequencies in the Galaxy: Corrections for the Effect of Evolutionary Status on Carbon Abundances". In: *ApJ* 797, 21, p. 21. DOI: [10.1088/0004-637X/797/1/21](https://doi.org/10.1088/0004-637X/797/1/21). arXiv: [1410.2223 \[astro-ph.SR\]](https://arxiv.org/abs/1410.2223).
- Pols, O. R. et al. (2009). "The Puzzling Frequencies of CEMP and NEMP Stars". In: *PASA* 26, pp. 327–329. DOI: [10.1071/AS08076](https://doi.org/10.1071/AS08076). arXiv: [0910.1489 \[astro-ph.SR\]](https://arxiv.org/abs/0910.1489).
- Pols, Onno R. et al. (1998). "Stellar evolution models for $Z = 0.0001$ to 0.03 ". In: *MNRAS* 298.2, pp. 525–536. DOI: [10.1046/j.1365-8711.1998.01658.x](https://doi.org/10.1046/j.1365-8711.1998.01658.x).
- Raikh, M. E. and D. G. Iakovlev (1982). "Thermal and electrical conductivities of crystals in neutron stars and degenerate dwarfs". In: *Ap&SS* 87, pp. 193–203. DOI: [10.1007/BF00648915](https://doi.org/10.1007/BF00648915).
- Randich, S., G. Gilmore, and Gaia-ESO Consortium (2013). "The Gaia-ESO Large Public Spectroscopic Survey". In: *The Messenger* 154, pp. 47–49.

- Randich, S. et al. (2018). “The Gaia-ESO Survey: open clusters in Gaia-DR1 . A way forward to stellar age calibration”. In: *A&A* 612, A99, A99. DOI: [10.1051/0004-6361/201731738](https://doi.org/10.1051/0004-6361/201731738). arXiv: [1711.07699](https://arxiv.org/abs/1711.07699) [[astro-ph.SR](#)].
- Reid, I. N. and J. E. Gizis (1998). “The Distance to NGC 6397 by M-Subdwarf Main-Sequence Fitting”. In: *AJ* 116, pp. 2929–2935. DOI: [10.1086/300653](https://doi.org/10.1086/300653). eprint: [astro-ph/9809024](https://arxiv.org/abs/astro-ph/9809024).
- Reimers, D. (1975). “Circumstellar envelopes and mass loss of red giant stars”. In: *Problems in stellar atmospheres and envelopes*, pp. 229–256.
- Reimers, D. and D. Koester (1988). “Spectroscopic identification of white dwarfs in galactic clusters.” In: *The Messenger* 54, pp. 47–51.
- Riello, M. et al. (2003). “The Red Giant Branch luminosity function bump”. In: *A&A* 410, pp. 553–563. eprint: [arXiv:astro-ph/0308431](https://arxiv.org/abs/astro-ph/0308431).
- Rieutord, M. and A. Beth (2014). “Dynamics of the radiative envelope of rapidly rotating stars: Effects of spin-down driven by mass loss”. In: *A&A* 570, A42, A42. DOI: [10.1051/0004-6361/201423386](https://doi.org/10.1051/0004-6361/201423386). arXiv: [1407.0946](https://arxiv.org/abs/1407.0946) [[astro-ph.SR](#)].
- Robinson, F. J. et al. (2003). “Three-dimensional convection simulations of the outer layers of the Sun using realistic physics”. In: *MNRAS* 340, pp. 923–936. DOI: [10.1046/j.1365-8711.2003.06349.x](https://doi.org/10.1046/j.1365-8711.2003.06349.x). eprint: [astro-ph/0212296](https://arxiv.org/abs/astro-ph/0212296).
- Roederer, I. U. et al. (2014). “A Search for Stars of Very Low Metal Abundance. VI. Detailed Abundances of 313 Metal-poor Stars”. In: *AJ* 147, 136, p. 136. DOI: [10.1088/0004-6256/147/6/136](https://doi.org/10.1088/0004-6256/147/6/136). arXiv: [1403.6853](https://arxiv.org/abs/1403.6853) [[astro-ph.SR](#)].
- Ryan, S. G. and A. J. Norton (2010). *Stellar Evolution and Nucleosynthesis*.
- Salaris, M. and S. Cassisi (2006). *Evolution of Stars and Stellar Populations*.
- Salaris, M., A. Chieffi, and O. Straniero (1993). “The alpha-enhanced isochrones and their impact on the FITS to the Galactic globular cluster system”. In: *ApJ* 414, pp. 580–600. DOI: [10.1086/173105](https://doi.org/10.1086/173105).
- Salaris, M. et al. (2015). “Post first dredge-up [C/N] ratio as age indicator. Theoretical calibration”. In: *A&A* 583, A87, A87. DOI: [10.1051/0004-6361/201526951](https://doi.org/10.1051/0004-6361/201526951). arXiv: [1509.06904](https://arxiv.org/abs/1509.06904) [[astro-ph.SR](#)].
- Salvadori, S., Á. Skúladóttir, and E. Tolstoy (2015). “Carbon-enhanced metal-poor stars in dwarf galaxies”. In: *MNRAS* 454, pp. 1320–1331. DOI: [10.1093/mnras/stv1969](https://doi.org/10.1093/mnras/stv1969). arXiv: [1506.03451](https://arxiv.org/abs/1506.03451).
- Santrich, O. J. K., C. B. Pereira, and N. A. Drake (2013). “Chemical analysis of giant stars in the young open cluster NGC 3114”. In: *A&A* 554, A2, A2.
- Sarajedini, A. (1999). “WIYN Open Cluster Study. III. The Observed Variation of the Red Clump Luminosity and Color with Metallicity and Age”. In: *AJ* 118, pp. 2321–2326. DOI: [10.1086/301112](https://doi.org/10.1086/301112).
- Schaller, G. et al. (1992). “New grids of stellar models from 0.8 to 120 solar masses at $Z = 0.020$ and $Z = 0.001$ ”. In: *A&AS* 96, pp. 269–331.
- Schiavon, R. P. et al. (2005). “A Library of Integrated Spectra of Galactic Globular Clusters”. In: *ApJS* 160, pp. 163–175. DOI: [10.1086/431148](https://doi.org/10.1086/431148). eprint: [astro-ph/0504313](https://arxiv.org/abs/astro-ph/0504313).
- Schiavon, R. P. et al. (2017). “APOGEE chemical abundances of globular cluster giants in the inner Galaxy”. In: *MNRAS* 466, pp. 1010–1018. DOI: [10.1093/mnras/stw3093](https://doi.org/10.1093/mnras/stw3093). arXiv: [1611.03086](https://arxiv.org/abs/1611.03086).

- Sengupta, S. and P. Garaud (2018). "The Effect of Rotation on Fingering Convection in Stellar Interiors". In: *ApJ* 862, 136, p. 136. DOI: [10.3847/1538-4357/aacbc8](https://doi.org/10.3847/1538-4357/aacbc8). arXiv: [1804.04258](https://arxiv.org/abs/1804.04258) [astro-ph.SR].
- Shetrone, M. et al. (2010). "Light-element Abundance Variations at Low Metallicity: The Globular Cluster NGC 5466". In: *AJ* 140, pp. 1119–1127. DOI: [10.1088/0004-6256/140/4/1119](https://doi.org/10.1088/0004-6256/140/4/1119). arXiv: [1009.0649](https://arxiv.org/abs/1009.0649).
- Shetrone, M. D. (2003). "Carbon Isotopes in Globular Clusters Down to the Bump in the Luminosity Function". In: *ApJ* 585, pp. L45–L48. DOI: [10.1086/374262](https://doi.org/10.1086/374262).
- Siess, L. (2009). "Thermohaline mixing in super-AGB stars". In: *A&A* 497, pp. 463–468. DOI: [10.1051/0004-6361/200811362](https://doi.org/10.1051/0004-6361/200811362).
- Siess, L., E. Dufour, and M. Forestini (2000). "An internet server for pre-main sequence tracks of low- and intermediate-mass stars". In: *A&A* 358, pp. 593–599.
- Smiljanic, R. et al. (2009). "CNONa and $^{12}\text{C}/^{13}\text{C}$ in giant stars of 10 open clusters". In: *A&A* 502, pp. 267–282.
- Smiljanic, R. et al. (2016). "The Gaia-ESO Survey: Sodium and aluminium abundances in giants and dwarfs. Implications for stellar and Galactic chemical evolution". In: 589, A115, A115. DOI: [10.1051/0004-6361/201528014](https://doi.org/10.1051/0004-6361/201528014). arXiv: [1602.03289](https://arxiv.org/abs/1602.03289) [astro-ph.SR].
- Smith, G. H. and S. L. Martell (2003). "Comparing Deep Mixing in Globular Cluster and Halo Field Giants: Carbon Abundance Data from the Literature". In: *Publ. Astron. Soc. Pac.* 115, pp. 1211–1219.
- Souto, D. et al. (2016). "Chemical Abundances in a Sample of Red Giants in the Open Cluster NGC 2420 from APOGEE". In: *ApJ* 830, 35, p. 35. DOI: [10.3847/0004-637X/830/1/35](https://doi.org/10.3847/0004-637X/830/1/35). arXiv: [1607.06102](https://arxiv.org/abs/1607.06102) [astro-ph.SR].
- Spina, L. et al. (2017). "The Gaia-ESO Survey: the present-day radial metallicity distribution of the Galactic disc probed by pre-main-sequence clusters". In: *A&A* 601, A70, A70. DOI: [10.1051/0004-6361/201630078](https://doi.org/10.1051/0004-6361/201630078). arXiv: [1702.03461](https://arxiv.org/abs/1702.03461) [astro-ph.SR].
- Spite, M. et al. (2005). "First stars VI - Abundances of C, N, O, Li, and mixing in extremely metal-poor giants. Galactic evolution of the light elements". In: *A&A* 430, pp. 655–668. DOI: [10.1051/0004-6361:20041274](https://doi.org/10.1051/0004-6361:20041274). eprint: [astro-ph/0409536](https://arxiv.org/abs/astro-ph/0409536).
- Spite, M. et al. (2006). "First stars IX - Mixing in extremely metal-poor giants. Variation of the $^{12}\text{C}/^{13}\text{C}$, [Na/Mg] and [Al/Mg] ratios". In: *A&A* 455, pp. 291–301. DOI: [10.1051/0004-6361:20065209](https://doi.org/10.1051/0004-6361:20065209). eprint: [astro-ph/0605056](https://arxiv.org/abs/astro-ph/0605056).
- Stahler, S. W., F. H. Shu, and R. E. Taam (1980). "The evolution of protostars. I - Global formulation and results". In: *ApJ* 241, pp. 637–654. DOI: [10.1086/158377](https://doi.org/10.1086/158377).
- Stancliffe, R. J. (2010). "The effects of thermohaline mixing on low-metallicity asymptotic giant branch stars". In: *MNRAS* 403, pp. 505–515.
- Stancliffe, R. J. et al. (2009). "The depletion of carbon by extra mixing in metal-poor giants". In: *MNRAS* 396, pp. 2313–2318.
- Stancliffe, R. J. et al. (2011). "Three-dimensional Hydrodynamical Simulations of a Proton Ingestion Episode in a Low-metallicity Asymptotic Giant Branch Star". In: *ApJ* 742, 121, p. 121.
- Steffen, M., B. Freytag, and H.-G. Ludwig (2005). "3D simulation of convection and spectral line formation in A-type stars". In: *13th Cambridge*

- Workshop on Cool Stars, Stellar Systems and the Sun*. Ed. by F. Favata, G. A. J. Hussain, and B. Battrick. Vol. 560. ESA Special Publication, p. 985. eprint: [astro-ph/0509464](https://arxiv.org/abs/astro-ph/0509464).
- Stellmach, S. and U. Hansen (2008). "An efficient spectral method for the simulation of dynamos in Cartesian geometry and its implementation on massively parallel computers". In: *Geochemistry, Geophysics, Geosystems* 9, Q05003, Q05003. DOI: [10.1029/2007GC001778](https://doi.org/10.1029/2007GC001778).
- Stellmach, S. et al. (2011). "Dynamics of fingering convection. Part 2 The formation of thermohaline staircases". In: *Journal of Fluid Mechanics* 677, pp. 554–571. DOI: [10.1017/jfm.2011.99](https://doi.org/10.1017/jfm.2011.99). arXiv: [1008.1808](https://arxiv.org/abs/1008.1808) [[physics.flu-dyn](https://arxiv.org/abs/1008.1808)].
- Suda, T. et al. (2008). "Stellar Abundances for the Galactic Archeology (SAGA) Database — Compilation of the Characteristics of Known Extremely Metal-Poor Stars". In: *Publ. Astron. Soc. Jpn.* 60, pp. 1159–1171. DOI: [10.1093/pasj/60.5.1159](https://doi.org/10.1093/pasj/60.5.1159). arXiv: [0806.3697](https://arxiv.org/abs/0806.3697).
- Sung, H. and M. S. Bessell (2010). "The Initial Mass Function and Young Brown Dwarf Candidates in NGC 2264. IV. The Initial Mass Function and Star Formation History". In: *AJ* 140, pp. 2070–2085. DOI: [10.1088/0004-6256/140/6/2070](https://doi.org/10.1088/0004-6256/140/6/2070). arXiv: [1010.0747](https://arxiv.org/abs/1010.0747) [[astro-ph.SR](https://arxiv.org/abs/1010.0747)].
- Sung, H. et al. (2002). "The Open Cluster NGC 2516. I. Optical Photometry". In: *AJ* 123, pp. 290–303. DOI: [10.1086/324729](https://doi.org/10.1086/324729).
- Suntzeff, N. B. (1981). "Carbon and nitrogen abundances in the giant stars of the globular clusters M3 and M13". In: *ApJS* 47, pp. 1–32. DOI: [10.1086/190750](https://doi.org/10.1086/190750).
- (1989). "CNO abundances in the metal-poor globular clusters." In: *The Abundance Spread within Globular Clusters: Spectroscopy of Individual Stars*. Ed. by G. Cayrel de Strobel, pp. 71–81.
- Sweigart, A. V. and J. G. Mengel (1979). "Meridional circulation and CNO anomalies in red giant stars". In: *ApJ* 229, pp. 624–641.
- Tadross, A. L. (2003). "Metallicity distribution on the galactic disk". In: *New Astronomy* 8, pp. 737–744. DOI: [10.1016/S1384-1076\(03\)00062-9](https://doi.org/10.1016/S1384-1076(03)00062-9).
- Tang, B. et al. (2017). "Two groups of red giants with distinct chemical abundances in the bulge globular cluster NGC 6553 through the eyes of APOGEE". In: *MNRAS* 465, pp. 19–31. DOI: [10.1093/mnras/stw2739](https://doi.org/10.1093/mnras/stw2739). arXiv: [1610.06763](https://arxiv.org/abs/1610.06763).
- Tautvaišienė, G. et al. (2000). "Chemical composition of evolved stars in the open cluster M 67". In: *A&A* 360, pp. 499–508. eprint: [astro-ph/0006001](https://arxiv.org/abs/astro-ph/0006001).
- Tautvaišienė, G. et al. (2005). "Chemical composition of evolved stars in the open cluster NGC 7789". In: *A&A* 431, pp. 933–942. DOI: [10.1051/0004-6361:20041935](https://doi.org/10.1051/0004-6361:20041935).
- Tautvaišienė, G. et al. (2015). "The Gaia-ESO Survey: CNO abundances in the open clusters Trumpler 20, NGC 4815, and NGC 6705". In: *A&A* 573, A55, A55. DOI: [10.1051/0004-6361/201424989](https://doi.org/10.1051/0004-6361/201424989). arXiv: [1411.2831](https://arxiv.org/abs/1411.2831) [[astro-ph.SR](https://arxiv.org/abs/1411.2831)].
- Tautvaišienė, G. et al. (2016). "CNO abundances and carbon isotope ratios in evolved stars of the open clusters NGC 2324, NGC 2477, and NGC 3960". In: *A&A* 595, A16, A16. DOI: [10.1051/0004-6361/201629273](https://doi.org/10.1051/0004-6361/201629273). arXiv: [1608.08398](https://arxiv.org/abs/1608.08398).
- Thompson, I. B. et al. (2009). "THE CLUSTER AGES EXPERIMENT (CASE). IV. ANALYSIS OF THE ECLIPSING BINARY V69 IN THE GLOBULAR

- CLUSTER 47 Tuc". In: *The Astronomical Journal* 139.2, pp. 329–341. DOI: [10.1088/0004-6256/139/2/329](https://doi.org/10.1088/0004-6256/139/2/329). URL: <https://doi.org/10.1088/0004-6256/139/2/329>.
- Traxler, A., P. Garaud, and S. Stellmach (2011a). "Numerically Determined Transport Laws for Fingering ("Thermohaline") Convection in Astrophysics". In: *ApJ* 728, L29, p. L29.
- (2011b). "Thermohaline Mixing at Low Prandtl Numbers". In: *American Astronomical Society Meeting Abstracts #217*. Vol. 43. Bulletin of the American Astronomical Society, p. 311.01.
- Trefzger, D. V. et al. (1983). "Carbon and nitrogen abundances in giant stars of the metal-poor globular cluster M15". In: *AJ* 266, pp. 144–159. DOI: [10.1086/160765](https://doi.org/10.1086/160765).
- Tsvilev, A. P. et al. (2013). "Determination of the primordial helium abundance from radio recombination line observations: New data. The source W51". In: *Astronomy Letters* 39, pp. 737–745. DOI: [10.1134/S106377371310006X](https://doi.org/10.1134/S106377371310006X).
- Twarog, B. A., K. M. Ashman, and B. J. Anthony-Twarog (1997). "Some Revised Observational Constraints on the Formation and Evolution of the Galactic Disk". In: *AJ* 114, p. 2556. DOI: [10.1086/118667](https://doi.org/10.1086/118667). eprint: [astro-ph/9709122](https://arxiv.org/abs/astro-ph/9709122).
- Ulrich, R. K. (1972). "Thermohaline Convection in Stellar Interiors." In: *ApJ* 172, p. 165.
- van Leeuwen, F. (2009). "Parallaxes and proper motions for 20 open clusters as based on the new Hipparcos catalogue". In: *A&A* 497, pp. 209–242. DOI: [10.1051/0004-6361/200811382](https://doi.org/10.1051/0004-6361/200811382). arXiv: [0902.1039](https://arxiv.org/abs/0902.1039) [[astro-ph](https://arxiv.org/abs/astro-ph).GA].
- VandenBerg, D. A., P. A. Bergbusch, and P. D. Dowler (2006). "The Victoria-Regina Stellar Models: Evolutionary Tracks and Isochrones for a Wide Range in Mass and Metallicity that Allow for Empirically Constrained Amounts of Convective Core Overshooting". In: *ApJS* 162, pp. 375–387. DOI: [10.1086/498451](https://doi.org/10.1086/498451). eprint: [astro-ph/0510784](https://arxiv.org/abs/astro-ph/0510784).
- Vassiliadis, E. and P. R. Wood (1993). "Evolution of low- and intermediate-mass stars to the end of the asymptotic giant branch with mass loss". In: *ApJ* 413, pp. 641–657.
- Vauclair, S. and S. Théado (2012). "Thermohaline Instabilities inside Stars: A Synthetic Study Including External Turbulence and Radiative Levitation". In: *ApJ* 753, 49, p. 49. DOI: [10.1088/0004-637X/753/1/49](https://doi.org/10.1088/0004-637X/753/1/49). arXiv: [1205.1329](https://arxiv.org/abs/1205.1329) [[astro-ph](https://arxiv.org/abs/astro-ph).SR].
- Vogt, H. (1925). "Zum Strahlungsgleichgewicht der Sterne". In: *Astronomische Nachrichten* 223, p. 229. DOI: [10.1002/asna.19242231403](https://doi.org/10.1002/asna.19242231403).
- von Zeipel, H. (1924a). "The radiative equilibrium of a rotating system of gaseous masses". In: *MNRAS* 84, pp. 665–683. DOI: [10.1093/mnras/84.9.665](https://doi.org/10.1093/mnras/84.9.665).
- (1924b). "The radiative equilibrium of a slightly oblate rotating star". In: *MNRAS* 84, pp. 684–701. DOI: [10.1093/mnras/84.9.684](https://doi.org/10.1093/mnras/84.9.684).
- Weiss, A. et al. (2004). "Models for extremely metal-poor halo stars". In: *A&A* 422, pp. 217–223.
- Williams, K. A. and M. Bolte (2007). "A Photometric and Spectroscopic Search for White Dwarfs in the Open Clusters NGC 6633 and NGC 7063". In: *AJ* 133, pp. 1490–1504. DOI: [10.1086/511675](https://doi.org/10.1086/511675). eprint: [astro-ph/0611929](https://arxiv.org/abs/astro-ph/0611929).

Yong, D. et al. (2016). “GRACES observations of young $[\alpha/\text{Fe}]$ -rich stars”.
In: *MNRAS* 459, pp. 487–495. DOI: [10.1093/mnras/stw676](https://doi.org/10.1093/mnras/stw676). arXiv:
[1603.07034](https://arxiv.org/abs/1603.07034) [[astro-ph.SR](https://arxiv.org/archive/astro-ph)].